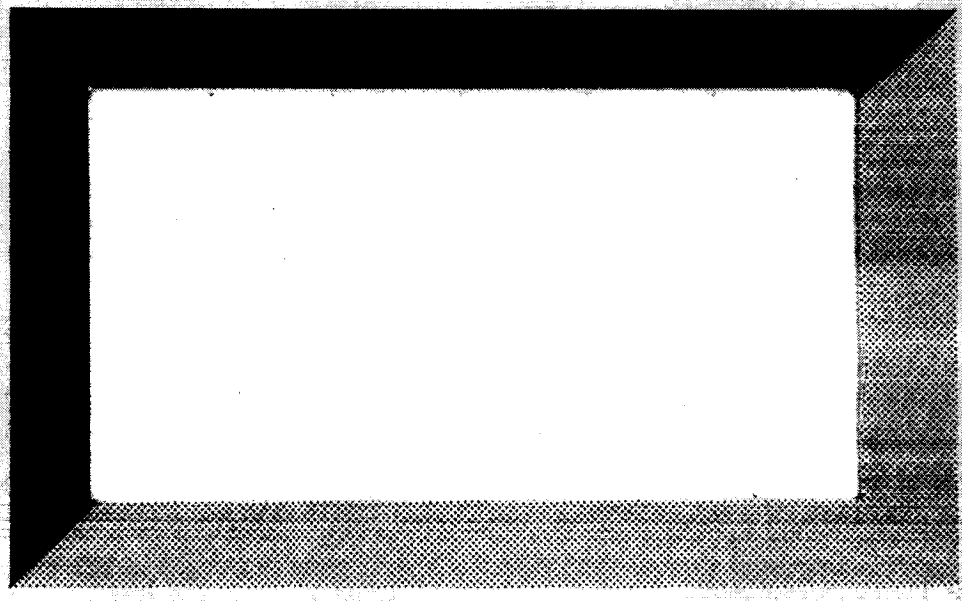

GAS TURBINE LABORATORY

MASSACHUSETTS INSTITUTE OF TECHNOLOGY

CAMBRIDGE, MASSACHUSETTS

A LINEARIZED EULER ANALYSIS OF UNSTEADY FLOWS IN TURBOMACHINERY

by

Kenneth C. Hall

GTL Report No. 190 June 1987

A LINEARIZED EULER ANALYSIS OF UNSTEADY FLOWS IN TURBOMACHINERY

by

Kenneth C. Hall

Abstract

A method for calculating unsteady flows in cascades is presented. The model, which is based on the linearized unsteady Euler equations, accounts for blade loading, shock motion, wake motion, and blade geometry. The mean flow through the cascade is determined by solving the full nonlinear Euler equations. Assuming the unsteadiness in the flow is small, then the Euler equations are linearized about the mean flow to obtain a set of linear variable coefficient equations which describe the small amplitude, harmonic motion of the flow. These equations are discretized on a computational grid via a finite volume operator and solved directly subject to an appropriate set of linearized boundary conditions. The steady flow, which must be calculated prior to the unsteady flow, is found via a Newton iteration procedure. Using this procedure, the nonlinear steady Euler equations are solved as a series of linear problems, each very similar to the unsteady linear problem. The similarity of the steady and unsteady solvers greatly reduces the effort which is needed to develop the two codes.

An important feature of the analysis is the use of shock fitting to model steady and unsteady shocks. Use of the Euler equations with the unsteady Rankine-Hugoniot shock jump conditions correctly models the generation of steady and unsteady entropy and vorticity at shocks. In particular, the low frequency shock displacement is correctly predicted.

Results of this method are presented for a variety of test cases. Predicted unsteady transonic flows in channels are compared to full nonlinear Euler solutions obtained using time-accurate, time-marching methods. The agreement between the two methods is excellent for small to moderate levels of flow unsteadiness. The method is also used to predict unsteady flows in cascades due to blade motion (the flutter problem) and incoming disturbances (the gust response problem). Comparison of the predicted unsteady flow to other semi-analytical and numerical methods gives good agreement. The linearized Euler method requires substantially less computational effort than the time-marching procedures, making the present method useful for aeroelastic analyses.

Acknowledgments

The primary funding for this research was provided by a grant from NASA Lewis Research Center (Grant Number NSG 3079) which was monitored by Dr. John Adamczyk, Mr. Donald Boldman, and Dr. Dan Hoyniak. Additional support was provided by the Aircraft Engine Business Group of the General Electric Company, the Alison Gas Turbine Operations of the General Motors Corporation, and the Lockheed-Georgia Company. The author gratefully acknowledges the generous support of the Fannie and John Hertz Foundation.

Contents

1 Introduction 6

2 Analysis of Quasi-One-Dimensional Flows 14
- 2.1 Linearized Quasi-One-Dimensional Euler Equations 15
- 2.2 Solution of the Steady Euler Equations 18
  - 2.2.1 Newton Iteration Equations 18
  - 2.2.2 Discretization of the Newton Iteration Equations 19
  - 2.2.3 Boundary Conditions 20
  - 2.2.4 Assembly of the Discrete Equations 21
  - 2.2.5 Subsonic Flow in a Converging-Diverging Channel 26
  - 2.2.6 Steady Shock Fitting 26
  - 2.2.7 Steady Transonic Channel Flow 32
- 2.3 Solution of the Linearized Unsteady Euler Equations 36
  - 2.3.1 Discretization of the Linearized Euler Equations 39
  - 2.3.2 Unsteady Channel Flow Boundary Conditions 39
  - 2.3.3 Assembly of the Discrete Equations 40
  - 2.3.4 Unsteady Subsonic Results 40
  - 2.3.5 Unsteady Shock Fitting 42
  - 2.3.6 Assembly of Unsteady Transonic Equations 45
  - 2.3.7 Unsteady Transonic Results 45
- 2.4 Summary 48

3 Advantages and Limitations of the Linearized Euler Analysis 49
- 3.1 Nonlinearities in Unsteady Flow 50
  - 3.1.1 Fourier Analysis of Unsteady Flows 51
  - 3.1.2 Numerical Examples 55
- 3.2 Comparison to Full Potential Theory 65
- 3.3 Summary 75

4 Fundamentals of Two-Dimensional Linearized Euler Theory 76
- 4.1 The Conservation Laws 77
  - 4.1.1 Integral Form of the Conservation Laws 77
  - 4.1.2 Integral Form of the Conservation Laws for Deforming Volumes . 79
  - 4.1.3 Differential Form of the Conservation Laws 80
- 4.2 Linearized Euler Equations 82

4.2.1 Field Equation Linearization 83
4.3 Solution of the Steady Euler Equations 86
4.3.1 The Linearized Newton Iteration Equations 86
4.3.2 Discretization of the Newton Iteration Equations 87
4.3.3 Steady Flow Boundary Conditions 92
4.3.4 Matrix Equation Structure 94
4.4 Unsteady Flow Calculations 97
4.4.1 Linearized Unsteady Euler Equation Discretization 98
4.4.2 Boundary Conditions of the Unsteady Flow Solution 99
4.4.3 Matrix Equations 103
4.5 Summary 103

5 Extensions of Linearized Euler Theory to Cascade Flow 104
5.1 Moving Airfoil Boundaries 106
5.2 Flow Discontinuities 108
5.2.1 Unsteady Shock Jump Conditions 109
5.2.2 Unsteady Wake Jump Conditions 112
5.2.3 Newton Iteration Solution Procedure for Flows with Shocks and Wakes 114
5.3 Periodic and Far Field Boundary Conditions 116
5.4 Surface Pressures 122
5.4.1 Moving Airfoils 122
5.4.2 The Shock Impulse 123
5.5 Summary 123

6 Results 125
6.1 The Flow in a Hyperbolic Channel 125
6.1.1 Accuracy of the Steady Solver 127
6.1.2 Convergence of Subsonic Solutions 132
6.1.3 Steady Choked Flow in a Hyperbolic Channel 134
6.1.4 Effect of Grid Resolution on Shock Location 137
6.1.5 Unsteady Subsonic Flow in a Hyperbolic Channel 137
6.1.6 Unsteady Transonic Flow in a Hyperbolic Channel 139
6.2 Two-Dimensional Transonic Diffuser Flow 146
6.2.1 Steady Diffuser Flow 147
6.2.2 Unsteady Transonic Diffuser Flow 149
6.3 The Gostelow Cascade 156
6.3.1 Steady Flow Through the Gostelow Cascade 156
6.3.2 Unsteady Flow in the Gostelow Cascade 159

7 Conclusions and Recommendations 177

Chapter 1

Introduction

The flutter and forced response of turbomachinery blading has been and continues to be a recurring problem in the development of turbomachinery. Nevertheless, the ability to predict these two aeroelastic phenomena has remained illusive. Although the structural dynamic modelling of rotors has steadily progressed over the years, the modelling of the unsteady aerodynamics of cascades still needs much improvement. The objective of this research is to model unsteady transonic flows in cascades using a computational scheme based on the linearized Euler equations. To date, much theoretical work has been performed in the field of unsteady flow in cascades. Most of it, however, has been based on the assumption of isentropic irrotational flow even through shocks. These methods do not allow for the production of steady and unsteady entropy and vorticity across shocks. This weakness in potential theory can, under certain circumstances, produce serious errors in the predicted shock motion and unsteady blade loading. A new method based on the linearized Euler equations will be presented in this report. The method correctly accounts for the production of steady and unsteady entropy and vorticity across shocks and therefore predicts unsteady transonic flows more accurately.

Theoretical research into unsteady flows in cascades has steadily progressed over the past three decades. The methods used can be roughly divided into three types: Analytical methods, semi-analytical methods, and numerical methods. In analytical methods, the partial differential equations which govern the unsteady flow in a cascade are solved exactly using applied mathematical techniques. Although closed-form solu-

tions can sometimes be obtained, the resulting complicated expressions must usually be evaluated numerically to understand them. Furthermore, these solutions have only been found for extremely simplified geometries. The semi-analytical methods use singularities such as vortices distributed along the surface of the airfoils and wakes to model the steady and unsteady flow. In fact, the distinction between the analytical and semi-analytical methods is small. In practice, both usually reduce the problem to integral equations involving kernel functions. Because of the complexity in determining these kernel functions for complicated flows, the mean flow through the cascade is usually assumed to be uniform or nearly uniform. Hence, the flow model often bears little resemblance to flows found in actual turbomachinery. The third approach is to discretize the field equations which describe the unsteady flow and solve them numerically. This computational approach has the advantage that arbitrary airfoil shapes can be analyzed. Furthermore, flow features such as blade thickness, blade loading, and moving shocks and wakes are accounted for. This ability to analyze fairly general geometries is obtained only with considerable computational effort. The computational methods can be subdivided further into two categories: time-marching and linearized harmonic. With time marching methods, the unsteady flow field is found as a function of time by marching a flow simulation in time. This approach, although straightforward, is computationally expensive as many time steps must be taken to reach a periodic state. In the linearized harmonic methods, the nonlinear field equations are linearized about some nominal mean flow, resulting in a set of linear variable coefficient field equations for the unsteady flow perturbations. If the additional simplifying assumption is made that the unsteady flow is harmonic in time, these equations are reduced to a set of time-independent partial differential equations for the complex amplitudes of the unsteady flow properties. These linearized harmonic field equations are discretized and solved directly. This is the approach taken in the present research.

Previous Work on Unsteady Aerodynamics

Whitehead [1] studied the unsteady flow of an incompressible fluid through a cascade of vibrating flat plate airfoils. In this model it is assumed that the mean flow is uniform

and undeflected by the cascade. Unsteady vorticity is distributed along the airfoils and shed vorticity is convected along the wake. The bound vorticity is distributed such that the velocity due to the vorticity is equal to the upwash velocity on the airfoil surfaces and the Kutta condition is satisfied. This model, however, failed to predict the experimentally observered bending flutter. Later Whitehead [2] extended his model to that of a cascade of flat plat airfoils for which the mean flow was not uniform, but was deflected or turned by the cascade. This new model did predict bending flutter and showed the importance of steady loading on the unsteady pressure distributions on vibrating airfoils. Atassi and Akai [3,4] used a model in which point singularities were distributed along the surface of a two-dimensional airfoil surface of finite camber and thickness. With this model they studied steady and unsteady incompressible flows through a cascade of thick cambered airfoils. Their results, like Whitehead's, showed the importance of the steady blade loading on the unsteady flow in the cascade.

Lane and Friedman [5], Whitehead [6], and Smith [7] all analyzed flat plate cascades vibrating in a uniform subsonic flow. With compressibility there is the added complication of acoustic modes and *acoustic resonance*. Under certain circumstances, acoustic waves will propagate away from the rotor unattenuated, while in other cases, the waves will be *cut-off*. Smith [7] performed experiments to validate his model. For unloaded cascades, the theory is successful in predicting the cut-off behavior as well as the amplitude of the acoustic waves. For steadily loaded cascades, the amplitudes of the acoustic waves were not predicted as well.

Several investigators [8,9,10,11,12] have studied the problem of a cascade of vibrating flat plate airfoils in a uniform supersonic flow which is axially subsonic. Although the analysis techniques are differ, all these investigators studied the same governing differential equations and boundary conditions. Hence, it is not surprising that all the results from these models are essentially the same. These models indicate that bending flutter will not occur at the reduced frequencies and Mach numbers at which real compressors actually exhibit bending flutter. Bendiksen [13] later used a perturbation scheme to calculate the effects due to small amounts of thickness, camber, and angle of attack as well as shock motion, and demonstrated the important role of shock motion

in flutter prediction. Goldstein, Braun, and Adamczyk [14] have proposed a model in which the steady flow is everywhere parallel but has a strong nonisentropic in-passage shock. Hence, although there is no turning, the blade row diffuses the flow due to the presence of a shock. That is to say that the blades carry a steady load due to the pressure rise across the shock. Further, in this theory the unsteady shock motion is correctly accounted for as well as the vorticity and entropy generation at the shock. Using this model, bending flutter is predicted for reduced frequencies (based on semichord) below about 0.3. This result is more in keeping with experimentally observed bending flutter in compressors operating at high back pressures.

The lesson learned from these analytical and semi-analytical models is clear. To model accurately the flow in a cascade, one must include the effects due to the steady blade loading. This means that the camber and thickness of the airfoil need to be accounted for, as well as the presence of shocks in the flow. Except for the incompressible case, this forces the investigator to turn to numerical methods because it is not possible to analytically solve linear field equations with complicated variable coefficients. To investigate subsonic flows, Verdon and Caspar [15] numerically determined the mean flow about a cascade of airfoils in subsonic flow using the *full potential* equations. The full potential equations were then linearized about the mean flow and solved numerically using a finite difference approximation. The computed unsteady pressure distribution agreed well with tests conducted by Carta [16] on a linear cascade of oscillating airfoils. Whitehead and Grant [17] performed a similar analysis but used finite elements to discretize the field equations. Later, Verdon and Caspar [18] extended their model to handle transonic flows. To accurately model the effect of shock motion, shock fitting was used. Whitehead [19] also extented his model to the transonic regime but used shock capturing to model the shock motion. Both models require some form of artificial viscosity to stabilize the calculations in the supersonic regions.

Several investigators have used time-marching schemes to analyze unsteady flows in turbomachinery. Ni and Sisto [20] used a time-marching Euler method to calculate the pressure loads on vibrating flat plate airfoils in compressible flow. Actually, the method can be considered a hybrid of the time-marching and harmonic techniques

as the quantities which are time-marched are the harmonic flow variables. Recently, Giles [21,22] has developed an Euler time-marching method based on Ni's Lax-Wendroff method [23] to study wake/rotor interaction. The ability to handle unequal rotor/stator pitches is accomplished by inclining the computational plane in time. This allows the calculations to be performed in a single blade passage. The code has the advantage that nonlinear, anharmonic flows can be modelled. However, for numerical stability, the time integration step size used in the integration must be fairly small. The maximum allowable time step is governed by the so-called CFL number. Because of this CFL number restriction, the size of the time steps are limited roughly by the size of the smallest cell in the domain. Hence, for accurate resolution of the flow, the required computational times become quite large.

Description of the Linearized Euler Analysis

In reality, both steady and unsteady flows in turbomachinery are extremely complicated. The fluid is viscous and heat-conducting and is most accurately described by the Navier-Stokes equations. However, if the Reynolds number is sufficiently high and the Prandtl number is order unity, and separation doesn't occur, the viscous and heat transfer effects are confined to narrow regions near the airfoil surfaces and in the wakes. Under these circumstances, the Euler equations are a good approximation to the behavior of the flow. The unsteady Euler equations are the starting point of the linearized Euler analysis. The Euler equations correctly account for the production of entropy and vorticity at shocks and therefore are the natural choice for calculating unsteady transonic flows.

The method is divided into two mains parts. The first step is to determine the steady flow. In order to fully account for such effects as blade thickness, loading, and strong in-passage shocks, the unsteady Euler equations should be linearized about the correct mean flow. So despite the fact that we are primarily interested in the unsteady behavior of the fluid, the steady flow will also have to be calculated. Because of the periodicity in a cascade, the flow can be computed in a single blade passage. Within this passage, the steady Euler equations are discretized on a computational grid using a conservative finite volume operator. The discretized equations are solved subject to an appropriate

set of boundary conditions using a Newton iteration procedure. Using this procedure, the nonlinear Euler equations are transformed into a series of linear equations [24,25]. These are solved directly using Gaussian elimination. The Newton iteration procedure is extremely efficient and usually converges within five to ten iterations.

Once the steady solution has been obtained, the unsteady flow can be calculated. The nonlinear time-dependent Euler equations are linearized about the steady solution to obtain the linearized unsteady equations. These equations are linear with variable coefficients and describe the small disturbance behavior of the flow. Since many unsteady flows of interest are periodic in time, the unsteady flow is assumed to be harmonic in time. Under this assumption, the explicit time dependency is eliminated from the problem. As with the steady Euler equations, the unsteady flow is computed in a single blade passage. The equations are discretized on a computational grid using a finite volume operator.

The application of the unsteady boundary conditions is a crucial step in the formulation of the problem. For example, because the computational domain is finite, an artificial boundary must be placed in front of the cascade. Waves which propagate from inside the blade passage must pass through this boundary without being reflected if the unsteady flow is to be correctly predicted. So-called nonreflecting boundary conditions are applied by use of a characteristic wave analysis.

An important feature of the present method is that steady and unsteady shocks and wakes are fitted rather than captured. Most CFD codes use shock capturing to model shocks. This usually means that some artificial viscosity is added to the scheme. The resulting captured shock is not a sharp discontinuity but is smeared over several grid points. The advantage to this approach is that shocks are automatically captured where ever they happen to be, but increased grid resolution is needed in the area of the shock to produce a good approximation to a jump discontinuity. Using shock fitting, the position of the shock is modelled explicitly with unsteady shock-jump conditions applied across the shock [26,27]. These conditions, like the Euler equations themselves, can be linearized to obtain a set of linearized shock jump conditions. Furthermore, the jump conditions fully account for the production of unsteady entropy and vorticity

through shocks. This is a major improvement over the current linearized full potential theories. In particular, at low reduced frequencies, the shock displacement predicted by the linearized potential theory is too large.

Outline

In Chapter 2 of this report, the basic method for solving quasi-one-dimensional steady and unsteady flows is presented. The purpose is to introduce the fundamental ideas without some of the complicating details required to analyze two-dimensional flows. Furthermore, the quasi-one-dimensional model problems presented in this chapter are ideal test vehicles for validating the basic methodology. In this chapter, all of the fundamental steps needed to analyze steady and unsteady flows are presented. They include the linearization of the nonlinear Euler equations, the discretization of the linearized Euler equations, the linearization and discretization of unsteady nonlinear boundary conditions, and the implementation of the direct solver used to solve these equations. Also discussed is the method of steady and unsteady shock fitting in one-dimension. Finally, the linearized Euler method is used to analyze model unsteady flow problems. These results are compared to those from a time-marching Euler code to demonstrate the validity of the linearized Euler method.

In Chapter 3, some of the advantages and limitations of the linearized Euler method are discussed. Using an existing time marching algorithm to solve quasi-one-dimensional model problems, the effects of nonlinearities are investigated. As will be shown, the nonlinear effects enter mainly through higher harmonics. The fundamental harmonic component is accurately represented by the linearized theory for small to moderate levels of unsteadiness. Also discussed are the advantages the linearized Euler method offers over linearized full potential methods. The latter represent the current state of the art in linearized theories for solving for unsteady flows through cascades. The fundamental assumption made in the potential methods is that the flow is isentropic and irrotational. Hence, although the methods are efficient, they do not correctly account for the unsteady shock behavior in transonic flows. This is illustrated by examining the linearized Euler and linearized potential solutions for simple quasi-one-dimensional

model problems.

In Chapter 4, the theory and numerical method for solving two-dimensional channel flow problems is presented. As in the one-dimensional problem, this process can be broken down into the linearization of the Euler equations, the linearization of the unsteady boundary conditions, the discretization of the field and boundary-condition equations, and the numerical solution of the discretized equations. In Chapter 5, the discussion of the two-dimensional theory and numerical method continues. Discussed are the extensions of the basic theory needed to calculate cascade flows. These include discussions of steady and unsteady shock fitting, wake fitting, moving airfoil boundary conditions, and nonreflecting far-field boundary conditions.

In Chapter 6, a variety of two-dimensional steady and unsteady flow calculations are presented. These include steady subsonic and transonic channel flows, unsteady subsonic and transonic channel flows, and steady and unsteady cascade flows. The unsteady cascade flows presented are of two types. The flutter problem, where the motion of the blades are prescribed and the unsteady blade loads are to be calculated, and the gust response problem, where an incoming gust is specified and the unsteady airloads on the stationary blades are to be calculated.

Finally in Chapter 7, some conclusions are drawn about the utility of the present method, and suggestions are given for areas of future research needed to improve the present method.

Chapter 2

Analysis of Quasi-One-Dimensional Flows

In this chapter, the linearized Euler analysis is applied to quasi-one-dimensional channel flow problems. By studying these relatively simple model problems, the fundamental linearized Euler analysis can be illustrated without some of the complications which arise in two-dimensional problems. In Section 2.1 the linearization of the Euler equations is examined. This linearization reduces the nonlinear time-dependent Euler equations to a set of linear variable-coefficient partial differential equations. The linear equations describe the small disturbance behavior of the unsteady flow. Because the Euler equations are linearized about a steady flow solution, this solution must be determined before the analysis of the linearized unsteady flow can be performed. In Section 2.2 the method for computing steady Euler flows is presented. The nonlinear Euler equations are solved using a Newton iteration technique. This method is not only computationally efficient, but also reduces the nonlinear problem to a series of linear problems each similar to the linearized unsteady Euler equations. This greatly reduces the development effort required to write both a steady and unsteady code since many the components will be nearly identical. Some sample subsonic and transonic quasi-one-dimensional flows will be calculated using this approach. In Section 2.3 the method for solving the linearized Euler equations will be discussed. As with the steady prob-

lem, the steps to be taken are the discretization of the field equations, and boundary conditions, the assembly of the equations into matrix form, and the solution of these linear equations.

2.1 Linearized Quasi-One-Dimensional Euler Equations

Consider the unsteady Euler equations for flow in a quasi-one-dimensional channel with area variation $A(x)$ as shown in Figure 2.1. The mass, momentum, and energy conservation equations are

$$\frac{\partial}{\partial t}A\mathbf{U} + \frac{\partial}{\partial x}A\mathbf{F} + A\frac{\partial}{\partial x}\mathbf{P} = 0 \tag{2.1}$$

where

$$\mathbf{U} = \begin{bmatrix} \rho \\ \rho u \\ e_0 \end{bmatrix} \quad \mathbf{F} = \begin{bmatrix} \rho u \\ \rho u^2 \\ \rho u h_0 \end{bmatrix} \quad \mathbf{P} = \begin{bmatrix} 0 \\ p \\ 0 \end{bmatrix}$$

where ρ, u, p, e_0, and h_0 are the static density, velocity, static pressure, total internal energy per unit volume, and total specific enthalpy, respectively. By definition, the total specific enthalpy is given by

$$h_0 = \frac{p+e}{\rho} \tag{2.2}$$

The total internal energy is the sum of the intrinsic energy plus the kinetic energy. For an ideal gas with constant specific heats, the intrinsic energy is $c_v T = \frac{1}{\gamma-1}\frac{p}{\rho}$. Under this assumption, Equation 2.2 can be rewritten as

$$h_0 = \frac{\gamma}{\gamma-1}\frac{p}{\rho} + \frac{1}{2}u^2 \tag{2.3}$$

Elimination of the total enthalpy and energy in favor of the three other primitive variables gives

$$\mathbf{U} = \begin{bmatrix} \rho \\ \rho u \\ \frac{p}{\gamma-1} + \frac{1}{2}\rho u^2 \end{bmatrix} \quad \mathbf{F} = \begin{bmatrix} \rho u \\ \rho u^2 \\ \frac{\gamma}{\gamma-1}pu + \frac{1}{2}\rho u^3 \end{bmatrix} \quad \mathbf{P} = \begin{bmatrix} 0 \\ p \\ 0 \end{bmatrix}$$

This form of the Euler equations will be used throughout, although the methods used here could be extended to consider a non-ideal gas if desired. These unsteady Euler

equations are strictly valid for inviscid adiabatic flow of a perfect gas. If the Reynolds number is sufficiently large and no separation occurs, however, they provide an adequate representation of the flow outside thin viscous boundary layers and wakes.

Note in particular that the unsteady Euler equations are nonlinear in the primitive variables ρ, u, and p. An exact solution would have to take into account these nonlinearities. One approach is to simulate the flow using a time marching simulation. Given enough spatial and temporal resolution and computer time, one could find the full nonlinear time-dependent solution. This approach, while straightforward, would be computationally expensive, and for many problems of interest, the effects of the nonlinearities are small and can be ignored.

The approach taken in the present research is to linearize the Euler equations about some nominal mean flow. If the unsteady part of the flow is small compared to the mean flow values, then this is a reasonable approximation to the full nonlinear Euler equations. The linearized equations could also be solved by time-marching. However, many unsteady flows of interest are periodic in time, especially in the area of aeroelasticity. Hence, the further simplification can be introduced that the unsteady part of the flow is harmonic in time. This assumption removes the explicit time dependency from the governing equations. Hence, the unsteady problem is reduced to solving a set of linear time-independent ordinary differential equations.

To start the linearization process, the flow can be expressed as the sum of two parts: a mean or steady flow component which satisfies the steady nonlinear Euler equations, and a small unsteady perturbation which is harmonic in time, i.e.,

$$\hat{\rho}(x,y,t) = \bar{\rho}(x,y) + \rho(x,y)e^{j\omega t} \tag{2.4}$$

$$\hat{u}(x,y,t) = U(x,y) + u(x,y)e^{j\omega t} \tag{2.5}$$

$$\hat{p}(x,y,t) = P(x,y) + p(x,y)e^{j\omega t} \tag{2.6}$$

where the perturbation variables ρ, u, and p are small compared to the mean-flow counterparts $\bar{\rho}$, U, and P, and are complex due to the harmonic motion assumption. Note the change in notation made to distinguish the different parts of the flow. The steady-flow variables are represented by upper case characters or by lower case characters with

an overbar, the perturbation variables are represented by lower case characters, and the total flow which is the sum of the two is now represented by lower case characters with a circumflex.

Substitution of the foregoing expansion into the one-dimensional Euler equations and collection of the zeroth- and first-order terms results in the one-dimensional steady Euler and linearized unsteady Euler equations. The zeroth order equations are just the original nonlinear Euler equations (Equation 2.1) with the time derivative term set to zero. For small unsteady perturbations the mean flow is independent of the unsteady part of the flow. The first-order equations are given by

$$j\omega A\mathbf{B_1}\mathbf{u} + \frac{\partial}{\partial x}A\mathbf{B_2}\mathbf{u} + A\frac{\partial}{\partial x}\mathbf{B_3}\mathbf{u} = 0 \tag{2.7}$$

where $\mathbf{u}$ is the vector of perturbation variables ρ, u, and p, and $\mathbf{B_1}$, $\mathbf{B_2}$, and $\mathbf{B_3}$ are variable coefficient matrices which depend on the mean flow variables $\bar{\rho}$, U, and P. The coefficient matrices are given by

$$\mathbf{B_1} = \frac{\partial \mathbf{U}}{\partial \mathbf{u}} = \begin{bmatrix} 1 & 0 & 0 \\ U & \bar{\rho} & 0 \\ \frac{1}{2}U^2 & \bar{\rho}U & \frac{1}{\gamma-1} \end{bmatrix}$$

$$\mathbf{B_2} = \frac{\partial \mathbf{F}}{\partial \mathbf{u}} = \begin{bmatrix} U & \bar{\rho} & 0 \\ U^2 & 2\bar{\rho}U & 0 \\ \frac{1}{2}U^3 & \frac{\gamma}{\gamma-1}P + \frac{3}{2}\bar{\rho}U^2 & \frac{\gamma}{\gamma-1}U \end{bmatrix}$$

$$\mathbf{B_3} = \frac{\partial \mathbf{P}}{\partial \mathbf{u}} = \begin{bmatrix} 0 & 0 & 0 \\ 0 & 0 & 1 \\ 0 & 0 & 0 \end{bmatrix}$$

These unsteady perturbation equations, and their two-dimensional equivalents (to be derived in Chapter 4), are the foundation of the analysis used in this work to analyze unsteady flows. They are valid so long as the unsteady perturbation variables are small compared to the mean-flow variables. In the next chapter, it will be shown using numerical experiments that the perturbations equations are a useful approximation to the full nonlinear Euler equations for fairly moderate levels of unsteadiness.

The general approach for solving unsteady flows is as follows. First, the mean flow is calculated using the steady Euler equations. This solution is then used to calculate the variable coefficients in the linearized unsteady equations. The linearized Euler equations are discretized and solved numerically to obtain the unsteady flow solution. The remainder of this chapter is devoted to explaining the details of this approach as applied to subsonic and transonic channel flows, as well as to presenting solutions to some model problems.

2.2 Solution of the Steady Euler Equations

2.2.1 Newton Iteration Equations

Before the unsteady flow can be calculated, one must first have solved for the steady flow. Although the purpose of this research is to better understand unsteady flows and to develop a linearized Euler solver, a steady Euler solver is also needed to calculate the steady flow which is used as the input to the unsteady Euler solver. Fortunately, the steady nonlinear Euler equations can be solved using a Newton iteration procedure [24,25] which converts the nonlinear ordinary differential equations into a series of linear ordinary differential equations each very similar to the linearized Euler problem. Again, the flow is assumed to be composed of two components: a base solution which is *not* assumed to satisfy the steady Euler equations, plus a small perturbation quantity which when added to the base solution will give an improved estimate of the true solution.

$$\hat{\rho}(x,y,t) = \bar{\rho}(x,y) + \rho(x,y) \tag{2.8}$$

$$\hat{u}(x,y,t) = U(x,y) + u(x,y) \tag{2.9}$$

$$\hat{p}(x,y,t) = P(x,y) + p(x,y) \tag{2.10}$$

where the correction perturbation variables ρ, u, and p are assumed to be small. Substitution of Equation 2.8-2.10 into the steady Euler equations, again collecting first-order perturbation terms, and neglecting higher order effects gives

$$\frac{\partial}{\partial x} A\mathbf{B}_2\mathbf{u} + A\frac{\partial}{\partial x}\mathbf{B}_3\mathbf{u} = -\left(\frac{\partial}{\partial x} A\mathbf{F} + A\frac{\partial}{\partial x}\mathbf{P}\right) \tag{2.11}$$

The terms on the right-hand-side are the residuals of the full nonlinear steady Euler equations evaluated from the current estimate of the flow ($\bar{\rho}$, U, and P) through the channel; those on the left-hand-side represent the first-order effect the correction. Equation 2.11 is solved numerically to determine the correction perturbations. These corrections are then added to the previous estimate of the solution to obtain an improved solution. Then, starting with this updated estimate of the flow, the entire process is repeated until it converges, although convergence is not guaranteed. When the method works, convergence is usually quite fast with a converged solution obtained in five to ten iterations.

Note the similarity of the Newton iteration perturbation equation (Equation 2.11) to the linearized unsteady Euler equations (Equation 2.7). The matrices $\mathbf{B_2}$ and $\mathbf{B_3}$ in Equation 2.11 are the same as those in Equation 2.7. The Newton iteration technique is an extremely efficient one for calculating steady one-dimensional and two-dimensional flows. Furthermore, because of the similarities to the unsteady problem, the effort required to construct the steady and unsteady codes is greatly reduced. Many components of the two codes are nearly identical.

2.2.2 Discretization of the Newton Iteration Equations

Consider first the discretization of the linearized steady Euler equations (Equation 2.11). These equations are discretized on a one-dimensional computational grid as shown in Figure 2.1. The grid has I nodes and hence $I-1$ conservation cells. At each of the nodes, the values of the primitive variables are stored. For each of the $I-1$ cells, the conservation equations are approximated by a central difference operator operating about the cell center. Hence, the Newton iteration equations for the steady flow are approximated at the ith cell by

$$\frac{(A\mathbf{B_2u})_{i+1} - (A\mathbf{B_2u})_i}{\Delta x_i} + A_{i+\frac{1}{2}} \frac{(\mathbf{B_3u})_{i+1} - (\mathbf{B_3u})_i}{\Delta x_i} = - \frac{(A\mathbf{F})_{i+1} - (A\mathbf{F})_i}{\Delta x_i} - A_{i+\frac{1}{2}} \frac{\mathbf{P}_{i+1} - \mathbf{P}_i}{\Delta x_i} \tag{2.12}$$

where

$$\Delta x_i = x_{i+1} - x_i$$

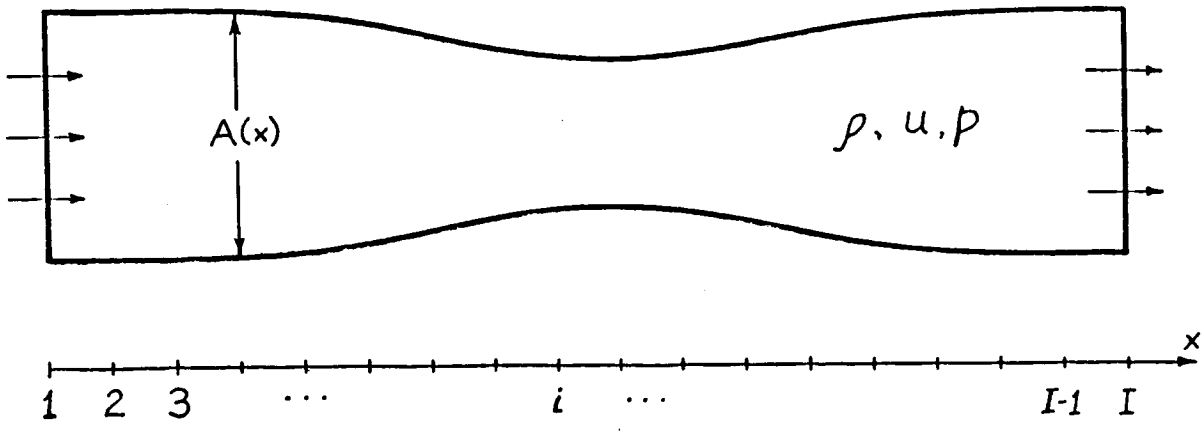

Figure 2.1: Channel geometry and one-dimensional grid use in numerical calculation of steady and unsteady flow

$$A_{i+\frac{1}{2}} = \frac{1}{2}(A_i + A_{i+1})$$

It can be shown that these difference equations are second order accurate. That is to say that the difference between the computed solution and the exact solution will be $O(\Delta x^2)$. These difference equations provide $3(I-1)$ equations for $3I$ unknowns. Still to be specified are the upstream boundary and downstream boundary conditions. The boundary conditions, like the field equations must be linearized for use in the Newton iteration solver. This linearization will be discussed in the next section.

2.2.3 Boundary Conditions

The boundary conditions, like the Euler equations, will, in general, be nonlinear functions of the primitive variables. Hence, to apply the boundary conditions in the Newton iteration scheme requires that they be linearized. In particular, for subsonic inlet flow, two boundary conditions must be specified. Usually the total pressure and density are given at the inlet of the channel. The total pressure and density are related to the velocity and the static values of pressure and density by

$$\frac{\gamma \hat{p}}{\hat{\rho}} + \frac{\gamma - 1}{2}\hat{u}^2 = \frac{\gamma P_{T0}}{\rho_{T0}} \tag{2.13}$$

and

$$\frac{\hat{p}}{\hat{\rho}^{\gamma}} = \frac{P_{T0}}{\rho_{T0}^{\gamma}} \tag{2.14}$$

These two inlet boundary conditions are linearized for the Newton iteration procedure just as the field equations were, i.e., by expanding the nonlinear boundary conditions in a perturbation series and collecting terms of first order to give

$$\frac{\gamma}{\overline{\rho}}p - \frac{\gamma P}{\overline{\rho}^2}\rho + (\gamma - 1)U u = \frac{\gamma P_{T0}}{\rho_{T0}} - \left(\frac{\gamma P}{\overline{\rho}} + \frac{\gamma - 1}{2}U^2\right) \tag{2.15}$$

and

$$\frac{1}{\overline{\rho}^{\gamma}}p - \frac{\gamma P}{\overline{\rho}^{\gamma+1}}\rho = \frac{P_{T0}}{\rho_{T0}^{\gamma}} - \frac{P}{\overline{\rho}^{\gamma}} \tag{2.16}$$

At the downstream boundary, the static pressure is prescribed so that

$$\hat{p} = p_{\text{exit}} \tag{2.17}$$

which when linearized becomes

$$p = p_{\text{exit}} - P \tag{2.18}$$

Although the problems considered in this report all have subsonic inflow and outflow, supersonic inflows and outflows could also be examined. For supersonic inflow, all three primitive variables would be specified at the inflow boundary. If the flow were supersonic at the exit, no boundary conditions would be specifed at the exit.

2.2.4 Assembly of the Discrete Equations

The two inlet and one exit boundary conditions, together with the $3(I-1)$ conservation equations, give $3I$ equations in $3I$ unknowns which completely specifies the problem. Now it is simply a matter of solving a set of linear equations to determine the perturbation variables. The most obvious way to set up the matrix equation to be solved is shown in Figure 2.2. The top two rows of the matrix equation are the inlet boundary conditions. Below them are the $I-1$ sets of conservation equations, three for each cell. Finally, at the bottom of the matrix is the single exit boundary condition. This arrangement works quite well providing a small bandwidth matrix equation to be solved by Gaussian elimination. However, a slightly different approach will be used to assemble the matrix equations.

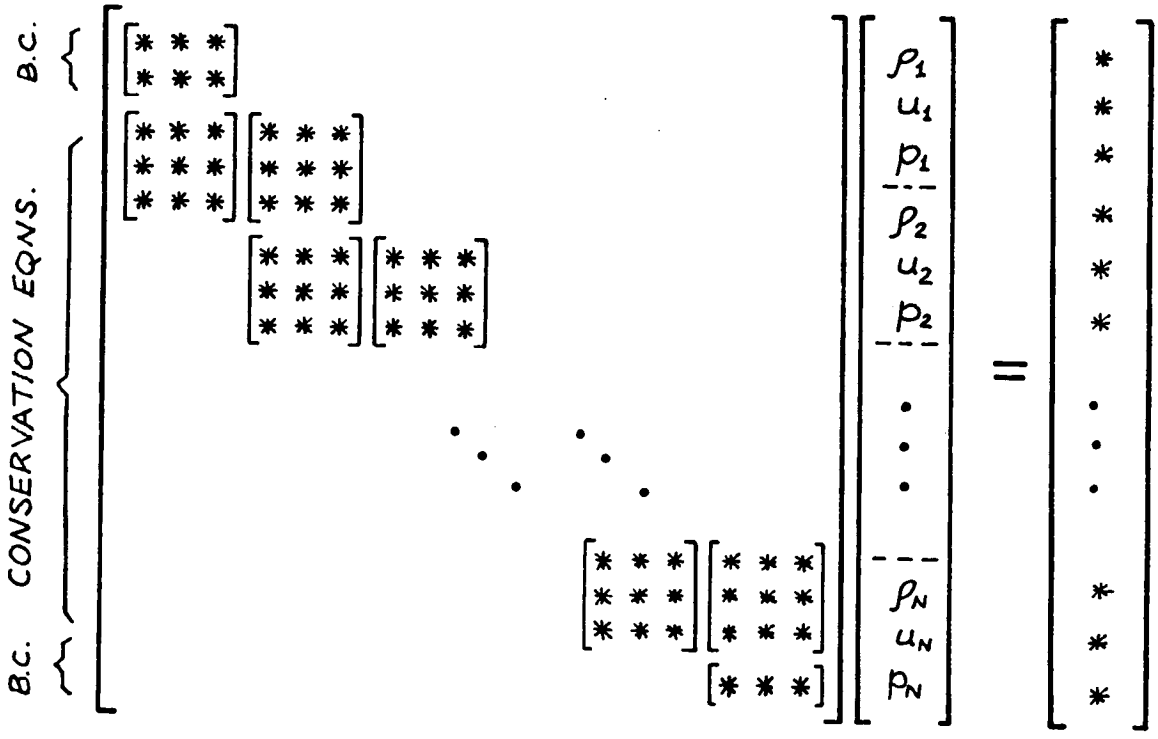

Figure 2.2: Conventional assembly of matrix equations for solution of the Newton iteration equations

Let the portion of the matrix having to do with the conservation equations is denoted by $\mathbf{M}$ and the corresponding right hand side by $\mathbf{f}$. Similarly the portion of the matrix having to do with the boundary conditions be denoted by $\mathbf{M}_{BC}$ and the corresponding right hand side by $\mathbf{f}_{BC}$. Then one can formulate the solution of the linear equations as a minimization problem. That is to say, we wish to minimize the the sum of the squares of the residuals of the conservation equations plus the sum of the boundary condition residuals. This is equivalent to the statement that

$$\left[\mathbf{M}^T\mathbf{M} + \mathbf{M}_{BC}^T\mathbf{M}_{BC}\right]\mathbf{u} = \mathbf{M}^T\mathbf{f} + \mathbf{M}_{BC}^T\mathbf{f}_{BC} \tag{2.19}$$

An Example

To demonstrate the use of this technique, consider the one-dimensional problem

$$\frac{\partial u}{\partial x} = f, \quad x \in [0,1], \quad u(0) = U \tag{2.20}$$

This equation can be discretized using a central difference operator to give

$$u_{i+1} - u_i = \Delta x f_{i+\frac{1}{2}} \tag{2.21}$$

where

$$\Delta x = x_{i+1} - x_i$$

$$f_{i+\frac{1}{2}} = \frac{1}{2}(f_i + f_{i+1})$$

Suppose that the domain is composed of three cells (four nodes) so that in matrix form, Equation 2.21 can be expressed as

$$\begin{bmatrix} -1 & 1 & 0 & 0 \\ 0 & -1 & 1 & 0 \\ 0 & 0 & -1 & 1 \end{bmatrix} \begin{bmatrix} u_1 \\ u_2 \\ u_3 \\ u_4 \end{bmatrix} = \begin{bmatrix} \Delta x f_{1+\frac{1}{2}} \\ \Delta x f_{2+\frac{1}{2}} \\ \Delta x f_{3+\frac{1}{2}} \end{bmatrix} \tag{2.22}$$

where $\Delta x = 1/3$. Note that at this point, there are fewer equations than unknowns since the boundary conditions are not included. For the present example, the boundary condition is applied at the left boundary so that

$$u_1 = U \tag{2.23}$$

or in matrix form

$$\begin{bmatrix} 1 & 0 & 0 & 0 \end{bmatrix} \begin{bmatrix} u_1 \\ u_2 \\ u_3 \\ u_4 \end{bmatrix} = U \tag{2.24}$$

The straightforward approach would be to place this equation above the the field equations to give

$$\begin{bmatrix} 1 & 0 & 0 & 0 \\ -1 & 1 & 0 & 0 \\ 0 & -1 & 1 & 0 \\ 0 & 0 & -1 & 1 \end{bmatrix} \begin{bmatrix} u_1 \\ u_2 \\ u_3 \\ u_4 \end{bmatrix} = \begin{bmatrix} U \\ \Delta x f_{1+\frac{1}{2}} \\ \Delta x f_{2+\frac{1}{2}} \\ \Delta x f_{3+\frac{1}{2}} \end{bmatrix} \tag{2.25}$$

Using the least-squares approach, however, the matrix is formed by minimizing the sum of the square of the residuals of the difference equations and the boundary conditions. Hence,

$$\left[\begin{bmatrix} 1 \\ 0 \\ 0 \\ 0 \end{bmatrix} \begin{bmatrix} 1 & 0 & 0 & 0 \end{bmatrix} + \begin{bmatrix} -1 & 0 & 0 \\ 1 & -1 & 0 \\ 0 & 1 & -1 \\ 0 & 0 & 1 \end{bmatrix} \begin{bmatrix} -1 & 1 & 0 & 0 \\ 0 & -1 & 1 & 0 \\ 0 & 0 & -1 & 1 \end{bmatrix} \right] \begin{bmatrix} u_1 \\ u_2 \\ u_3 \\ u_4 \end{bmatrix} =$$

$$\begin{bmatrix} 1 \\ 0 \\ 0 \\ 0 \end{bmatrix} U + \begin{bmatrix} -1 & 0 & 0 \\ 1 & -1 & 0 \\ 0 & 1 & -1 \\ 0 & 0 & 1 \end{bmatrix} \begin{bmatrix} \Delta x f_{1+\frac{1}{2}} \\ \Delta x f_{2+\frac{1}{2}} \\ \Delta x f_{3+\frac{1}{2}} \end{bmatrix} \tag{2.26}$$

After simplification, this becomes

$$\begin{bmatrix} 2 & -1 & 0 & 0 \\ -1 & 2 & -1 & 0 \\ 0 & -1 & 2 & -1 \\ 0 & 0 & -1 & 1 \end{bmatrix} \begin{bmatrix} u_1 \\ u_2 \\ u_3 \\ u_4 \end{bmatrix} = \begin{bmatrix} U - \Delta x f_{1+\frac{1}{2}} \\ \Delta x f_{1+\frac{1}{2}} - \Delta x f_{2+\frac{1}{2}} \\ \Delta x f_{2+\frac{1}{2}} - \Delta x f_{2+\frac{1}{2}} \\ \Delta x f_{3+\frac{1}{2}} \end{bmatrix} \tag{2.27}$$

Note that the matrix on the left-hand side is positive definite.

Consider, for example, the case of $f = 1$ and $U = 1$. Then the exact solution to $u_x = 1$ is $u = x + 1$. It is quite simple to verify that the above matrix equation gives the exact solution of $\mathbf{u} = [1, \frac{4}{3}, \frac{5}{3}, 2]$.

Interpretation of the Squaring Technique

The method described above resembles the least-squares finite element method [28,29]. In the finite element method, the solution to a differential equation is approximated by local shape functions. So for example, the approximate solution anywhere within a cell or element can be expressed in terms of the value of the function at the nodes of the element. The values of the discrete nodal values are then chosen such that the approximate solution satifies — in some sense — the partial differential equations. For the least-squares finite element method, the differential equation is "satisfied" if the residuals of the differential equation is minimized over the domain *and* the boundary condition residuals are minimized. In fact, the least-squares technique can be thought of as a variational principle for non-self-adjoint differential equations.

Originally in this research, least-squares finite elements were used to discretize the PDEs which describe the steady and unsteady channel flow — with dissapointing results. We found, as did Astley, Walkington, and Eversman [30], that the method as described above gives poor results unless higher order shape functions are used. The present method more nearly resembles *collocated least squares*, where the residuals are minimized at a finite number of stations rather than over a continuous region.

There are several advantages to the least-squares technique. Because the resulting equations are positive definite, it may be possible to make use of iterative matrix solvers which takes advantage of positive definiteness and sparseness, although in the present work only direct solvers were used. The best feature, however, is the ease with which boundary conditions are introduced. The assembly of the discrete field equations is independent of the boundary conditions. To introduce the boundary conditions, The squared boundary condition equations are simply added to the squared field equations. This is especially useful in the two-dimensional problem where reordering would be quite complicated.

2.2.5 Subsonic Flow in a Converging-Diverging Channel

In this section, a model channel flow problem will be solved using the method outlined above. The channel has an area distribution given by $A(x) = 1 - \frac{1}{4}\sin^2(\pi x)$ on the domain $x = [0, 1]$. The flow is from left to right with the inlet total pressure P_{T0} and density ρ_{T0} specified at the inlet, and the static pressure p_{exit} specified at the exit. For this case the total pressure P_{T0} and total density ρ_{T0} are 1.175 and 1.122. The exit pressure p_{exit} is 1.0. At this back pressure, the channel is not choked. A computational grid with 21 nodes was used ($\Delta x = 0.05$). Since the Euler equations are solved with a Newton iteration procedure, an initial solution must be assumed. The initial flow was assumed to be uniform with $\overline{\rho} = 1$, $U = 0.5$, and $P = 1$. The flow was calculated using the Newton iteration procedure in four iterations. The converged solution is shown in Figure 2.3 along with the exact solution. Not surprisingly, the two solutions are nearly identical. The second-order accurate scheme allows accurate results to be computed with relatively few nodes.

As is characteristic with the Newton iteration procedure, convergence is extremely fast when the solution estimate is not too far away from the actual solution. One drawback, however, is that the method is not guaranteed to converge and in fact can diverge quite spectacularly if a poor initial solution is chosen. Figure 2.4 shows the strong convergence history exhibited in this case. Plotted is the logarithm of the maximum residual versus the iteration number. One can see that initially, the convergence is slightly faster than linear on a semi-logarithmic scale. After three iterations, no further convergence is seen which is due to round-off error associated with finite computer precision. Figure 2.5 shows the initial pressure along with the calculated pressure after each of the first five iterations. This provides another illustration of the extremely fast convergence. Especially after the first iteration, the solution converges to its final value very quickly.

2.2.6 Steady Shock Fitting

In the previous section, we calculated the steady subsonic flow through a converging-diverging channel. If the flow is transonic, however, the presence of a sonic point and

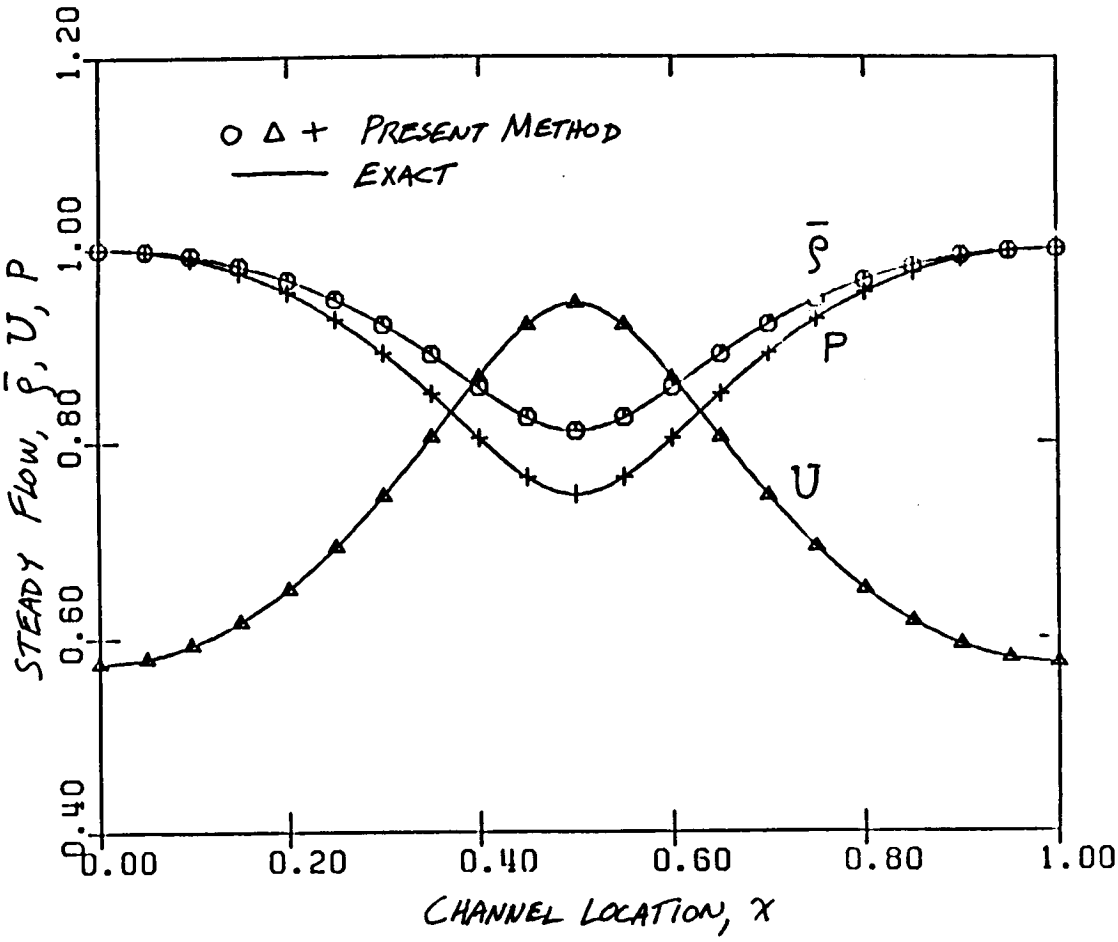

Figure 2.3: Calculated steady flow through converging-diverging channel. Also shown for comparison is the exact solution. Total inlet pressure to exit pressure ratio is 1.175.

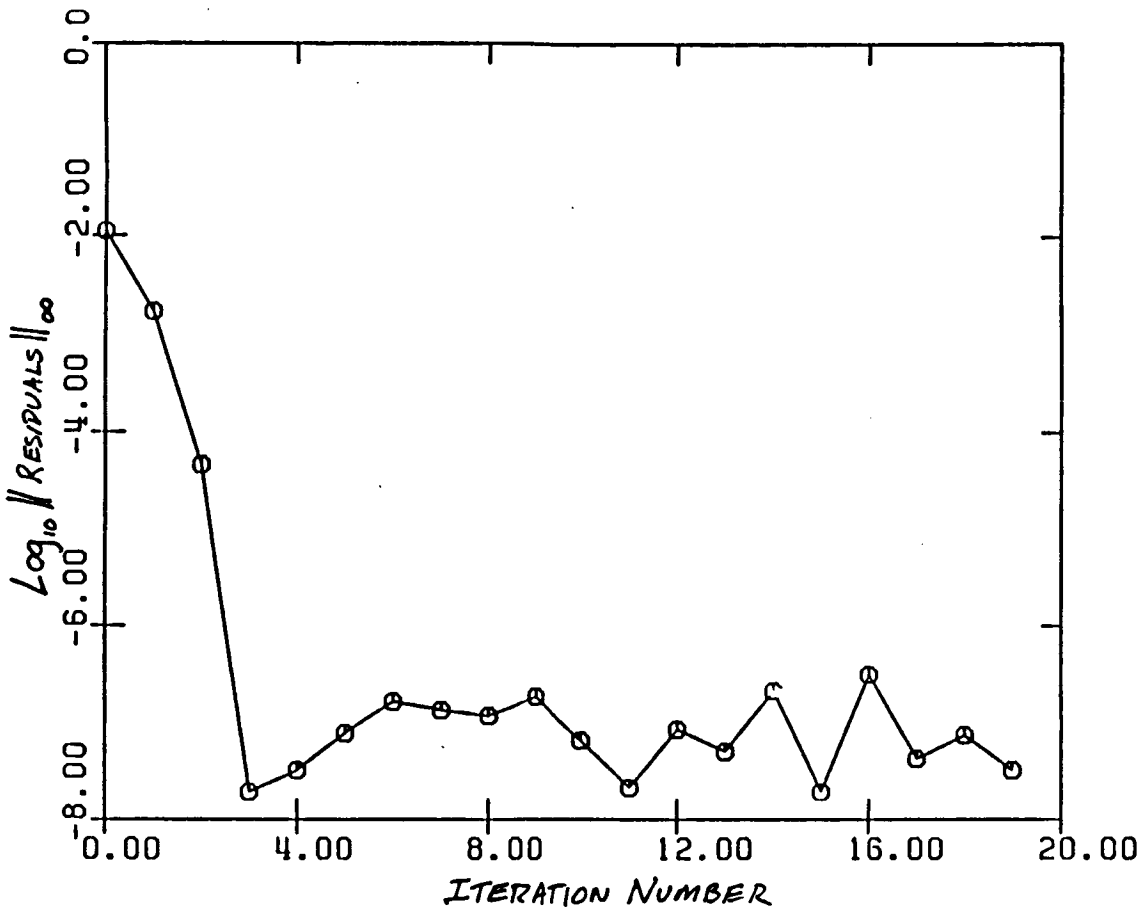

Figure 2.4: Convergence history of Newton iteration method.

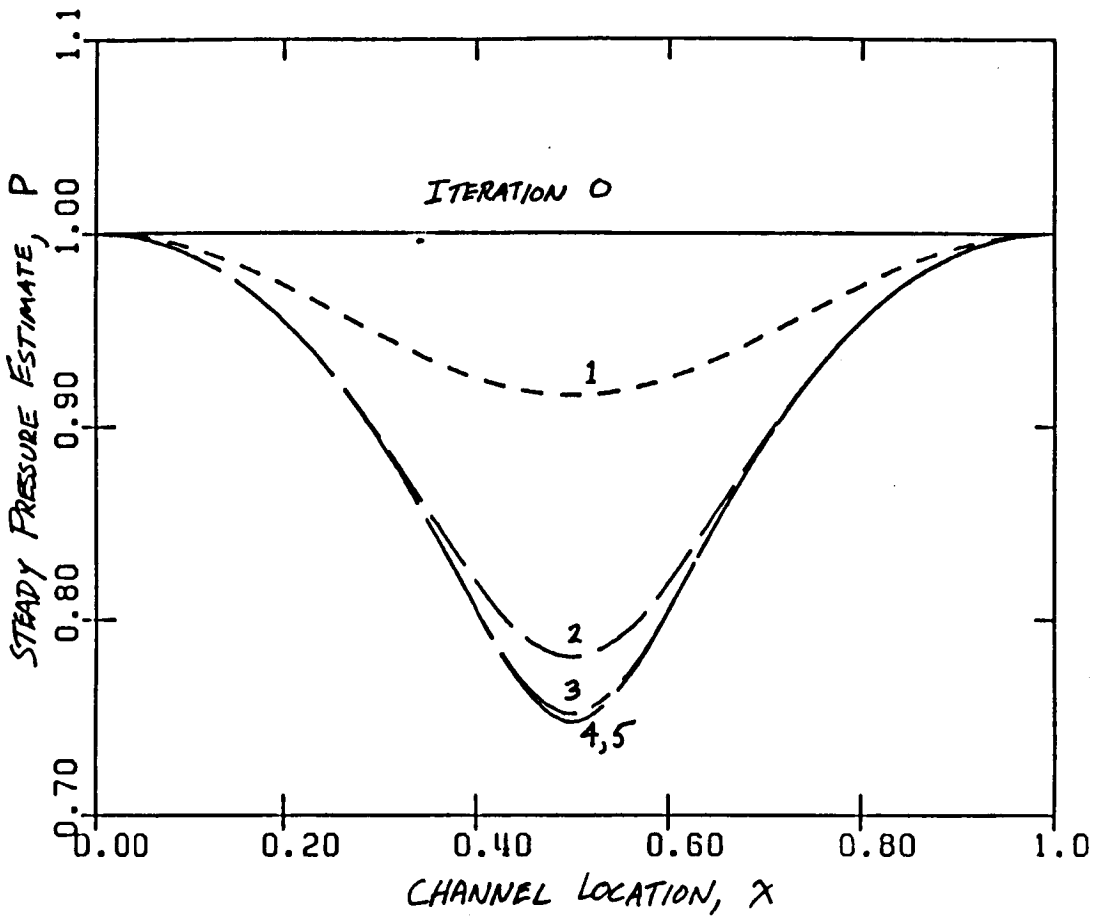

Figure 2.5: Computed pressure distribution history after each iteration. Note solution is converged after four iterations.

shock wave introduce additional complications to the problem. In this section, the numerical procedure for fitting the shock will be discussed, as well as the need for some smoothing to handle the sonic line.

The Euler equations are nonlinear partial differential equations and as such they admit so-called *weak solutions*, i.e., solutions which contain jump discontinuities which satisfy the differential equations in an integral sense. The physical manifestation of this mathematical idealization is a shock wave. Consider once again the steady Euler equations. If these equations are satisfied everywhere, then

$$\int_{X_s-\epsilon}^{X_s+\epsilon} \left(\frac{\partial}{\partial x} A\mathbf{F} + A \frac{\partial}{\partial x} \mathbf{P} \right) dx = 0 \tag{2.28}$$

where the integration runs from one side of the shock to the other. As ϵ approaches zero, the limit of the integral gives the condition

$$[[\mathbf{F} + \mathbf{P}]] = 0 \tag{2.29}$$

where the symbol $[[\cdots]]$ denotes the difference in the enclosed quantity across the discontinuity. Equation 2.29 (the Rankine-Hugoniot equations) relates the flow on one side of the shock to that on the other side.

These jump conditions can be linearized about a current estimate of the flow solution to obtain linearized shock-jump conditions for use with the Newton iteration procedure. These are given by

$$[[(\mathbf{B}_2 + \mathbf{B}_3)\,\mathbf{u}]] = -\,[[\mathbf{F} + \mathbf{P}]] \tag{2.30}$$

and are applied at what will be the new estimate of the shock location. The term on the right hand side represents the jump condition at the *new* shock location calculated from the *old* flow estimate. This is not a particularly useful form of the jump equations since the new shock location is not known a priori. Instead, a new variable is introduced which is the distance the shock moves from the current shock location to the new shock location. With the aid of this additional perturbation variable, the shock jump conditions can be expressed in terms of the flow at the current shock position without a priori knowledge of the new shock position by extrapolating the shock jump conditions from the current shock position to the new shock position, i.e.,

$$[[(\mathbf{B}_2 + \mathbf{B}_3)\,\mathbf{u}]] + \frac{\partial}{\partial x} \left([[(\mathbf{B}_2 + \mathbf{B}_3)\,\mathbf{u}]] \right) x_s = -\,[[\mathbf{F} + \mathbf{P}]] - \frac{\partial}{\partial x} \left([[\mathbf{F} + \mathbf{P}]] \right) x_s \tag{2.31}$$

where now this condition is applied at the current shock position rather than the new shock position. Note that the second term on the left-hand side of Equation 2.31 is second order and can be neglected. Hence retaining only first-order effects gives

$$\left[\left[(\mathbf{B_2}+\mathbf{B_3})\,\mathbf{u}+x_s\frac{\partial}{\partial x}(\mathbf{F}+\mathbf{P})\right]\right]=-\left[[\mathbf{F}+\mathbf{P}]\right] \tag{2.32}$$

The numerical procedure is as follows. An initial shock position is assumed. The grid is then constructed as before except that at the shock there are two grid points, one grid point corresponding to the flow on the upstream side of the shock, and one corresponding to the flow on the downstream side. These two nodes comprise the shock cell. The conservation equations are applied to the conservation cells as before, but at the shock cell the linearized shock-jump conditions are applied with one-sided, three-point, second-order accurate differences used to evaluate the gradients in the base flow.

Assuming the flow is subsonic at the inlet and exit, two upstream and one downstream boundary conditions are imposed as in the subsonic example. But this does not completely specify the problem. Taking count of the equations and unknowns, we have I grid points each with three perturbation variables *plus* the extra shock position perturbation variable for a total of $3I+1$ unknowns. There are $3(I-2)$ conservation equations arising from the $I-2$ conservation cells, three jump conditions at the shock cell, and two upstream and one downstream boundary condition for a total of $3I$ equations. Unfortunately, we are one equation short. This is *not* due to the addition of the shock perturbation variable but rather to the presence of a sonic point in the flow. Giles [31] solved this problem by adding a special equation at the sonic point which describes the behavior of the J^- characteristic. A more common approach, which was also used in this research, is to add a small amount of smoothing to the equations to stabilize the sonic point. The smoothing is added to the matrix equation *after* the squaring procedure described earlier. A small amount of a Laplacian like operator is added to the "stiffness" matrix. The operator is positive semi-definite which preserves the symmetry of the equations and makes the system positive definite. The final equation matrix equations is

$$\left[\mathbf{M}^T\mathbf{M}+\mathbf{M}_{BC}^T\mathbf{M}_{BC}+\epsilon\mathbf{L}\right]\mathbf{u}=\mathbf{M}^T\mathbf{f}+\mathbf{M}_{BC}^T\mathbf{f}_{BC}+\epsilon\mathbf{f}_L \tag{2.33}$$

where

$$\mathbf{f}_L = -\mathbf{LU}$$

and ϵ is a small parameter used to control the level of smoothing introduced into the scheme.

The Newton iteration procedure is then as follows. An initial transonic flow is assumed, including the initial position of the shock. The linearized conservation equations, shock jump equations, and boundary conditions are set up and "squared" as described above. A small amount of Laplacian smoothing is then added to the system. The system of equations is solved using a sparse Gaussian elimination solver to obtain the perturbation primitive variables and the perturbation in the shock position. The primitive variables are updated, then the grid is readjusted so that the double-noded shock cell is coincident with the new shock position. This requires that the updated primitive variables be interpolated from the old grid to the new grid. The entire procedure is repeated until convergence is achieved. The procedure exhibits rapid convergence when it works, but convergence is not guaranteed. In practice the method usually converges in less than ten iterations if a reasonable initial guess is made.

2.2.7 Steady Transonic Channel Flow

To demonstrate the shock fitting algorithm, we will consider the flow through the same convergent divergent channel previously considered in Section 2.2.5. This time, however, the total pressure and density are somewhat higher so that the flow is choked. The total inlet pressure P_{T0} and total density ρ_{T0} are 1.25 and 1.173, respectively. The exit static pressure p_{exit} is 1.0. The initial shock position is assumed to be $X_s = 0.8$. Recall that a poor initial guess can cause the procedure to diverge. Therefore, one should use whatever experience and knowledge one has about the nature of the actual solution to pick as reasonable a first guess as possible. The initial starting solution for the Newton iteration procedure is shown in Figure 2.6. Starting with this initial solution, the Newton iteration procedure was run for enough iterations to insure a converged solution. The converged solution is shown in Figure 2.7 along with the exact solution. Again excellent agreement is seen between the computed solution and the

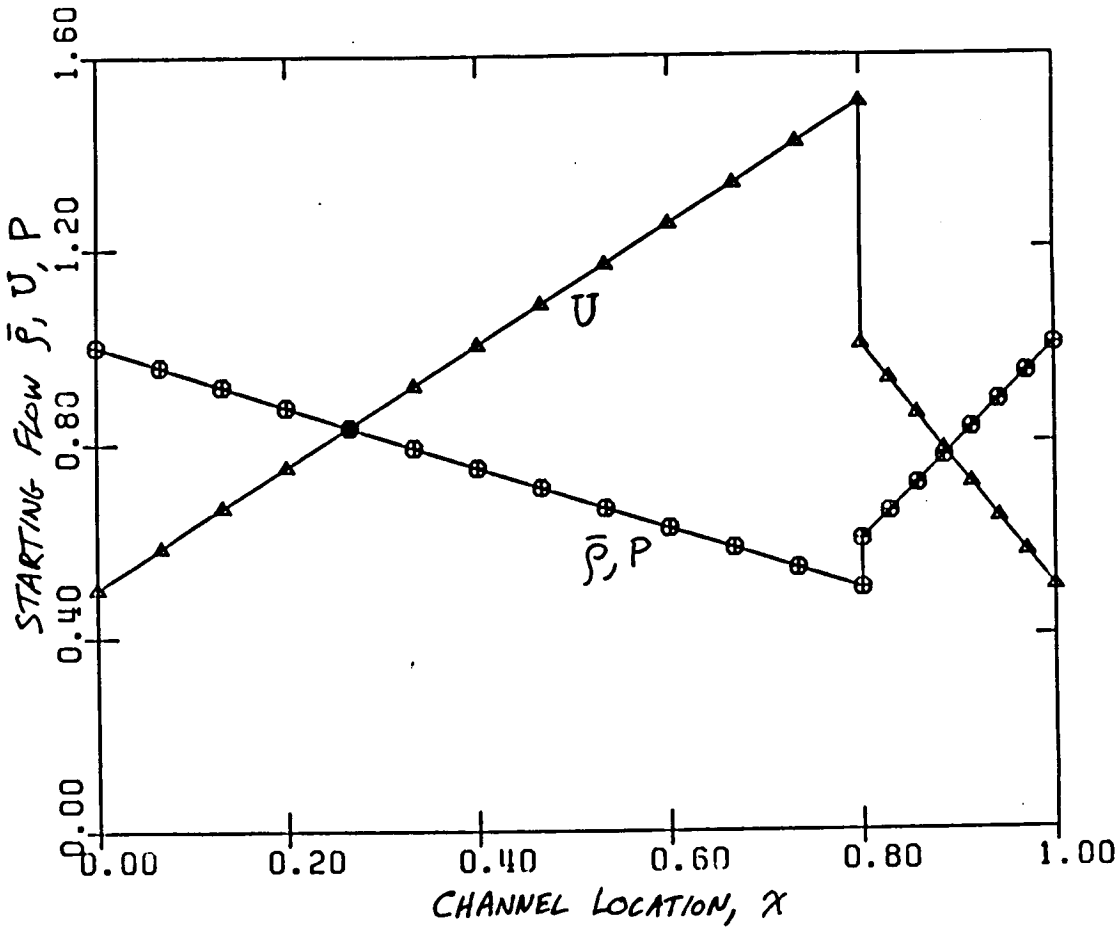

Figure 2.6: Initial base flow through channel used in Newton iteration procedure.

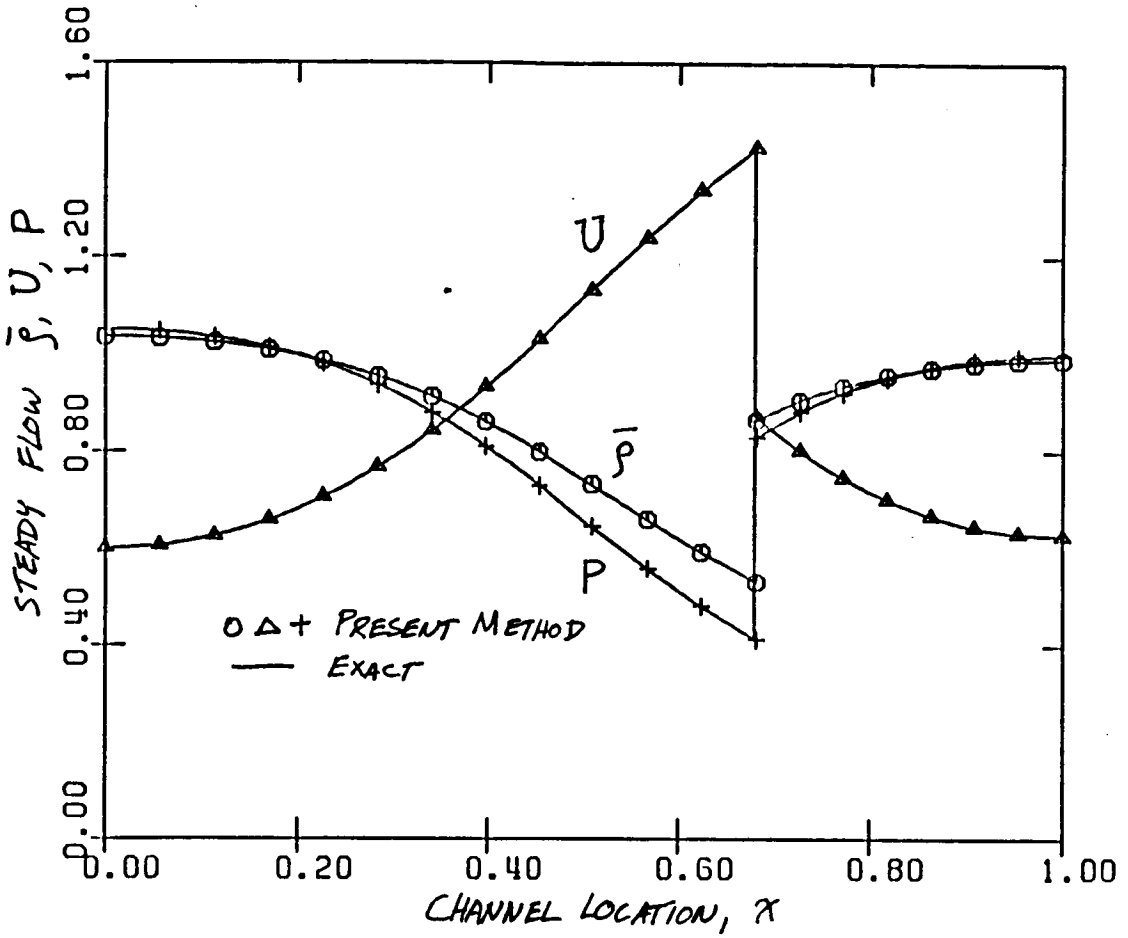

Figure 2.7: Converged solution for choked flow in one-dimensional channel. Total inlet to exit pressure ration is 1.25.

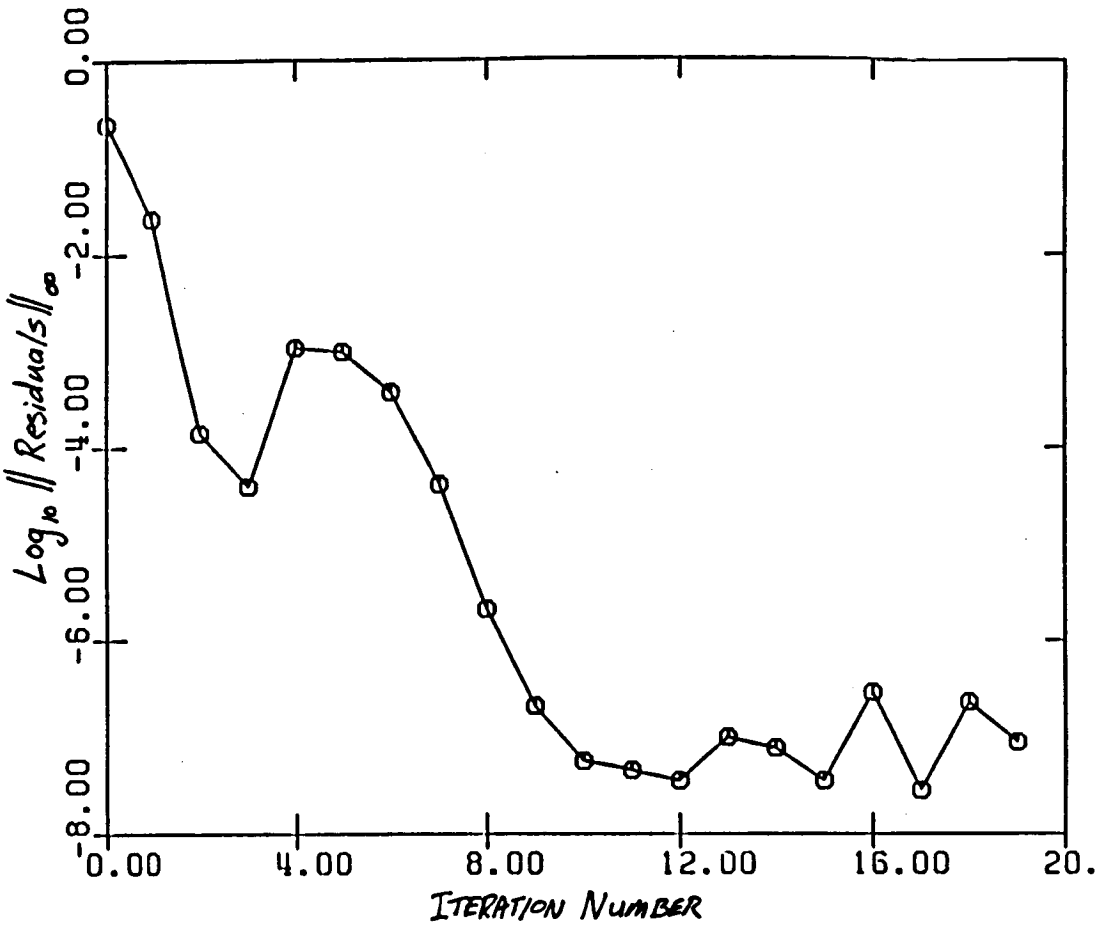

Figure 2.8: Convergence history of choked flow calculation. Initially the solution "wanders" but then converges very quickly.

exact solution. Note in particular the precise definition of the shock arising from the use of shock fitting. The shock position is calculated to be $X_s = 0.6805$ while the exact shock position is $X_s = 0.6788$. This accurate an estimate of the shock position could not be obtained using shock capturing with the same grid resolution since the uncertainty in a captured shock's position is on the order of a few conservation cells.

As with the subsonic steady flow calculation, convergence is extremely fast. The maximum residuals after each iteration are shown in Figure 2.8. Note that the convergence history can be divided into roughly three phases. In the first phase, the convergence is slow and erratic, with the residuals even increasing on occasion. In the second phase, the residuals decrease rapidly and nearly linearly on a logarithmic scale.

Beyond this point, round off errors preclude any improvement in the solution and the computation is for all intents converged. The three phases of convergence can also be seen in Figure 2.9. Plotted is the computed shock position after each iteration as well as the perturbation in shock position. For the first four iterations, the shock position "bounces" around quite a bit. This corresponds to the initial phase of convergence. If the computation is to diverge, it will usually happen in the first few iterations. Once the solution gets in the neighborhood of the actual solution, the shock position quickly converges to its final value. After about ten iterations, the shock has settled in its final position, save for extremely small excursions due to round-off error.

Because the numerical algorithm is second order accurate, the computed solution should differ from the exact solution by $O(\Delta x^2)$. As a test of this hypothesis, the grid resolution was varied from three conservation cells up to 96 conservation cells. For each case, the steady shock position was calculated. Figure 2.10 shows the error in the computed shock position as a function of the average cell size. Note that on a logarithmic scale, the error curve has a slope of about two, demonstrating the scheme is second order accurate. In particular, for a Δx of about 0.04, the error in the computed shock position is less than 0.1 percent of the channel length.

2.3 Solution of the Linearized Unsteady Euler Equations

In the previous section, steady subsonic and steady transonic flows through a one-dimensional channel were calculated. In this section, unsteady perturbation flows about these mean flows will be calculated. These solutions will be compared against a time-accurate time-marching scheme to verify the results. Although the flows calculated here are fairly simple one-dimensional flows, they will demonstrate many of the salient features of the present analysis.

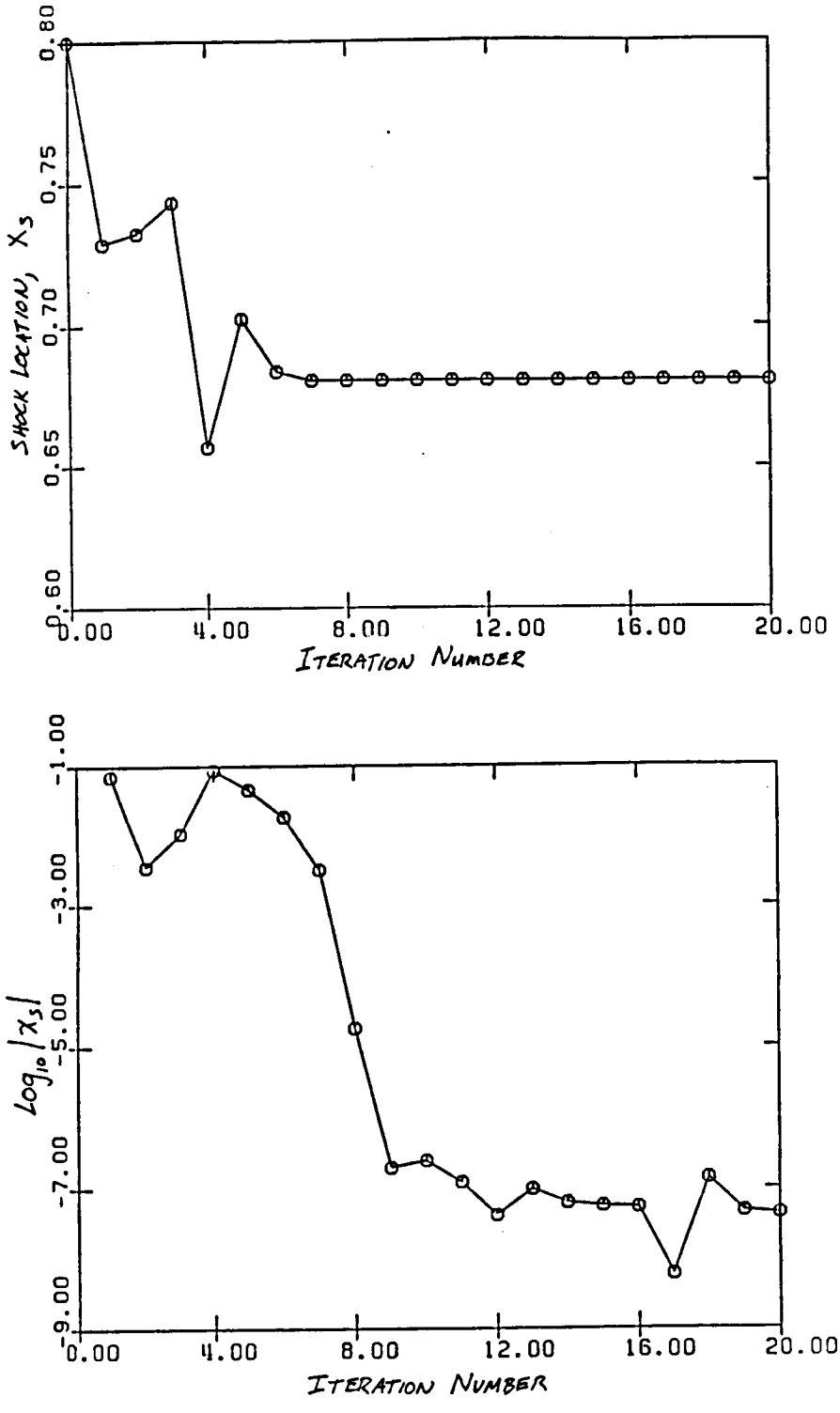

Figure 2.9: Computed shock position history. The upper plot shows the shock position after each iteration. The lower plot shows change in position from one iteration to the next.

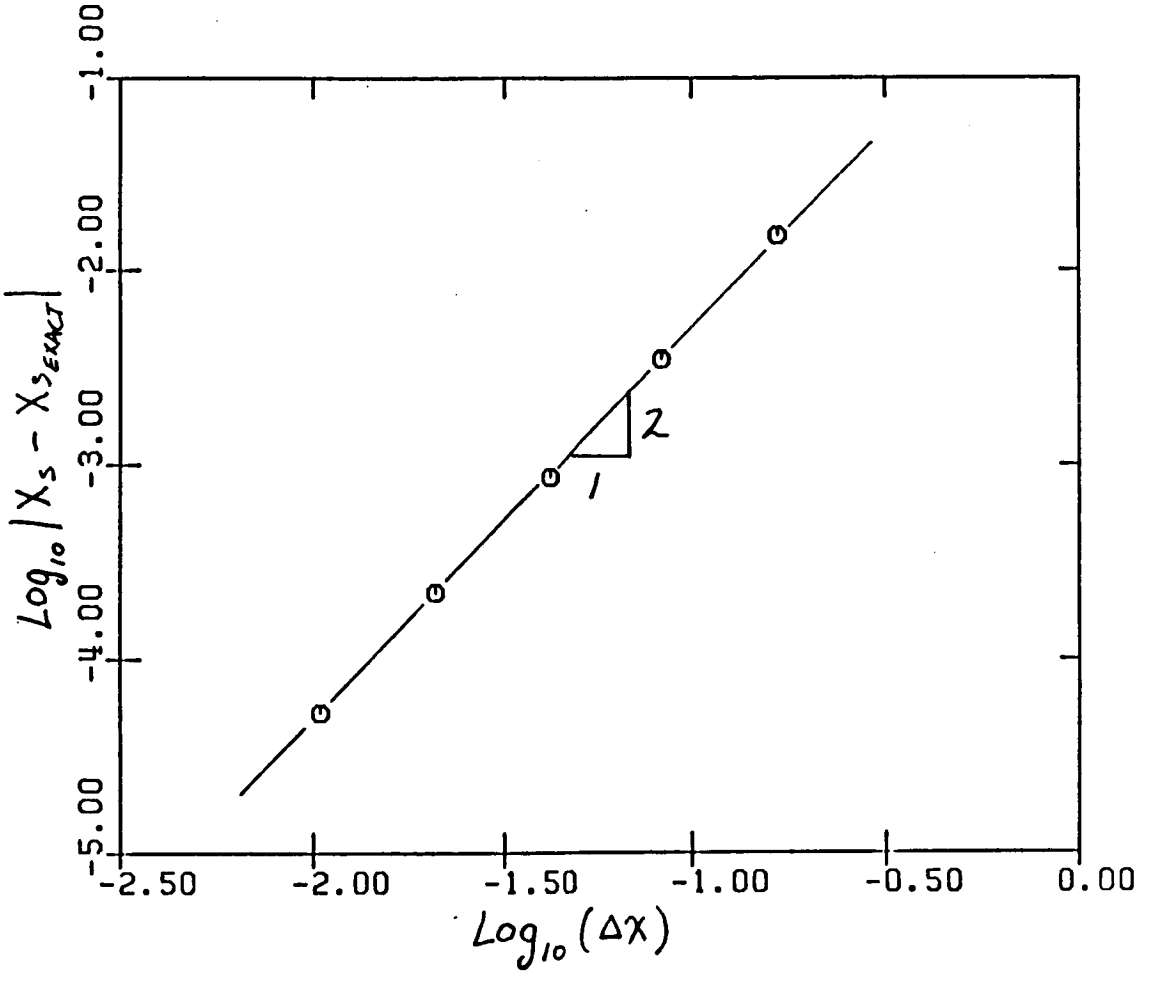

Figure 2.10: Accuracy of computed shock position as a function of grid resolution. Slope of 2 indicates sheme is $O(\Delta x^2)$.

2.3.1 Discretization of the Linearized Euler Equations

The linearized Euler equations (Equation 2.7) are discretized using a cell centered finite difference scheme given by

$$j\omega\left(A\mathbf{B}_1\right)_{i+\frac{1}{2}}\frac{\mathbf{u}_{i+1}+\mathbf{u}_i}{2}+\frac{\left(A\mathbf{B}_2\mathbf{u}\right)_{i+1}-\left(A\mathbf{B}_2\mathbf{u}\right)_i}{\Delta x_i}+$$

$$A_{i+\frac{1}{2}}\frac{\left(\mathbf{B}_3\mathbf{u}\right)_{i+1}-\left(\mathbf{B}_3\mathbf{u}\right)_i}{\Delta x_i}=0 \tag{2.34}$$

These difference equation are second order accurate in Δx. Note also that they are *complex* due to the harmonic assumption. It can be shown, at least in the constant area case, that these equations are nondissipative. That is to say that the pressure and entropy waves do not grow or decay. This is due to the central differencing. The equations are, however, dispersive. The waves may not "travel" at quite the right speed. This is especially true of the shorter wavelength waves.

2.3.2 Unsteady Channel Flow Boundary Conditions

In the two-dimensional cascade flow problem, the unsteady boundary conditions reflect will real physical problems encountered in turbomachinery such as inlet distortion, potential disturbances from neighboring blade rows, incoming vorticity and entropy waves, or motion of the cascade blades themselves. In these one-dimensional model problems, the boundary conditions are somewhat contrived, but must be mathematically well posed. If the flow is subsonic at the inlet and exit, then two boundary conditions will be required at the inlet, and one will be required at the exit. If the flow is supersonic, three are required at the inlet and none are required at the exit.

In the examples considered in this chapter, the flow at he inlet and exit are subsonic, and hence, the unsteady total pressure and total density will be specified at the inlet and the unsteady static pressure will be specified at the exit. At the inlet the boundary conditions can be expressed as

$$\frac{\gamma P_T}{\rho_T}=\gamma\frac{P_{T0}+\Delta P_T e^{j\omega t}}{\rho_{T0}+\Delta\rho_T e^{j\omega t}}=\frac{\gamma\hat{p}}{\hat{\rho}}+\frac{\gamma-1}{2}\hat{u}^2 \tag{2.35}$$

$$\frac{P_T}{\rho_T^\gamma}=\frac{P_{T0}+\Delta P_T e^{j\omega t}}{\left(\rho_{T0}+\Delta\rho_T e^{j\omega t}\right)^\gamma}=\frac{\hat{p}}{\hat{\rho}^\gamma} \tag{2.36}$$

which when linearized become

$$\frac{\gamma}{\bar{\rho}}p - \frac{\gamma P}{\bar{\rho}^2}\rho + (\gamma - 1)U u = \frac{\gamma P_{T0}}{\rho_{T0}}\left(\frac{\Delta P_T}{P_{T0}} - \frac{\Delta \rho_T}{\rho_{T0}}\right) \tag{2.37}$$

and

$$\frac{1}{\bar{\rho}^\gamma}p - \frac{\gamma P}{\bar{\rho}^{\gamma+1}}\rho = \frac{P_{T0}}{\rho_{T0}^\gamma}\left(\frac{\Delta P_T}{P_{T0}} - \frac{\gamma \Delta \rho_T}{\rho_{T0}}\right) \tag{2.38}$$

Note in particular that if the inlet low is isentropic (to first order), the expression on the right hand side of Equation 2.38 vanishes. Similarly, the downstream static pressure boundary condition is

$$\hat{p} = p_{\text{exit}} = P_{\text{exit}} + \Delta P_{\text{exit}} e^{j\omega t} \tag{2.39}$$

which when linearized becomes

$$p = \Delta P_{\text{exit}} \tag{2.40}$$

2.3.3 Assembly of the Discrete Equations

The numerical boundary conditions together with the finite difference equations completely specify the linear equations to be solved. As with the Newton iteration equations, the equations are "squared" to produce a positive definite matrix equation given by

$$\left[\mathbf{M}^H\mathbf{M} + \mathbf{M}_{BC}^H\mathbf{M}_{BC}\right]\mathbf{u} = \mathbf{M}_{BC}^H\mathbf{f}_{BC} \tag{2.41}$$

where the transpose operator has been replaced by the Hermitian operator because the original matrices are complex. The resulting positive definite matrix is Hermitian.

2.3.4 Unsteady Subsonic Results

As an example, we will compute the small disturbance unsteady flow in a channel. The steady flow about which the Euler equations are linearized is the subsonic flow considered in Section 2.2.5. Recall that the inlet total pressure P_{T0} is 1.175, and the inlet total density ρ_{T0} is 1.122. Downstream the static pressure P_{exit} is 1.0. Because the linearized unsteady Euler equations are linear and homogeneous, the calculated flow scales with the unsteady boundary conditions. For convenience then, The total pressure at the inlet varies as $\Delta P_T = 1.0$. The excitation frequency ω is 1.257. Since the steady

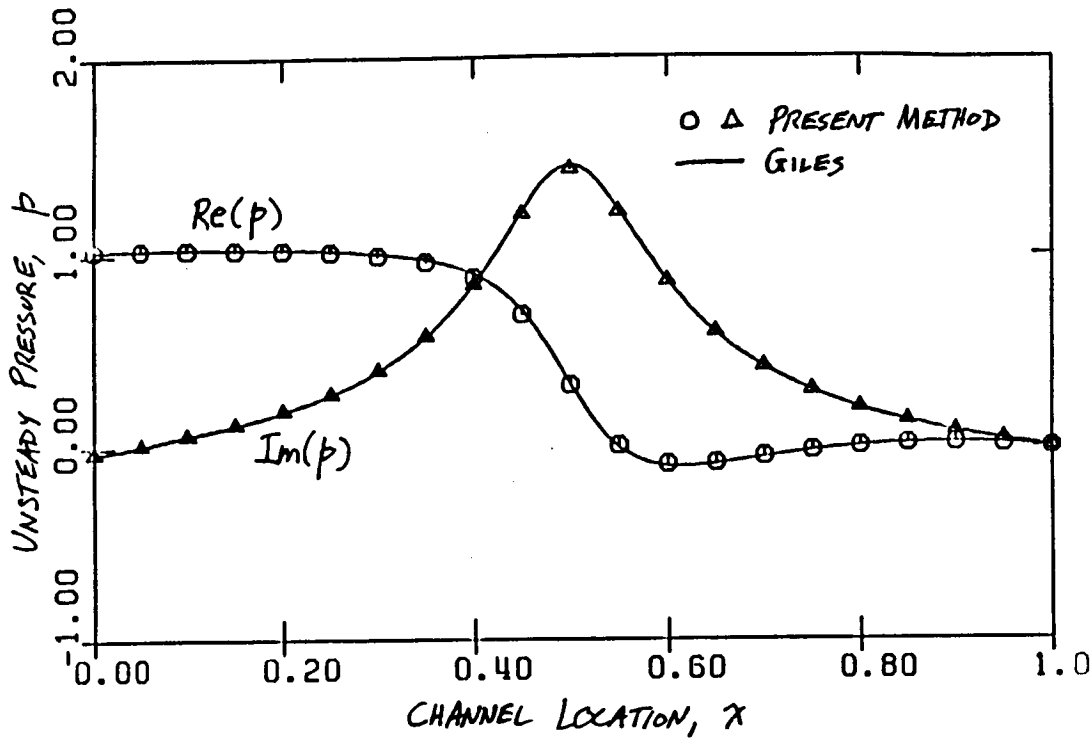

Figure 2.11: Unsteady pressure distribution due to upstream total pressure and density variation. Excitation frequency ω is 1.047.

velocity in the channel and the channel length are order unity, one can think of this frequency as a reduced frequency. The total density is varied such that the inlet flow is isentropic ($\Delta P_T/P_T = \gamma \Delta \rho_T/\rho_{T0}$). Downstream the static pressure variation ΔP_{exit} is set to zero (this is a reflecting boundary condition). The calculated unsteady pressure distribution is shown in Figure 2.11. Because the perturbation variables are complex, both the real and imaginary parts of the pressure must be presented to completely describe the pressure distribution. Alternatively, one could present the magnitude and phase of the pressure at each point. The former is preferred, however, since physically the real and imaginary parts each represent a snapshot of the flow at a particular instant in time.

To validate the linearized Euler method, these results were compared to those obtained from the time-accurate, time-marching code of Giles [31]. This code is unique in that shocks are fit rather than captured, and no artificial viscosity is required although

special treatment is required at sonic points. The procedure was to first time march the code with steady state boundary conditions until the solution had nearly converged. Then the code was restarted, but this time the upstream total pressure was varied sinusoidally in time with the total density chosen such that the inlet flow was isentropic. Downstream, the static pressure was held constant. Because the time-marching code is nonlinear, the total pressure variation was chosen to be very small so that the results can be compared to linearized theory. (In the next chapter, the effect nonlinearities due to larger levels of unsteadiness will be examined.) After any initial unsteady transients have decayed, the unsteady flow is periodic and very nearly sinusoidal. The time history was then Fourier transformed to convert the time domain results into the frequency domain so that they can be compared directly to the linearized Euler results. These time marching results are compared to the linearized Euler results in Figure 2.11. Note the excellent agreement between the two methods.

For the next case, the frequency ω is increased to 2.094 The calculated pressure distribution is shown in Figure 2.12. Again, good agreement is seen between the linearized Euler theory and the time-marching code.

These results demonstrate the validity of the small disturbance approach. If one is interested in small disturbance flows which are nearly harmonic in time, the linearized Euler method offers an alternative to the time marching Euler approach. Furthermore, the linearized Euler method requires less computational time than the time marching technique. In one dimension, the CPU time is reduced by three orders of magnitude, while in two dimensions, the CPU time reduction is more moderate at one to two orders of magnitude. On the other hand, the linearized Euler method is not suitable for flows with large disturbances, or flows which are not periodic.

2.3.5 Unsteady Shock Fitting

If the mean flow is transonic, then the calculation of the unsteady flow has the added complexity of a moving shock. The complexity arises because the shock is moving, but the grid is stationary. Therefore, just as in the case of the Newton iteration procedure for shock fitting, we will need some form of extrapolation to accurately model the shock

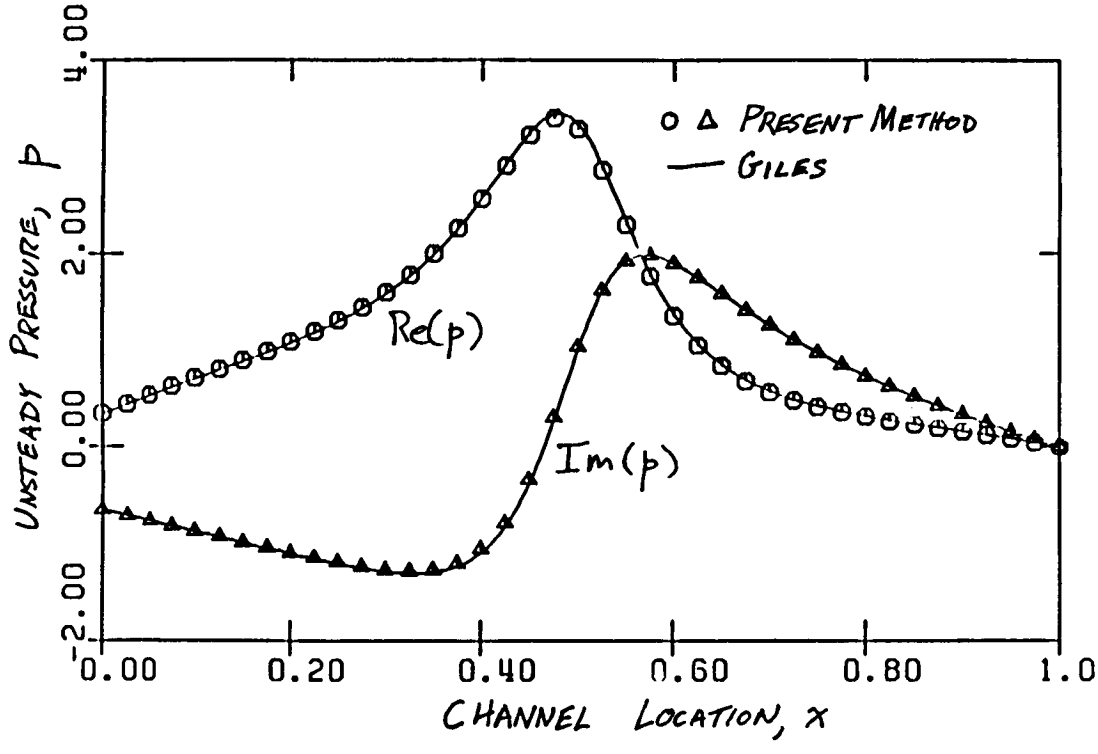

Figure 2.12: Unsteady pressure distribution due to upstream total pressure and density variation. Excitation frequency ω is 2.094.

motion.

The starting point of the analysis are the full nonlinear unsteady shock jump conditions. To derive them, a change in coordinate systems is made. The new coordinate system is fixed to the moving shock. Hence

$$\tilde{x} = x - x_s(t) \tag{2.42}$$

$$\tilde{t} = t \tag{2.43}$$

using the chain rule of differentiation yields

$$\frac{\partial}{\partial x} = \frac{\partial}{\partial \tilde{x}} \tag{2.44}$$

$$\frac{\partial}{\partial t} = \frac{\partial}{\partial \tilde{t}} - v_s \frac{\partial}{\partial \tilde{x}} \tag{2.45}$$

where v_s is the instantaneous shock speed in the *fixed* coordinate system. Using the above expressions for the differential operators to derive the unsteady Euler equations in the shock coordinate system gives

$$\left(\frac{\partial}{\partial \tilde{t}} - v_s \frac{\partial}{\partial \tilde{x}}\right) A\mathbf{U} + \frac{\partial}{\partial \tilde{x}} A\mathbf{F} + A \frac{\partial}{\partial \tilde{x}} \mathbf{P} = 0 \tag{2.46}$$

Integration of this equation from just upstream to just downstream of the shock gives the desired shock jump conditions. Because the time derivative is bounded in the shock frame of reference and the interval of the integration goes to zero, the time derivative does not appear in the shock-jump condition. The spatial derivatives, however, act like impulses at the shock, and hence, integration of these impulses yields the jump condition

$$[[\mathbf{F} + \mathbf{P} - v_s \mathbf{U}]] = 0 \tag{2.47}$$

These jump conditions give the nonlinear relationship between the flow on either side of a moving shock. These are the unsteady Rankine-Hugoniot equations.

Next, let us assume that like the primitive variables, the shock motion is also harmonic in time. Hence the shock position is composed of mean part plus a harmonic variation.

$$\hat{x}_s(t) = X_s + x_s e^{j\omega t} \tag{2.48}$$

Therefore, the instantaneous shock velocity is $x_s e^{j\omega t}$. Linearizing the shock jump condition gives

$$[[(\mathbf{B}_2 + \mathbf{B}_3)\,\mathbf{u} - j\omega x_s \mathbf{U}]] = 0 \tag{2.49}$$

It is emphasized that the jump condition is applied at the instantaneous position of the shock. As with the Newton iteration shock jump equations, we can extrapolate from the nominal shock position to the instantaneous shock position and apply the shock jump condition at the nominal shock. Keeping only first order terms gives

$$\left[\left[(\mathbf{B}_2 + \mathbf{B}_3)\,\mathbf{u} + x_s \frac{\partial}{\partial x}(\mathbf{F} + \mathbf{P}) - j\omega x_s \mathbf{U}\right]\right] = 0 \tag{2.50}$$

2.3.6 Assembly of Unsteady Transonic Equations

The matrix equations are assembled in essentially the same way the steady transonic equations were assembled. Note that because of the transition form subsonic to supersonic flow at the sonic line, there will not be quite enough equations for unknowns. Hence, a small amount of smoothing is introduced to stabilize the sonic point. The resulting matrix equations are given by

$$\left[\mathbf{M}^H\mathbf{M} + \mathbf{M}_{BC}^H\mathbf{M}_{BC} + \epsilon\mathbf{L}\right]\mathbf{u} = \mathbf{M}_{BC}^H\mathbf{f}_{BC} \tag{2.51}$$

2.3.7 Unsteady Transonic Results

As an example, the unsteady small disturbance flow about a steady transonic flow through a converging diverging channel is considered. The base flow is the one considered in Section 2.2.7. The inlet total pressure P_{T0} is 1.25 while the inlet total density ρ_{T0} is 1.173. Downstream the static pressure P_{exit} is 1.0. For the perturbation flow, the unsteady variation in the upstream total pressure ΔP_T is 1.0, with a frequency ω of 1.257. The total density $\Delta\rho_T$ is chosen such that the inlet flow is isentropic. Downstream, the variation in static pressure ΔP_{exit} is set to zero. The computed unsteady pressure distribution is shown in Figure 2.13. Also plotted is the time-marching solution of Giles [31]. Note the generally good agreement between the two theories except at the throat the time-marching code has a localized problem. Nevertheless, away from the throat, the agreement is excellent. The shock motion is also in good agreement. The complex shock

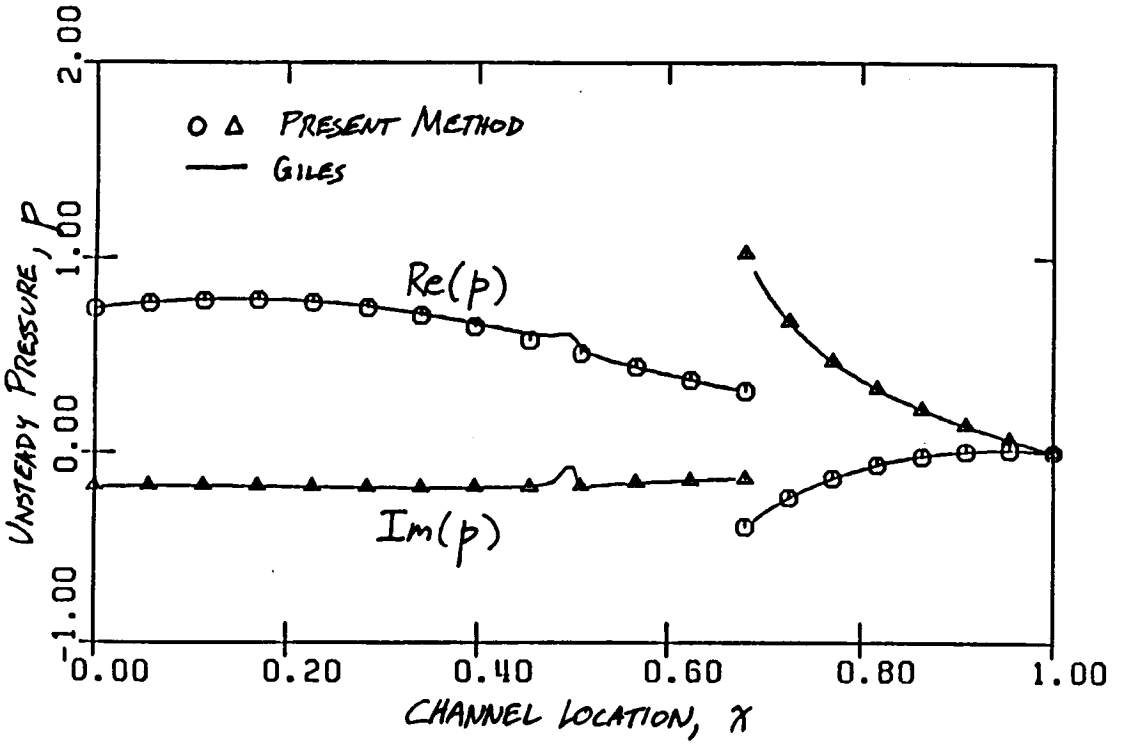

Figure 2.13: Unsteady pressure distribution for choked flow in one-dimensional channel. Upstream total density and pressure is varied with a frequency $\omega = 1.257$

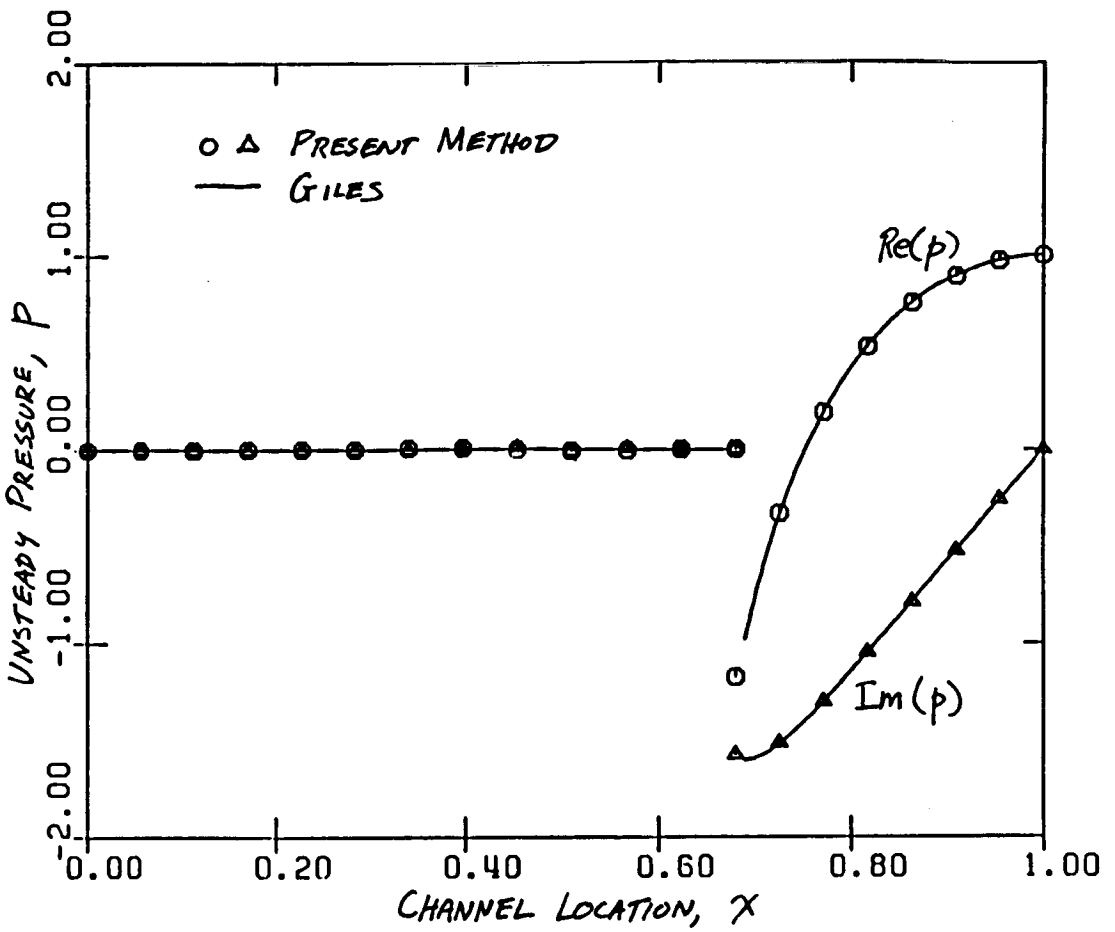

Figure 2.14: Unsteady pressure distribution for a downstream pressure perturbation with frequency ω of 3.1416. Note that ahead of the shock, the pressure is zero.

motion as computed by the linearized Euler theory is $x_s = -.1724 - 0.8522j$ while the equivalent shock motion predicted by the time-marching code is $x_s = -.1707 - 0.8697j$.

As a final example, consider the case of a downstream pressure perturbation. Upstream the total pressure and density perturbations are set to zero. The excitation frequency ω is 3.1416. The computed pressure distribution is shown in Figure 2.14. Note again the excellent agreement between the linearized Euler theory and the time-marching Euler theory. Also, ahead of the shock, the pressure is zero for both theories as it should be, since small disturbances cannot travel upstream in a supersonic region.

2.4 Summary

In this chapter, the numerical method for calculating small disturbance flows in a one-dimensional channel was presented. Although only one-dimensional model problems were analyzed, the theory is essentially the same for two-dimensional problems which we will consider in later chapters.

Also presented was a Newton iteration procedure for solving for the steady channel flow. The method is extremely efficient with subsonic problems typically converging in about five iterations, and transonic problems converging in about ten iterations. Furthermore, since the Newton iteration procedure is so similar to the unsteady linearized Euler method, there is a significant savings in code development time. The steady code is second-order accurate and computed steady flows agree well with exact solutions.

Unsteady pressure distributions were calculated for several model unsteady flow problems. These solutions were compared to a time-accurate time-marching scheme with excellent agreement.

Shock fitting was used to model the position of both steady and unsteady shocks. This allows for a sharp definition of the shock with relatively few conservation cells. Furthermore, unlike captured shocks, the computed shock position for the steady flow and the computed shock motion for the unsteady flow are second order accurate. In the steady case, the computed shock position is nearly indistinguishable from the exact shock position. In the unsteady case, the unsteady shock motion agrees well with the unsteady motion computed using a time-accurate time-marching scheme.

In the next chapter, the differences between the linearized Euler theory and the linearized full potential theory will be examined, as well as the limitations the linearization places on the linearized Euler theory.

Chapter 3

Advantages and Limitations of the Linearized Euler Analysis

In the previous chapter, the linearized Euler anlaysis used to predict small disturbance, quasi-one-dimensional unsteady flows was presented. In later chapters, the method will be extended to two-dimensional channel and cascade flows. Before proceeding, however, two important issues will be addressed in this chapter. The first issue is whether the linearized Euler method is useful for evaluating unsteady flow problems with finite levels of unsteadiness in the flow. The second is whether the method does a significantly better job at predicting unsteady flows than the currently available and less computationally expensive full potential methods.

The fundamental assumption on which the linearized analyses are based is that the flow can be divided into two parts: a mean flow component and a much smaller unsteady component. The linearized analysis asymptotically approaches the full time-dependent nonlinear analysis as the unsteadiness goes to zero. But if the unsteadiness is finite, nonlinear effects may also be important. In Section 3.1, we will examine the behavior of the full nonlinear Euler equations for various levels of unsteadiness. An asymptotic analysis of the Euler equations shows that the linear assumption is valid unless the square of the unsteadiness is significant. Numerical examples will demonstrate that the linearized Euler analysis does a good job of predicting the unsteady behavior even for

moderate levels of unsteadiness.

The second issue is whether the linearized Euler analysis provides a significant improvement in modelling of unsteady flows over the current generation of linearized unsteady full potential methods. Because of the larger computational effort required to perform the linearized Euler analysis, its use would be unwarranted for cases in which the potential method gives accurate predictions. For flows which are isentropic and irrotational, the two methods in principle will provide identical predictions. For non-isentropic flows, such as flows with shocks, the two methods will not agree. The question is how strong the shocks must be before the two methods begin to differ significantly, and what are the mechanisms which produce these differences. In Section 3.2, we will show that the isentropic assumption inherent in the potential methods can produce errors which are significant even for flows with weak shocks. Furthermore, the potential methods are shown to become unreliable for shocked flows at low reduced frequencies.

3.1 Nonlinearities in Unsteady Flow

Much of the work in unsteady flows in cascades has been based on the assumption that the fluid flow in a cascade can be linearized about some nominal steady flow. For relatively small perturbations in the flow, this is a reasonable assumption and certainly goes a long way toward simplifying the nonlinear unsteady compressible flow equations. But the perturbation analysis may not be valid for flows with finite perturbations or for the levels of unsteadiness typically found in turbomachines. In this section, the effect of nonlinearities will be examined using two approaches. In Section 3.1.1, a Fourier series analysis is used to demonstrate the appearence of higher harmonic components due to nonlinearities. In Section 3.1.2, a series of numerical experiments will be performed using a time-accurate time-marching Euler code to quantitatively demonstrate the effect of nonlinearities on unsteady flow solutions for finite flow perturbations.

3.1.1 Fourier Analysis of Unsteady Flows

To begin our discussion, consider again the continuity equation for flow in a quasi-one-dimensional channel.

$$A\frac{\partial \rho}{\partial t} + \frac{\partial}{\partial x}\rho u A = 0 \tag{3.1}$$

The continuity equation, like the momentum and energy equations, is nonlinear in the primitive variables and homogeneous. Since the Euler equations are homogeneous, any unsteadiness will arise from the applied boundary conditions such as those due to upstream flow perturbations or downstream pressure perturbations. Suppose that these external excitations are sinusoidal in time with frequency ω. Because the Euler equations are nonlinear, the exact time dependent solution in general will not be sinusoidal. However, after any initial transients which arise due to the initial conditions decay away, the flow will be periodic in time with period $T = 2\pi/\omega$. Therefore, the primitive variables can be expanded in a complex Fourier series with fundamental frequency ω [32].

$$\rho(x,t) = \sum_{n=-\infty}^{\infty} \rho_n(x) e^{jn\omega t} \tag{3.2}$$

$$u(x,t) = \sum_{n=-\infty}^{\infty} u_n(x) e^{jn\omega t} \tag{3.3}$$

$$p(x,t) = \sum_{n=-\infty}^{\infty} p_n(x) e^{jn\omega t} \tag{3.4}$$

where ρ_n, u_n, and p_n are complex functions of x alone.

To obtain the Fourier coefficients, a Fourier transform is used to convert the time history of the periodic flow into the frequency domain. For complex Fourier series, the transform is given by

$$\rho_0(x) = \frac{1}{T}\int_0^T \rho(x,t)\, dt \tag{3.5}$$

$$\rho_n(x) = \frac{1}{T}\int_0^T \rho(x,t) e^{-jn\omega t}\, dt \tag{3.6}$$

Alternatively, one could represent the periodic time history of the flow in a Fourier sine and cosine series. Hence, for example, the density is given by

$$\rho(x,t) = \rho_0(x) + \sum_{n=1}^{\infty} \rho_{cn}(x)\cos(n\omega t) + \sum_{n=1}^{\infty} \rho_{sn}(x)\sin(n\omega t) \tag{3.7}$$

where the coefficients ρ_0, ρ_{cn}, and ρ_{sn} are given by

$$\rho_0(x) = \frac{1}{T}\int_0^T \rho(x,t)\,dt \tag{3.8}$$

$$\rho_{cn}(x) = \frac{2}{T}\int_0^T \rho(x,t)\cos(\omega n t)\,dt \tag{3.9}$$

$$\rho_{sn}(x) = \frac{2}{T}\int_0^T \rho(x,t)\sin(\omega n t)\,dt \tag{3.10}$$

The Fourier sine and cosine series is really equivalent to the complex Fourier series. The relationship between the complex Fourier series coefficients and the sine and cosine series coefficients is

$$\rho_{cn}(x) = (\rho_n(x) + \rho_{-n}(x)) \tag{3.11}$$

$$\rho_{sn}(x) = \frac{1}{j}(\rho_n(x) - \rho_{-n}(x)) \tag{3.12}$$

Furthermore, if the function $\rho(x,t)$ is a real function, then

$$\rho_{cn}(x) = \mathrm{Re}(\rho_n(x)) \tag{3.13}$$

$$\rho_{sn}(x) = -\mathrm{Im}(\rho_n(x)) \tag{3.14}$$

$$\rho_{-n} = \rho_n^* \tag{3.15}$$

where the * symbol indicates the conjugate operator.

So long as the flow is periodic, the Fourier series representation is a perfectly general way to describe the flow. More importantly, however, is the fact that the Fourier series representation allows us to systematically examine the effects of nonlinearities in the flow. The general procedure is to substitute the complex Fourier series representation of the primitive variables into the Euler equations. The resulting partial differential equations are then in terms of the Fourier coefficients. Hence, the differential equations describe the way the coefficients are related to one another. A careful asymptotic analysis of the behavior of the Fourier coefficients provides insight into the behavior of the nonlinear flow.

To begin, Equations 3.2-3.4 are substituted into the Euler equations. Wherever products of primitive variables occur, the multiplication of the Fourier series is carried out term by term. For example, in the continuity equation the multiplication of the

product ρu is carried out term by term and the resulting series is rearranged in like powers of $\exp(j\omega t)$. For the continuity equation to hold, the resulting series should vanish term by term. Hence we have that

$$\frac{\partial}{\partial x}A\left(\rho_0 u_0 + \rho_1 u_{-1} + \rho_2 u_{-2} + \cdots + \rho_{-1} u_1 + \rho_{-2} u_2 + \cdots\right) = 0 \tag{3.16}$$

$$j\omega A\rho_1 + \frac{\partial}{\partial x}A\left(\rho_0 u_1 + \rho_1 u_0 + \rho_2 u_{-1} + \cdots + \rho_{-1} u_2 + \rho_{-2} u_3 + \cdots\right) = 0 \tag{3.17}$$

$$-j\omega A\rho_{-1} + \frac{\partial}{\partial x}A\left(\rho_0 u_{-1} + \rho_{-1} u_0 + \rho_{-2} u_1 + \cdots + \rho_1 u_{-2} + \rho_2 u_{-3} + \cdots\right) = 0 \tag{3.18}$$

$$2j\omega A\rho_2 + \frac{\partial}{\partial x}A\left(\rho_1 u_1 + \rho_2 u_0 + \rho_3 u_{-1} + \cdots + \rho_0 u_2 + \rho_{-1} u_3 + \cdots\right) = 0 \tag{3.19}$$

$$-2j\omega A\rho_{-2} + \frac{\partial}{\partial x}A\left(\rho_{-1} u_{-1} + \rho_{-2} u_0 + \rho_{-3} u_1 + \cdots + \rho_0 u_{-2} + \rho_1 u_{-3} + \cdots\right) = 0 \tag{3.20}$$

and so forth.

To solve completely for the periodic flow in the channel, one would have to solve simultaneously for all the Fourier coefficients. This of course is impossible since in principle one would have to solve an infinite number of nonlinear simultaneous differential equations. Nevertheless, some insight into the effects of nonlinearities on higher harmonic content can be found by looking at the asymptotic behavior of the Fourier components as the perturbation level gets small. Let us assume for the moment that $\rho_0 \gg \rho_{\pm 1} \gg \rho_{\pm n}$ and $u_0 \gg u_{\pm 1} \gg u_{\pm n}$. Then to leading order, the Fourier coefficients are given by

$$\frac{\partial}{\partial x}\rho_0 u_0 A = 0 \tag{3.21}$$

$$j\omega A\rho_1 + \frac{\partial}{\partial x}A\left(\rho_0 u_1 + \rho_1 u_0\right) = 0 \tag{3.22}$$

$$2j\omega A\rho_2 + \frac{\partial}{\partial x}A\left(\rho_1 u_1 + \rho_2 u_0 + \rho_0 u_2\right) = 0 \tag{3.23}$$

Equation 3.21 is simply the steady state continuity equation. That is to say that the leading order behavior of the mean flow continuity equation is equivalent to the steady flow continuity equation. Equation 3.22 is the linearized continuity equation on which the unsteady analysis developed in this report is based. Finally, Equation 3.23 is the leading order behavior of the second harmonic component in the flow. Note that the second harmonic component is excited by the perturbation product of the fundamental

components $\rho_1 u_1$. This means that for small levels of unsteady flow, the unsteady motion of the fluid will be nearly harmonic in time as this product is extremely small. However, as the level of unsteadiness gets larger, the product will become larger until at some point the second harmonic content will become significant. The component of the second fundamental frequency present will be approximately proportional to the square of the excitation level.

We have just seen that to leading order, the linearized Euler equations give the correct results. Next consider the higher order corrections to Equations 3.21-3.23. Keeping only the next highest order terms in the mean flow equation gives

$$\frac{\partial}{\partial x}\left(A\rho_0 u_0 + \frac{1}{2}(\rho_{c1}u_{c1} + \rho_{s1}u_{s1})\right) = 0 \tag{3.24}$$

In other words, the mean flow is altered by the presence of unsteadiness. This effect, although second order, can be important if the unsteadiness is large. These modifying terms in the continuity equation (and also in the momentum and energy equations) are analogous to the Reynolds stress terms which appear in the analysis of turbulent flows. Because the equations which describe the unsteady flow are nonlinear, the mean flow is not the same as the steady flow. For boundary layers, this means that the mean flow for a laminar (steady) flow is not the same as the mean flow for a turbulent (unsteady) flow. For aeroelastic problems, it means that the steady pressure distribution on an airfoil is not the same as the mean pressure distribution on a vibrating airfoil. Fortunately, this effect is second order and therefore vanishes as the unsteadiness becomes small.

Similarly, the higher order corrections to the first order (linearized) Euler equations are third order, or two orders higher than the leading order behavior. Therefore the linearized equations are valid so long as the square of the unsteadiness is not significant. Said another way, the difference between the results of the linearized Euler analysis and an exact solution will be of the order of the square of the unsteadiness. This sort of asymptotic analysis shows qualitatively that the linearized Euler analysis is valid for small to moderate levels of unsteadiness. In the next section, a time-marching Euler code will be used to determine the unsteady flow in a channel for increasing levels of unsteadiness. The results will be compared to the qualitative analysis of this section.

3.1.2 Numerical Examples

In Section 3.1.2, the qualitative behavior of nonlinearities in unsteady flow was examined by looking at the asymptotic behavior of the various Fourier components of the flow. In this section, we will numerically examine the effects of nonlinearities on unsteady flows by performing a numerical experiment. In this experiment, a time-accurate Euler code is used to calculate the unsteady flow in a quasi-one-dimensional channel. The source of the unsteadiness in the flow is a harmonic variation in the upstream total pressure and density. The calculated time history of the flow can then be Fourier transformed to obtain the Fourier components of the flow.

For this numerical experiment, the one-dimensional, time-accurate, conservative, implicit Euler code of Giles [31] was used as the test vehicle. The general procedure is to first run the code with steady boundary conditions at the inlet and exit of the channel. The code is time marched until the flow reaches a steady state solution. Then, using this solution as a starting point, the code is restarted, but this time the boundary conditions are sinusoidal in time. The code is time marched sufficiently long enough so that initial transients will have decayed. The resulting unsteady flow will be periodic in time although not necessarily sinusoidal due to the nonlinear nature of the Euler equations. The time history of one period of the flow is then Fourier transformed to obtain the zeroth, first, and second Fourier components of the flow.

For the first case studied, the nominal mean flow was subsonic. The channel is defined on the domain $x \in [0,1]$ and has the area distribution $A(x) = 1 - \frac{1}{4}\sin^2(\pi x)$. Shown in Figure 2.3 are the nominal steady pressure, density, and velocity through the channel. For this case, the upstream total pressure P_{T0} was set to 1.175, the upstream total density ρ_{T0} to 1.122, and the downstream static pressure P_{exit} to unity. Giles' code was time marched until a steady state solution was obtained.

Next, to investigate the unsteady flow in the channel, the code was restarted and the upstream total pressure upstream was varied as $P_T = P_{T0} + \Delta P_T \cos(\omega t)$ with a frequency ω of 1.0472. The upstream total density was varied such that the inlet flow was isentropic. For the cases reported here, the total pressure variation ΔP_T was 0.005, 0.01, 0.02, 0.05, and 0.10. Downstream, the pressure was held fixed at unity. Giles'

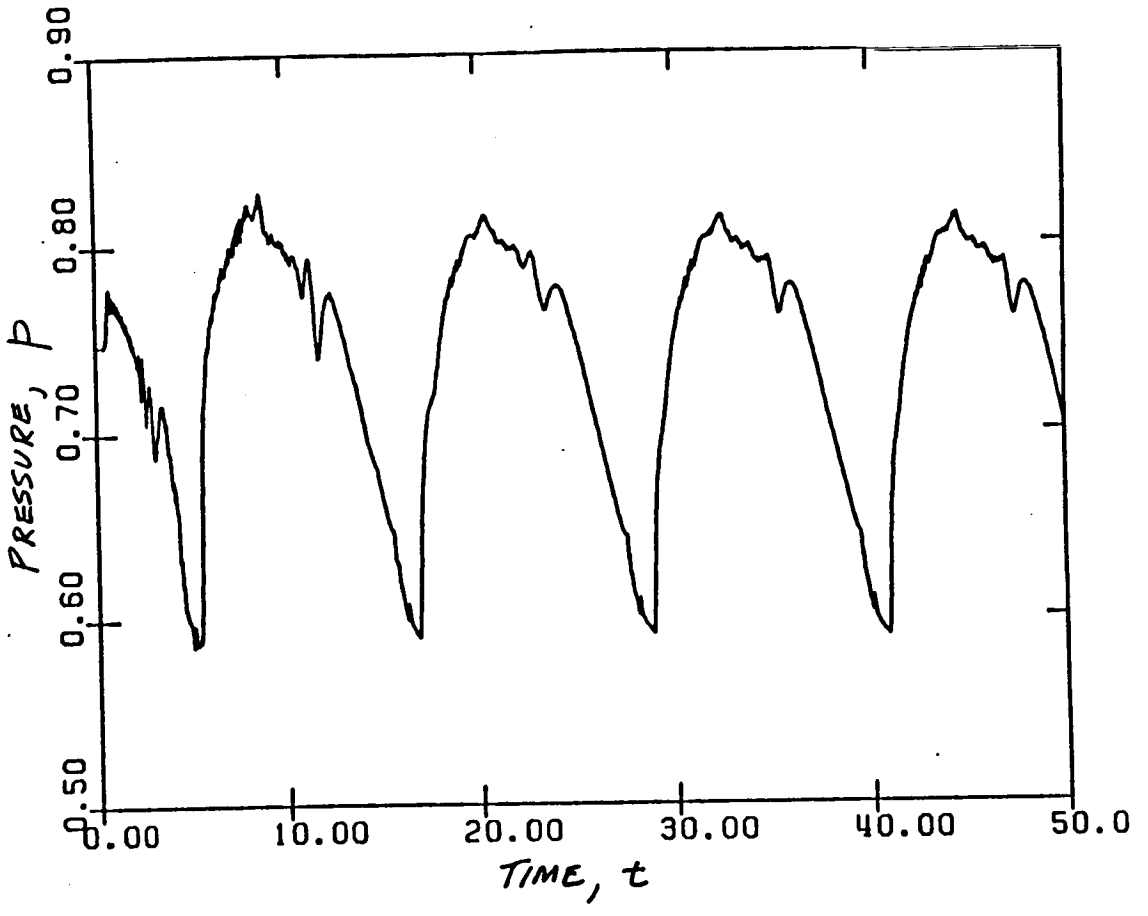

Figure 3.1: Pressure at the throat of a converging-diverging channel for an upstream variation in total pressure and density. The excitation frequency ω is 1.0472. Note the higher harmonics present in the flow.

code was time marched long enough for the flow to reach a periodic state, that is, until all transient behavior dependent on the initial conditions had decayed away. Then, one period of the response was Fourier transformed to determine the harmonic content of the flow.

Figure 3.1 shows a typical calculated time history of the flow in the channel. For this case, $\Delta P_T = 0.05$, and $\omega = 1.0472$. Plotted is the calculated pressure as a function of time at the throat of the channel. Clearly, the flow is not sinusoidal in time, but rather is periodic (or nearly so after the transients have passed) and contains a significant level of higher harmonic content. Figure 3.2 shows the computed harmonic content of the

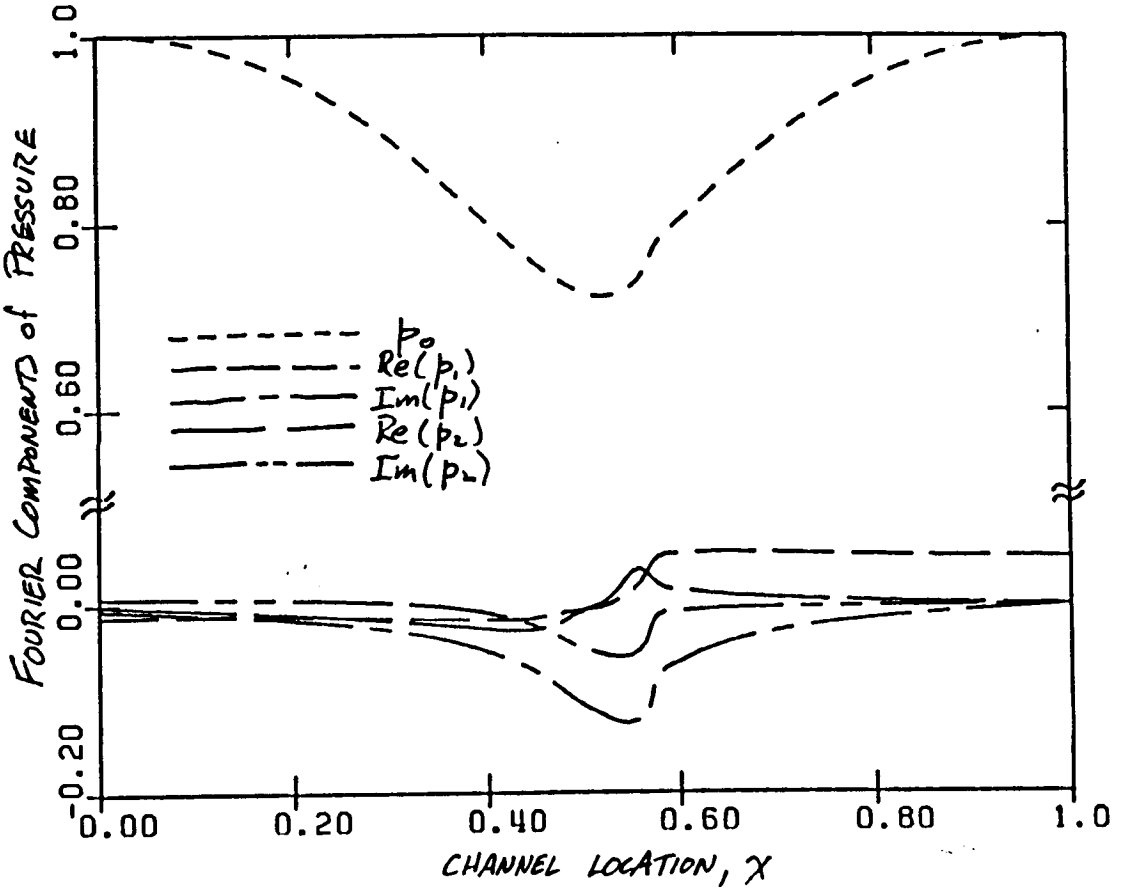

Figure 3.2: Harmonic content of unsteady subsonic flow in a converging-diverging channel for an upstream variation in total pressure and density. The excitation frequency ω is 1.0472. Note the significant levels of the second harmonic.

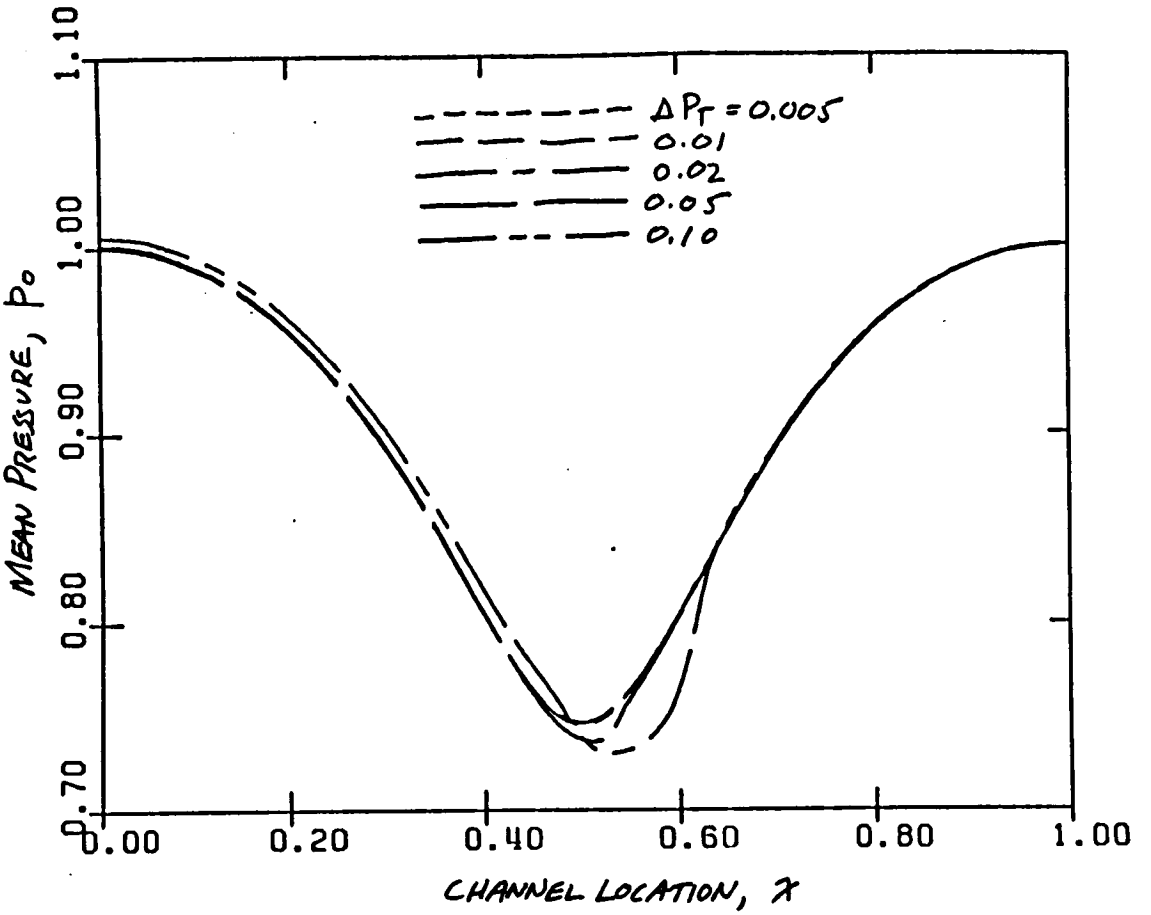

Figure 3.3: Mean flow through a converging-diverging channel for various levels of upstream excitation. The excitation frequency ω is 1.0472

zeroth, first, and second harmonic frequencies. The large level of the higher harmonic (second) content indicates that for this level of unsteadiness in the flow, nonlinear effects are important, at least if one wishes to determine the precise time history of the flow.

Figure 3.3 shows the mean flow through the channel for various levels of upstream total pressure variation. Note that for total pressure variations of 0.005, 0.010, and 0.020, the mean pressures are nearly indistinguishable from one another. For a total pressure variation of 0.050, the mean pressure deviates slightly from the steady solution at the throat. For a total pressure variation of 0.100, the difference is even more pronounced. Recall that the mean flow is modified by a Reynolds stress like term in regions of large flow unsteadiness. As will be seen shortly, the region of greatest unsteadiness

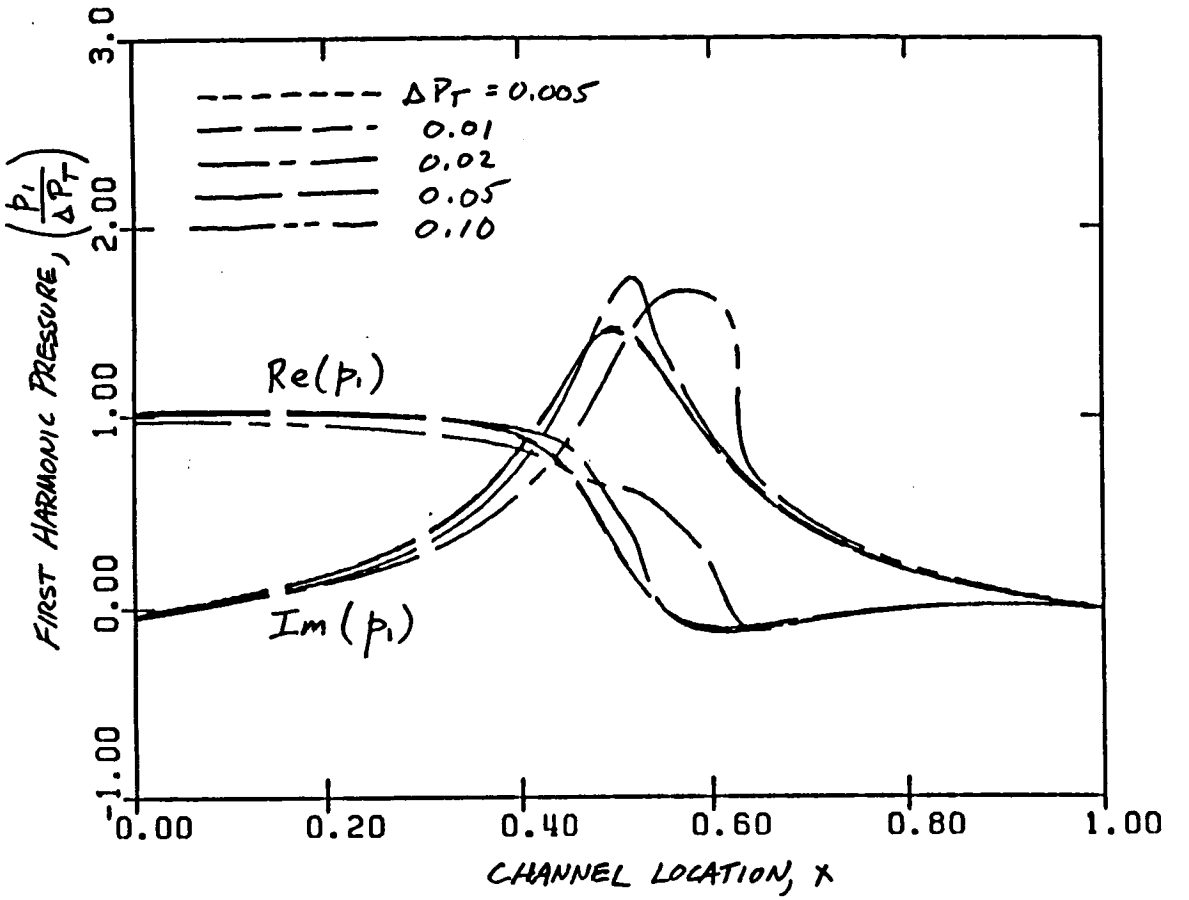

Figure 3.4: First harmonic component in unsteady pressure for increasing levels of unsteadiness in the flow.

is in the neighborhood of the throat. Hence, this is where nonlinear effects will first be noticed.

Shown in Figure 3.4 are the first harmonic components calculated from Giles' results. So that they all appear on the same scale, the results are scaled by the excitation level ΔP_T. The linear theory and the time-marching solution for a total pressure variation ΔP_T of 0.005, 0.01, and 0.02 give virtually identical results. Even the $\Delta P_T = 0.05$ case, which has significant levels of higher (second) harmonic components, has good agreement with the linearized theory. For higher levels of unsteadiness, however, the results begin to differ significantly.

Next we wish to test the hypothesis that the second harmonic components are pro-

portional to the square of the excitation level for low levels of unsteadiness. Figure 3.5 shows the second harmonic components scaled by ΔP_T^2. Note that for $\Delta P_T = 0.005$, 0.01, and 0.02, the components agree well with one another. For higher levels of unsteadiness, the agreement is not as good, but are still of the same order. These results demonstrate clearly that for small levels of unsteadiness, the second harmonic terms appear with the square of the level of unsteadiness.

Note that in all three cases, the zeroth, first and second harmonic components begin to deviate from the small their limiting values at a total pressure variation ΔP_T of about 0.05. At this level of inlet disturbance, the magnitude of the first harmonic component of the pressure is a maximum near the throat and has a magnitude of about 0.075 or about ten percent of the local pressure. The second harmonic component is around four percent of the steady pressure at the throat. Although one case is hardly representative of all unsteady flows, this example does give a feeling for the level of unsteadiness at which the linearized Euler analysis is no longer valid.

As a second example, consider the transonic channel flow shown in Figure 2.7. The inlet total pressure and density are 1.25 and 1.173 respectively. The exit static pressure is 1.0. This back pressure is low enough to choke the flow. The flow enters the channel subsonically, passes through the sonic line at the throat, becomes supersonic, then shocks and exits the channel subsonically. Unsteadiness is introduced in this example by varying the back pressure sinusoidally in time such that $p_{\text{exit}} = P_{\text{exit}} + \Delta p_{\text{exit}} \cos(\omega t)$ where the frequency ω is 1.0472. This unsteady back pressure produces unsteady flow aft of the shock as well as motion of the shock itself. The flow upstream of the shock will be quiescent unless the shock motion is so large that the shock moves upstream of the throat. The linear theory predicts that the unsteady pressure and shock motion will be sinusoidal.

As with the subsonic case, Giles' code was time marched until a steady-state solution was obtained. Then the code was restarted and run for various levels of unsteady back pressure. For the cases studied here, the unsteady variations of the back pressure Δp_{exit} are 0.010, 0.020, 0.040, and 0.080. For all cases except the last, the shock oscillated back and forth in the channel without passing through the throat. For the last case, however,

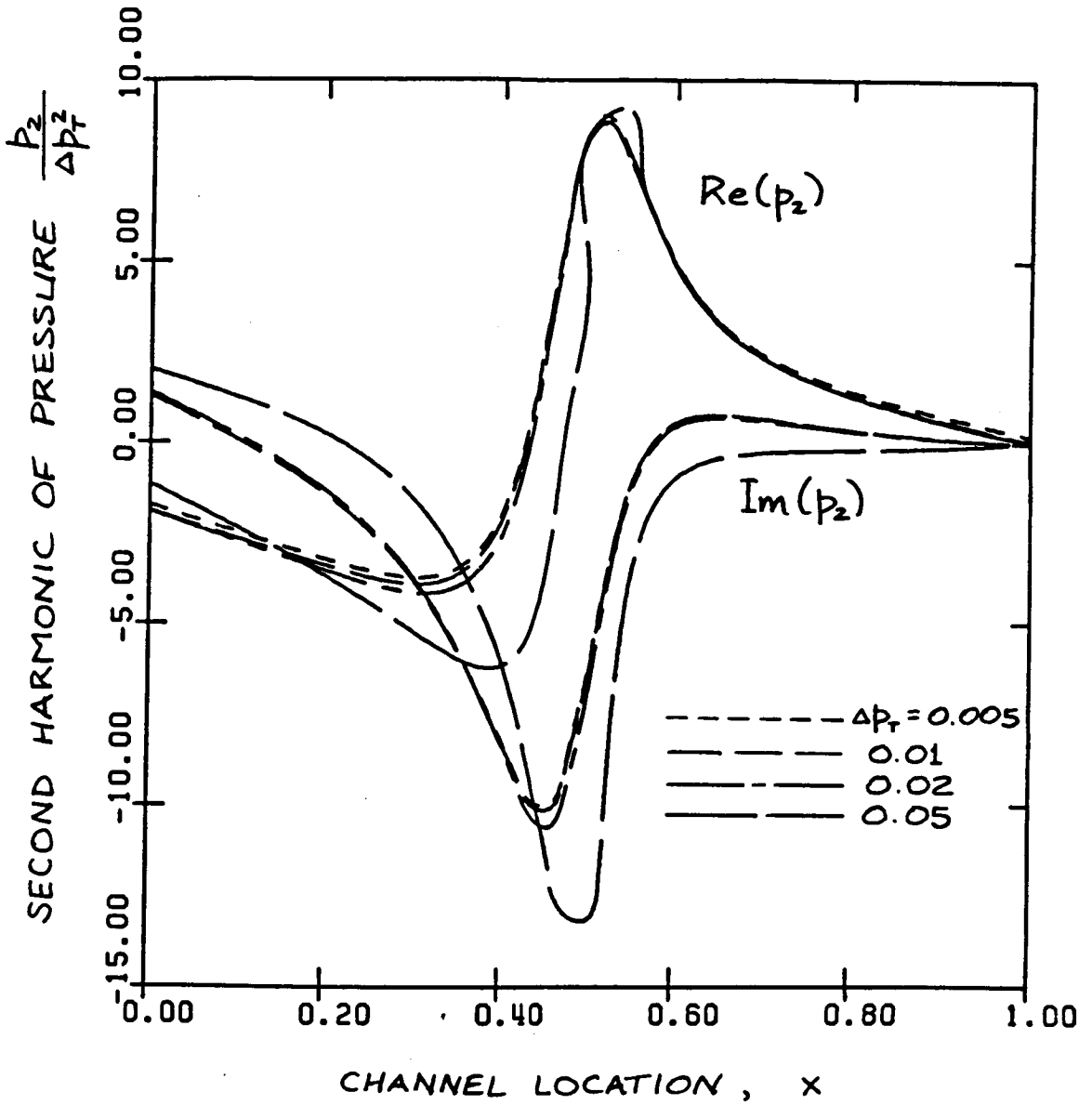

Figure 3.5: Second harmonic component in unsteady pressure for increasing levels of unsteadiness in the flow.

Table 3.1: Fourier components of nonlinear shock motion for various levels of unsteady back pressure.

Δp_{exit}	x_{s0}	$\frac{Re(z_{s1})}{\Delta p_{exit}}$	$\frac{Im(z_{s1})}{\Delta p_{exit}}$	$\frac{Re(z_{s2})}{\Delta p^2_{exit}}$	$\frac{Im(z_{s2})}{\Delta p^2_{exit}}$
0.01	0.6791	−0.0999	1.1846	0.9950	−1.3732
0.02	0.6782	−0.0934	1.1918	0.7949	−1.8210
0.04	0.6737	−0.0554	1.2214	0.7171	−2.0072
Linear	0.6805	−0.0996	1.1777	—	—

the shock motion was great enough so that the shock passed completely through the throat and then disappeared slightly ahead of the throat. At a later time in the cycle the shock reformed in the aft section of the channel and the cycle was repeated.

The unsteady pressure time histories were Fourier transformed to obtain the zeroth-, first-, and second-harmonic components of the flow. These results for the zeroth- and first-harmonic are shown in Figures 3.6-3.7. The pressure in this region is anharmonic due the passing of the shock and the corresponding sudden pressure rise or fall. Therefore, the Fourier transform of this time history will resemble an impulse in the vicinity of the shock. The harmonic components of the time history are not presented in the region of the channel in which the shock oscillated. Figure 3.6 shows the mean flow through the channel along with the computed steady flow. Note that the mean flow is indistinguishable from the steady flow in all cases (at least away from the shock).

Shown in Figure 3.7 is the first-harmonic component of the unsteady shocked flow as computed from the time-marching code. The results are scaled by Δp_{exit}. Behind the shock, the unsteady pressure distributions are nearly identical for all of the cases although the case where Δp_{exit} is 0.080 differs very slightly from the other cases and the linear solution. Upstream of the shock, the flow is quiescent except for this last case. The shock passing upstream through the throat allows the downstream influence to be felt upstream of the throat.

Table 3.1.2 shows the mean, first harmonic, and second harmonic components of the shock motion. The mean position of the shock is seen to move slightly forward with

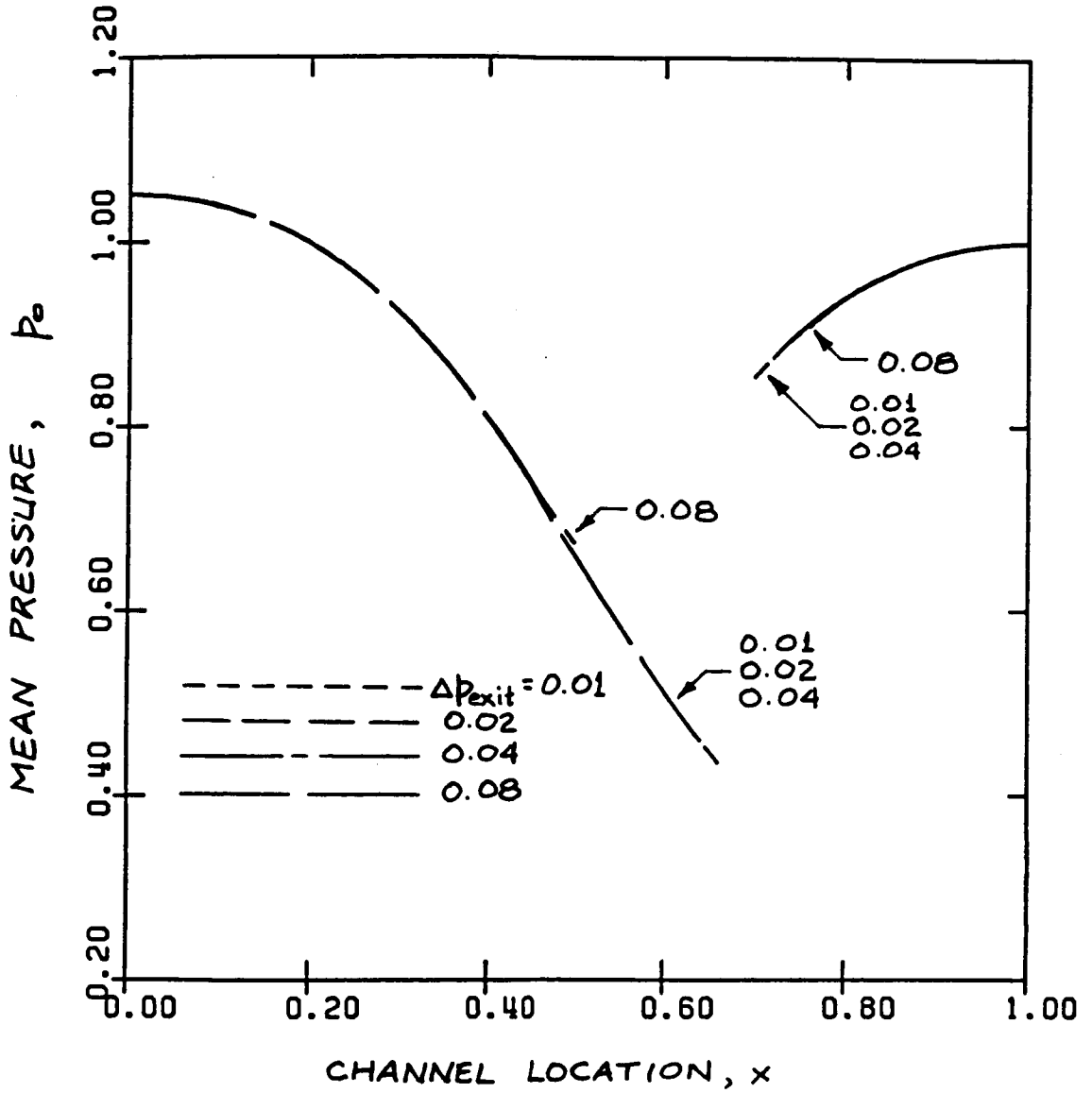

Figure 3.6: Mean transonic flow in quasi-one-dimensional channel for various levels of unsteady back pressure. Note that the mean flow away from the shock is nearly indistinguishable from the steady flow in the channel.

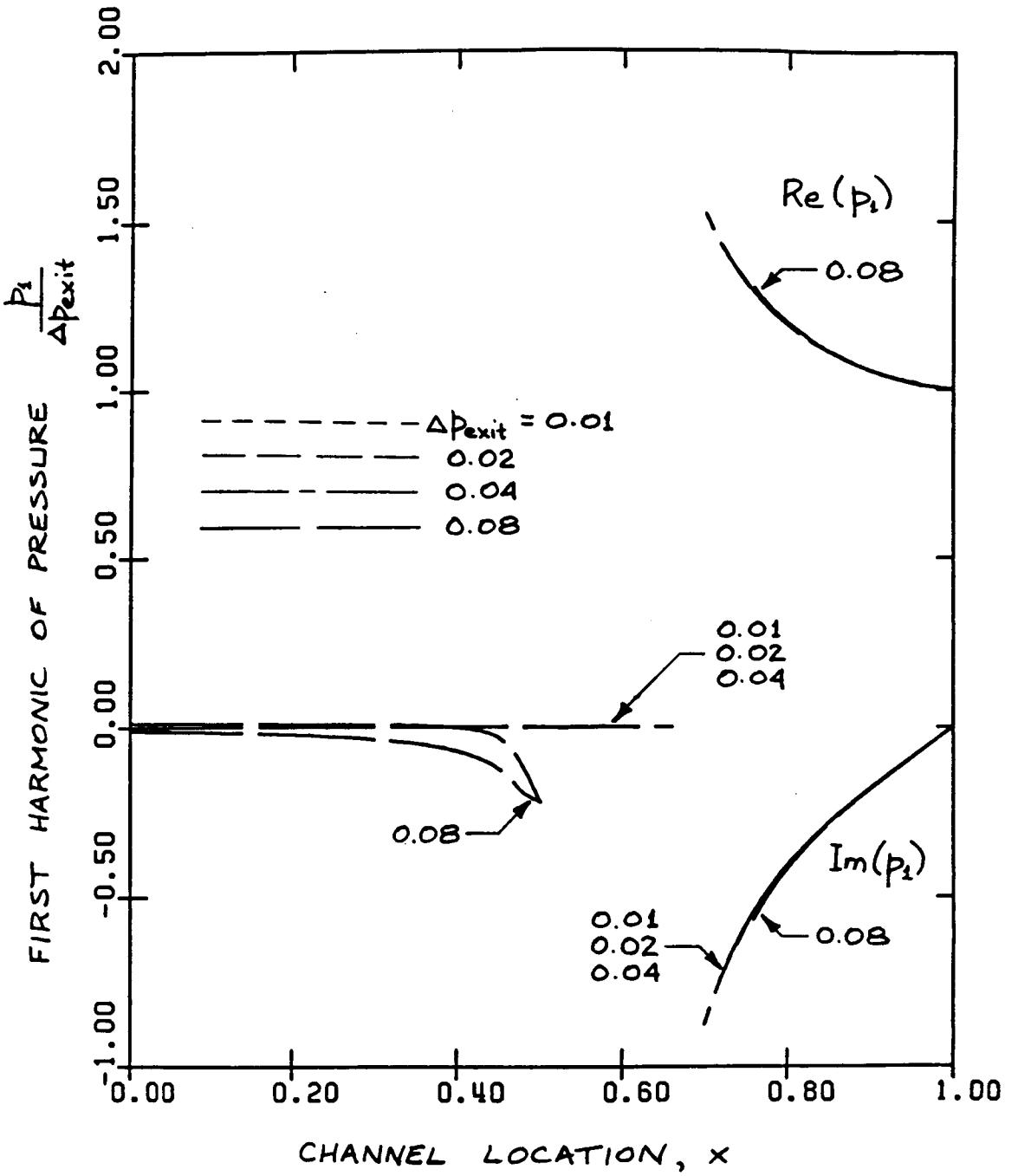

Figure 3.7: First harmonic component of unsteady transonic flow in channel for various levels of unsteady back pressure. Note that the Fourier components for the different levels of back pressure are indistinguishable from one another except for the $\Delta p_{exit} = 0.08$ case. For this high level of unsteadiness, the shock passes through the throat, disappears, and then reforms aft of the throat.

increasing downstream back pressure variation. The situation is somewhat analogous to a nonlinear spring. It is easier to move the shock a finite distance forward than it is to move it aft. This occurs because the shock gets weaker as it moves forward and stronger as it moves aft. The first-harmonic content is seen to agree quite well with linear theory for the first two cases. The magnitude of shock motion agrees to within about 1.2 percent and the phase agrees to within less than 0.5 degrees. For the case of Δp_{exit} of 0.040, the error is about 3.5 percent in magnitude, while the phase is off by about 2.3 degrees. This is a truly remarkable result considering the total shock excursion is about 10 percent of the channel length for this case. For shock excursions much larger than this, the linear analysis is no longer valid as the shock disappears and reappears over the cycle.

These results have important implications for the aeroelastic analysis of turbomachinery. As a rough rule of thumb, a linearized analysis should be regarded as suspect if the amplitudes of the unsteady part of the flow flow is greater than ten percent of the total local values. For example, to predict the onset of flutter, which is governed by the behavior of the unsteady flow for very small flow perturbations, the unsteady flow may be modelled via a small perturbation analysis. other hand, the blades cannot. to predict the forced response of the blading due to incoming wakes or inlet distortion, the unsteady flow may or may not be analyzed accurately using a linearized analysis depending on the level of unsteadiness.

3.2 Comparison to Full Potential Theory

Some of the most widely used methods for predicting subsonic and transonic unsteady flows through real cascades are those based on linearized full potential theory [33,19]. However, the isentropic assumption inherent in the potential theory places a limit on its ability to accurately predict unsteady flows containing shocks (just as the inviscid assumption may place limitations on the linearized Euler method). In this section, we will compare results based on linearized Euler theory to those based on full potential theory. In particular, it will be shown that the isentropic assumption can produce serious errors in the predicted shock motion even for relatively weak shocks,

especially for low reduced frequencies.

For some transonic flow problems, the full potential equations provide a useful approximation. By assuming the flow is irrotational the velocity can be expressed as the gradient of a single scalar function, i.e., the velocity potential. If the flow is further assumed to be isentropic, the other primitive variables can also be expressed in terms of this potential. The equations which describe this irrotational and isentropic fluid motion are essentially a statement of mass conservation so that momentum and energy will, in general, not be conserved at shocks. Nevertheless, these equations have been shown to give reasonably good predictions of steady transonic flows for Mach numbers less than about 1.3. The purpose of this section is test whether linearized unsteady flow predictions based on the potential equations also give good results for such Mach numbers.

Numerical Comparison of Full Potential and Euler Theories

As a test of the linearized full potential theory, let us return to the example presented in Sections 2.2.7 and 2.3.7. We wish to compare the steady and unsteady transonic flows predicted by the Euler theories to those computed by the potential theory. First consider the steady flow problem. For the Euler solution, we specified the upstream total pressure and density and the downstream static pressure. Picking this back pressure fixes the location of the shock in the channel. Once the flow is choked, decreasing the back pressure further does not increase the mass flow through the channel. Further, the pressure at the exit of the channel is somewhat less than the pressure at the inlet due to the total pressure loss across the shock. The situation is somewhat different in the potential flow problem. If the flow is choked, then the pressure is a function of the local area alone. This function is multi-valued having a subsonic and a supersonic branch. But if the flow is choked, and the flow is subsonic at both the inlet and the exit, then (if the channel is symmetric) the pressure at the exit must be equal to the inlet pressure. In other words, one cannot arbitrarily set the back pressure and get a valid solution to the full potential equations. This is because there is no total pressure loss through the shock. Hence, there is no mechanism to set the shock position in the potential theory.

This situation is shown graphically in Figure 3.8.

Therefore, to compare the potential and Euler solutions, we choose the back pressure of the potential solution to be consistent with the incoming static pressure, and the shock position to coincide with the Euler solution shock position. The Euler and potential base flows are shown in Figure 3.9. Note that ahead of the shock, the two flows are identical. Downstream of the shock, however, the pressure and density predicted from the potential theory are larger than those predicted from the Euler theory, while the velocity is smaller. If one were only interested in steady solutions, these differences might be considered small and acceptable. As we will see, however, these relatively small differences can produce much more significant errors in the predicted unsteady flows.

Consider once again the unsteady transonic flow problem presented first considered in Section 2.3.7. Upstream, the total pressure and density are varied harmonically with a frequency ω of 1.257, while downstream the static pressure is held constant. Figure 3.10 shows the computed unsteady pressure distributions for the linearized Euler and linearized potential theories. Ahead of the shock, the two theories produce identical results. This is hardly surprising since ahead of the shock the flow is isentropic. Downstream, however, there are some differences between the two solutions. More disturbing, the computed shock motions differ significantly. The difference between the phases of the two predicted shock motions is 30.5 degrees. Furthermore, the shock displacement predicted by potential theory is 26 percent less that that predicted by Euler theory. Why then are there such large differences in the unsteady results?

Part of the answer lies in the differences in the steady pressure, density, and velocity downstream of the shock. These quantities determine the speed at which pressure waves travel in the fluid. These pressure waves are sometimes referred to as the J^- and J^+ characteristics. The speeds at which these waves travel are given by

$$c_{J^-} = U - C \tag{3.25}$$

$$c_{J^+} = U + C \tag{3.26}$$

where C is the local speed of sound. Note that downstream of the shock, the character-

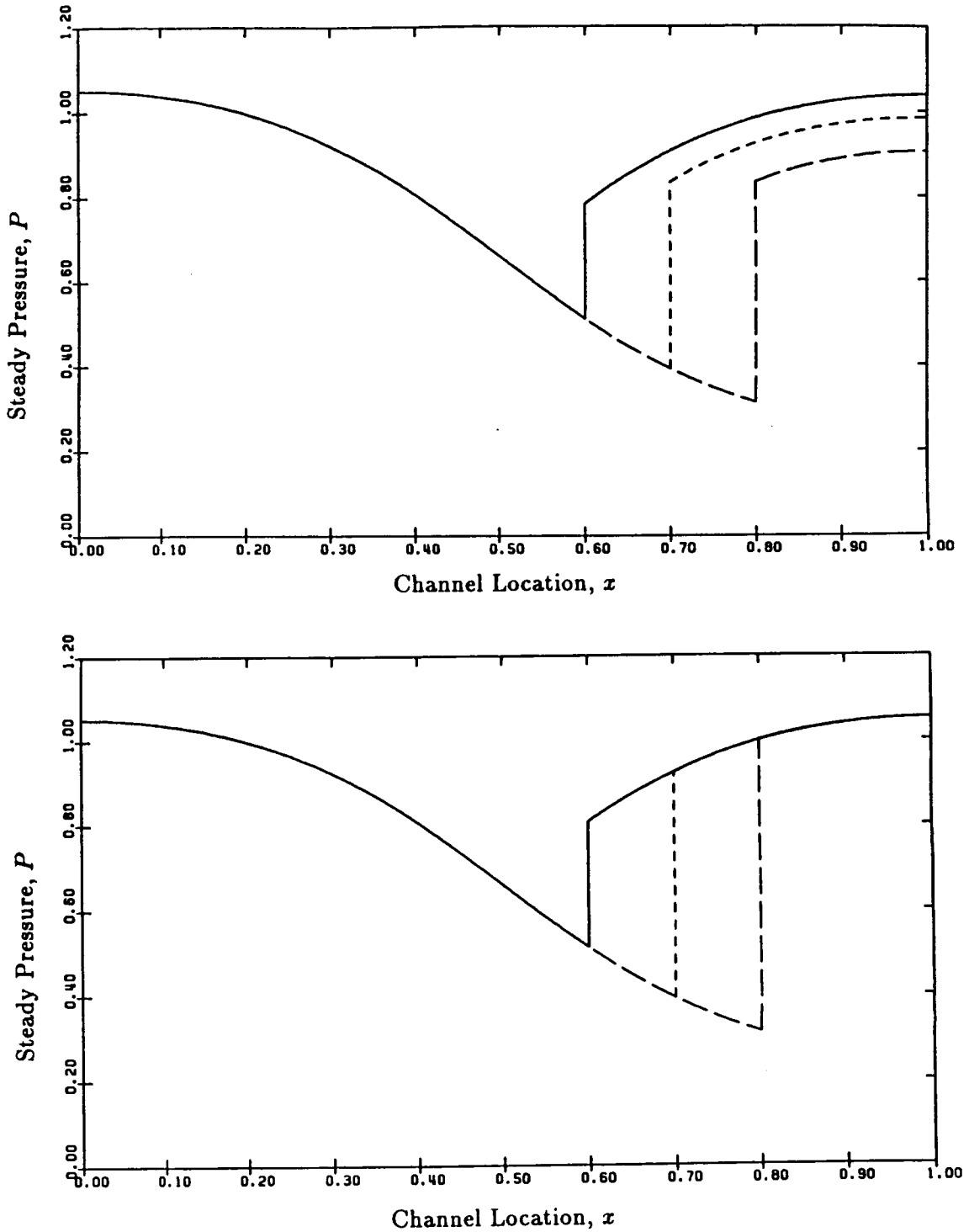

Figure 3.8: Effect of back pressure on the shock position of choked flow in a one-dimensional converging-diverging channel for Euler (upper) and potential (lower) theories. Note that for potential theory, the back pressure is unique, and cannot be varied to fix the shock location.

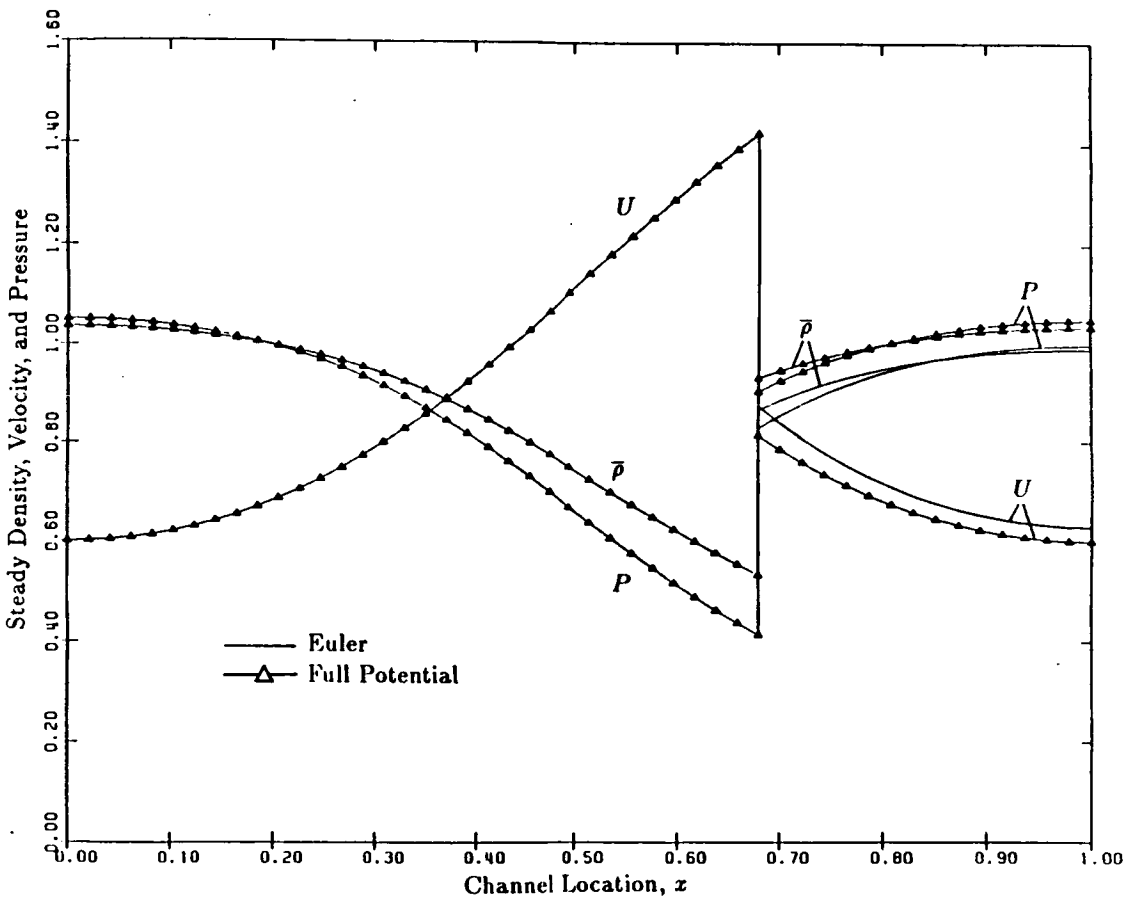

Figure 3.9: Steady base flow about which unsteady Euler and potential flows are calculated. Note the flows are identical ahead of the shock, but differ slightly behind the shock.

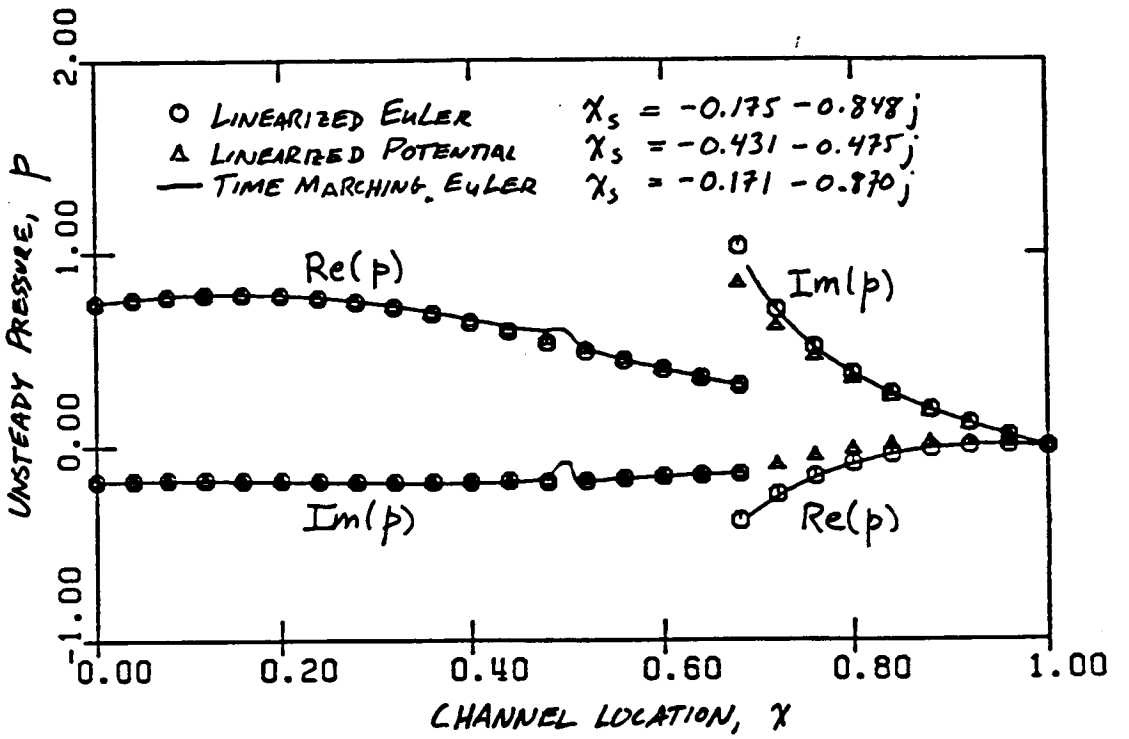

Figure 3.10: Unsteady transonic flow calculated from Euler and potential theories. Upstream the total pressure is varied isentropically with a frequency ω of 1.257

istic speeds differ for the Euler and potential theories. Hence, any disturbance which is reflected off of the exit boundary and propagates forward will move at the wrong speed in the potential theory. This upstream travelling pressure wave arrives at the shock at the wrong time, causing a phase error in the shock motion. This is at least part of the reason for the difference between the two theories.

One could argue that this model problem is too contrived, that for more physical problems, a radiation boundary condition would be required at the exit flow boundary. Hence, this upstream travelling pressure wave would not be present (or at least less prevalent) and this problem would be alleviated. To some extent this is a fair criticism of this model problem. Therefore, for our next model problem, we will apply a radiation boundary condition at the exit. This is done by setting the incoming characteristic variable to zero. A characteristic analysis (see Chapter 5) shows that the incoming characteristic is given by

$$w_{J-} = u - \frac{1}{\sqrt{\gamma \bar{\rho} \bar{P}}} p \tag{3.27}$$

for the Euler theory and

$$w_{J-} = u - \frac{1}{\sqrt{\gamma \bar{\rho} \bar{P}}} p = (1 - M)u + j\omega\phi \tag{3.28}$$

for the potential theory. The static-pressure exit-boundary conditions were replaced by requiring the incoming characteristic to be zero. Figure 3.11 shows the computed results. The agreement is somewhat better, but note that the predicted shock motions still do not agree that well. In particular, the difference shock motion predicted by the potential theory lags that predicted by the Euler theory by 26.8 degrees. This phase lag was identified as a problem with potential theory by Ashley [34].

Next, the two codes were run for the same case except that the forcing frequency was lowered to $\omega = 0.1$. The results are shown in Figure 3.12 Note that now the disagreement becomes worse, especially for the predicted shock displacements. The magnitude of this shock displacement predicted using potential theory is 5.9 times larger than that predicted from the Euler theory. The phase difference between the predicted shock motions is 83 degrees. Earlier, we saw that the zero frequency shock displacement (i.e., the steady shock position) depends on the ratio of the back pressure to the total

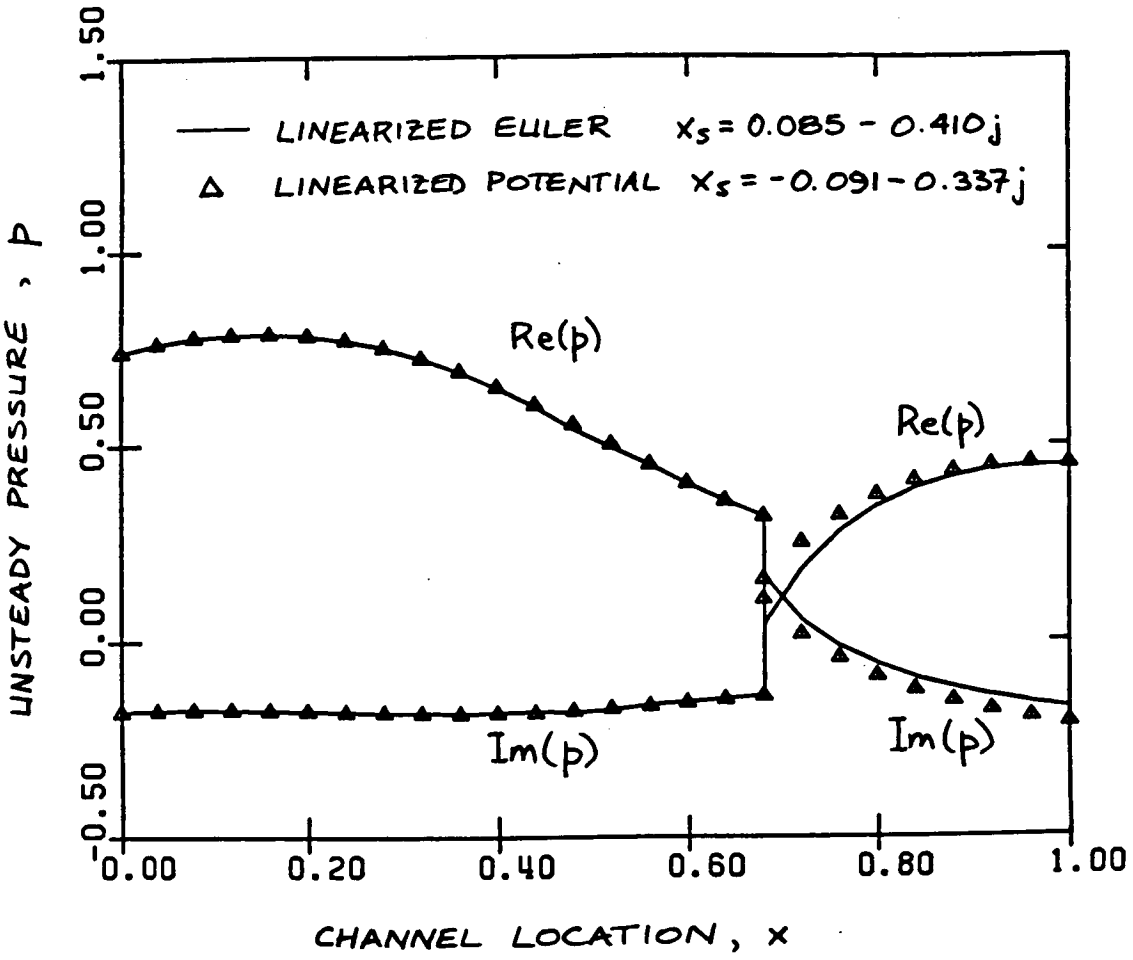

Figure 3.11: Unsteady transonic flow with radiation outflow condition. Upstream the total pressure is varied isentropically with a frequency ω of 1.257

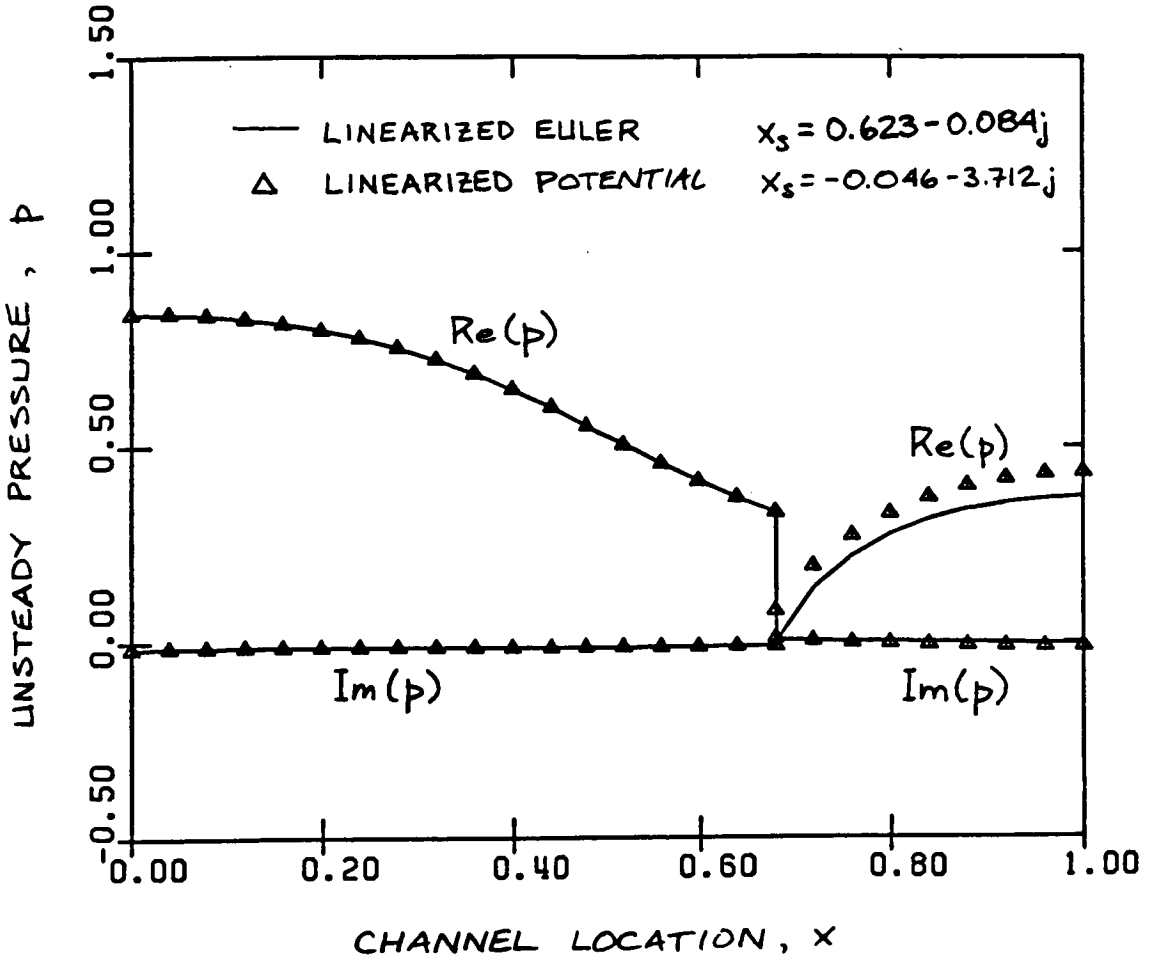

Figure 3.12: Low frequency transonic channel flow ($\omega = 0.1$). Note large difference between shock motions predicted by Euler and potential theories.

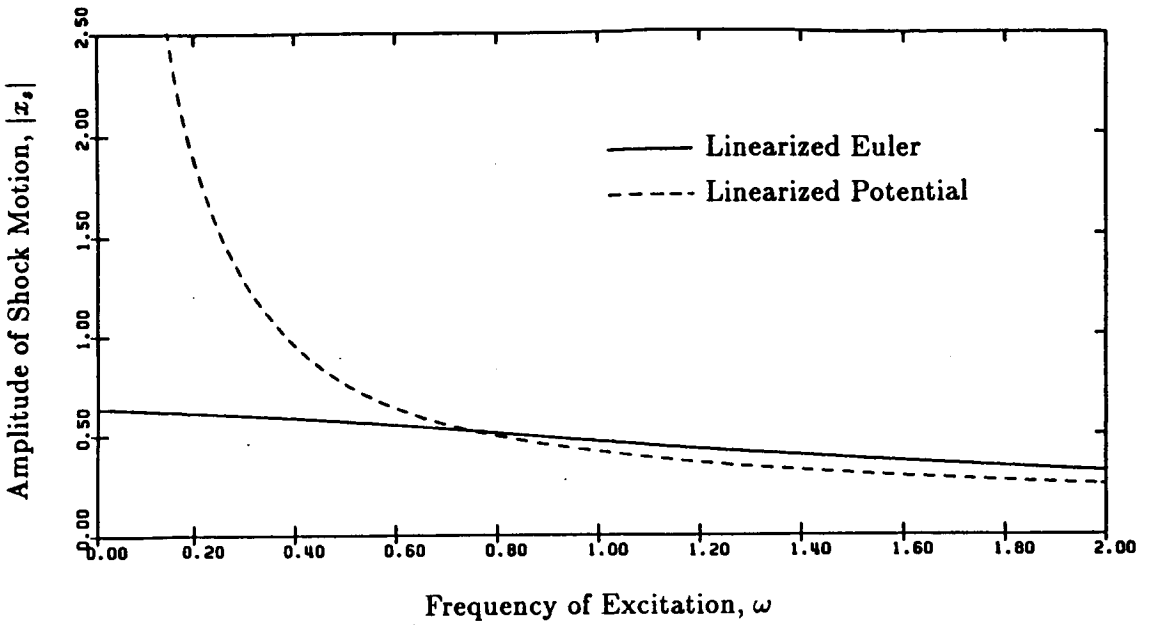

Figure 3.13: Frequency response of shock motion. Shown is the amplitude of shock motion versus frequency of unsteady back pressure. Note that as the frequency approaches zero, the potential shock motion is unbounded while the Euler shock motion reaches a finite value.

inlet pressure. In other words, the displacement of the shock per unit change in this pressure ratio is equal to the slope of the steady shock position as a function of pressure ratio. For the Euler theory, this slope is finite. But in the potential theory, the steady shock can can occur anywhere behind the throat with the exit pressure fixed as shown in Figure 3.8. That is to say that the slope of the shock position curve is *infinite*. Hence, for low frequencies, the shock motion becomes very large and is unbounded as the frequency goes to zero.

Figure 3.13 shows a frequency response plot showing the shock motion in the channel versus the frequency of excitation. As before, the upstream total pressure and density are varied, while downstream, radiation boundary conditions are applied. Note that for the Euler theory, the shock motion amplitude approaches a finite value as the excitation frequency approaches zero. The potential theory, on the other hand, predicts an unbounded response at zero frequency. This phenomenon is due to the isentropic assumption of the potential theory which does not allow for a loss in total pressure

across the shock. Hence, there exists no mechanism to constrain the motion of the shock. It should be mentioned that it may be possible to modify the potential theory to partially account for the steady and unsteady entropy generation at shocks. Recent work by Fuglsang and Williams [35] demonstrated that such corrections greatly improve the steady and unsteady flow predictions of the transonic small potential methods.

3.3 Summary

In this chapter, some of the advantages and limitations of the present method have examined. It was demonstrated that the linearized unsteady Euler analysis compares well with the nonlinear Euler analysis so long as the unsteadiness in the flow is less than about 10 percent of the mean flow. Hence, the linearized Euler analysis is useful for most aeroelastic analyses. Furthermore, it is believed that the linearized Euler analysis provides a significant improvement over current linearized potential analyses in the modelling of flows with shocks.

Chapter 4

Fundamentals of Two-Dimensional Linearized Euler Theory

Unsteady flows present many problems in the design and operation of turbomachinery ranging from noise, to unsteady heat transfer, to stall and surge. In this work, however, we are mainly concerned with the aeroelastic aspects of unsteady flows. In other words, we wish to determine the unsteady loads felt by the engine structure due to the unsteady flow field. In particular, the two main aeroelastic phenomena of interest are the flutter and forced response of blade rows. For the purposes of studying these problems, we will assume that the flow is adiabatic, inviscid, and compressible, but may be rotational and nonisentropic. These assumptions are reasonable so long as the flow remains attached and the blade boundary layers and wakes are confined to narrow regions.

In Section 4.1 the conservation principles for an adiabatic, inviscid, compressible fluid will be presented in both integral and differential form. These different forms of the fundamental physical laws which govern the flow are each useful for different parts of the unsteady flow analysis. For instance, the integral forms are preferred for the derivation of shock and wake jump conditions and for the numerical integration tech-

niques, while the differential form is useful in analyzing the far-field behavior of the fluid. In Section 4.2, the linearization of the nonlinear Euler equations is presented. These linearized equations are at the heart of the unsteady flow analysis. The linearization is carried about some nominal steady flow. Hence, before the unsteady flow can be analyzed, the steady solution must be known. In Section 4.3 the basic steady Euler solver is introduced. The steady Euler equations are solved using a Newton iteration procedure. Finally, in Section 4.4 the details of the linearized unsteady Euler solver are presented. This includes the discretization of the field equations, the linearization and discretization of the unsteady boundary conditions, and the numerical solution of the resulting equation set.

4.1 The Conservation Laws

The conservation equations are well known (see for example [36]) but are discussed here for completeness. In this section, three different forms of the conservation equations are presented. Although all three are equivalent, their different forms are advantageous for different aspects of the analysis of unsteady flows. In Section 4.1.1 the integral form of the conservation laws will be presented for the case of a control volume fixed in space. In Section 4.1.2, this integral form of the conservation laws is extended to the case of a deformable control volume. This form is particularly useful for the derivation of shock and wake jump conditions. Finally in Section 4.1.3, the differential form of the conservation equations, known as the Euler equations are presented. These are useful for analyzing the far-field behavior of the unsteady flow.

4.1.1 Integral Form of the Conservation Laws

We will consider the conservation principles applied to a non-heat conducting, inviscid fluid. The quantities to be conserved are mass, momentum, and energy. Consider a fluid passing through a region D enclosed by a surface S which is fixed in space as shown in Figure 4.1. The statement of conservation of mass is that the rate of increase of mass within the volume is equal to the rate at which mass flows into the region through the

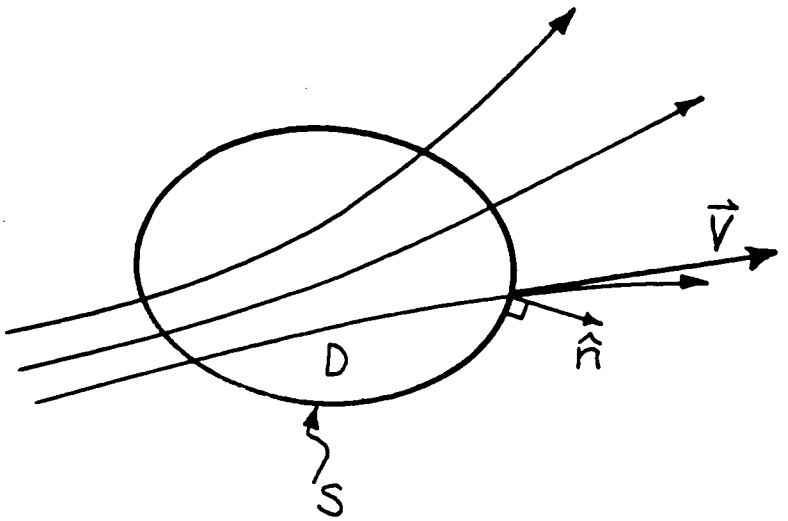

Figure 4.1: Control volume used to derive momentum equations. The volume is assumed to be fixed in space with the fluid flowing through the volume's surface.

surface (the mass flux). In mathematical terms

$$\int_D \frac{\partial}{\partial t}\rho \, dD = -\int_S \rho \mathbf{V} \cdot \mathbf{n} \, dS \tag{4.1}$$

The minus sign on the right hand side of Equation 4.1 is due to the fact that a velocity vector $\mathbf{V}$ in the direction of the outward normal $\mathbf{n}$ corresponds to mass flowing *out* of the region, not in.

In a similar way, the conservation of momentum can be expressed. The statement of the conservation of momentum is that the rate of change of momentum of a group of fluid particles is equal to the sum of the body forces acting on the fluid particles plus the integrated surface forces acting on the surface. In the absence of body forces, we have that

$$\int_D \frac{\partial}{\partial t}\rho \mathbf{V} \, dD + \int_S \rho \mathbf{V}(\mathbf{V} \cdot \mathbf{n}) \, dS = -\int_S p\mathbf{n} \, dS \tag{4.2}$$

The first term in Equation 4.2 represents the rate of change of momentum within the region D, while the second term represents the rate at which momentum leaves the domain (the momentum flux). The two terms combined represent the rate of change

of momentum of the group of fluid particles which pass through the surface S at any instant of time. This then is equal to the sum of the forces acting on the boundary of the surface S.

Finally, the conservation of energy is considered. In this case, the net rate of energy increase of a group of fluid particles is equal to the work done on them by external forces. Hence we have that

$$\int_D \frac{\partial}{\partial t}(e + \frac{\rho V^2}{2})\, dD + \int_S (e + \frac{\rho V^2}{2})\mathbf{V} \cdot \mathbf{n}\, dS = -\int_S p\mathbf{V} \cdot \mathbf{n}\, dS \qquad (4.3)$$

where e is the internal energy per unit volume of the fluid. The term $\rho V^2/2$ represents the kinetic energy per unit volume. The rate of change of total energy of a group of fluid particles is equal to the two terms on the left hand side of Equation 4.3. This in turn is equal to the rate of external work done by the static pressure acting on the surface S.

4.1.2 Integral Form of the Conservation Laws for Deforming Volumes

The integral conservation Equations (Equations 4.1, 4.2, and 4.3) were presented for the case of a fixed volume in space. Although this form of the conservation laws is especially useful for deriving the differential form of the conservation equations, and consequently for the numerical integration of the conservation laws, a more general form of these equations allows for the domain D enclosed by the surface S to move rather than to be fixed in space. This latter form is useful for deriving the shock jump and wake jump conditions.

Consider the situation shown in Figure 4.2. A surface S encloses a control volume D. The vector R traces out the surface of the control volume. This surface vector is a function of time, however, so that the enclosed volume is not constant. Hence, the flux through the boundary is not only a function of the fluid velocity $\mathbf{V}$, but also of the velocity of the surface $\frac{\partial \mathbf{R}}{\partial t}$. As before, the time rate of change of the enclosed volume of mass is equal to the mass flux through the surface, but the flux is now composed of

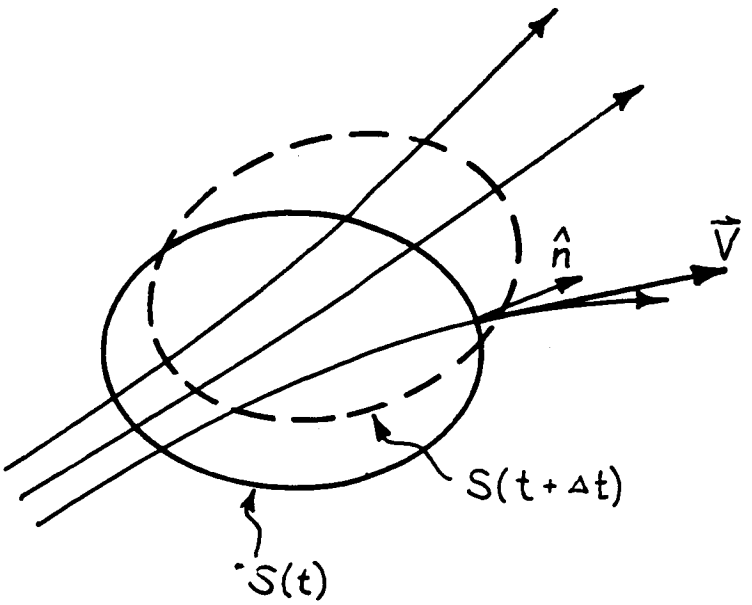

Figure 4.2: Nonstationary control volume. The flux through the control volume surface is composed of two parts: The flux due to the fluid motion, and the flux due to the motion of the control volume surface.

two parts.

$$\frac{d}{dt}\int_D \rho dD = -\int_S \rho\left(\mathbf{V} - \frac{\partial}{\partial t}\mathbf{R}\right)\cdot \mathbf{n} dS \tag{4.4}$$

Note that the time derivative appears *outside* the volume integral.

Similarly, one can express the conservation of momentum and energy as

$$\frac{d}{dt}\int_D \rho \mathbf{V} dD + \int_S \rho \mathbf{V}(\mathbf{V} - \frac{\partial}{\partial t}\mathbf{R})\cdot \mathbf{n} dS = -\int_S p\mathbf{n} dS \tag{4.5}$$

$$\frac{d}{dt}\int_D (e + \rho V^2/2) dD + \int_S (e + \rho V^2/2)(\mathbf{V} - \frac{\partial}{\partial t}\mathbf{R})\cdot \mathbf{n} dS = -\int_S p\mathbf{V}\cdot \mathbf{n} dS \tag{4.6}$$

4.1.3 Differential Form of the Conservation Laws

In the previous two sections, the conservations laws were presented in integral form. Often, however, it is more useful to express the conservation equations in differential form. The divergence theorem can be used to make this transformation. For example, consider the conservation of mass in integral form (Equation 4.1). Using the divergence theorem, the integral on the right hand side can be converted from a surface integral

into a volume integral. After this transformation, the integral form of the conservation of mass becomes

$$\int_D \left(\frac{\partial}{\partial t}\rho + \nabla \cdot (\rho \mathbf{V}) \right) dD = 0 \tag{4.7}$$

If Equation 4.7 is to hold for any arbitrary region of fluid, then it must be that the integrand vanishes identically everywhere within the fluid.

The conservation of momentum and energy can be similarly reduced to partial differential equations. Together with the conservation of mass, these equations are the well known Euler equations which are given by

$$\frac{\partial}{\partial t}\begin{bmatrix} \rho \\ \rho u \\ \rho v \\ e_0 \end{bmatrix} + \frac{\partial}{\partial x}\begin{bmatrix} \rho u \\ \rho u^2 + p \\ \rho uv \\ \rho u h_0 \end{bmatrix} + \frac{\partial}{\partial y}\begin{bmatrix} \rho v \\ \rho uv \\ \rho v^2 + p \\ \rho v h_0 \end{bmatrix} = 0 \tag{4.8}$$

where e_0 is the total internal energy per unit volume, and h_0 is the total enthalpy per unit mass. So at this point we have six unknowns and four equations. The unknowns are ρ, u, v, p, e, and h_0. The additional equations needed come from the definition of enthalpy, and the relationship between the energy and the state of the fluid. These latter two relationships can be used to eliminate the total internal energy and total enthalpy from Equation 4.8 in favor of the four primitive variables ρ, u, v, and p. The enthalpy, and total energy are given by

$$h_0 = \frac{(e_0 + p)}{\rho} \tag{4.9}$$

$$e_0 = e + \frac{1}{2}\rho(u^2 + v^2) \tag{4.10}$$

The internal energy e is in general a complex function of the state of the gas, but for an ideal gas with constant specific heats, the internal energy is given by $e = \frac{1}{\gamma - 1}p$. Hence, under this assumption, the Euler equations can be expressed as

$$\frac{\partial}{\partial t}\begin{bmatrix} \rho \\ \rho u \\ \rho v \\ \frac{p}{\gamma-1} + \frac{1}{2}\rho(u^2 + v^2) \end{bmatrix} + \frac{\partial}{\partial x}\begin{bmatrix} \rho u \\ \rho u^2 + p \\ \rho uv \\ \frac{\gamma}{\gamma-1}pu + \frac{1}{2}\rho u(u^2 + v^2) \end{bmatrix} +$$

$$\frac{\partial}{\partial y}\begin{bmatrix} \rho v \\ \rho uv \\ \rho v^2 + p \\ \frac{\gamma}{\gamma-1}pv + \frac{1}{2}\rho v(u^2+v^2) \end{bmatrix} = 0 \tag{4.11}$$

With the Euler equations expressed in this form, we have four unknowns and four equations. This form, although slightly less general than Equation 4.8, will be used throughout this report. Implicit in these equations is the assumption of an ideal gas.

Note that from Equation 4.8 we see that for steady flows we have that $\mathbf{V}\cdot\nabla h_0$ is zero. This means that total enthalpy is constant along streamlines in steady flows. Hence, if the total enthalpy is constant in the upstream region of a given flow, the total enthalpy will be constant everywhere in the flow. In this case, the flow is said to be homoenergetic. If the flow is homoenergetic, the energy equation can be eliminated from Equations 4.8 and 4.11, as well as one of the primitive variables. Eliminating the pressure p in favor of the remaining primitive variables, and making the same assumptions as before about the nature of the fluid gives

$$\frac{\partial}{\partial x}\begin{bmatrix} \rho u \\ \rho u^2 + p \\ \rho uv \end{bmatrix} + \frac{\partial}{\partial y}\begin{bmatrix} \rho v \\ \rho uv \\ \rho v^2 + p \end{bmatrix} = 0 \tag{4.12}$$

where

$$p = \frac{\gamma - 1}{\gamma}\left[\rho h_0 - \frac{1}{2}\rho\left(u^2 + v^2\right)\right]$$

This form of the steady Euler equations simplifies the numerical computation of the steady flow. Having only three equations per computational node instead of four cuts the computational time by a factor of about two for the direct solver used in this research.

4.2 Linearized Euler Equations

In the first part of this chapter, the Euler equations were presented in a few of their many forms. In this section, the Euler equation are linearized to obtain the two-dimensional unsteady linearized Euler equations. As in Chapter 2, the analysis is

composed of two main parts. In the first part, the steady flow is determined. In the second part, the Euler equations are linearized about the steady operating point. The linearized Euler equations are then be used to compute the unsteady flow. As shown in Chapter 3, this unsteady solution will be valid so long as the resulting flow perturbations are relatively small. In this section, the linearized Euler equations will be developed.

4.2.1 Field Equation Linearization

As in Chapter 2, the full time dependent flow is then approximated as the sum of a mean and a small perturbation component.

$$\hat{\rho}(x,y,t) = \overline{\rho}(x,y) + \rho(x,y,t) \tag{4.13}$$

$$\hat{u}(x,y,t) = U(x,y) + u(x,y,t) \tag{4.14}$$

$$\hat{v}(x,y,t) = V(x,y) + v(x,y,t) \tag{4.15}$$

$$\hat{p}(x,y,t) = P(x,y) + p(x,y,t) \tag{4.16}$$

Further, it is assumed that the perturbation is much smaller in magnitude than the corresponding mean component. It should be pointed out that this approximation is valid asymptotically as the perturbation in the flow tends toward zero. It is *not* an exact representation of the flow. As shown in Chapter 3, however, this approximation gives good predictions for moderate levels of unsteadiness.

Next, the perturbation assumptions (Equations 4.13-4.16) are substituted into the Euler equations (Equation 4.11). Collecting terms of equal order and neglecting terms of higher order produces the equation for the steady flow, and the equations for the unsteady perturbation quantities. The steady flow equations are given by

$$\frac{\partial}{\partial x}\begin{bmatrix} \overline{\rho}U \\ \overline{\rho}U^2 + P \\ \overline{\rho}UV \\ \frac{\gamma}{\gamma-1}PU + \frac{1}{2}\overline{\rho}U(U^2+V^2) \end{bmatrix} + \frac{\partial}{\partial y}\begin{bmatrix} \overline{\rho}V \\ \overline{\rho}UV \\ \overline{\rho}V^2 + P \\ \frac{\gamma}{\gamma-1}PV + \frac{1}{2}\overline{\rho}V(U^2+V^2) \end{bmatrix} = 0 \tag{4.17}$$

which is just the original equations with time derivative terms set to zero. More inter-

esting are the first order perturbation equations, which are given by

$$\frac{\partial}{\partial t}\begin{bmatrix} 1 & 0 & 0 & 0 \\ U & \bar{\rho} & 0 & 0 \\ V & 0 & \bar{\rho} & 0 \\ \frac{1}{2}(U^2+V^2) & \bar{\rho}U & \bar{\rho}V & \frac{1}{\gamma-1} \end{bmatrix}\begin{bmatrix} \rho \\ u \\ v \\ p \end{bmatrix} +$$

$$\frac{\partial}{\partial x}\begin{bmatrix} U & \bar{\rho} & 0 & 0 \\ U^2 & 2\bar{\rho}U & 0 & 1 \\ UV & \bar{\rho}V & \bar{\rho}U & 0 \\ \frac{1}{2}U(U^2+V^2) & \frac{\gamma}{\gamma-1}P+\frac{3}{2}\bar{\rho}U^2+\frac{1}{2}\bar{\rho}V^2 & \bar{\rho}UV & \frac{\gamma U}{\gamma-1} \end{bmatrix}\begin{bmatrix} \rho \\ u \\ v \\ p \end{bmatrix} +$$

$$\frac{\partial}{\partial y}\begin{bmatrix} V & 0 & \bar{\rho} & 0 \\ UV & \bar{\rho}V & \bar{\rho}U & 0 \\ V^2 & 0 & 2\bar{\rho}V & 1 \\ \frac{1}{2}V(U^2+V^2) & \bar{\rho}UV & \frac{\gamma}{\gamma-1}P+\frac{1}{2}\bar{\rho}U^2+\frac{3}{2}\bar{\rho}V^2 & \frac{\gamma V}{\gamma-1} \end{bmatrix}\begin{bmatrix} \rho \\ u \\ v \\ p \end{bmatrix} = 0 \qquad (4.18)$$

These equations are *linear* in the perturbation variables. The mean flow components are known from the solution of Equation 4.17. Hence, the matrices premultiplying the perturbation variables are known variable coefficient matrices. Note also that the perturbation equations are in so-called conservation form. One could in principle time march these linear equations to obtain an unsteady solution to the Euler equations valid for small deviations away from the mean flow. However, if the flow of interest is periodic in time, then the unsteady perturbation can be represented as a Fourier series. Hence, for example, the density can be expressed as

$$\rho(x,y,t) = \sum_{n=-\infty}^{+\infty} \rho_n(x,y)e^{jn\omega t} \qquad (4.19)$$

where ω is the fundamental frequency given by $\omega = 2\pi/T$. But since the first-order equations are linear, the behavior of each Fourier component can be analyzed individually, then summed together to form the total solution. Hence, without loss of generality, the Fourier components will be analyzed term by term. Furthermore, many flows of interest are not only periodic, but are also nearly harmonic. Hence, we let

$$\rho(x,y,t) \;\rightarrow\; \rho(x,y)e^{j\omega t} \qquad (4.20)$$

$$u(x,y,t) \rightarrow u(x,y)e^{j\omega t} \tag{4.21}$$

$$v(x,y,t) \rightarrow v(x,y)e^{j\omega t} \tag{4.22}$$

$$p(x,y,t) \rightarrow p(x,y)e^{j\omega t} \tag{4.23}$$

The perturbation amplitudes ρ, u, v, and p are complex. Substitution of the harmonic assumption into the linearized Euler equations gives

$$j\omega \begin{bmatrix} 1 & 0 & 0 & 0 \\ U & \bar{\rho} & 0 & 0 \\ V & 0 & \bar{\rho} & 0 \\ \frac{1}{2}(U^2+V^2) & \bar{\rho}U & \bar{\rho}V & \frac{1}{\gamma-1} \end{bmatrix} \begin{bmatrix} \rho \\ u \\ v \\ p \end{bmatrix} +$$

$$\frac{\partial}{\partial x} \begin{bmatrix} U & \bar{\rho} & 0 & 0 \\ U^2 & 2\bar{\rho}U & 0 & 1 \\ UV & \bar{\rho}V & \bar{\rho}U & 0 \\ \frac{1}{2}U(U^2+V^2) & \frac{\gamma}{\gamma-1}P+\frac{3}{2}\bar{\rho}U^2+\frac{1}{2}\bar{\rho}V^2 & \bar{\rho}UV & \frac{\gamma U}{\gamma-1} \end{bmatrix} \begin{bmatrix} \rho \\ u \\ v \\ p \end{bmatrix} +$$

$$\frac{\partial}{\partial y} \begin{bmatrix} V & 0 & \bar{\rho} & 0 \\ UV & \bar{\rho}V & \bar{\rho}U & 0 \\ V^2 & 0 & 2\bar{\rho}V & 1 \\ \frac{1}{2}V(U^2+V^2) & \bar{\rho}UV & \frac{\gamma}{\gamma-1}P+\frac{1}{2}\bar{\rho}U^2+\frac{3}{2}\bar{\rho}V^2 & \frac{\gamma V}{\gamma-1} \end{bmatrix} \begin{bmatrix} \rho \\ u \\ v \\ p \end{bmatrix} = 0 \tag{4.24}$$

Equation 4.24 can be expressed in matrix notation as

$$j\omega \mathbf{B}_1\mathbf{u} + \frac{\partial}{\partial x}\mathbf{B}_2\mathbf{u} + \frac{\partial}{\partial y}\mathbf{B}_3\mathbf{u} = 0 \tag{4.25}$$

Thus we can solve for all time by considering a single set of linear variable-coefficient equations for each frequency of interest. Since only a single set of equations must be solved, the linearized approach should be computationally more efficient than one involving time marching. The former is well-suited for the flutter problem in cascades as well as the inlet distortion problem. It is not so well-suited for the case of an unsteady flow through a cascade which is driven by the wakes from the upstream stator because this sort of disturbance, although *periodic*, is not *harmonic*. This problem could, perhaps, be better handled by time marching. However, one could in principle decompose the wake disturbance into Fourier components, solve for each of these components individually, and then sum the results to obtain the total solution.

4.3 Solution of the Steady Euler Equations

In the previous section, the linearized unsteady Euler equations were presented. Because these equations are linearized about some nominal steady flow, the steady flow must first be calculated before the unsteady analysis can proceed. In this section, the basic method for calculating the steady flow is discussed. This procedure closely parallels the procedure used to calculate steady one-dimensional flows first presented in Chapter 2. The nonlinear steady Euler equations are solved using a Newton iteration procedure. The nonlinear problem is reduced to a series of linear partial differential equations, each very similar to the unsteady linearized Euler equations. Each of these linear problems is discretized on a computational grid and solved directly. The details of this entire process are given below.

4.3.1 The Linearized Newton Iteration Equations

The Newton iteration method for solving two-dimensional partial differential equations is an extremely fast algorithm [24]. Furthermore, the method reduces the nonlinear steady Euler equations to a series of linear ones, each of which is similar to the linearized unsteady Euler equations. Each linear problem can be solved directly using, for example, a Gaussian elimination routine. Unfortunately, the Newton method is not guaranteed to converge. With some care, however, the procedure usually converges.

Consider the steady Euler equations (Equation 4.17). Let us assume that an estimate of the actual solution is known. Then the exact solution is assumed to be the sum of the approximate solution plus a small correction. Hence

$$\hat{\rho}(x,y) = \bar{\rho}(x,y) + \rho(x,y) \tag{4.26}$$

$$\hat{u}(x,y) = U(x,y) + u(x,y) \tag{4.27}$$

$$\hat{v}(x,y) = V(x,y) + v(x,y) \tag{4.28}$$

$$\hat{p}(x,y) = P(x,y) + p(x,y) \tag{4.29}$$

where the left hand side is the "exact" solution, or at least a much improved estimate. The two terms on the right hand side are the current estimate of the solution and the

correction, respectively. The correction is assumed to be small compared to the current estimate of the solution. Substitution of the assumed solution into the steady Euler equations, expanding the result into a power series, and then truncating second- and higher-terms gives the steady linearized Euler equations, i.e.,

$$\frac{\partial}{\partial x}\mathbf{B}_2\mathbf{u} + \frac{\partial}{\partial y}\mathbf{B}_3\mathbf{u} = -\left(\frac{\partial \mathbf{F}}{\partial x} + \frac{\partial \mathbf{G}}{\partial y}\right) \tag{4.30}$$

where $\mathbf{u}$ is the vector of correction perturbations $[\rho, u, v]^T$. The term on the right-hand side are the residuals of the steady equation based on the current estimate of the flow $[\bar{\rho}, U, V]^T$. The left hand side represents the first order correction to the residuals due to the correction perturbations $\mathbf{u}$. The variable coefficient matrices are given by

$$\mathbf{B}_2 = \frac{\partial \mathbf{F}}{\partial \mathbf{u}} \tag{4.31}$$

$$\mathbf{B}_3 = \frac{\partial \mathbf{G}}{\partial \mathbf{u}} \tag{4.32}$$

Note the similarity of the Newton iterations equations to the linearized unsteady Euler equations (Equation 4.24). The two linearizations are basically the same. The main differences are that the linearized unsteady equations contain a homogeneous term arising from the time-derivative term, while the Newton iteration equation contains an inhomogeneous term which represents the residuals of the current solution estimate.

The basic Newton iteration procedure is to start with a reasonable guess for the steady flow solution. The iteration equations are then discretized on a computational grid and solved subject to an appropriate set of boundary conditions. Having determined the corrections, these are then added to the current estimate of the solution to obtain an improved estimate. The entire process is repeated until a converged solution is obtained. For subsonic flows, convergence usually occurs after about five iterations. For transonic flow calculations, the procedure usually converges in from five to ten iterations.

4.3.2 Discretization of the Newton Iteration Equations

The Newton iteration equations are linear variable coefficient equations. In general, however, these equations cannot be solved exactly and, therefore, must be solved numerically. In this section, the discretization procedure is discussed.

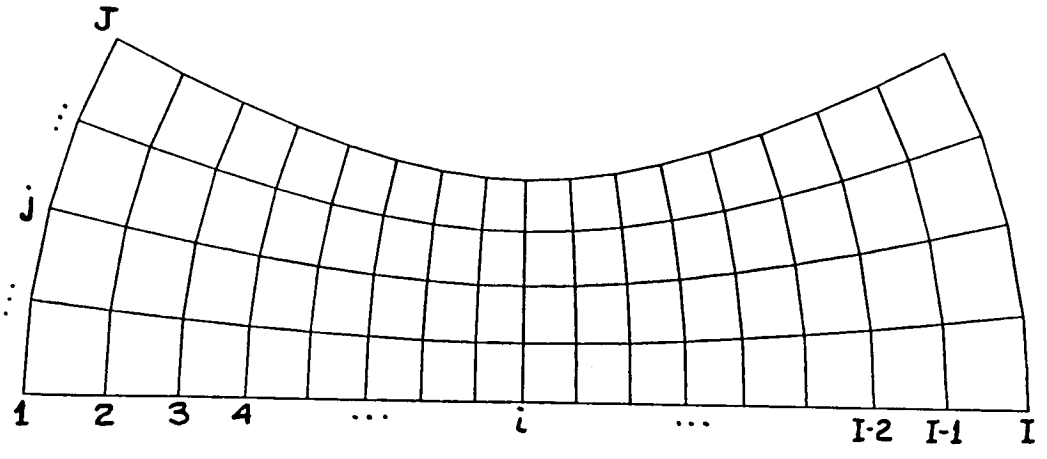

Figure 4.3: Typical grid used in calculation of steady and unsteady channel flows.

A typical grid used to calculate channel flows is shown in Figure 4.3. The nodes are referenced by two subscripts (i,j) denoting the node number in the streamwise and normal directions. In the streamwise direction, the nodes are numbered from 1 to I, while in the normal direction the nodes are numbered form 1 to J. There are a total of $(I-1)(J-1)$ cells. At each of these cells, the Newton equations are discretized using a finite volume operator similar to the one used by Ni [23]. Consider once again the Newton equations. If the Newton equations are satisfied everywhere within a conservation cell, then the area integral of the equations is also satisfied and given by

$$\iint \left(\frac{\partial}{\partial x}\mathbf{B_2 u} + \frac{\partial}{\partial y}\mathbf{B_3 u}\right) dx\,dy = -\iint \left(\frac{\partial \mathbf{F}}{\partial x} + \frac{\partial \mathbf{G}}{\partial y}\right) dx\,dy \tag{4.33}$$

where the limits of integration are over a single conservation cell. Using the divergence theorem, this area integral is converted into a line integral of the form.

$$\oint (\mathbf{B_2 u}, \mathbf{B_3 u}) \cdot \mathbf{n}\, ds = -\oint (\mathbf{F}, \mathbf{G}) \cdot \mathbf{n}\, ds \tag{4.34}$$

where $\mathbf{n}$ is the outward unit normal of the cell. This is the form of the Newton equations which are discretized.

Consider a typical conservation cell as shown in Figure 4.4 The primitive variables are stored at the cell corners. That is to say the scheme is a node-centered scheme. The trapezoidal rule is used to integrate the line integrals in Equation 4.34. For example, to calculate the right hand side, the values of $\mathbf{F}$ and $\mathbf{G}$ are calculated at each of the nodes. These values are averaged from the two nodes on each face, the dot product with $\mathbf{n}\Delta s$ is formed, and the contributions from the four faces are summed. Hence, integration around the cell gives

$$\begin{aligned}\oint (\mathbf{F}, \mathbf{G}) \cdot \mathbf{n}\, ds \approx & \frac{\mathbf{F}_{i,j} + \mathbf{F}_{i+1,j}}{2}\Delta y_1 + \frac{\mathbf{F}_{i+1,j} + \mathbf{F}_{i+1,j+1}}{2}\Delta y_2 \\ & + \frac{\mathbf{F}_{i+1,j+1} + \mathbf{F}_{i,j+1}}{2}\Delta y_3 + \frac{\mathbf{F}_{i,j+1} + \mathbf{F}_{i,j}}{2}\Delta y_4 - \frac{\mathbf{G}_{i,j} + \mathbf{G}_{i+1,j}}{2}\Delta x_1 \\ & - \frac{\mathbf{G}_{i+1,j} + \mathbf{G}_{i+1,j+1}}{2}\Delta x_2 - \frac{\mathbf{G}_{i+1,j+1} + \mathbf{G}_{i,j+1}}{2}\Delta x_3 - \frac{\mathbf{G}_{i,j+1} + \mathbf{G}_{i,j}}{2}\Delta x_4\end{aligned} \tag{4.35}$$

where

$$\Delta x_1 = x_{i+1,j} - x_{i,j}$$

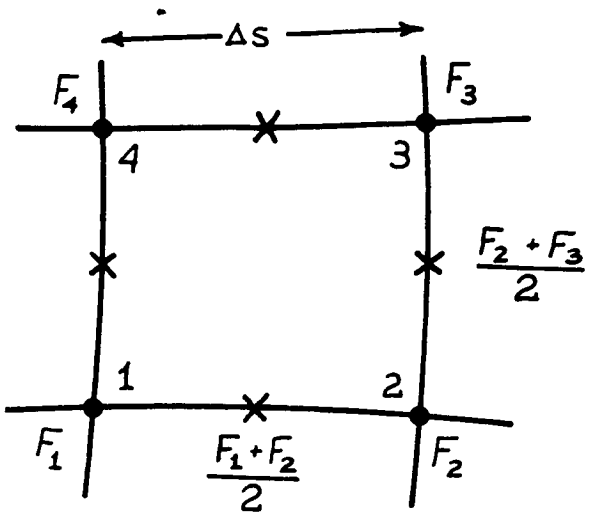

Figure 4.4: Discretization of residuals using a finite volume integration

$$
\begin{aligned}
\Delta x_2 &= x_{i+1,j+1} - x_{i+1,j} \\
\Delta x_3 &= x_{i,j+1} - x_{i+1,j+1} \\
\Delta x_4 &= x_{i,j} - x_{i,j+1} \\
\Delta y_1 &= y_{i+1,j} - y_{i,j} \\
\Delta y_2 &= y_{i+1,j+1} - y_{i+1,j} \\
\Delta y_3 &= y_{i,j+1} - y_{i+1,j+1} \\
\Delta y_4 &= y_{i,j} - y_{i,j+1}
\end{aligned}
$$

Rearranging slightly gives

$$
\begin{aligned}
\oint (\mathbf{F}, \mathbf{G}) \cdot \mathbf{n}\, ds \approx \mathbf{F}_{i,j} \frac{\Delta y_4 + \Delta y_1}{2} + \mathbf{F}_{i+1,j} \frac{\Delta y_1 + \Delta y_2}{2} \\
+ \mathbf{F}_{i+1,j+1} \frac{\Delta y_2 + \Delta y_3}{2} + \mathbf{F}_{i,j+1} \frac{\Delta y_3 + \Delta y_4}{2} - \mathbf{G}_{i,j} \frac{\Delta x_4 + \Delta x_1}{2} \\
- \mathbf{G}_{i+1,j} \frac{\Delta x_1 + \Delta x_2}{2} - \mathbf{G}_{i+1,j+1} \frac{\Delta x_2 + \Delta x_3}{2} - \mathbf{G}_{i,j+1} \frac{\Delta x_3 + \Delta x_4}{2}
\end{aligned} \tag{4.36}
$$

Similarly, the homogeneous portion of Equation 4.34 is discretized by

$$
\begin{aligned}
\oint (\mathbf{B}_2\mathbf{u}, \mathbf{B}_3\mathbf{u}) \cdot \mathbf{n}\, ds \approx (\mathbf{B}_2\mathbf{u})_{i,j} \frac{\Delta y_4 + \Delta y_1}{2} + (\mathbf{B}_2\mathbf{u})_{i+1,j} \frac{\Delta y_1 + \Delta y_2}{2} \\
+ (\mathbf{B}_2\mathbf{u})_{i+1,j+1} \frac{\Delta y_2 + \Delta y_3}{2} + (\mathbf{B}_2\mathbf{u})_{i,j+1} \frac{\Delta y_3 + \Delta y_4}{2} - (\mathbf{B}_3\mathbf{u})_{i,j} \frac{\Delta x_4 + \Delta x_1}{2} \\
- (\mathbf{B}_3\mathbf{u})_{i+1,j} \frac{\Delta x_1 + \Delta x_2}{2} - (\mathbf{B}_3\mathbf{u})_{i+1,j+1} \frac{\Delta x_2 + \Delta x_3}{2} - (\mathbf{B}_3\mathbf{u})_{i,j+1} \frac{\Delta x_3 + \Delta x_4}{2}
\end{aligned} \tag{4.37}
$$

This discretization scheme is second-order accurate. Furthermore, because the scheme is node centered, no extrapolation to the boundaries is required, as with cell-centered schemes, to apply boundary conditions. The major flaw with the scheme is that it admits *sawtooth* or *hourglass* modes. A sawtooth mode averages to zero at the face centers. Hence, such modes do not contribute to the numerical integration around the cell. To eliminate such modes, a small amount of smoothing must be added to the scheme. This is true of Ni's time-marching scheme as well. The addition of smoothing is not totally undesirable as some smoothing must be added to stabilize the solution at the sonic line for transonic problems. Regardless, very small amounts of smoothing are required in practice, but not enough to significantly alter the solution.

4.3.3 Steady Flow Boundary Conditions

In addition to the discretization of the conservation equations, appropriate boundary conditions must be specified, linearized, and then discretized for use in the Newton iteration procedure. To start, consider the boundary conditions associated with two-dimensional channel flows. For channel flows, there are three boundary regions: the inflow boundary, the outflow boundary, and the channel walls. At each of these regions, one or more boundary conditions will usually be applied.

Flow Tangency Condition

Along the solid wall boundaries of the channel, the flow is required to be tangent to the wall. That is to say that no mass flows through the wall. This boundary condition is expressed as

$$(\hat{u}, \hat{v}) \cdot \mathbf{n} = 0 \tag{4.38}$$

where $\mathbf{n}$ is the local unit normal to the wall. Expanding Equation 4.38 in terms of the current estimate of the flow and the correction, we have that

$$(u, v) \cdot \mathbf{n} = -(U, V) \cdot \mathbf{n} \tag{4.39}$$

As this flow tangency condition is already linear in the correction perturbation variables, no linearization step is required.

This boundary condition is applied at the face centers to the cell faces along the channel walls. The normal is taken to be the normal of the face center and the velocities are averaged from the nodes at the ends of the face. Hence, the discretized flow tangency condition is given by

$$-\frac{u_{i,j} + u_{i+1,j}}{2}\Delta y + \frac{v_{i,j} + v_{i+1,j}}{2}\Delta x = \frac{U_{i,j} + U_{i+1,j}}{2}\Delta y - \frac{V_{i,j} + V_{i+1,j}}{2}\Delta x \tag{4.40}$$

where

$$\Delta x = x_{i+1,j} - x_{i,j}, \quad \Delta y = y_{i+1,j} - y_{i,j}$$

Outflow Boundary Conditions

For the channel flows considered in this report, the outflow is subsonic. Hence, a single boundary condition is applied along the outflow boundary. Although a variety of boundary conditions could be applied, in the present effort, the static pressure will be specified at the outflow boundary. Since the steady Euler equations are being solved with a reduced set of primitive variables, the pressure must be specified in terms of the density and velocity. Hence, the exit pressure is given by

$$\hat{p}_{exit} = \frac{\gamma - 1}{\gamma}\left[\hat{\rho}h_0 - \frac{1}{2}\hat{\rho}\left(\hat{u}^2 + \hat{v}^2\right)\right] \tag{4.41}$$

Linearizing this boundary condition about the current estimate of the flow gives

$$\begin{aligned}\frac{\gamma - 1}{\gamma}\left[h_0 - \frac{1}{2}\left(U^2 + V^2\right)\right]\rho - \frac{\gamma - 1}{\gamma}\bar{\rho}Uu - \frac{\gamma - 1}{\gamma}\bar{\rho}Vv = \\ P_{exit} - \frac{\gamma - 1}{\gamma}\left[\bar{\rho}h_0 - \frac{1}{2}\bar{\rho}\left(U^2 + V^2\right)\right] \\ = P_{exit} - P\end{aligned} \tag{4.42}$$

Equation 4.42 is applied at each of the J nodes along the outflow boundary.

Inflow Boundary Condition

For a subsonic homenergetic inflow, two boundary conditions are required at the inflow boundary. In the present work, the flow angle and total density will be specified. A third implicit assumption due to the homoenergetic assumption is that the total pressure is specified. The total density is given by

$$\rho_{T\,inlet} = \hat{\rho}\left(1 - \frac{\hat{u}^2 + \hat{v}^2}{2h_0}\right)^{\frac{-1}{\gamma - 1}} \tag{4.43}$$

which, when linearized, becomes.

$$\begin{aligned}\left(1 - \frac{U^2 + V^2}{2h_0}\right)^{\frac{-1}{\gamma-1}}\rho + \frac{\bar{\rho}U}{(\gamma - 1)h_0}\left(1 - \frac{U^2 + V^2}{2h_0}\right)^{\frac{-\gamma}{\gamma-1}}u + \\ \frac{\bar{\rho}V}{(\gamma - 1)h_0}\left(1 - \frac{U^2 + V^2}{2h_0}\right)^{\frac{-\gamma}{\gamma-1}}v = \rho_{T\,inlet} - \bar{\rho}\left(1 - \frac{U^2 + V^2}{2h_0}\right)^{\frac{-1}{\gamma-1}}\end{aligned} \tag{4.44}$$

Equation 4.44 is applied at each of the J nodes along the inflow boundary.

The last boundary condition to be specified is the angle of the incoming flow. For a channel whose walls are parallel at the inlet, the flow at the inlet will be parallel to the walls. For channel whose walls are not parallel, the specified flow angle will vary along the inflow boundary. Nevertheless, at each node on the inflow boundary, the flow angle must be specified. Let this flow angle be denoted by α. Then

$$\hat{u}\sin(\alpha) - \hat{v}\cos(\alpha) = 0 \tag{4.45}$$

or

$$u\sin(\alpha) - v\cos(\alpha) = -U\sin(\alpha) + V\cos(\alpha) \tag{4.46}$$

Equation 4.46 is specified at each of the inflow boundary nodes.

At this point, we should determine whether the number of equations is enough to specify all of the unknowns. Figure 4.5 shows where the conservation equations and boundary conditions are applied on a grid used to calculate flow in a channel. Since the computation grid has IJ nodes, the total number of unknowns is $3IJ$. The equations available to solve for these unknowns are the conservation equations plus the various boundary conditions. There are $(I-1)(J-1)$ conservation cells with 3 conservation equations per cell for a total of $3(I-1)(J-1)$ equations. There are $2J$ inflow boundary conditions, J outflow boundary conditions, and $2(I-1)$ wall boundary conditions. The total number of equations is then $3IJ - I + 1$ equations. In other words, there are $I-1$ equations too few. This shortage of equations is due to the method of discretizing the equations. These $I-1$ degrees of freedom are sawtooth modes admitted as solutions to the rank deficient system of equations. To eliminate them, smoothing will be added to the equations after preconditioning them as discussed in the next section.

4.3.4 Matrix Equation Structure

Written in shorthand form, the discretized equations which describe the linearized unsteady flow can be expressed as

$$\mathbf{Mu} = \mathbf{f} \tag{4.47}$$

The matrix $\mathbf{M}$ is a supermatrix which is block bidiagonal. Each of these blocks is in turn also a supermatrix which is block bidiagonal. Each of these blocks is a three by

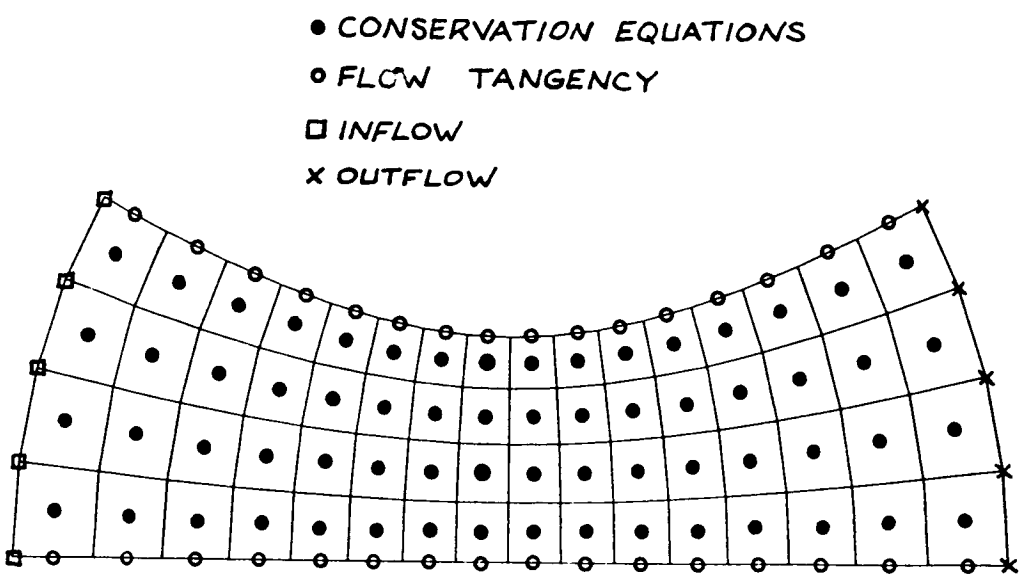

Figure 4.5: Location of conservation equations and boundary conditions on a typical channel flow computational grid.

three matrix. Note in particular that the last row of the supermatrices is zero. This is because there are IJ nodes but only $(I-1)(J-1)$ conservation equations.

Similarly, the boundary conditions can be expressed in matrix form as

$$\mathbf{M}_{BC}\mathbf{u} = \mathbf{f}_{BC} \tag{4.48}$$

where the matrix $\mathbf{M}_{BC}$ has many fewer rows than columns and is sparse.

An equivalent system of equations can be formed by "squaring" the conservation equations and the boundary conditions and summing them to give

$$\left[\mathbf{M}^T\mathbf{M} + \mathbf{M}_{BC}^T\mathbf{M}_{BC}\right]\mathbf{u} = \mathbf{M}^T\mathbf{f} + \mathbf{M}_{BC}^T\mathbf{f}_{BC} \tag{4.49}$$

One interpretation of Equation 4.49 is that the solution of it minimizes the square of the residuals (sets to zero) of the original equation set. Of course, the "squared" equations are still rank deficient and admit sawtooth modes. However, the matrix equations are now positive semi-definite. The rank deficiency is eliminated, along with the sawtooth modes, by adding a small amount of positive semi-definite smoothing to the equation set. A finite element Laplacian operator $\mathbf{L}$ is used. Hence, the resulting system of positive definite equations is given by

$$\left[\mathbf{M}^T\mathbf{M} + \mathbf{M}_{BC}^T\mathbf{M}_{BC} + \epsilon\mathbf{L}\right]\mathbf{u} = \mathbf{M}^T\mathbf{f} + \mathbf{M}_{BC}^T\mathbf{f}_{BC} + \epsilon\mathbf{f}_L \tag{4.50}$$

where

$$\mathbf{f}_L = -\mathbf{L}\mathbf{U}$$

and ϵ is a small parameter introduced so that only a small amount of smoothing is added so as to eliminate the sawtooth modes without significantly modifying the solution.

This process of forming the equations to be solved can be viewed as a kind of constrained optimization. The quantity to be optimized is the smoothness of the solution subject to the constraint that the conservation equations and the boundary conditions be satisfied. This construction is similar to techniques in numerical optimizations. A cost function to be minimized is modified by adding constraint penalty functions. For this example, the modified cost function is given by

$$R = \frac{1}{2}(\mathbf{M}\mathbf{u} - \mathbf{f})^2 + \frac{1}{2}(\mathbf{M}_{BC}\mathbf{u} - \mathbf{f}_{BC})^2 + \frac{\epsilon}{2}(\mathbf{u}+\mathbf{U})^T\mathbf{L}(\mathbf{u}+\mathbf{U}) \tag{4.51}$$

Minimizing this scalar with respect to the perturbation variables $\mathbf{u}$ gives

$$\frac{\partial R}{\partial \mathbf{u}} = \left[\mathbf{M}^T\mathbf{M} + \mathbf{M}_{BC}^T\mathbf{M}_{BC} + \epsilon\mathbf{L}\right]\mathbf{u} - \left(\mathbf{M}^T\mathbf{f} + \mathbf{M}_{BC}^T\mathbf{f}_{BC} + \epsilon\mathbf{f}_L\right) = 0 \qquad (4.52)$$

which is exactly equivalent to Equation 4.49.

This provides a rational approach for the addition of smoothing to the problem. Furthermore, the resulting equations are positive definite. Unfortunately, the resulting equations tend to be poorly conditioned. Hence, double precision arithmetic is used in the computer code to avoid potential round-off problems when performing Gaussian elimination on the matrix equations. The bandwidth of the matrix is also increased. The super matrices are now block tridiagonal. Said another way, the original equations were derived from operations which involved four nodes. The new operator is a nine-point operator.

The foregoing matrix equations are solved directly using a Gaussian elimination scheme. The solver takes advantage of the known sparseness, but does not reorder the equations for maximum efficiency. The computer time required to solve this system of equations is $O(I(3J)^3)$. The amount of storage required is $O(I(3J)^2)$. Hence, additional grid resolution in the normal direction greatly increases both CPU and storage requirements.

4.4 Unsteady Flow Calculations

In the previous section, the numerical method for solving the steady two-dimensional flow through a channel was described. The steady flow must be calculated before one can solve the unsteady Euler equations to obtain unsteady flow predictions. In this section, the numerical method for solving the linearized unsteady Euler equations will be detailed. In Section 4.4.1, the method of discretizing the linearized unsteady Euler equations is discussed. In Section 4.4.2, the treatment of the boundary conditions for unsteady channel flow are presented. The three steps involved are the specification of the (nonlinear) boundary conditions, the linearization of the boundary conditions, and the discretization of the linearized boundary conditions. Finally, in Section 4.4.3, the conditioning of the matrix equations is discussed.

4.4.1 Linearized Unsteady Euler Equation Discretization

The discretization of the linearized unsteady Euler equations is similar to the discretization of the Newton iteration equations. The starting point is the linearized unsteady Euler equations, i.e.,

$$j\omega \mathbf{B}_1\mathbf{u} + \frac{\partial}{\partial x}\mathbf{B}_2\mathbf{u} + \frac{\partial}{\partial y}\mathbf{B}_3\mathbf{u} = 0 \tag{4.53}$$

If these equations hold over an entire conservation cell, then the integral over the cell must also be zero. Hence

$$\iint \left(j\omega \mathbf{B}_1\mathbf{u} + \frac{\partial}{\partial x}\mathbf{B}_2\mathbf{u} + \frac{\partial}{\partial y}\mathbf{B}_3\mathbf{u} \right) dx\, dy = 0 \tag{4.54}$$

The second and third terms can be converted to a line integral by application of the divergence theorem. The resulting integral equation is given by

$$\iint j\omega \mathbf{B}_1\mathbf{u}\, dx\, dy + \oint (\mathbf{B}_2\mathbf{u}, \mathbf{B}_3\mathbf{u}) \cdot \mathbf{n}\, ds = 0 \tag{4.55}$$

The next step is to numerically aproximate these integrals. The last two integrals can be evaluated using a trapezoidal integration around the cell as with the steady equations. The first term, however, is approximated by the average value of the integrand at the four corner nodes multiplied by the area of the conservation cell. The discretized linearized Euler equations are then given by

$$\begin{aligned}
&\iint j\omega \mathbf{B}_1\mathbf{u}\, dx\, dy + \oint (\mathbf{B}_2\mathbf{u}, \mathbf{B}_3\mathbf{u}) \cdot \mathbf{n}\, ds \approx \\
&j\omega A \frac{(\mathbf{B}_1\mathbf{u})_{i,j} + (\mathbf{B}_1\mathbf{u})_{i+1,j} + (\mathbf{B}_1\mathbf{u})_{i+1,j+1} + (\mathbf{B}_1\mathbf{u})_{i,j+1}}{4} \\
&+(\mathbf{B}_2\mathbf{u})_{i,j} \frac{\Delta y_4 + \Delta y_1}{2} + (\mathbf{B}_2\mathbf{u})_{i+1,j} \frac{\Delta y_1 + \Delta y_2}{2} + (\mathbf{B}_2\mathbf{u})_{i+1,j+1} \frac{\Delta y_2 + \Delta y_3}{2} \\
&+(\mathbf{B}_2\mathbf{u})_{i,j+1} \frac{\Delta y_3 + \Delta y_4}{2} - (\mathbf{B}_3\mathbf{u})_{i,j} \frac{\Delta x_4 + \Delta x_1}{2} - (\mathbf{B}_3\mathbf{u})_{i+1,j} \frac{\Delta x_1 + \Delta x_2}{2} \\
&- (\mathbf{B}_3\mathbf{u})_{i+1,j+1} \frac{\Delta x_2 + \Delta x_3}{2} - (\mathbf{B}_3\mathbf{u})_{i,j+1} \frac{\Delta x_3 + \Delta x_4}{2} = 0
\end{aligned} \tag{4.56}$$

where A is the area of the ijth cell. This discretization of the linearized Euler equations is second-order accurate in the linear dimension of the cell. Note further that the equations are homogeneous and the perturbation variables are complex.

As with the discretization of the steady Euler equations, the discretization of the linearized unsteady Euler equations admits sawtooth modes. This problem is typical of node based schemes. For this reason, a small amount of smoothing must be added to the assembled equation set.

4.4.2 Boundary Conditions of the Unsteady Flow Solution

Up to now, nothing has been said about the boundary conditions which will be required to specify the unsteady flow in a channel. These conditions may reflect a real physical problem to be solved, or may be somewhat more contrived. Regardless, they must be well posed. For channel flows, the boundary conditions can be divided into three regions of the flow: inflow, outflow, and solid wall boundary conditions. The number of boundary conditions required at the inflow and outflow boundaries depends on the local Mach number. As with the linearized unsteady Euler equations, setting up the numerical equations is divided into three parts: specification of the governing boundary conditions, linearization, and discretization.

Solid Wall Boundary Conditions

Consider the wall boundary shown in Figure 4.6. Because the wall is solid, there is no mass flux through the surface. This is the flow tangency condition as expressed mathematically as

$$(\hat{u}, \hat{v}) \cdot \mathbf{n} = 0 \tag{4.57}$$

where $\mathbf{n}$ is the outward normal to the wall surface. Expansion of Equation 4.57 in terms of the mean flow and the unsteady flow components gives

$$\left(ue^{j\omega t}, ve^{j\omega t}\right) \cdot \mathbf{n} = -(U, V) \cdot \mathbf{n} \tag{4.58}$$

But because the mean flow satisfies the flow tangency condition, the right hand side of Equation 4.58 is zero. Hence, the unsteady flow tangency condition is given by

$$(u, v) \cdot \mathbf{n} = 0 \tag{4.59}$$

Because this boundary condition is already linear, the linearization step can be skipped. The final step is the discretization of Equation 4.59. The boundary condition is applied

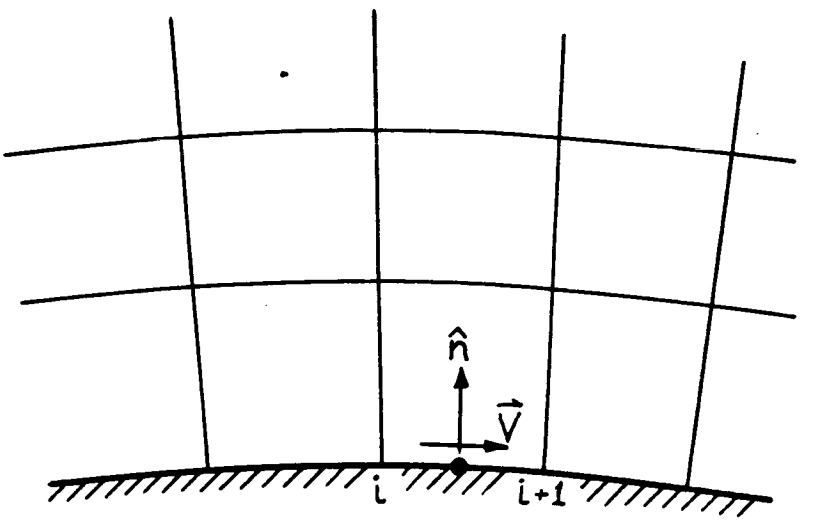

Figure 4.6: Application of flow tangency condition along channel wall

at the centers of the wall boundary faces. The velocity at the face center is taken to be the average of the velocities at the two nodes, and the normal is taken to be the normal of the face. Hence, the flow tangency condition is discretized as

$$-\frac{u_{i,j}+u_{i+1,j}}{2}\Delta y+\frac{v_{i,j}+v_{i+1,j}}{2}\Delta x=0 \tag{4.60}$$

where

$$\Delta x=x_{i+1,j}-x_{i,j},\quad \Delta y=y_{i+1,j}-y_{i,j}$$

Outflow Boundary Conditions

For the two-dimensional channel flows considered in this report, the flow at the exit of the channel is subsonic. Hence, one boundary condition is required. For the moment, the unsteady back pressure is specified along the outflow boundary. The unsteady back pressure at the exit of the channel is given by

$$\hat{p}=P_{exit}+\Delta p_{exit}e^{j\omega t} \tag{4.61}$$

where P_{exit} is the steady exit pressure. Hence, the unsteady portion of the outflow boundary condition is given by

$$p=\Delta p_{exit} \tag{4.62}$$

This boundary condition, like the flow tangency condition, is also linear so that the linearization phase of the discretization of the boundary condition is not required. Equation 4.62 is applied at each of the nodes along the outflow boundary.

Note that this is a reflecting boundary condition. That is to say that waves which impinge on the outflow boundary will be partially reflected. Thus Equation 4.62 is a nonphysical boundary condition. In the next chapter, a more sophisticated nonreflecting boundary condition will be developed for cascade flows.

Inflow Boundary Conditions

For subsonic inflow, three boundary conditions must be specified at the inflow boundary. For now, the quantities specified will be the total pressure, total density, and inlet flow

angle. The unsteady total pressure variation is assumed to be

$$P_T = P_{T0} + \Delta P_T e^{j\omega t} \tag{4.63}$$

where P_{T0} is the mean total pressure and ΔP_T is a small perturbation in the total pressure. Similarly, the total density is given by

$$\rho_T = \rho_{T0} + \Delta \rho_T e^{j\omega t} \tag{4.64}$$

Hence, we have that the total enthalpy is given by

$$\frac{\gamma}{\gamma-1}\frac{P_T}{\rho_T} = \frac{\gamma}{\gamma-1}\frac{P_{T0}+\Delta P_T e^{j\omega t}}{\rho_{T0}+\Delta\rho_T e^{j\omega t}} = \frac{\gamma}{\gamma-1}\frac{\hat{p}}{\hat{\rho}} + \frac{1}{2}\left(\hat{u}^2+\hat{v}^2\right) \tag{4.65}$$

Similarly, a quantity closely related to the entropy is

$$\frac{P_T}{\rho_T^\gamma} = \frac{\hat{p}}{\hat{\rho}^\gamma} = \frac{P_{T0}+\Delta P_T e^{j\omega t}}{\left(\rho_{T0}+\Delta\rho_T e^{j\omega t}\right)^\gamma} \tag{4.66}$$

These boundary conditions are clearly nonlinear functions of the total pressure and density perturbations. Expanding the expressions into perturbation series in powers of ΔP_T and $\Delta \rho_T$ and truncating the second- and higher-order terms gives the zeroth- and first-order boundary conditions. The zeroth-order equations are satisfied by the mean flow. The first-order unsteady boundary conditions are

$$\frac{\gamma}{\gamma-1}\left(\frac{1}{\bar{\rho}}\right)p - \frac{\gamma}{\gamma-1}\left(\frac{P}{\bar{\rho}^2}\right)\rho + Uu + Vv = \frac{\gamma}{\gamma-1}\frac{\Delta P_T}{\rho_{T0}} - \frac{\gamma}{\gamma-1}\frac{P_{T0}}{\rho_{T0}^2}\Delta\rho_T \tag{4.67}$$

and

$$\frac{P}{\bar{\rho}^\gamma}\left[\frac{p}{P} - \gamma\frac{\rho}{\bar{\rho}}\right] = \frac{P_{T0}}{\rho_{T0}^\gamma}\left[\frac{\Delta P_T}{P_{T0}} - \gamma\frac{\Delta\rho_T}{\rho_{T0}}\right] \tag{4.68}$$

Note in particular that if the flow is isentropic to first-order, then the right hand side of Equation 4.68 (and hence, the left) is zero.

The inlet flow angle is assumed to be time-invariant for the channel flow problems considered in this report. Hence

$$\hat{u}\sin(\alpha) - \hat{v}\cos(\alpha) = 0 \tag{4.69}$$

which when linearized becomes

$$u\sin(\alpha) - v\cos(\alpha) = 0 \tag{4.70}$$

4.4.3 Matrix Equations

The assembly of the linear equations for the unsteady analysis is similar to that for the Newton equations used in the steady flow analysis. Because the unsteady equations are complex, however, the transpose operator is replaced by the Hermitian operator. The resulting matrix equations are

$$\left[\mathbf{M}^H\mathbf{M} + \mathbf{M}_{BC}^H\mathbf{M}_{BC} + \epsilon\mathbf{L}\right]\mathbf{u} = \mathbf{M}_{BC}^H\mathbf{f}_{BC} \tag{4.71}$$

Because the linearized unsteady Euler equations are homogeneous, the only inhomogeneous term in Equation 4.71 comes from the boundary conditions. This matrix equation is Hermitian and positive definite.

4.5 Summary

In this chapter, the basic method used to numerically calculate two-dimensional unsteady flows has been presented. The major steps in the analysis are the discretization of the governing nonlinear equations, the linearization of the boundary conditions, the discretization of the linearized field equations and boundary conditions, the assembly of the discretized equations into matrix form, and the solution of the matrix equations. At this point, fairly simple two-dimensional flows may be analyzed. In the next chapter, the extensions of this method which are needed to analyze more complicated flows, such as cascade flows or flows with shocks, will be presented.

Chapter 5

Extensions of Linearized Euler Theory to Cascade Flow

In Chapter 4, the fundamental aspects of the linearized Euler analysis were presented. With this foundation, fairly simple two-dimensional channel flows can be analyzed. In this chapter, the extensions to the theory which are needed to analyze more complicated steady and unsteady cascade flows are presented. In particular, the extensions needed to accommodate steady and unsteady shocks, steady and unsteady wakes, moving airfoil boundaries, and acoustic radiation in the far-field are addressed. The treatment of these flow features closely parallels the methods used by Verdon [33] and Verdon, Adamczyk, and Caspar [37] to analyze potential flows.

Shown in Figure 5.1 are the five main boundary surfaces to be considered in this chapter. They are the moving airfoils, the upstream periodic boundaries, the downstream wake slip-planes, the upstream far-field boundary, and the downstream far-field boundary. Furthermore, if a shock occurs in the domain, a sixth internal boundary must be considered to connect the two regions of continuous flow upstream and downstream of the shock. In Section 5.1 the boundary conditions applied at moving airfoils will be considered. This boundary condition will allow the flutter problems to be analyzed. In Section 5.2 the treatment of steady and unsteady shocks and wakes is discussed. As in the previous one-dimensional analysis, a fitting procedure is used to accurately

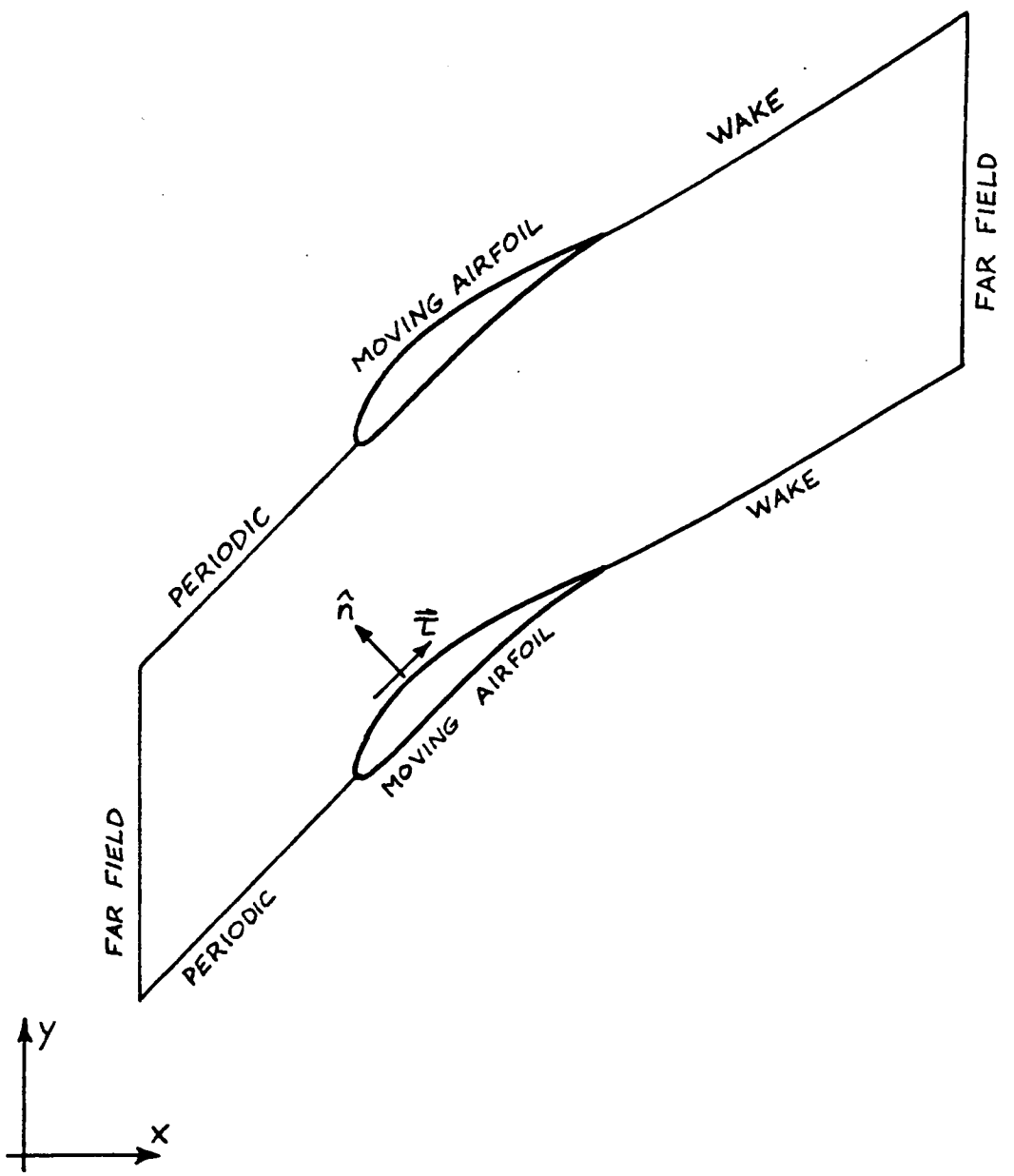

Figure 5.1: Single cascade passage used for calculation of unsteady flows. Note five main boundary surfaces: moving airfoils, upstream periodic boundary, downstream periodic/wake slip-plane, upstream far-field boundary, and downstream far-field boundary.

describe the mean position and the motion of the shock. Similarly, wake fitting is used to model the mean position and motion of the wake. In Section 5.3, the periodic and far-field boundary conditions will be considered. The use of periodic allows the steady and linearized unsteady flows to be analyzed by looking at a single blade passage, greatly reducing the required computational effort. Finally, the treatment of the far-field boundary conditions is examined. Because the computational domain must be finite, the far-field boundaries are placed at a finite distance in front of and behind the cascade. Yet they must allow disturbances to pass through them as if they were not there. Hence, special nonreflecting boundary conditions must be employed.

5.1 Moving Airfoil Boundaries

In this section the boundary conditions applied to a moving airfoil are discussed. Although the analytical boundary condition is straightforward, the numerical boundary condition is complicated slightly by the fact that the grid is fixed in space while the airfoil is supposed to vibrate harmonically.

To start, consider the boundary condition for a solid airfoil moving through a fluid. Suppose the surface of the airfoil at any point in time is described by the position vector $\hat{\mathbf{R}}$. Then the boundary condition (flow tangency) at the surface of the airfoil is

$$\hat{\mathbf{V}} \cdot \hat{\mathbf{n}} - \frac{\partial \hat{\mathbf{R}}}{\partial t} \cdot \hat{\mathbf{n}} = 0 \tag{5.1}$$

where $\hat{\mathbf{n}}$ is the unit normal to the surface. This boundary condition simply states that there is no mass flux through the surface of the airfoil. Note further that the unit normal to the airfoil $\hat{\mathbf{n}}$ is a function of the airfoil surface position vector $\hat{\mathbf{R}}$. Hence, Equation 5.1 is nonlinear. To linearize this boundary condition we assume that the airfoil surface position, like the field variables, can be represented as the sum of two components: one describing the mean location and the other a small perturbation in this location which is a function of time, i.e.,

$$\hat{\mathbf{R}}(s,t) = \mathbf{R}(s) + \mathbf{r}(s,t) \tag{5.2}$$

$$\hat{\mathbf{n}}(s,t) = \bar{\mathbf{n}}(s) + \mathbf{n}(s,t) \tag{5.3}$$

$$\hat{r}(s,t) = \bar{r}(s) + r(s,t) \tag{5.4}$$

where $\hat{r}$ is the unit vector tangent to the airfoil surface and the airfoil surface vector $\hat{\mathbf{R}}$ has been expressedas a function of the distance s along the surface of the airfoil. Then the unit normal $\hat{\mathbf{n}}$ and unit tangent $\hat{r}$ at the moving airfoil surface are related to the corresponding vectors $\bar{\mathbf{n}}$ and $\bar{r}$ and the mean surface position by

$$\hat{\mathbf{n}} = \bar{\mathbf{n}} - \bar{r}\frac{\partial r_n}{\partial s} \tag{5.5}$$

$$\hat{r} = \bar{r} + \bar{\mathbf{n}}\frac{\partial r_n}{\partial s} \tag{5.6}$$

These equations are asymptotically valid for small airfoil motions.

Substitution of the perturbation assumption for the motion of the airfoil surface and the primitive flow variables into the flow tangency condition (Equation 5.1), and collection of terms of equal order gives the zeroth-order (mean) and the first-order (linearized unsteady) boundary conditions. The mean-flow boundary conditions are simply

$$\mathbf{V} \cdot \bar{\mathbf{n}} = 0 \tag{5.7}$$

The Newton linearization and discretization for use with the steady solver was discussed in Chapter 4.

The first-order unsteady boundary condition is

$$\mathbf{v} \cdot \bar{\mathbf{n}} = \frac{\partial r_n}{\partial t} + V_t\frac{\partial r_n}{\partial s} \tag{5.8}$$

where the subscripts n and t denote the component in the normal and tangential directions respectively. Equation 5.8 says that the upwash on the blades is composed of two components. The first is due simply to the velocity of the airfoil normal to its surface. The second term is due to the rotation of the airfoil. If the flow is quasi-steady so that the first term disappears, an upwash will still be induced by rotation of the airfoil. A nose down motion of the airfoil requires that a positive upwash occur so that the flow will remain tangent to the airfoil surface.

It should be emphasized that Equation 5.8 must be applied at the instantaneous position of the airfoil surface and not the mean location. This is a problem computationally since the grid we use is fixed in space. Hence, an additional term is required to

extrapolate this boundary condition from the instantaneous airfoil position to its mean position. As a result, the boundary condition at the mean surface is

$$\mathbf{v} \cdot \overline{\mathbf{n}} = \frac{\partial r_n}{\partial t} + V_t \frac{\partial r_n}{\partial s} - \mathbf{r} \cdot \nabla(V_n) \tag{5.9}$$

If the flow to be analyzed is harmonic, then the operator $\frac{\partial}{\partial t}$ is replaced by $j\omega$.

Equation 5.9 can be discretized in a straightforward manner. The numerical boundary condition is applied at the centers of the cell faces which lie along the boundary of the airfoil surface. The mean normal and tangent of the airfoil surface are taken to be the normal and tangent to the cell face. Because the airfoil motion is prescribed, $\mathbf{r}$, r_n and $\frac{\partial r_n}{\partial s}$ are known. The only real difficulty is in the evaluation of the gradient of the normal component of the mean velocity V_n. This is evaluated using a first-order accurate difference operator which uses the values of the mean normal velocity V_n at the four corners of the boundary cell. Because this procedure errors of $O(\Delta x)$ into the scheme at the airfoil boundaries, there is the possibility of degrading the accuracy of the entire method. Fortunately, the cells next to the wall are usually very small, and the gradient term is often small, limiting the effect of this first order error. Although not implemented at present, a second order approximation could be used.

5.2 Flow Discontinuities

The Euler equations are nonlinear and admit so-called *weak solutions*. Weak solutions are those which are not everywhere differentiable, but nonetheless satisfy the integral form of the conservation equations. Flows which contain shocks or wakes fall into this category. In real flows, shocks and wakes have some small but finite thickness. However in the absence of viscosity, shocks and wakes are modelled as surfaces at which the flow variables are discontinuous. In this section, the so-called jump conditions which govern the behavior the flow at these surfaces are developed. These jump conditions will subsequently be used to *fit* shocks and wakes in the present steady and unsteady flow analyses.

In Sections 5.2.1 and 5.2.2, the steady and unsteady wake- and shock-jump conditions will be discussed. These conditions relate the flow on one side of a wake or shock

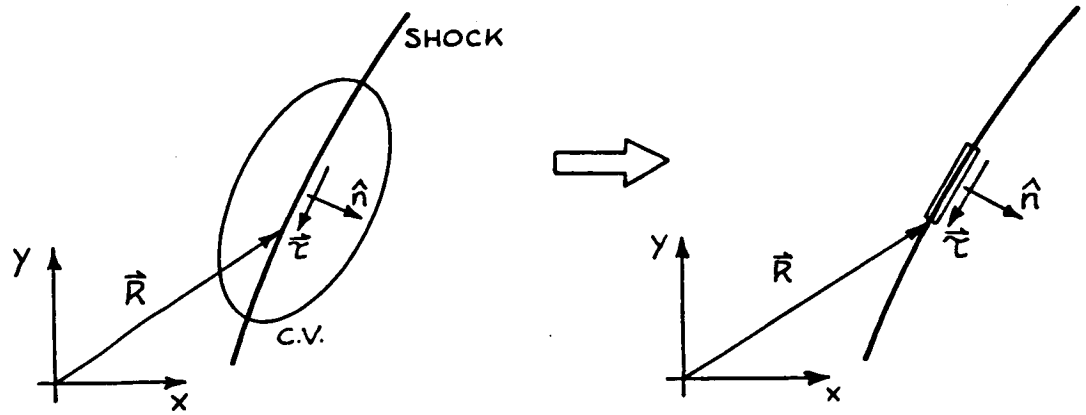

Figure 5.2: Control volume used for the derivation of the shock jump conditions. The volume goes to zero in such a way that only a small portion of the shock is enclosed.

to the flow on the other side. These nonlinear jump conditions will be linearized for for use with the linearized unsteady analysis.

5.2.1 Unsteady Shock Jump Conditions

Nonlinear Shock Jump conditions

To derive the unsteady shock jump conditions, we make use of the integral conservation laws as expressed Equations 4.4, 4.5, and 4.6. Consider a volume D which contains a segment of a shock as shown in Figure 5.2. The shock position is described by the vector $\mathbf{R}$. The vectors $\mathbf{n}$ and τ are the unit normal and the unit tangent to the shock surface, respectively. In general, the shock will not be stationary, but will move through the fluid. Next, we imagine the surface S to shrink until it just encloses a small length of the shock. Evaluations of the integrals in Equations 4.4, 4.5, and 4.6 gives the desired shock jump conditions from the integral conservation equations. For example, the continuity of mass requires that

$$[[\rho \mathbf{V} \cdot \mathbf{n}]] = [[\rho]] \frac{\partial \mathbf{R}}{\partial \mathbf{t}} \cdot \mathbf{n} \tag{5.10}$$

The symbol $[[\cdots]]$ denotes the difference in the enclosed quantity across a discontinuity. Equation 5.10 enables us to connect the two regions of continuous flow on either side of a shock. Similarly, the momentum and energy conditions are given by

$$[[\rho \mathbf{V}\mathbf{V}\cdot\mathbf{n}+p\mathbf{n}]] = [[\rho \mathbf{V}]]\frac{\partial \mathbf{R}}{\partial t}\cdot\mathbf{n} \tag{5.11}$$

$$\left[\left[(e+p+\rho V^2/2)\mathbf{V}\cdot\mathbf{n}\right]\right] = \left[\left[(e+\rho V^2/2)\right]\right]\frac{\partial \mathbf{R}}{\partial t}\cdot\mathbf{n} \tag{5.12}$$

Note in particular the important role the normal component of the shock velocity has in the shock jump conditions (Equations 5.10-5.12. In fact, the tangential direction does not appear at all. Without much loss in generality, we can think of the motion of the shock as being normal to its surface. Alternatively, we can consider the shock to move in the direction of some arbitrary line (so long as this line is not tangent to the shock) such as a computational grid line since there is no constraint on the tangential motion of the shock.

The momentum shock jump condition can be further simplified by looking at the components in the direction normal to and tangential to the shock. The normal and tangential momentum shock-jump conditions become

$$\left[\left[\rho V_n^2+p\right]\right] = [[\rho V_n]]\frac{\partial \mathbf{R}}{\partial t}\cdot\mathbf{n} \tag{5.13}$$

$$\left[\left[\rho V_t\left(V_n-\frac{\partial \mathbf{R}}{\partial t}\cdot\mathbf{n}\right)\right]\right] = 0 \tag{5.14}$$

where the subscripts n and t refer to the normal and tangential directions, respectively. The tangential component of the shock-jump condition can be further simplified by use of Equation 5.10 to show that the jump in tangential velocity across the shock must be zero, i.e.,

$$[[V_t]] = 0 \tag{5.15}$$

Linearized Shock Jump Conditions

The shock and wake jump conditions may also be linearized. As in the linearization of the field equations, a perturbation series is assumed to represent the total flow field. As with the moving airfoil, the motion of the shock is described by a surface vector $\hat{\mathbf{R}}$

which is composed of a mean plus an unsteady part. Hence, the surface vector as well as the unit vectors normal to and tangent to the shock are given by

$$\hat{\mathbf{R}}(s,t) = \mathbf{R}(s) + \mathbf{r}(s,t) \tag{5.16}$$

$$\hat{\mathbf{n}}(s,t) = \overline{\mathbf{n}}(s) + \mathbf{n}(s,t) = \overline{\mathbf{n}} - \overline{\tau}\frac{\partial r_n}{\partial s} \tag{5.17}$$

$$\hat{\tau}(s,t) = \overline{\tau}(s) + \tau(s,t) = \overline{\tau} + \overline{\mathbf{n}}\frac{\partial r_n}{\partial s} \tag{5.18}$$

Substitution of these small perturbation assumptions for the shock displacement and the primitive fluid-dynamic variables into the nonlinear shock-jump conditions, and collection of terms of zeroth and first order gives the nonlinear mean and the linearized unsteady shock-jump conditions. The steady jump conditions are

$$[[\overline{\rho}V_n]] = 0 \tag{5.19}$$

$$\left[\left[\overline{\rho}V_n^2 + P\right]\right] = 0 \tag{5.20}$$

$$[[V_t]] = 0 \tag{5.21}$$

$$\left[\left[\left(\frac{\gamma}{\gamma-1}P + \frac{1}{2}\overline{\rho}V^2\right)V_n\right]\right] = 0 \tag{5.22}$$

and the linearized unsteady shock conditions are

$$\left[\left[\overline{\rho}v_n + \rho V_n - \overline{\rho}V_t\frac{\partial r_n}{\partial s} - \frac{\partial r_n}{\partial t}\overline{\rho}\right]\right] = 0 \tag{5.23}$$

$$\left[\left[p + \rho V_n^2 + 2\overline{\rho}V_n v_n\right]\right] = 0 \tag{5.24}$$

$$\left[\left[v_t + V_n\frac{\partial r_n}{\partial s}\right]\right] = 0 \tag{5.25}$$

$$\left[\left[\frac{1}{2}\rho V^2 V_n + \overline{\rho}V_n\mathbf{V}\cdot\mathbf{v} + \frac{\gamma}{\gamma-1}V_n p + \left(\frac{\gamma}{\gamma-1}P + \frac{1}{2}\overline{\rho}V^2\right)v_n - \left(\frac{\gamma}{\gamma-1}P + \frac{1}{2}\overline{\rho}V^2\right)V_t\frac{\partial r_n}{\partial s} - \left(\frac{1}{\gamma-1}P + \frac{1}{2}\overline{\rho}V^2\right)\frac{\partial r_n}{\partial t}\right]\right] = 0 \tag{5.26}$$

In Equations 5.22 and 5.26 the energy has been expressed in terms of the four primitive variables. These shock jump conditions are valid at the instantaneous position of the shock. This form of the shock jump conditions is not always convenient. For example, suppose we are trying to calculate a flow with a shock using a stationary grid. At time t_0 the shock is aligned with a grid line and the shock jump conditions may be applied

directly. A short time later the shock will have moved a small distance away from the grid line. We can extrapolate the variables from the fixed grid to the new shock location to obtain a slightly modified set of shock jump conditions. They are given by

$$\left[\left[\overline{\rho}v_n + \rho V_n - \overline{\rho}V_t\frac{\partial r_n}{\partial s} - \frac{\partial r_n}{\partial t}\overline{\rho} + \mathbf{r}\cdot\nabla(\overline{\rho}V_n)\right]\right] = 0 \tag{5.27}$$

$$\left[\left[p + \rho V_n^2 + 2\overline{\rho}V_n v_n + \mathbf{r}\cdot\nabla(P + \overline{\rho}V_n^2)\right]\right] = 0 \tag{5.28}$$

$$\left[\left[v_t + V_n\frac{\partial r_n}{\partial s} + \mathbf{r}\cdot\nabla(V_t)\right]\right] = 0 \tag{5.29}$$

$$\begin{aligned}\left[\left[\frac{1}{2}\rho V^2 V_n + \overline{\rho}V_n\mathbf{V}\cdot\mathbf{v} + \frac{\gamma}{\gamma-1}V_n p + \left(\frac{\gamma}{\gamma-1}P + \frac{1}{2}\overline{\rho}V^2\right)v_n\right.\right.\\ - \left(\frac{\gamma}{\gamma-1}P + \frac{1}{2}\overline{\rho}V^2\right)V_t\frac{\partial r_n}{\partial s} - \left(\frac{1}{\gamma-1}P + \frac{1}{2}\overline{\rho}V^2\right)\frac{\partial r_n}{\partial t}\\ \left.\left. + \mathbf{r}\cdot\nabla\left(\left(\frac{\gamma}{\gamma-1}P + \frac{1}{2}\overline{\rho}V^2\right)V_n\right)\right]\right] = 0\end{aligned} \tag{5.30}$$

The unknowns in Equation 5.30 are the magnitude of the shock displacement $\mathbf{r}$, and the perturbation variables ρ, u, v, and p on either side of the shock. Known are the steady flow variables $\overline{\rho}$, U, V, and P. As with the linearized field equations, the time derivative operator $\frac{\partial}{\partial t}$ may be replaced by $j\omega$ if the flow is harmonic.

5.2.2 Unsteady Wake Jump Conditions

Nonlinear Wake Jump Conditions

Although the jump conditions presented in Section 5.2.1 were derived for the case of a shock discontinuity, in fact they are valid for any surface at which the flow variables are discontinuous including blades and wakes. The blades and wakes are surfaces through which mass does not flow and therefore, the flow tangency condition also applies at wake surfaces. However, whereas the motion of the airfoils is prescribed, the wake motion must be determined as part of the solution.

Because the mass flux through the wake is zero, the conservation of tangential momentum and energy are automatically satisfied. The remaining jump condition is the normal momentum. An examination of the normal momentum jump condition reveals

that the condition reduces to the requirement that the pressure be continuous across the wake. Thus, the three conditions which are applied at the wake surface are

$$(\hat{\mathbf{V}} \cdot \hat{\mathbf{n}})_{\text{upper}} = \frac{\partial \hat{\mathbf{R}}}{\partial t} \cdot \hat{\mathbf{n}} \tag{5.31}$$

$$(\hat{\mathbf{V}} \cdot \hat{\mathbf{n}})_{\text{lower}} = \frac{\partial \hat{\mathbf{R}}}{\partial t} \cdot \hat{\mathbf{n}} \tag{5.32}$$

$$[[\hat{p}]] = 0 \tag{5.33}$$

Hence, pressure and the normal component of velocity are required to be continuous across a wake. The tangential velocity and density will generally be discontinuous. One final requirement on the wake position is that the wake be attached to the trailing edge of the airfoil.

Linearized Wake Conditions

The unsteady wake conditions are linearized in a fashion similar to the unsteady shock jump linearization. The wake surface $\hat{\mathbf{R}}$ is described by a perturbation series as are the primitive variables. These assumptions are substituted into the wake equations (Equations 5.31–5.33). Collection of terms of equal order provides the zeroth-order (mean) and the first-order (linearized unsteady) wake conditions. The steady jump conditions are

$$(\mathbf{V} \cdot \overline{\mathbf{n}})_{\text{lower}} = 0 \tag{5.34}$$

$$(\mathbf{V} \cdot \overline{\mathbf{n}})_{\text{upper}} = 0 \tag{5.35}$$

$$[[P]] = 0 \tag{5.36}$$

The linearized unsteady wake jump conditions are given by

$$\left(\mathbf{v} \cdot \overline{\mathbf{n}} - \frac{\partial r_n}{\partial t} - V_t \frac{\partial r_n}{\partial s}\right)_{\text{lower}} = 0 \tag{5.37}$$

$$\left(\mathbf{v} \cdot \overline{\mathbf{n}} - \frac{\partial r_n}{\partial t} - V_t \frac{\partial r_n}{\partial s}\right)_{\text{upper}} = 0 \tag{5.38}$$

$$[[p]] = 0 \tag{5.39}$$

Equations 5.37–5.39 are applied at the instantaneous wake positions. The corresponding conditions that apply at the mean wake positions are

$$\left(\mathbf{v}\cdot\overline{\mathbf{n}} - \frac{\partial r_n}{\partial t} + V_t\frac{\partial r_n}{\partial s} + \mathbf{r}\cdot\nabla(V_n)\right)_{\text{lower}} = 0 \tag{5.40}$$

$$\left(\mathbf{v}\cdot\overline{\mathbf{n}} - \frac{\partial r_n}{\partial t} + V_t\frac{\partial r_n}{\partial s} + \mathbf{r}\cdot\nabla(V_n)\right)_{\text{upper}} = 0 \tag{5.41}$$

$$[[p + \mathbf{r}\cdot\nabla P]] = 0 \tag{5.42}$$

5.2.3 Newton Iteration Solution Procedure for Flows with Shocks and Wakes

In Chapter 4, the basic Newton iteration procedure used to solve two-dimensional steady flow problems was discussed. The extension of the method to two-dimensional flows with shocks is discussed briefly below. Moretti [26,27] has pioneered the use of shock fitting in Euler codes. Although the idea of modelling the shock as a line discontinuity is similar, the implementation of the present shock fitting technique is different. Moretti uses a time-marching algorithm to determine the steady shock location. In the present method, however, the shock position is found using a direct method.

The basic procedure for fitting two-dimensional steady shocks is the same as for the one-dimensional flows. First, an initial position of the shock is assumed. The grid is generated such that a double grid line straddles the shock. Hence, the flow is divided into an upstream and downstream region. The flow in the two regions are coupled together by applying the shock-jump conditions at the face centers of cells lying along the shock. At each of the double nodes, an additional variable is introduced which is the distance the shock will be displaced from this initial guess. Because shock fitting is part of the Newton iteration procedure, the nonlinear steady shock-jump conditions will be linearized by assuming that the correction to the assumed shock position is small as is the correction to the primitive variables. Using these assumptions, the linearized steady shock-jump conditions are

$$\left[\left[\bar{\rho}v_n + \rho V_n - \bar{\rho}V_t\frac{\partial r_n}{\partial s} + \mathbf{r}\cdot\nabla(\bar{\rho}V_n)\right]\right] = -[[\bar{\rho}V_n]] \tag{5.43}$$

$$\left[\left[p + \rho V_n^2 + 2\bar{\rho}V_n v_n - 2\bar{\rho}V_n V_t\frac{\partial r_n}{\partial s} + \mathbf{r}\cdot\nabla(P + \bar{\rho}V_n^2)\right]\right] = -\left[\left[\bar{\rho}V_n^2 + P\right]\right] \tag{5.44}$$

$$\left[\left[v_t + V_n \frac{\partial r_n}{\partial s} + \mathbf{r} \cdot \nabla(V_t)\right]\right] = -\left[[V_t]\right] \tag{5.45}$$

$$\left[\left[\frac{1}{2}\rho V^2 V_n + \overline{\rho} V_n \mathbf{V} \cdot \mathbf{v} + \frac{\gamma}{\gamma - 1} V_n p + \left(\frac{\gamma}{\gamma - 1} P + \frac{1}{2}\overline{\rho} V^2\right) v_n \right.\right.$$
$$\left.\left. - \left(\frac{\gamma}{\gamma - 1} P + \frac{1}{2}\overline{\rho} V^2\right) V_t \frac{\partial r_n}{\partial s} - \mathbf{r} \cdot \nabla \left(\left(\frac{\gamma}{\gamma - 1} P + \frac{1}{2}\overline{\rho} V^2\right) V_n\right)\right]\right] =$$
$$-\left[\left[\left(\frac{\gamma}{\gamma - 1} P + \frac{1}{2}\overline{\rho} V^2\right) V_n\right]\right] \tag{5.46}$$

These boundary conditions are discretized at the centers of the cell faces lying on the shock using second-order accurate differencing techniques.

Assuming that the conservation equations and the other boundary conditions have been discretized and assembled, Gaussian elimination is used to solve for the corrections to the primitive variables. Also obtained as part of the solution is the correction to the shock position. First, the primitive variables are updated using the corrections. Then, using the correction in the shock position, the grid is deformed so that the double grid lines coincide with the new shock location. But we are not quite done. Because the grid nodes have moved, the primitive variables stored at the old node locations must be extrapolated to the new node locations. This completes one Newton iteration. The entire process is repeated until convergence.

Described above is the procedure used to fit shocks using the four conservation equations. If, however, the steady flow is homoenergetic, then the energy equation may be eliminated. The procedure for fitting shocks is essentially the same as just described except that there will only be three shock-jump conditions.

Although not discussed in detail here, the procedure for fitting wakes is similar to the procedure for fitting shocks. The nonlinear steady wake jump conditions are linearized for use with the Newton iteration procedure. At each step of the iteration, the double grid line which represents the wake is moved to coincide with the new estimate of the wake location.

5.3 Periodic and Far Field Boundary Conditions

Periodic Boundary Conditions

The periodic boundaries upstream and downstream of the blades requires special treatment. The flows which we will consider are harmonic in time and periodic in the cascade circumferential direction. The line which extends from the leading edge of the blade forward in the axial direction is a periodic boundary. For steady flow, the state of the fluid along this line will be equal to the state of the fluid along the corresponding line for the adjacent blade. Similarly on the wake boundary, the flow just above the wake of one blade will be the same as the flow just above the wake of the adjacent blade. These are known as the periodicity conditions. They allow us to calculate the flow through the entire cascade by considering a single blade passage.

For unsteady flow, the periodicity condition is slightly different. In this case the unsteady flow along the periodic boundary will be the same as the flow along the periodic boundary of the adjacent blade but phase shifted by the *interblade phase angle*. For the flutter problem, the blades are assumed to vibrate in such a way that a travelling wave is set up in the rotor. The interblade phase angle σ is the phase difference between the motion of a given blade and its neighbor. Mathematically, this periodicity condition is expressed as

$$f(x, y + s) = f(x, y)e^{j\sigma} \tag{5.47}$$

where f is any one of the perturbation variables and s the distance between blades. This boundary condition is applied at all the boundary nodes along the upstream periodic boundaries.

Far-Field Boundary Conditions

To analyze the upstream far-field behavior of the unsteady flow requires a bit of work. Because we will be solving for the unsteady flow in a cascade numerically, the computational domain cannot extend indefinitely in the axial direction. Usually, the computational domain will extend only about one chord length in front of the blade row. At this upstream boundary of the computational domain, we need to apply an appropriate set

of conditions which will allow unsteady disturbances to pass out of the domain without being reflected. The analysis below is somewhat similar to the characteristic boundary analysis used in time marching-schemes. In such schemes (unlike the present method), it is often assumed that any unsteady disturbances which impinge on the upstream boundary strike it with the wave fronts parallel to the boundary. That is, the partial derivative with respect to the tangential direction is negligible. This assumption results is the well known one-dimensional characteristic boundary conditions. The characteristic variables represent vorticity, entropy, and two isentropic pressure waves. However, if the wave fronts are not parallel to the boundary, the wave will be partially reflected back into the computational domain. For steady state calculations, this slows convergence. For unsteady flow calculations, this produces errors in the predicted unsteady flow quantities. Recently, several investigators have suggested higher-order nonreflecting boundary conditions which produce smaller reflections [38,39,40]. Fortunately, in the present analysis, *exact* nonreflecting boundary conditions can be imposed along the upstream boundary. This procedure is described below.

Consider the cascade passage shown in Figure 5.1. Note that the x- and y-axes are aligned with the axial and tangential flow directions. We assume that sufficiently far upstream of the rotor the flow is uniform. Hence the linearized Euler equations can be expressed as

$$\mathbf{B}_1 \frac{\partial \mathbf{u}}{\partial t} + \mathbf{B}_2 \frac{\partial \mathbf{u}}{\partial x} + \mathbf{B}_3 \frac{\partial \mathbf{u}}{\partial y} = 0 \tag{5.48}$$

where $\mathbf{B}_1$, $\mathbf{B}_2$, and $\mathbf{B}_3$ are the matrices which appear in Equation 4.24, and $\mathbf{u}$ is the vector of perturbation variables $[\rho,\ u,\ v,\ p]^T$. If the cascade is vibrating with interblade phase angle σ, then the solution has a spatial period in the tangential direction of $2\pi s/\sigma$. Because we are interested in the behavior of waves in the far-field, a more natural representation of the solution upstream of the rotor is given by the Fourier series

$$\mathbf{u}(x,y,t) = \sum_{i=-\infty}^{\infty} \tilde{\mathbf{u}}_i e^{(j\omega t + j\beta_i y + jk_i x)} \tag{5.49}$$

where $\beta_i = (\sigma + 2\pi i)/s$, and k_i is a spatial wave number to be determined. Substitution of Equation 5.49 into Equation 5.48 and collection of terms leads to

$$\sum_{i=-\infty}^{\infty} \left[\omega \mathbf{B}_1 + k_i \mathbf{B}_2 + \beta_i \mathbf{B}_3\right] \tilde{\mathbf{u}}_i e^{(j\omega t + j\beta_i y + jk_i x)} = 0 \tag{5.50}$$

For this equation to hold, each term of the infinite series must vanish. Hence,

$$[\omega \mathbf{B}_1 + k_i \mathbf{B}_2 + \beta_i \mathbf{B}_3]\, \tilde{\mathbf{u}}_i = 0 \tag{5.51}$$

Recall that ω and β_i are prescribed quantities. Equation 5.51 is then an eigenvalue problem for the eigenvalue k_i and the eigenvector $\tilde{\mathbf{u}}_i$. After some matrix manipulation, we can express this eigenvalue problem in a slightly more convenient form, i.e.,

$$-\mathbf{B}_2^{-1}\,[\omega \mathbf{B}_1 + \beta_i \mathbf{B}_3]\, \tilde{\mathbf{u}}_i = k_i \tilde{\mathbf{u}}_i \tag{5.52}$$

Here, the matrix on the left hand side is known, and the eigenvalues and eigenvectors are to be determined. These eigen-quantities are important since they determine the nature of the travelling waves, as well as the speed and direction in which they travel. In particular, it can be shown that the so-called characteristic variables are directly related to the eigenvectors. To demonstrate this, we make a linear transformation from the four primitive variables (Fourier coefficients) $\tilde{\mathbf{u}}_i$ to the four characteristic variables $\tilde{\mathbf{w}}_i$. Hence we have that

$$\tilde{\mathbf{u}}_i = \mathbf{T}\tilde{\mathbf{w}}_i \tag{5.53}$$

$$\tilde{\mathbf{w}}_i = \mathbf{T}^{-1}\tilde{\mathbf{u}}_i \tag{5.54}$$

Substitution of Equation 5.53 into Equation 5.52 and pre-multiplication by $\mathbf{T}^{-1}$ gives

$$-\mathbf{T}^{-1}\mathbf{B}_2^{-1}\,[\omega \mathbf{B}_1 + \beta_i \mathbf{B}_3]\, \mathbf{T}\tilde{\mathbf{w}}_i = k_i \tilde{\mathbf{w}}_i \tag{5.55}$$

were $\mathbf{T}$ is chosen so as to diagonalize the right hand side. That to say, $\mathbf{T}$ is the matrix of right eigenvectors while $\mathbf{T}^{-1}$ is the matrix of left eigenvectors. By solving this eigenvalue problem, it can be shown that the four characteristic variables are given by

$$\begin{aligned}
\tilde{\mathbf{w}}_i &= \mathbf{T}^{-1}\tilde{\mathbf{u}}_i \\
&= \begin{bmatrix}
0 & \beta_i V + \omega & -\beta_i U & -\dfrac{\sqrt{\beta_i^2(U^2+V^2-\bar{a}^2)+2\beta_i\omega V+\omega^2}}{\bar{\rho}\bar{a}} \\
0 & \beta_i V + \omega & -\beta_i U & \dfrac{\sqrt{\beta_i^2(U^2+V^2-\bar{a}^2)+2\beta_i\omega V+\omega^2}}{\bar{\rho}\bar{a}} \\
1 & 0 & 0 & -\dfrac{1}{\bar{a}^2} \\
0 & \beta_i U & \beta_i V + \omega & \dfrac{\beta_i}{\bar{\rho}}
\end{bmatrix}
\begin{bmatrix} \tilde{\rho}_i \\ \tilde{u}_i \\ \tilde{v}_i \\ \tilde{p}_i \end{bmatrix}
\end{aligned} \tag{5.56}$$

The corresponding wave numbers are

$$k_{1i} = \frac{U(\omega + \beta_i V) + \sqrt{\beta_i^2(U^2 + V^2 - \bar{a}^2) + 2\beta_i \omega V + \omega^2}}{U^2 - \bar{a}^2} \tag{5.57}$$

$$k_{2i} = \frac{U(\omega + \beta_i V) - \sqrt{\beta_i^2(U^2 + V^2 - \bar{a}^2) + 2\beta_i \omega V + \omega^2}}{U^2 - \bar{a}^2} \tag{5.58}$$

$$k_{3i} = -\frac{\beta_i V + \omega}{U} \tag{5.59}$$

$$k_{4i} = -\frac{\beta_i V + \omega}{U} \tag{5.60}$$

The characteristic variables represent the downstream and upstream moving pressure waves, an entropy wave, and a vorticity wave for the given wave number β_i. The speed at which these waves propagate, and the nature of their propagation, are related to their respective wave numbers. If the wave number is real, then the wave propagates unattenuated and is said to be superresonant. If the imaginary part of the wave number is negative, then the wave grows in the x-direction. If the imaginary part of the wave number is positive, then the wave attenuates in the x-direction. These are so-called subresonant modes [15].

Note also that the wave numbers are nonlinear functions of the temporal frequency ω, which is an indication that the system is *dispersive*. This means that the energy stored in the waves of different wave numbers will in general travel at different speeds through the fluid. In a dispersive system, the phase velocity and group velocity are different. The phase velocity is the speed at which a wave appears to move if one follows the wave peak. The group velocity is the velocity a packet of waves of a given wave number moves. The group velocity determines the direction of movement of the characteristic variables.

The phase velocity, denoted by c, is the speed at which a wave appears to move if one follows a wave crest. Hence, the phase velocity is given simply by

$$c = -\frac{\omega}{k} \tag{5.61}$$

The group velocity C is the speed at which a packet of waves of a given wave number moves. It can be shown that this speed is given by

$$C = -\frac{\partial \omega}{\partial k} = -\left(\frac{\partial k}{\partial \omega}\right)^{-1} \tag{5.62}$$

If the waves propagate unattenuated, then it is the group velocity which determines which of the characteristic variables are to be prescribed at the far-field boundary. The waves which enter the domain must be specified. For the flutter problem, this means the incoming waves would be set to zero. For the gust response problem, the values of the characteristic variables would be chosen so as to model the incoming entropy and vorticity waves.

Due to the square root which appears in the expression for the pressure wave numbers, it is possible for the wave numbers to be complex. In this case it is the imaginary part of the wave number which determines which characteristic values must be specified. The pressure wave which decays in the x-direction is the one which must be specified at the upstream. Whenever the conditions are such that pressure waves do not propagate, the waves are said to be cut-off [41]. The condition where a wave just propagates is known as acoustic resonance [6].

Discretization of the Upstream Far-Field Boundary Condition

The procedure for specifying the upstream boundary condition is as follows. Along the upstream boundary, there are J boundary points. But because the first and last points are related by the periodicity condition, there are really only $J-1$ independent points. To avoid confusion, let these $J-1$ points be indexed by n. Then the harmonic perturbation variables can be expressed along the far-field boundary by a linear transformation. So for example the pressure is given by

$$\mathbf{u}_n = \sum_{i=-\frac{J-1}{2}}^{\frac{J-1}{2}-1} \tilde{\mathbf{u}}_i e^{j\beta_i y_n} \tag{5.63}$$

where y_n is the location of the nth node along the inlet boundary, $\mathbf{u}_i$ is the amplitude of the ith Fourier component of the primitive variables, and β_i is the ith wave number. Equation 5.63 can be expressed in matrix form

$$\mathbf{u} = \mathbf{E}\tilde{\mathbf{u}} \tag{5.64}$$

where now $\mathbf{u}$ is understood to mean all the perturbation primitive variables along the upstream far-field boundary, and $\tilde{\mathbf{u}}$ is understood to mean the Fourier components of

the primitive variables. Inverting this relationship gives the inverse transform

$$\tilde{\mathbf{u}} = \mathbf{E}^{-1}\mathbf{u} \tag{5.65}$$

The vector $\tilde{\mathbf{u}}$ is composed of $J-1$ submatrices denoted by $\tilde{\mathbf{u}}_i$. The characteristic boundary conditions are applied to each of these subvectors. If the flow is subsonic at the inlet, then three boundary conditions must be specified for each $\tilde{\mathbf{u}}_i$. These boundary conditions correspond to setting the values of the incoming pressure wave, the entropy wave, and the vorticity wave, and can be expressed as

$$\mathbf{K}_i\tilde{\mathbf{u}}_i = \mathbf{f}_i \tag{5.66}$$

where

$$\mathbf{K}_i = \begin{bmatrix} 0 & \beta_i V + \omega & -\beta_i U & \frac{\sqrt{\beta_i^2(U^2+V^2-\bar{a}^2)+2\beta_i\omega V+\omega^2}}{\bar{\rho}\bar{a}} \\ 1 & 0 & 0 & -\frac{1}{\bar{a}^2} \\ 0 & \beta_i U & \beta_i V + \omega & \frac{\beta_i}{\bar{\rho}} \end{bmatrix} \tag{5.67}$$

and $\mathbf{f}_i$ represnets the specified levels of the incoming waves. Usually, $\mathbf{f}_i$ will be zero. The exception is the case where $i = 0$ which corresponds to the fundamental wave number. For the flutter problem, $\mathbf{f}_0$ is set to zero. For the gust response problem, $\mathbf{f}_0$ is chosen to represent the incoming gust.

The $J-1$ conditions can be expressed in matrix form as

$$\mathbf{K}\tilde{\mathbf{u}} = \mathbf{f} \tag{5.68}$$

where $\mathbf{K}$ is a matrix with $3(J-1)$ columns and $4(J-1)$ rows. This matrix is sparse and could be called block diagonal, with $\mathbf{K}_i$ on the diagonals. The vector $\mathbf{f}$ has mostly zero entries except for the three entries which specify the incoming gusts. Making use of the inverse transform (Equation 5.65) gives

$$\mathbf{K}\mathbf{E}^{-1}\mathbf{u} = \mathbf{f} \tag{5.69}$$

Note that these boundary conditions couple all of the nodes along the far-field boundary since $\mathbf{K}\mathbf{E}^{-1}$ is not sparse. These boundary conditions are added to the discretized conservation equations by the squaring technique introduced in Chapter 4.

Downstream Far-Field Boundary Conditions

The boundary conditions at the downstream far-field boundary are handled in essentially the same fashion as the upstream far-field boundary condition except for two important differences. First, if the outflow is subsonic, only one boundary condition for each tangential wave number β_i is applied. This boundary condition corresponds to the upstream moving pressure wave. Secondly, the velocity (and the density) are not continuous across the wake. Hence, the flow is divided into two parts: a continuous part which is continuous through the wake, and a discontinuous part which satisfies the jump in velocity in the wake but has no unsteady pressure associated with it. The nonreflecting boundary condition is then applied to the continuous part only. For a more complete description of this technique, see Reference [37].

5.4 Surface Pressures

Once the unsteady flow through a cascade has been calculated, the results can be used to calculate the unsteady lift and moment acting on the blade by integrating the surface pressure over the surface of the airfoil. This process is slightly complicated by the fact that the airfoil may be vibrating so that the unsteady pressures at the mean blade location are not the same as at the instantaneous blade location, and because there may be shocks oscillating on the surface of the airfoil giving rise to an anharmonic pressure distribution

5.4.1 Moving Airfoils

To determine the unsteady pressure at the surface of the airfoil requires that the unsteady pressure perturbation p, and the gradient of the steady pressure ∇P at the mean blade location be known. To obtain the surface pressure at the instantaneous blade location, one simply extrapolates from the mean to the instantaneous location. Hence, to first order,

$$pe^{j\omega t}\Big|_{\text{surface}} = pe^{j\omega t}\Big|_{\text{mean}} + \nabla P \cdot \mathbf{r}e^{j\omega t} \tag{5.70}$$

where $\mathbf{r}$ is the prescribed unsteady blade motion.

5.4.2 The Shock Impulse

A slightly more complicated problem is that of shock motion on the surface of an airfoil. Suppose now that the airfoil is stationary but a shock is oscillating on the surface of the airfoil. Away from the shock, the unsteady pressure is simply given by the perturbation pressure $pe^{j\omega t}$. But in regions close to the mean shock location, the unsteady pressure is anharmonic due to the passing of the shock. As the shock passes over a given point on the surface, there is an order unity jump in the pressure. Figure 5.3 shows this situation graphically. Plotted is the pressure on the surface of an airfoil at a given instant in time along with the mean pressure distribution. The difference in the instantaneous pressure and the mean pressure is the unsteady pressure. Away from the shock, the difference is first order. In the region between the mean and instantaneous shock locations, the pressure difference is order unity, but the difference is shock locations is first order. Hence, the anharmonic pressure produces first-order contributions when integrated to obtain the lift or moment. Because the shock motion is harmonic, this contribution is also harmonic to first order. For aeroelastic calculations, one can consider the anharmonic pressure due to the shock motion to be a harmonic impulse. This impulse is represented as

$$p_{\text{impulse}}e^{j\omega t} = -x_s \Delta P e^{j\omega t} \tag{5.71}$$

where ΔP is the mean pressure jump across the shock and x_s is the complex amplitude of shock motion along the blade.

5.5 Summary

In this chapter, the boundary conditions needed to analyze unsteady cascade flows have been presented. Of special interest are the treatments of flow discontinuities and far-field boundaries. Unsteady shocks and wakes are analyzed using shock and wake fitting procedure rather than by capturing. Fitting allows an accurate representation of these discontinuities without excessive grid resolution. The far-field boundary conditions are specified using nonreflecting boundary conditions. These boundary conditions also allow one to specify incoming gusts for the gust response problem.

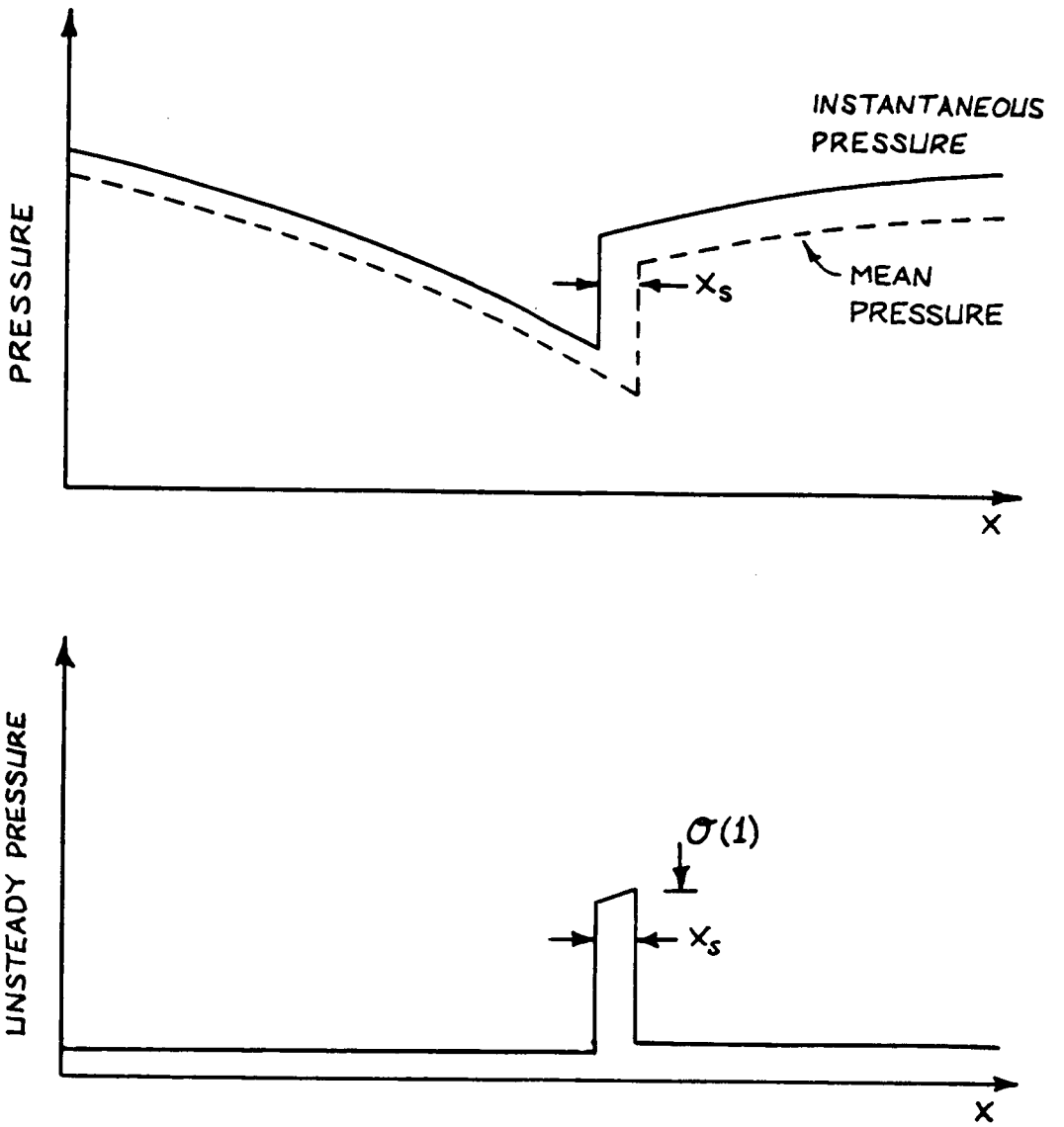

Figure 5.3: Anharmonic unsteady pressure due to shock motion. Upper plot shows the mean and instantaneous pressures on an airfoil surface. Lower plot shows the difference between the instantaneous and mean pressures. Note the "impulse" due to the shock motion.

Chapter 6

Results

In this chapter, a variety of steady and unsteady flow solutions are presented to demonstrate the capabilities of the present Euler analysis. In Section 6.1, steady and unsteady, subsonic and transonic flows through a hyperbolic channel are examined. The main purpose of these examples is to demonstrate the accuracy and convergence properties of the present method for steady flow calculations, to demonstrate the steady shock fitting capabilities, and to demonstrate the ability of the present method to accurately predict unsteady shock motion. In Section 6.2, the results of the present method are compared to a time-marching method. It is shown that the two methods are in good agreement so long as the level of unsteadiness is moderate, and that the present method is computationally much more efficient. Finally, in Section 6.3, some steady and unsteady cascade flows are presented. The unsteady flows are due to both blade motion (the flutter problem) and incoming vortical and entropic waves (the forced response problem). Here again, the method is shown to give good agreement with semi-analytical and time-marching methods, but are obtained with a fraction of the computational effort required by the time-marching methods.

6.1 The Flow in a Hyperbolic Channel

The first test to be considered is the flow through a hyperbolic channel. This geometry was studied by Emmons [42,43] in the mid 1940s and was chosen here as an

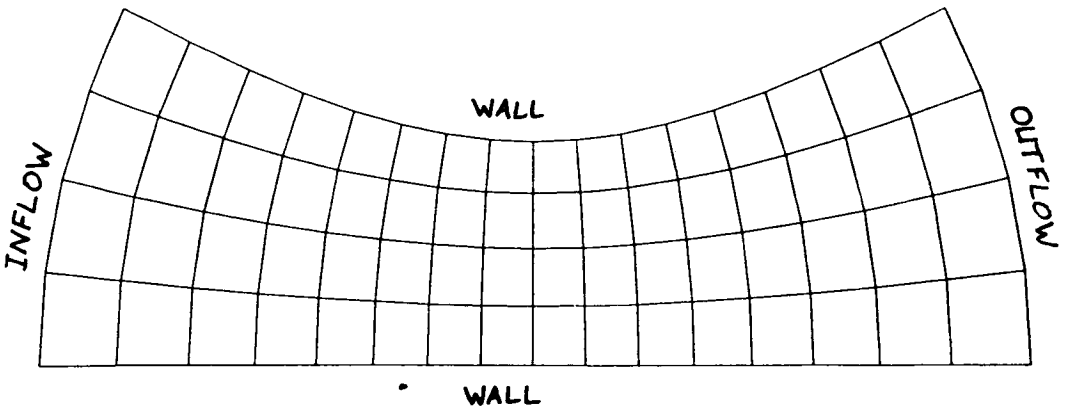

Figure 6.1: Typical grid used to calculate steady and unsteady flows through hyperbolic channel.

initial test case for several reasons. First, the flow through this geometry is highly two dimensional, i.e., there is significant variation in flow properties across the width of the channel so that it represents more than just a slight extension of one-dimensional flow. Second, if a shock occurs, it will be curved because of the highly two-dimensional flow field. As such, the hyperbolic channel is a good test geometry on which to evaluate the steady shock-fitting algorithm. Finally, the published results of Emmons' allow some qualitative comparisons with the present steady flow results.

The channel itself is defined by a transformation from ξ, η coordinates to x, y coordinates by

$$x = \sinh(\xi)\cos(\eta) \tag{6.1}$$

$$y = \cosh(\xi)\sin(\eta) \tag{6.2}$$

In the ξ, η coordinate system, the channel is rectangular extending from $\xi = -1.05$ to $\xi = 1.05$ and $\eta = 0$ to $\eta = 0.6$. A typical computational grid used to compute the steady and unsteady flows through this channel is shown in Figure 6.1. The upper wall is curved while the lower wall is straight. Emmons calculated both subsonic and

transonic flows through this channel geometry using a numerical method in which a stream function was determined using a relaxation technique.

6.1.1 Accuracy of the Steady Solver

The first use of the hyperbolic flow geometry will be to check the order of accuracy of the steady flow solver. In Chapter 4 the claim was made that the present scheme is second-order accurate. In other words, if the linear dimension of the conservation cells is $\mathcal{O}(\Delta x)$, then the norm of the error of the computed solution (a measure of the difference between the exact solution and the numerical solution) is $\mathcal{O}(\Delta x^2)$. Although the exact solution is not known for this geometry, it is known that for subsonic flows the total pressure should be constant throughout the channel. Hence, the norm of the total pressure error is also a measure of the solution accuracy.

The following procedure was used. Grids with increasingly fine resolutions were used to calculate the steady flow through the hyperbolic channel. The boundary conditions are such that the flow is subsonic throughout the channel. Upstream the total pressure and density were specified to be unity. Downstream, the exit pressure was specified to be 0.92. The steady flow was calculated using the Newton iteration procedure outlined in earlier chapters. Once a converged solution was obtained, the L_2 norm (the root mean square) of the total pressure loss was calculated.

Figures 6.2–6.5 show the grids used to calculate the steady flow along with the steady Mach number contours and total pressure contours. The grids used contained 8×2, 16×4, 32×8, and 64×16 cells respectively. As expected, the 8×2 grid gives only fair results with a total pressure loss in the vicinity of the throat of about 3 percent. The solution is dramatically better for the 16×4 grid with about a 1 percent total pressure loss at the throat. The 32×8 and the 64×16 grid give nearly exact solutions with less than 0.3 and 0.1 percent total pressure loss, respectively. The Mach number contours for these last two cases are indistinguishable from one another.

Shown in Figure 6.6 is the norm of the total pressure loss as a function of grid resolution. When plotted on a logarithmic plot, the slope of the curve gives the order of accuracy of the method. Note in particular that the slope of the curve is very nearly 2

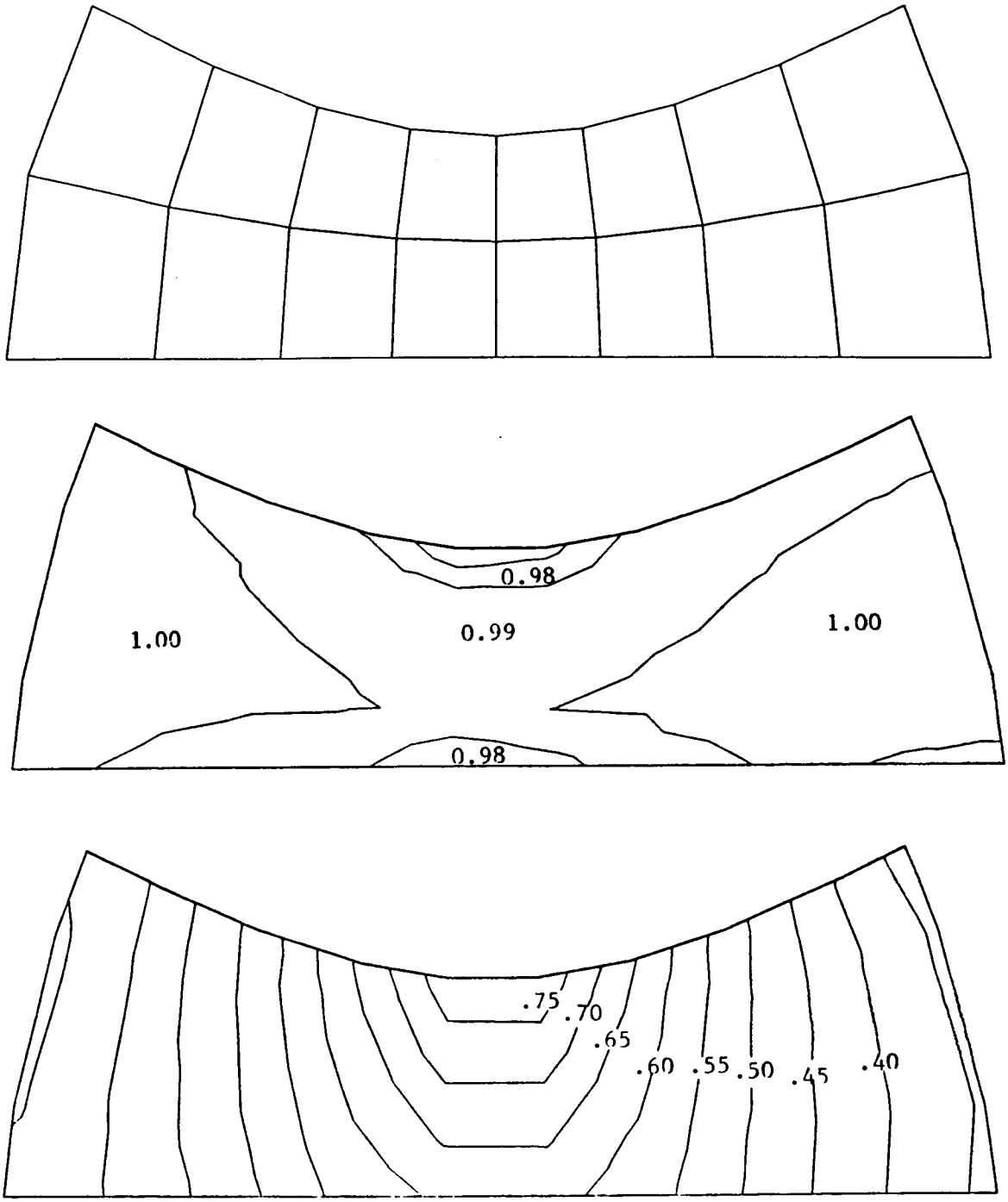

Figure 6.2: Very coarse resolution grid used to calculate steady subsonic flow in a hyperbolic channel. Also shown are the computed total pressure and Mach number contours.

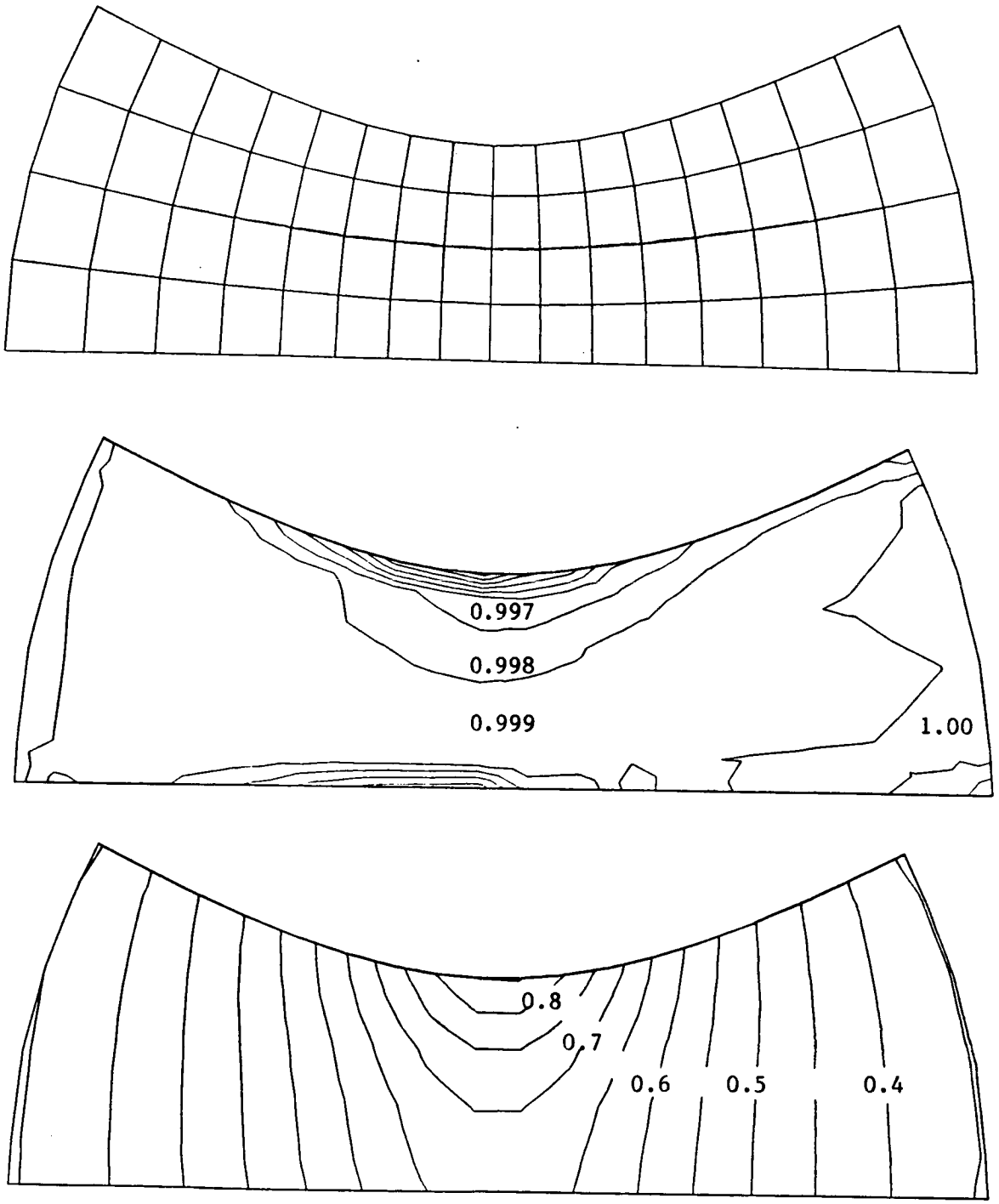

Figure 6.3: Coarse resolution grid used to calculate steady subsonic flow in a hyperbolic channel. Also shown are the computed total pressure and Mach number contours.

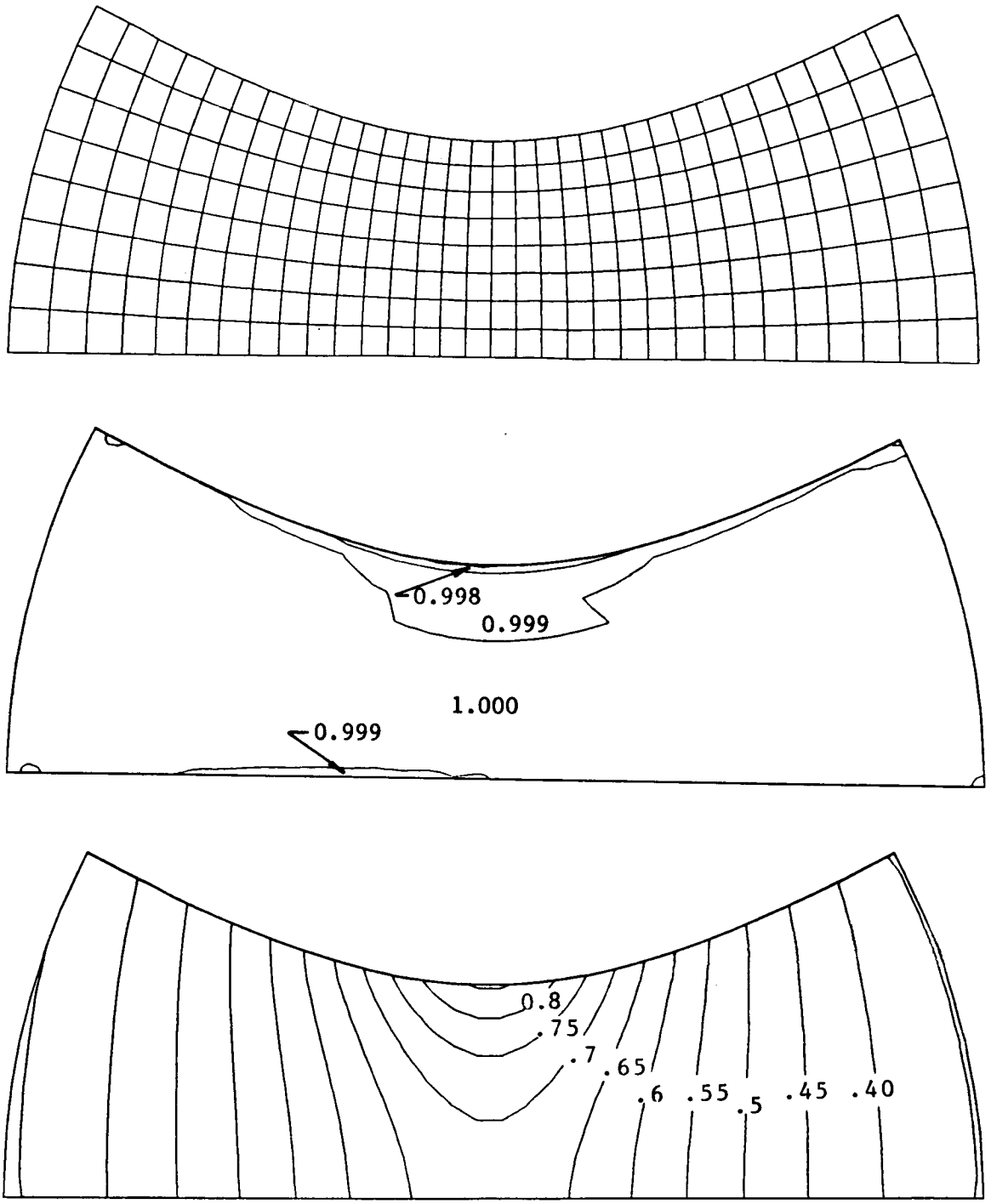

Figure 6.4: Medium resolution grid used to calculate steady subsonic flow in a hyperbolic channel. Also shown are the computed total pressure and Mach number contours.

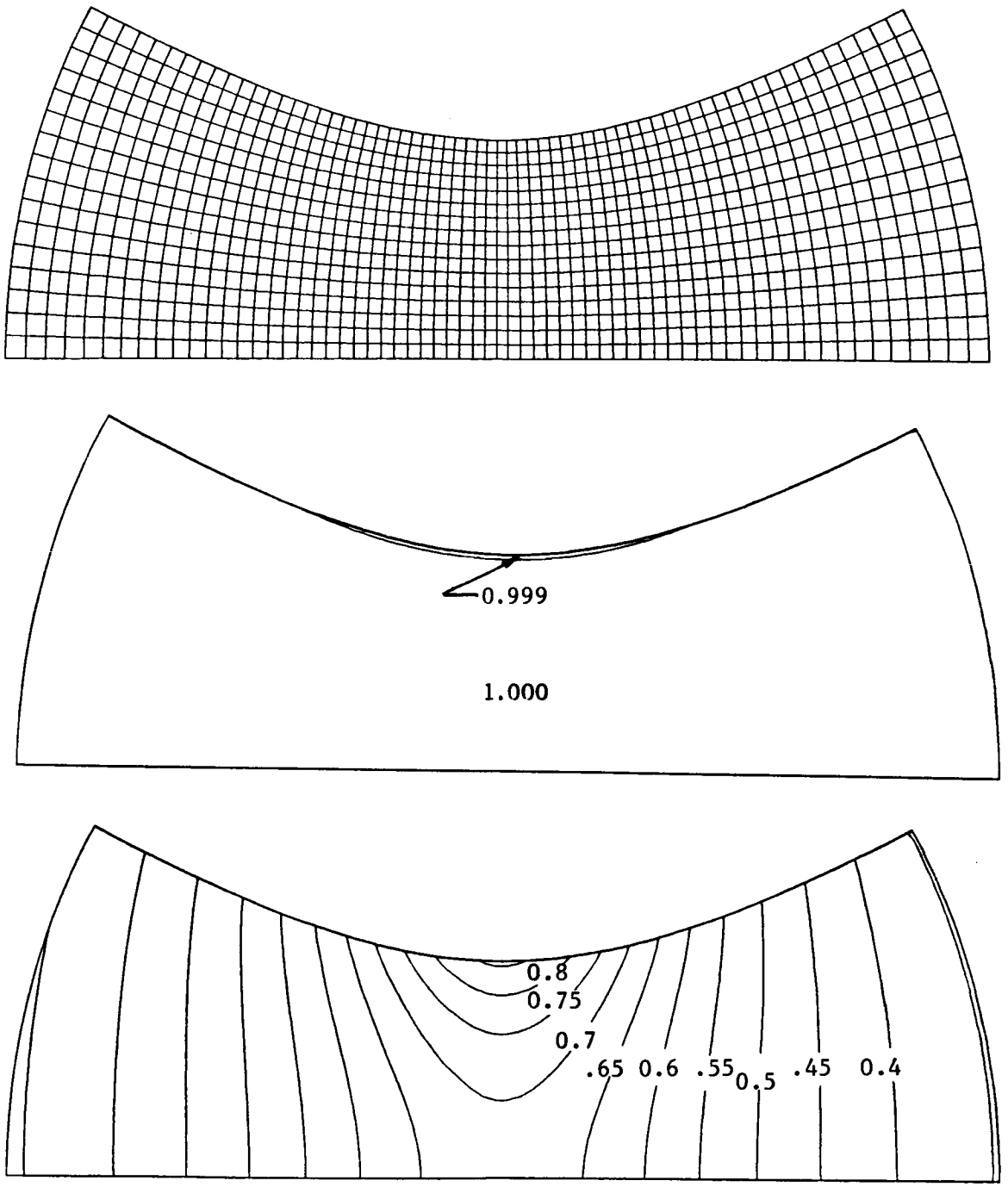

Figure 6.5: Fine resolution grid used to calculate steady subsonic flow in a hyperbolic channel. Also shown are the computed total pressure and Mach number contours.

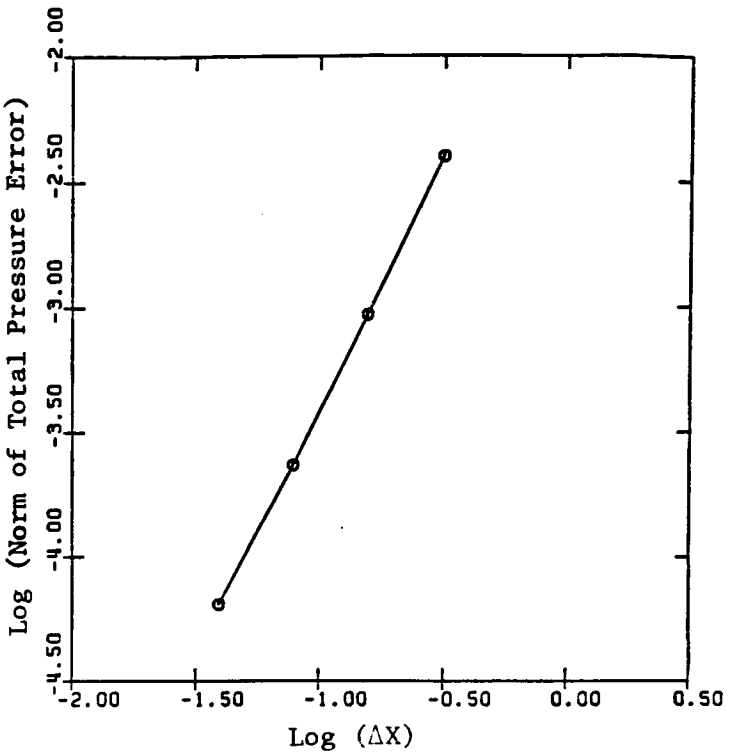

Figure 6.6: Norm of total pressure error as a function of grid resolution. Note the slope is very nearly 2 demonstrating second-order accuracy.

indicating the scheme is second-order accurate.

6.1.2 Convergence of Subsonic Solutions

In this section, the convergence properties of the Newton iteration procedure will be numerically investigated. Consider again the solution presented above for the 32×8 grid. The converged solution is shown in Figure 6.4. To obtain this solution requires a finite number of iterations. In Figure 6.7, the norm of the residuals of the discretized Euler equations is plotted as a function of iteration number. Note the extremely fast convergence. This behavior is typical of the Newton iteration procedure. After four iterations, no further progress is made. Smoothing and round off errors prevent the solution from ever approaching the exact solution to the numerical equations. Nevertheless, this example demonstrates the extremely fast convergence to the final solution.

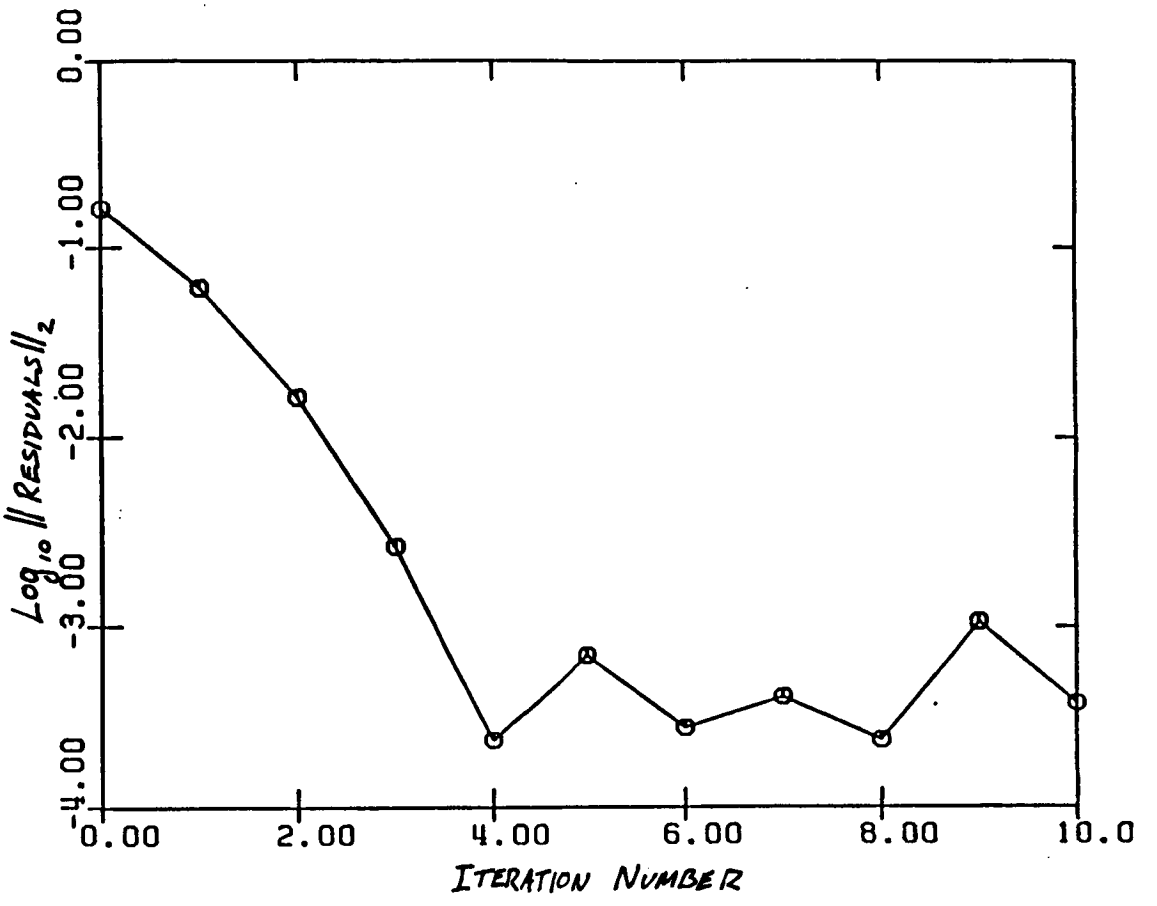

Figure 6.7: Convergence of subsonic flow solution. Plotted is the norm of the residuals of the discretized Euler equations at each iteration.

6.1.3 Steady Choked Flow in a Hyperbolic Channel

In this section, transonic (choked) flow in a hyperbolic channel will be considered. As with the subsonic case, the total pressure and density at the inlet is specified to be unity. Downstream, the static pressure is set to 0.85. At this back pressure, the flow will be choked. The flow becomes supersonic as it passes through the throat and "shocks down" aft of the throat. This test case is a good one for evaluating the shock fitting portion of the present method.

The shock is initially supposed to span the channel width at some somewhat arbitrary location. The grid is generated so that a double grid line is imposed at this shock. One iteration of the Newton procedure is run to obtain a new estimate of the solution along with a new estimate of the shock location. The grid is then altered so that the new shock grid lines are aligned with the new estimate of the shock position. The updated solution is extrapolated from the old grid to the new grid, and the entire procedure is repeated until it converges.

Figure 6.8 shows a typical convergence history. Shown are the Mach number contours and shock positions after each iteration. Note that the shock converges rapidly to its final position. This is somewhat easier to see in Figure 6.9 Shown in one channel are the shock positions after each iteration. Note that after the third iteration, the shock is nearly at its final converged position. Additional iterations produce shock positions which virtually overplot this one.

Figure 6.10 shows the total pressure in the channel. Note that ahead of the shock, where the flow is isentropic, the total pressure is constant. Downstream, however, there is some total pressure loss due to the shock. The contours of total density are aligned with the local streamlines. Note the gradient in the total pressure as one moves from the lower wall toward the upper wall. This gradient appears because the shock strength varies from one side of the channel to the other. The Mach number is higher at the top of the channel and hence the shock is stronger resulting in a larger total pressure loss. Note further that the shock is normal to the wall at both the upper and lower walls. Because oblique shocks turn the flow coming into the shock, the shock must be normal, or there must be another shock reflected off of the wall.

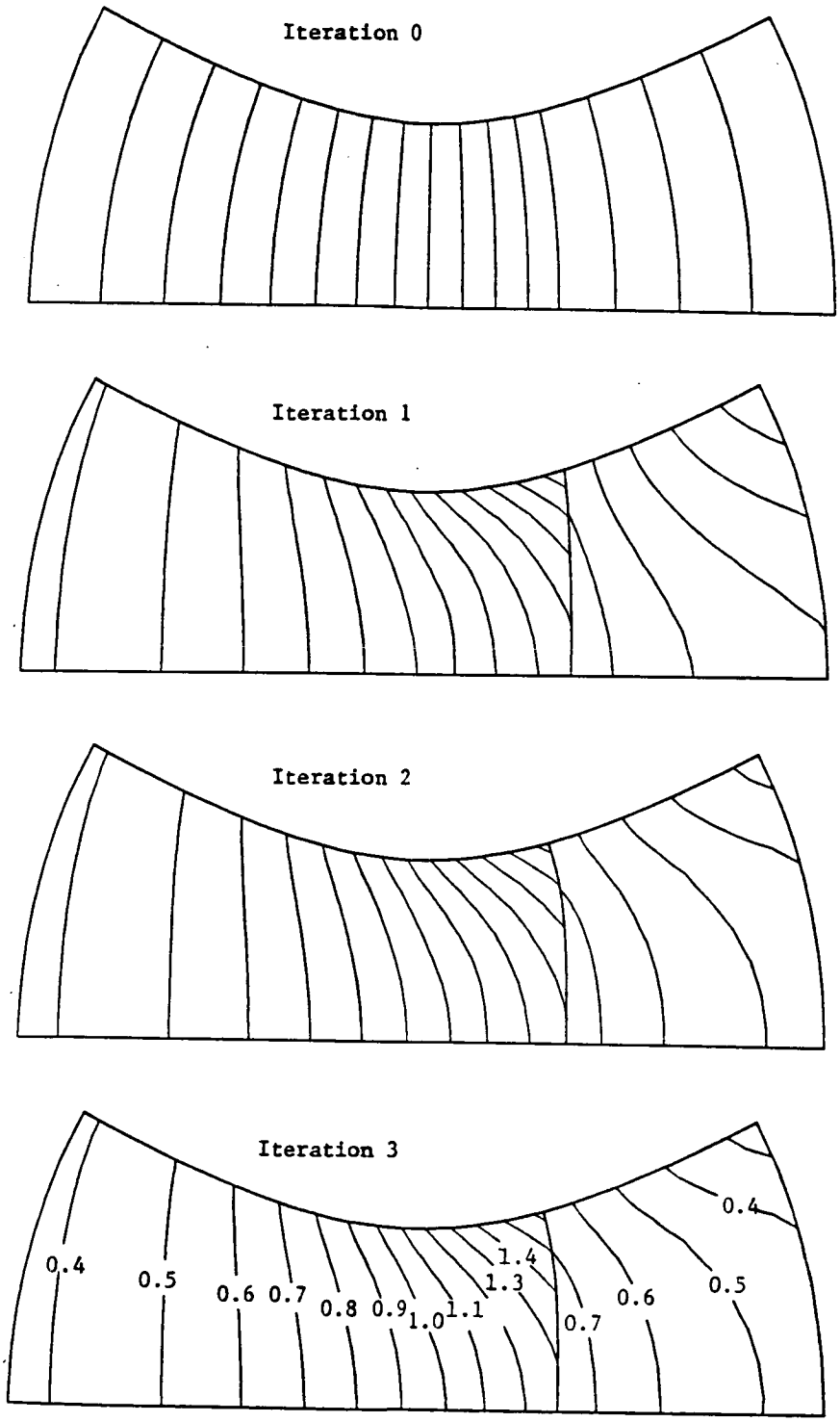

Figure 6.8: Convergence history of Mach number contours for choked flow problem. Note that convergence is extremely fast after the first few iterations.

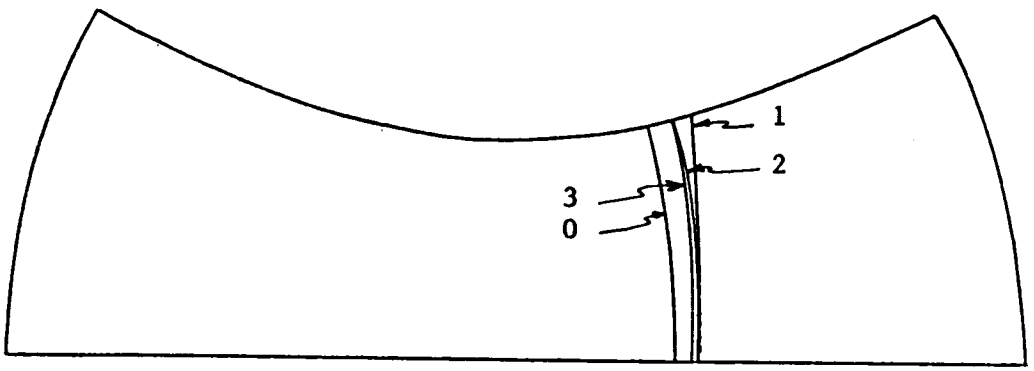

Figure 6.9: Convergence history of shock position. Position is converged after about three iterations.

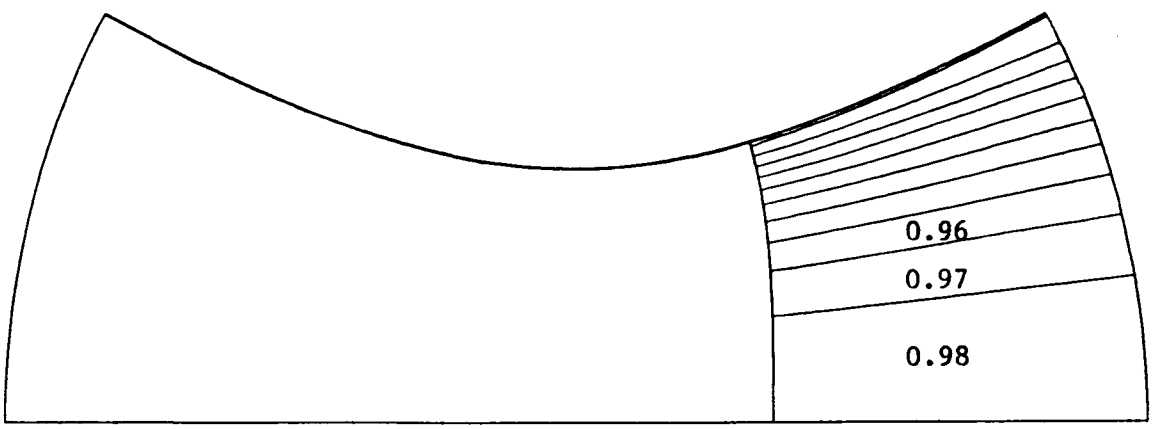

Figure 6.10: Total pressure contours in choked hyperbolic channel. Note that ahead of the shock, the total pressure is constant. Downstream, lines of constant total pressure follow streamlines. The shock is strongest along upper channel wall.

6.1.4 Effect of Grid Resolution on Shock Location

For Euler codes which use shock capturing to locate the position of the shock, a fine grid is needed in the vicinity of the shock to accurately position the shock. Recently, investigators have used adaptive gridding techniques to refine the grid around shocks [44,45]. Hence, fine grid resolution is used only where needed, making these schemes more efficient for a given level of desired accuracy. With shock fitting, however, the grid need not be extremely fine at the shock. To demonstrate this feature, the case presented in the previous section was computed on a 16×4, 32×8, and 62×16 grid. The converged computed solutions are shown in Figure 6.11. Note that even the coarsest grid gives good agreement with the fine grid solution.

More interesting is the predicted shock location. Shown in Figure 6.12 are the computed shock positions plotted in a single channel. Note that the computed shock positions for the 32×8 grid and the 64×16 grid are identical to within the thickness of the plotted lines. Even the coarse 16×4 grid computed shock position agrees extremely well with the other two solutions. Although the difference is perceptible, it is extremely small, considerably smaller than the size of the finest grid cells. This is an important result. Shock fitting provides an accurate estimate of the shock location even on coarse grids.

6.1.5 Unsteady Subsonic Flow in a Hyperbolic Channel

In the previous section, steady subsonic flows in a hyperbolic channel were analyzed. These solution are needed before one can calculate the unsteady flow since the full nonlinear equations are linearized about the steady solution. In this section, the unsteady flow in the hyperbolic channel will be examined. The steady flow is that first presented in Section 6.1.1. The flow is everywhere subsonic. The inlet total pressure and density are 1.0, while the exit static pressure is 0.92. The unsteadiness is introduced by perturbing the upstream total pressure and density while holding the downstream pressure constant. For the first case, the grid is a 32×8 cell grid. Upstream, the total pressure and density variations are 1.0 and 0.714 respectively. This choice of total pressure variation is the linearized approximation to an isentropic total pressure and

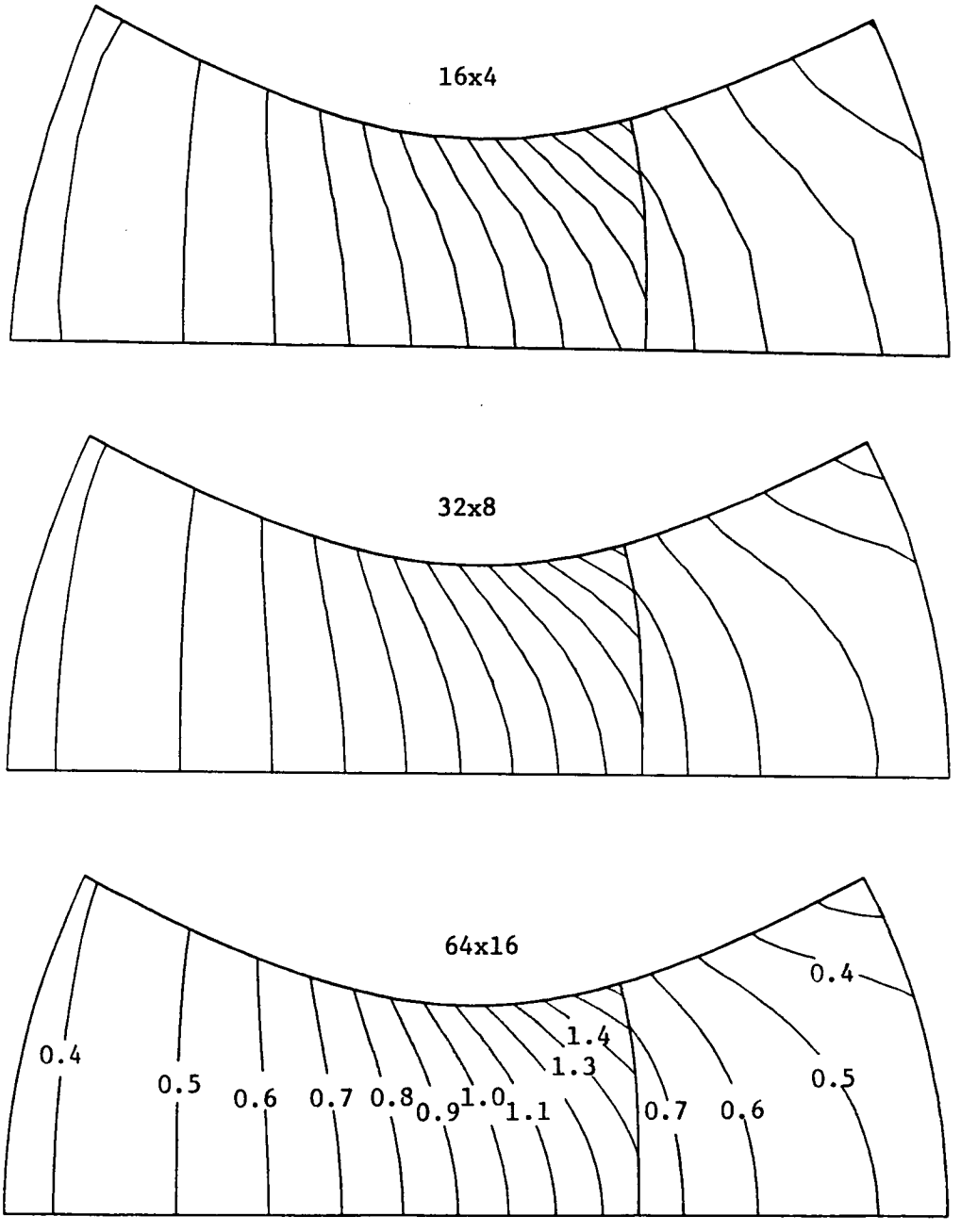

Figure 6.11: Effect of grid resolution on computed transonic flow solution in hyperbolic channel. Note that accurate solutions are obtained with fairly coarse grids.

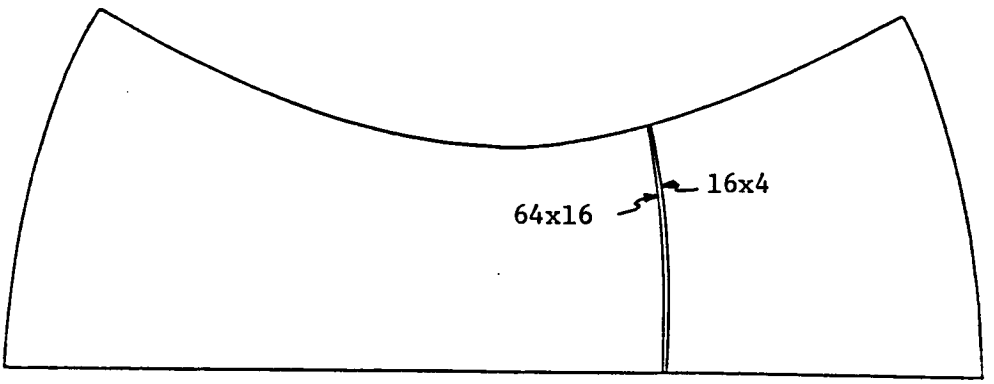

Figure 6.12: Effect of grid resolution on computed shock position. Note that the coarse grid gives essentially the same estimate of the shock location.

density variation. The frequency of this variation is 1.0.

Figure 6.13 shows the real part and imaginary part of the calculated pressure along the lower wall of the channel. Note that the unsteady pressure goes to zero at the exit of the channel as specified. Note also the amplification of the pressure at the throat of the channel. Unfortunately, there are no other known results with which to compare these results. In a later section, the present method will be used to compute the unsteady flow in another channel geometry. There, the present method will be compared to a time-marching Euler code.

6.1.6 Unsteady Transonic Flow in a Hyperbolic Channel

In the previous section, the unsteady subsonic flow through a channel was calculated. Although an interesting test case, it does not demonstrate the true strength of the linearized Euler method. Subsonic flows can be handled perfectly well using linearized full potential methods. To predict unsteady small disturbance flows with shocks, the linearized Euler method will give a more accurate representation of the actual flow. In

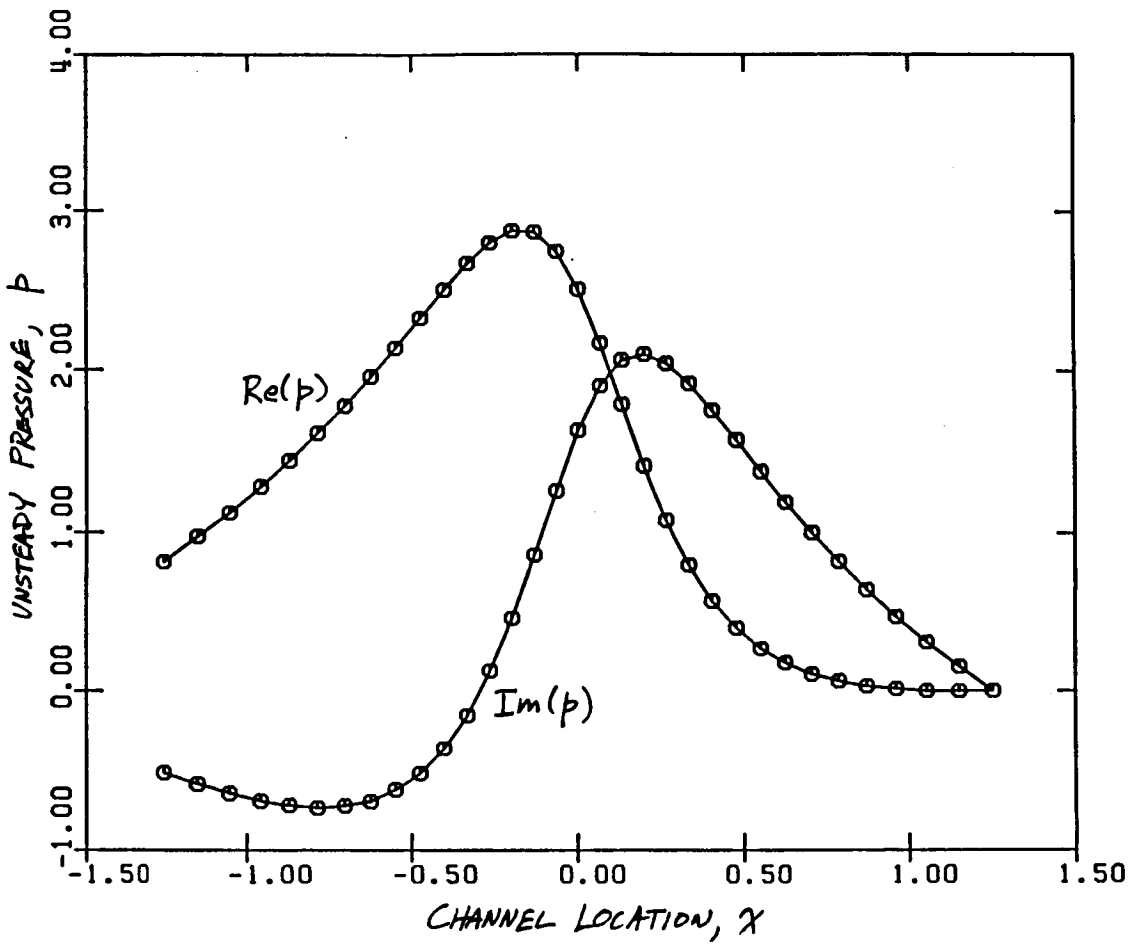

Figure 6.13: Unsteady pressure along lower wall for an upstream perturbation in total pressure and density. Forcing frequency ω is 1.0.

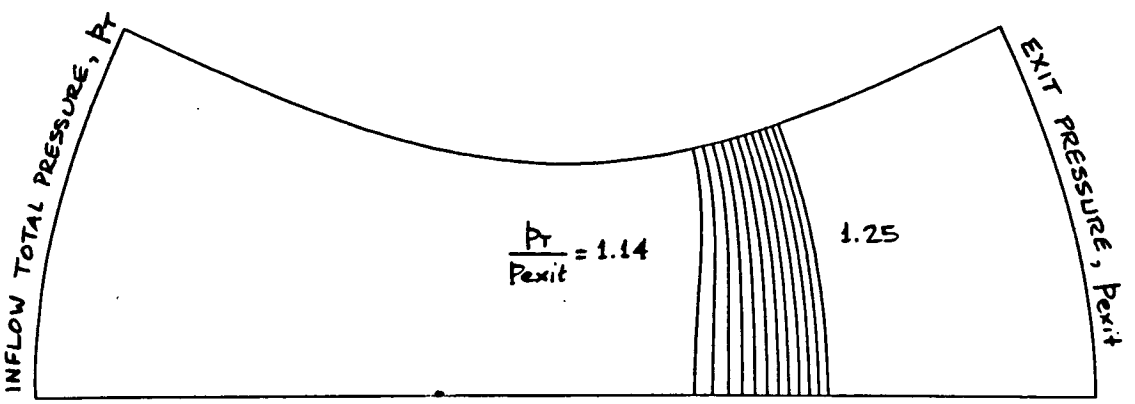

Figure 6.14: Shock position in channel for various levels of total inlet pressure to exit static pressure ratio.

this section some unsteady transonic flows will be considered.

Quasi-Steady Transonic Flow

Consider the full nonlinear but steady flow through the hyperbolic channel. As the back pressure is decreased (or the inlet total pressure is increased), the shock will move further back in the channel as shown in Figure 6.14. One can then consider the shock position as a function of the channel pressure ratio. Figure 6.15 shows the calculated steady shock position along the lower wall as a function of this pressure ratio. The slope of this curve is then approximately the distance the shock will be displaced for a small change in pressure ratio.

Returning to the unsteady theory, if the frequency of the inlet total pressure perturbation is small, then the unsteady shock motion will be in phase with the inlet total pressure perturbation, and the amplitude of the shock motion per unit total pressure ratio perturbation should equal the slope of the steady shock position versus pressure ratio curve. This provides a consistency check of the low frequency capabilities of the

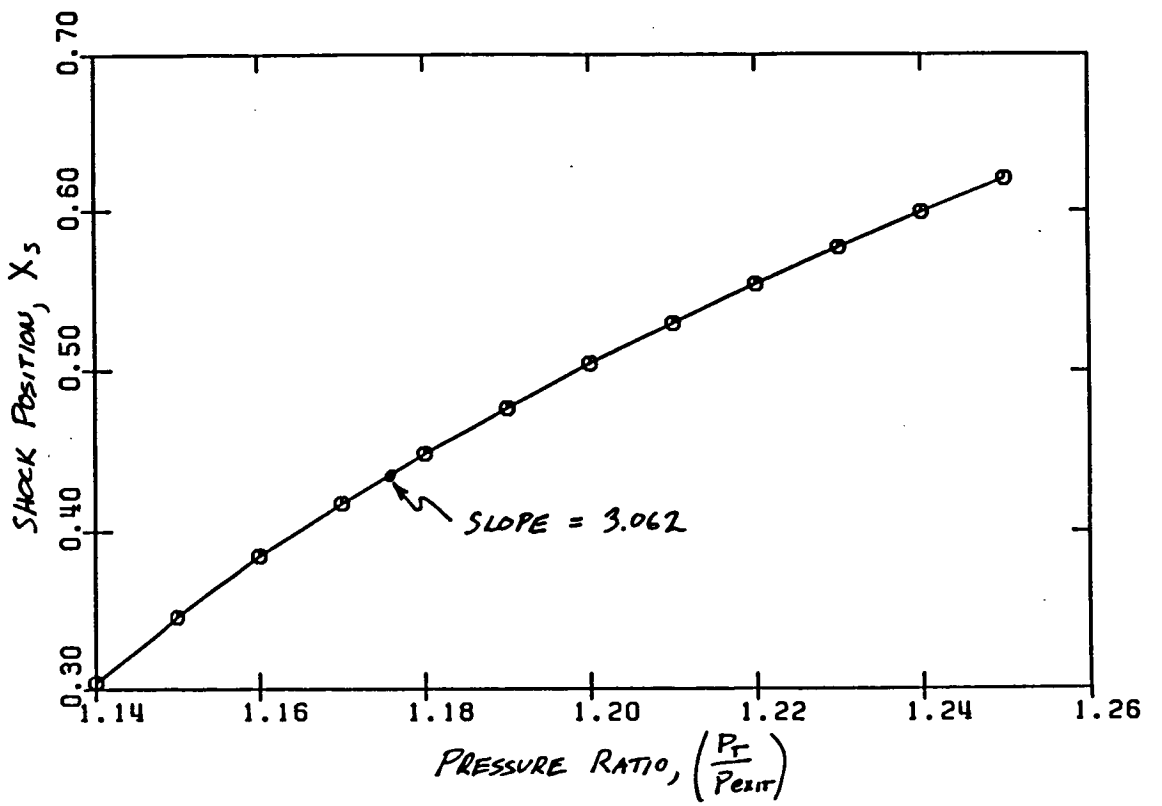

Figure 6.15: Shock position along lower channel wall as a function of total inlet pressure to exit static pressure ratio.

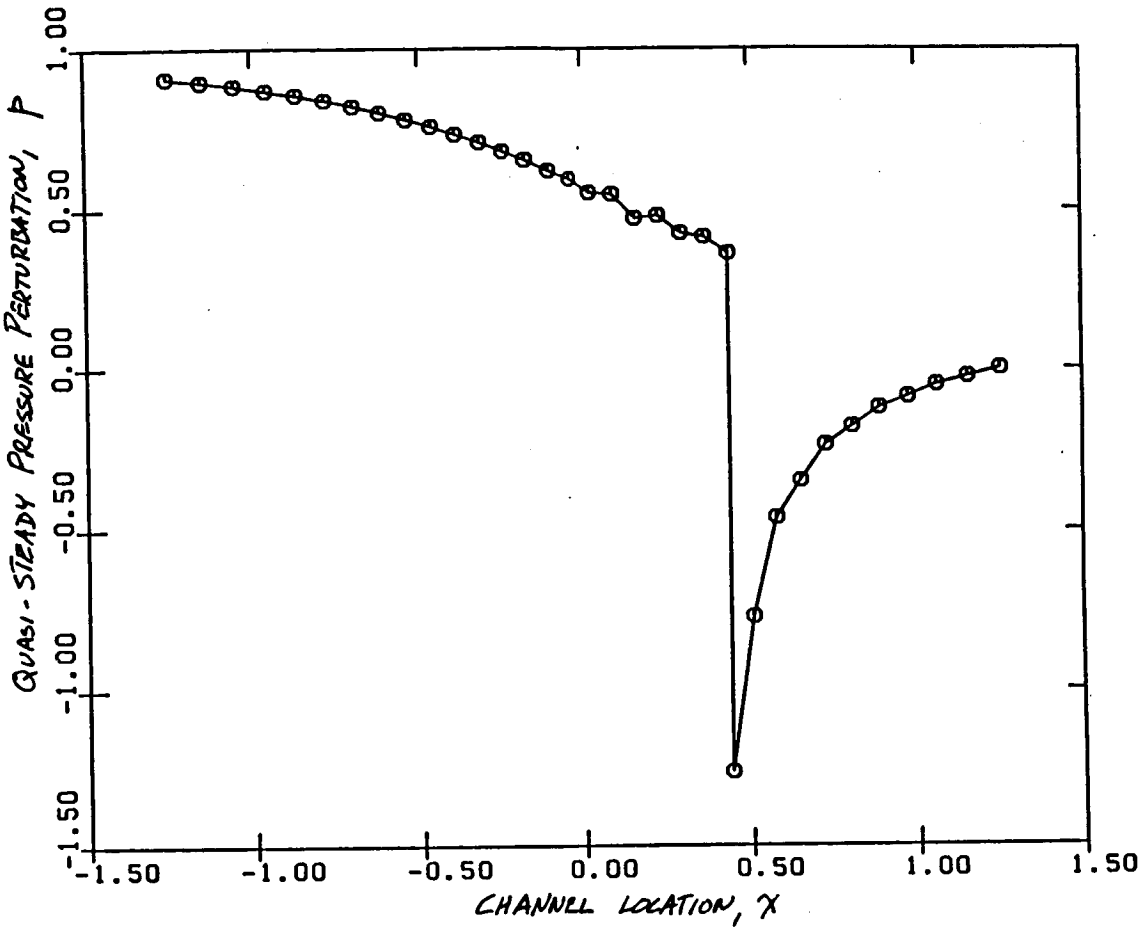

Figure 6.16: Quasi-steady pressure distribution in hyperbolic channel along lower wall for isentropic increase in inlet total pressure.

unsteady code. The steady flow of Section 6.1.3 was used as the base flow for the unsteady calculations. Recall that the steady inlet total pressure and density were set to unity while the static pressure was 0.85. For the unsteady calculations, the inlet total pressure perturbation was set to unity while the total density perturbation was set to 0.714. The excitation frequency was 0.0. Downstream, the static pressure was held constant.

Figure 6.16 shows the real part of the "unsteady" pressure distribution in the channel. Of course, the imaginary part is zero. The predicted shock displacement at the lower and upper walls is 3.598 and 2.436 respectively. Note that the upper part of the shock does not move as far as the lower part of the shock. This is because the Mach

number varies more quickly at the upper part of the channel. Hence, the change in shock strength per unit distance moved is stronger along the upper wall. This has the effect of restricting the shock motion more along the upper part of the wall. Also, the shock motion is finite. As obvious as this sounds, this is an important feature of the present method. The motion is finite because the unsteady shock strength is correctly predicted (for this case the quasi-steady motion) by the linearized shock jump conditions. This is not true of the linearized full potential methods. Because these methods assume an isentropic shock, there is no mechanism to fix the location of the steady shock in choked flows. Therefore, as the frequency becomes small, the shock motion becomes infinite. Said another way, the slope of the shock position versus back pressure curve is infinite.

As a consistency check, the slope of the shock position curve (Figure 6.15) for a steady inlet total pressure to exit pressure of 1.176 is 3.062. Next, it is observed that if the exit pressure is held constant, then

$$\frac{\partial X_s}{\partial (P_t/P_{\text{exit}})} = \frac{1}{P_{\text{exit}}} \frac{\partial X_s}{\partial P_t} \tag{6.3}$$

Hence, for an exit pressure of 0.85, the change in shock position per unit change in upstream total pressure is 3.602. The predicted shock motion using the linearized unsteady Euler theory at zero frequency is 3.598. This excellent agreement shows that the linearized unsteady theory is consistent with the nonlinear steady theory for very low frequencies. Next, truly unsteady (not quasi-steady) shocked flow will be considered.

Unsteady Transonic Flow

For this example, the unsteady boundary conditions are the same as for the quasi-steady example except that the excitation frequency is now 2.0. The calculated unsteady pressure distribution along the lower channel wall is shown in Figure 6.17. Note that at the exit of the channel, the unsteady pressure is zero as specified. This sort of boundary condition reflects incident waves. That is to say that waves moving downstream will reflect sending waves upstream through the channel.

Figure 6.18 shows the unsteady shock motion. Shown is the shock position at four different times in one complete cycle. Note three important features of the shock

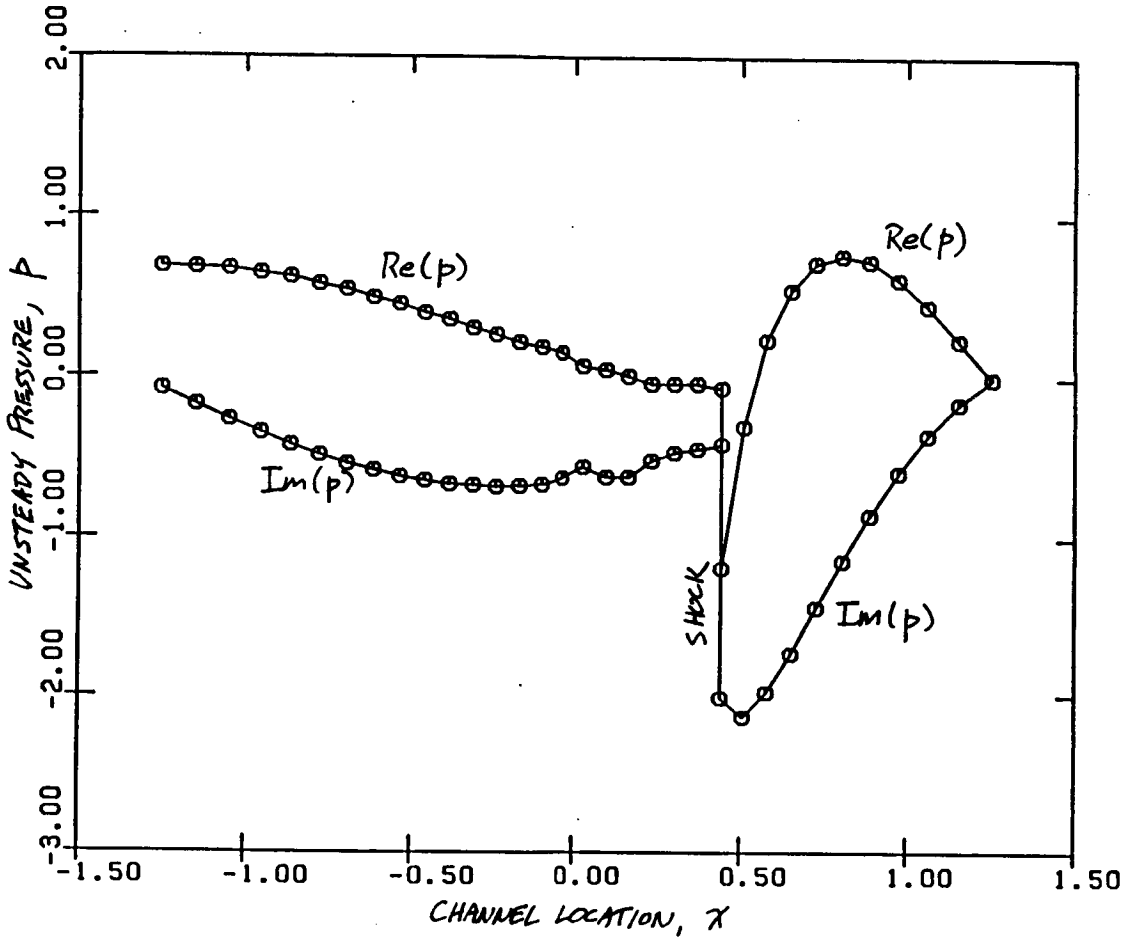

Figure 6.17: Unsteady pressure on lower wall of hyperbolic channel for upstream variation in total pressure and density. Forcing frequency ω is 2.0.

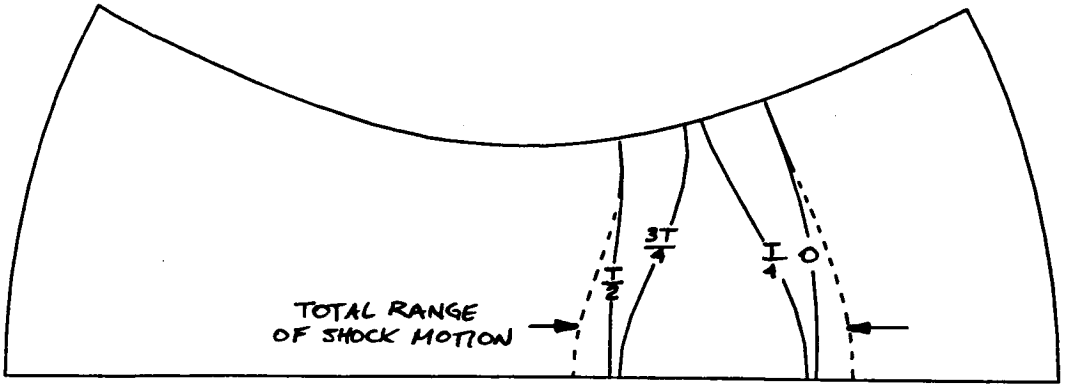

Figure 6.18: Unsteady shock motion at four times during harmonic cycle. Note that upper portion of shock leads lower part.

motion. First, the shock remains normal to the wall at all times. This is a necessary condition if the flow is to remain tangent to the wall. Secondly, the upper part of the shock does not move as far as the lower part of the shock. The shock is stronger at the upper wall and must move through higher Mach number gradients. This tends to restrict the motion of the upper part of the shock. And third, the upper part of the shock leads the lower part. This is a slightly more complicated feature. Along the upper wall ahead of the shock, the Mach number tends to be higher than along the lower wall. This means that the forward moving pressure and convection waves tend to arrive at the shock earlier at the upper part of the shock. Similarly, downstream of the shock, because of the higher total pressure loss along the upper wall, the backward moving pressure wave moves faster along the upper wall than along the lower. Hence, any reflected waves will arrive at the upper part of the shock more quickly than at the lower part. Both of these effects tend to cause the upper part of the shock to lead the lower.

6.2 Two-Dimensional Transonic Diffuser Flow

In this section, the steady and unsteady flow in a transonic diffuser will be examined. Steady and unsteady flows in this geometry have been numerically modelled [46] using

a time-accurate time-marching code. In this section, the results of the present method will be compared those obtained from the time-accurate time-marching Euler code. The advantage of a time-marching code is that it fully accounts for nonlinear effects in unsteady flow. Unfortunately, the number of time-accurate time steps needed to calculate the unsteady flow is dominated by the smallest computational cells in the domain. Hence, if the grid resolution is very fine to accurately model the moving shock behavior using shock capturing, the computational effort required to determine the unsteady flow will be great. As will be shown, even moderate levels of unsteadiness can be predicted accurately and efficiently using the linearized Euler method. Large levels of unsteadiness, however, produce highly nonlinear flows which cannot be represented in the linearized framework and are better analyzed using a time-marching technique.

The geometry of the diffuser is shown in Figure 6.19. Normalizing lengths by the throat height, the channel is 12.5 long, the inlet is 1.4114 high, and the exit is 1.5 high. Note in particular the gentle divergence of the channel after the throat. This will tend to make for large shock motions for low frequency inlet or exit disturbances.

Two flow conditions will be analyzed using the present method and the time-marching flux vector splitting method of Allmaras and Giles [46]. The first is simply a steady nominal flow through the channel. Upstream, the total pressure and density are specified. Downstream, the back pressure is given. For a low enough back pressure, a shock will form aft of the throat. The second flow to be considered is the same as the first except that the back pressure is varied harmonically in time. This causes the shock to move fore and aft in the channel.

6.2.1 Steady Diffuser Flow

Consider the steady flow through the diffuser. Upstream the total pressure and density are specified. Downstream the static pressure is specified to be 0.80 of the upstream total pressure. At this pressure ratio, the flow is choked and a shock forms downstream of the throat. The grid used to calculate the steady flow using the present method, and the grid used by Allmaras [47] to calculate the steady flow are shown in Figure 6.19. Because shock fitting is used in the present method, less resolution is

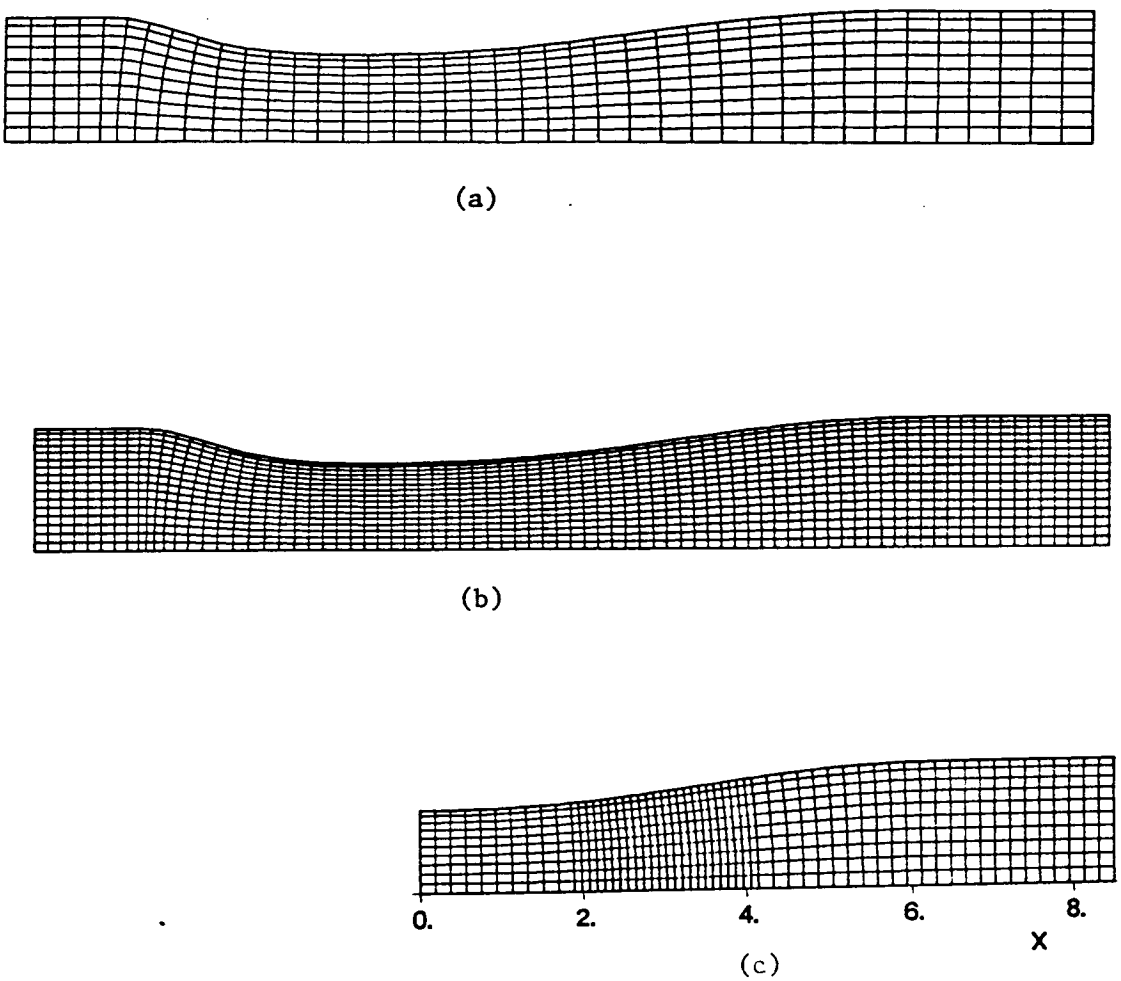

Figure 6.19: Grids used to calculate steady and unsteady flows in transonic diffuser: a) grid used with present method for both steady and unsteady flow calculations; b) grid used by Allmaras for steady flow calculations; and c) grid used by Allmaras for unsteady flow calculations.

needed to accurately model the shock. The grid used with the present method is 40×10 cells. Allmaras used an 80×16 cell grid.

The computed steady flow solutions for the two methods are shown in Figure 6.20. The Newton iteration procedure used in the present method converged in less than ten iterations. Note the generally excellent agreement between the two methods. The major difference between the two is the representation of the shock. Nevertheless, the fitted shock position found using the present method falls within the region of the smeared captured shock of the time-marching algorithm. Also, the total pressure loss after the shock agrees well for both methods.

6.2.2 Unsteady Transonic Diffuser Flow

In the second half of this example, unsteadiness is introduced by varying the downstream pressure sinusoidally in time. The mean pressure is the same as above and the amplitude of the pressure perturbation is 10 percent of the mean exit pressure. The reduced frequency of the forced excitation is 3.125 based on the sonic speed of sound and the diffuser length. For the unsteady calculation made using the present method, the same grid was used as for the steady calculation. Allmaras used a slightly different grid for his steady calculation which is shown in Figure 6.19. Note that there is a region of increased grid resolution downstream of the throat. This area roughly corresponds to the region over which the shock will move. The time-marching code was marched three periods of excitation to achieve a periodic solution. Because the two methods were run on different types of computers, it is difficult to compare CPU times precisely. A rough estimate, however, is that the time marching code required about 50 times more CPU time than the linearized Euler code.

The calculated pressure contours are shown side by side in Figure 6.21. Shown are the instantaneous pressure contours at eight points during a single cycle for the present method and the time-marching method. Note that although the contours are not identical, there is good qualitative agreement between the two methods. This can also be seen in Figure 6.22. Plotted are the instantaneous pressures along the lower wall at eight points in the cycle. Here it is seen again that qualitatively the two solutions

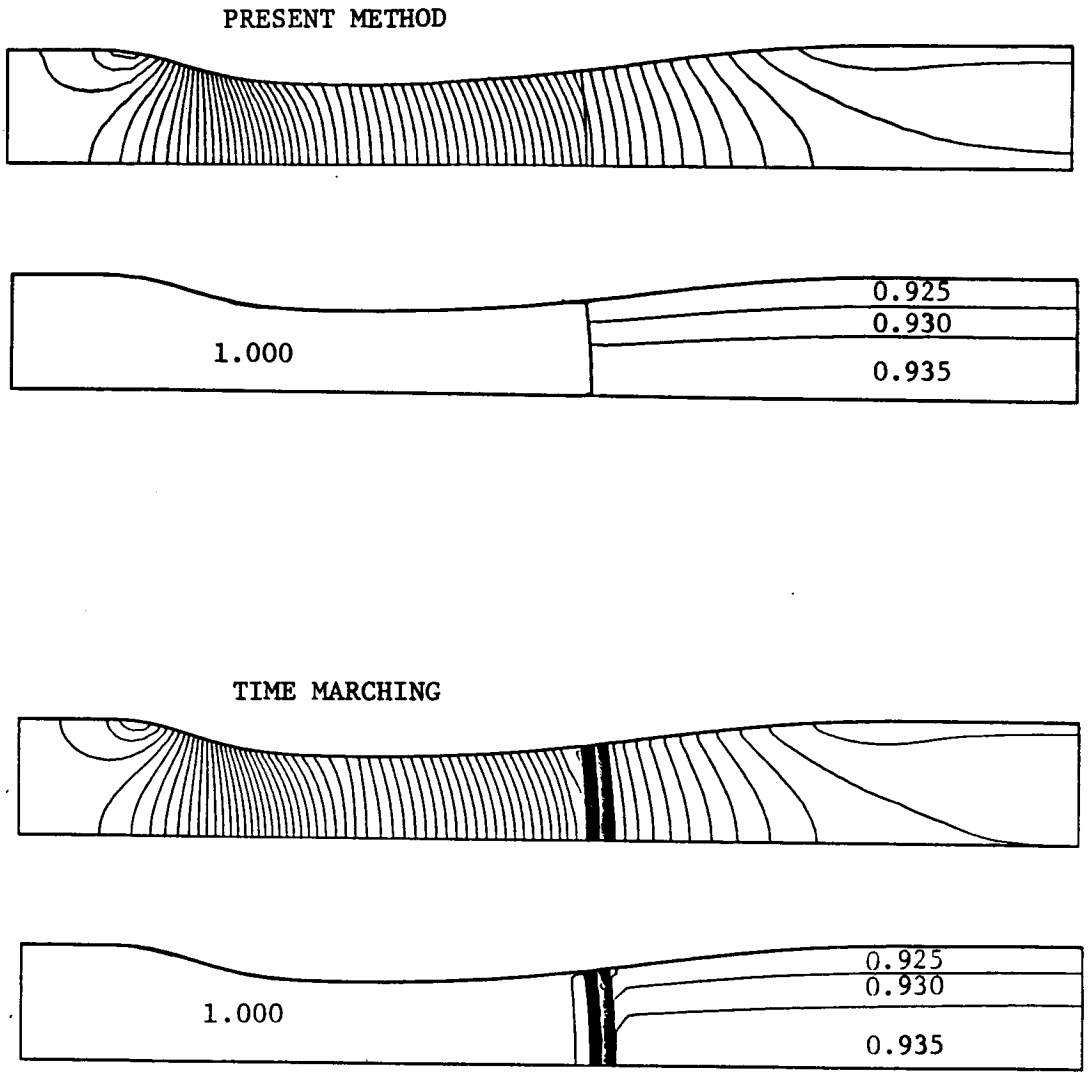

Figure 6.20: Steady Mach number and total pressure contours as calculated using present method and time-marching scheme. Note excellent agreement between the two solutions.

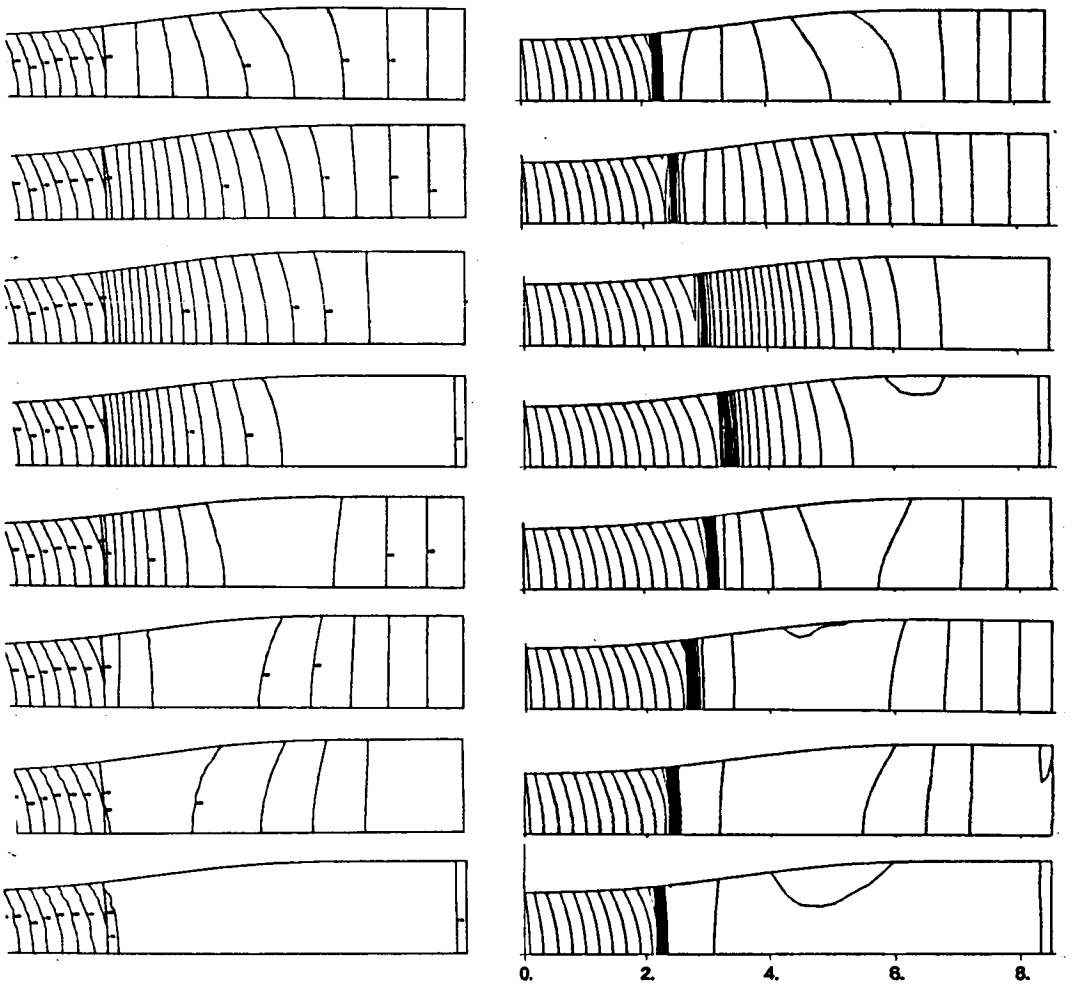

Figure 6.21: Instantaneous pressure contours at eight points in one cycle of unsteadiness: a) present method; and b) time-marching results. Note the good qualitative agreement if not in detail. Reduced frequency $\overline{\omega}$ based on sonic speed of sound and diffuser length is 3.125.

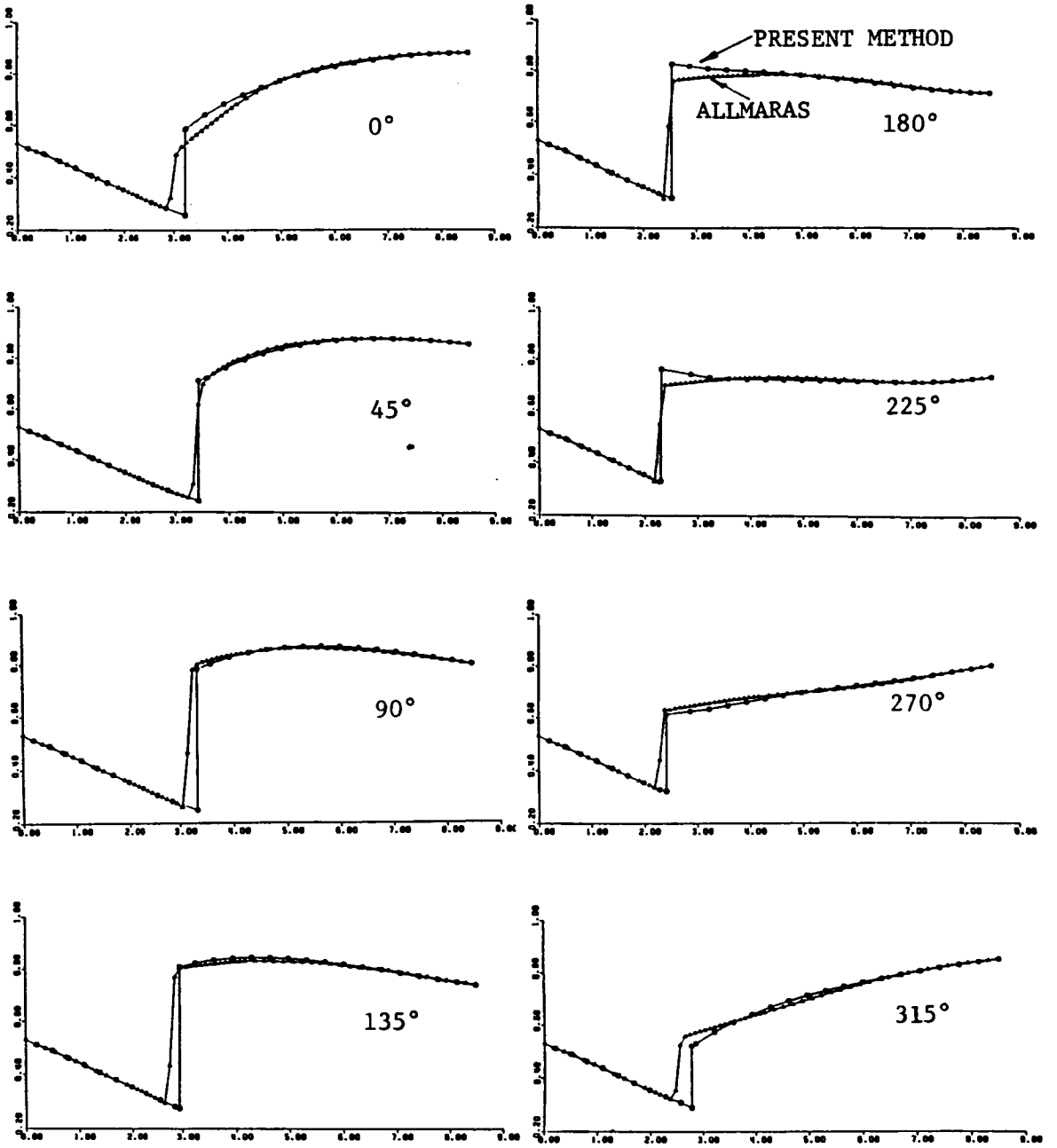

Figure 6.22: Instantaneous pressure along lower diffuser wall at eight points in one cycle of unsteadiness.

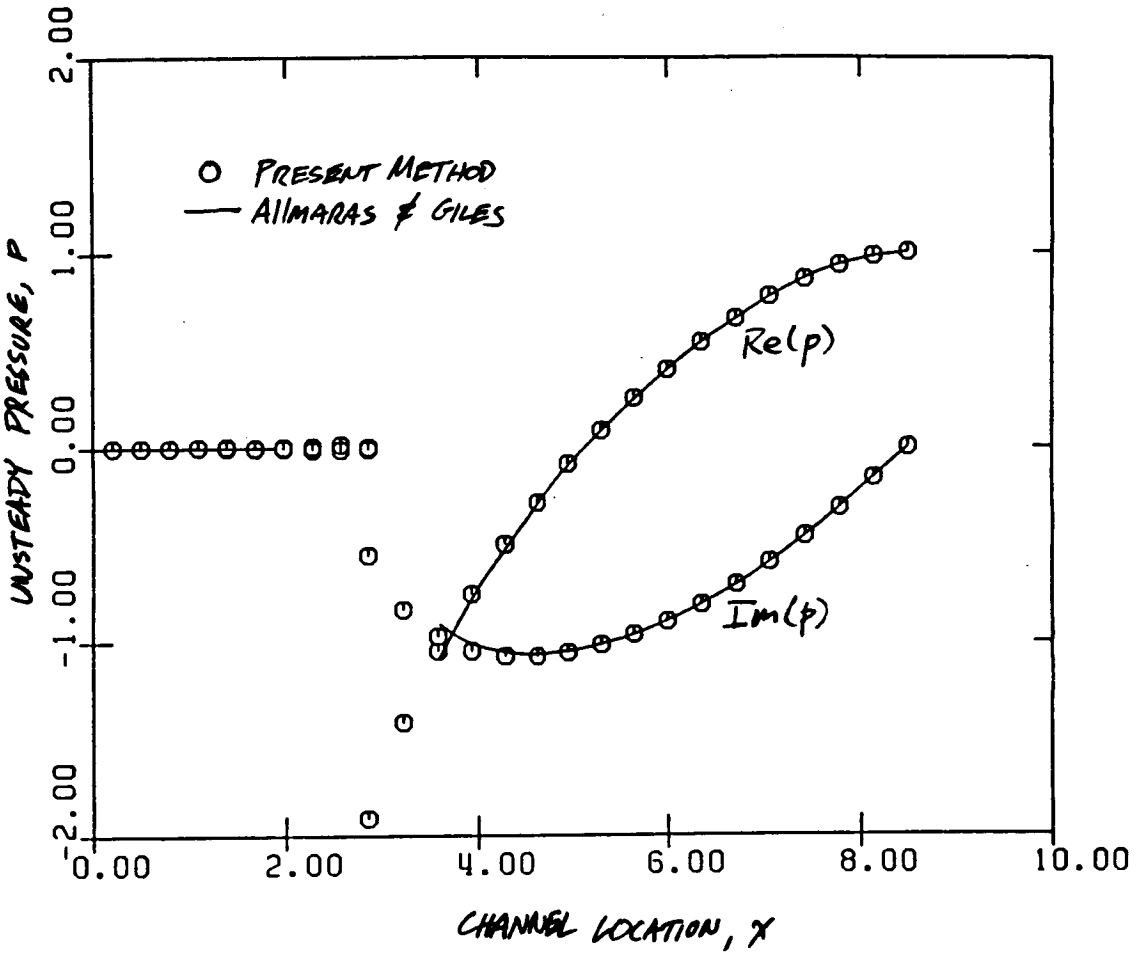

Figure 6.23: First harmonic component of unsteady diffuser flow. Note almost perfect agreement despite the fairly moderate level of unsteadiness in the diffuser.

agree with one another, but in detail they differ somewhat.

From these comparisons, one might say that the agreement is only fair. However, the differences between the two are dominated by the higher harmonic content which is predicted by the time-marching scheme, but are not accounted for in the linearized Euler method. The first harmonic of the time-marching solution agrees quite well with the linearized code. To demonstrate this, the time marching results were Fourier transformed to extract the first harmonic content. The first harmonic component of the solution is plotted in Figure 6.23 along with the linearized Euler solution. Notice the almost exact agreement between the two theories. Hence, if one is mainly interested in the fundamental frequency component, the linearized Euler method will give good

results at moderate levels of unsteadiness.

For moderate levels of unsteadiness (say 10 percent) in the flow, the linearized Euler method gives an accurate description of the first harmonic content of the flow in the diffuser. For a higher level, however, the unsteadiness will be too large to be handled within the framework of linearization. As an example, consider the case were the variation of the back pressure is increased to 20 percent of the mean flow. The resulting flow as calculated by Allmaras and Giles [46] is shown in Figure 6.24. Notice that the shock forms toward the rear of the channel and moves forward toward the throat. It weakens and nearly disappears as a new shock is forming. Not only is the shock motion not sinusoidal, it is not even continuous. Such cases clearly cannot be analyzed using the linearized Euler method.

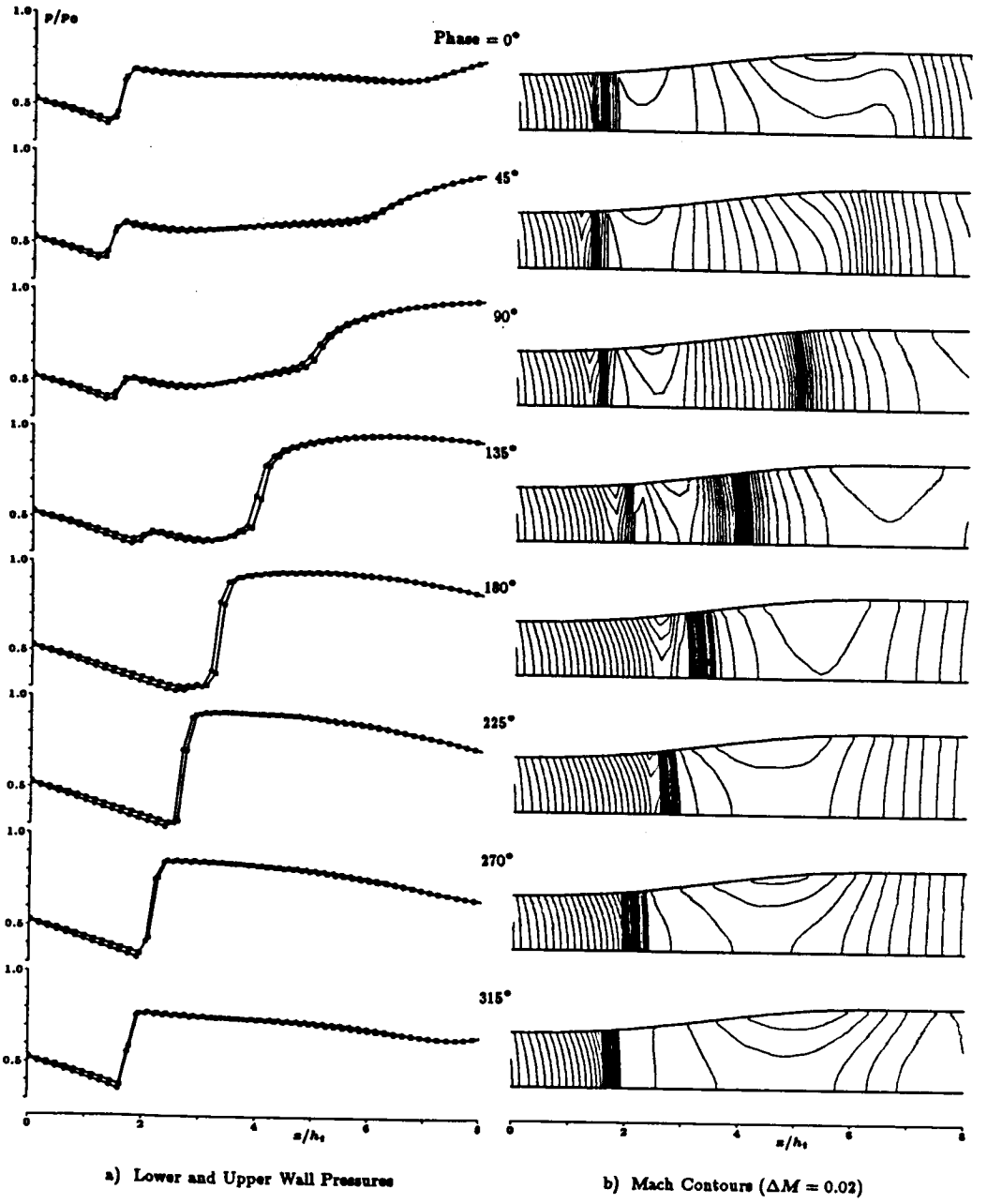

Figure 6.24: Diffuser flow variation due to a sinusoidal exit pressure excitation of 20% amplitude and reduced frequency of 3.125. The mean exit pressure to inlet total pressure ratio is 0.80. From [46].

6.3 The Gostelow Cascade

The next geometry considered is that of a cascade of Joukowski airfoils. The steady incompressible flow through this two-dimensional cascade has been examined by Gostelow [48] using a conformal transformation technique. The unsteady incompressible flow has been analyzed by Atassi and Akai [3,4] using a semi-analytical technique. Therefore, since steady and unsteady solutions exist for this geometry, it is a useful test case with which to evaluate the present linearized Euler method. First the steady flow through the cascade will be calculated using the present method. Then several different unsteady flow problems will be examined. These include unsteady flow due to the torsional vibrations of airfoils, and those due to incident vortical and entropic gusts.

6.3.1 Steady Flow Through the Gostelow Cascade

In this section, the present method is used to calculate the steady flow through the Gostelow cascade. An 80×16 node grid was generated for a single blade passage using a mixed algebraic and elliptic grid generator. The initial grid for the steady calculations is shown in Figure 6.25. The grid generator used is based on the elliptic grid generation technique of Thompson, Thames, and Mastin [49]. The grid is generated using this technique and then, in a post processing step, the grid is modified algebraically. For example, the part of the grid aft of the trailing edge was algebraically generated. Note that the normal grid lines are straight. This simplified the wake fitting somewhat. Ahead of the the airfoil, the elliptically generated grid was modified by fanning out the streamwise grid lines algebraically so that the nodes along the upstream far-field boundary are uniformly spaced. This improves the performance of the upstream far-field nonreflecting boundary conditions. The quality of the grid will often determine the quality of the computed solution as much as the computational method itself. To get good solutions with moderate grid resolution required that grid points be clustered in regions of high flow gradients. Figure 6.26 shows the grid clustering around the leading edge.

The boundary conditions for the steady flow problem are as follows. Upstream of the cascade the total pressure and density were specified to be unity. The incoming flow

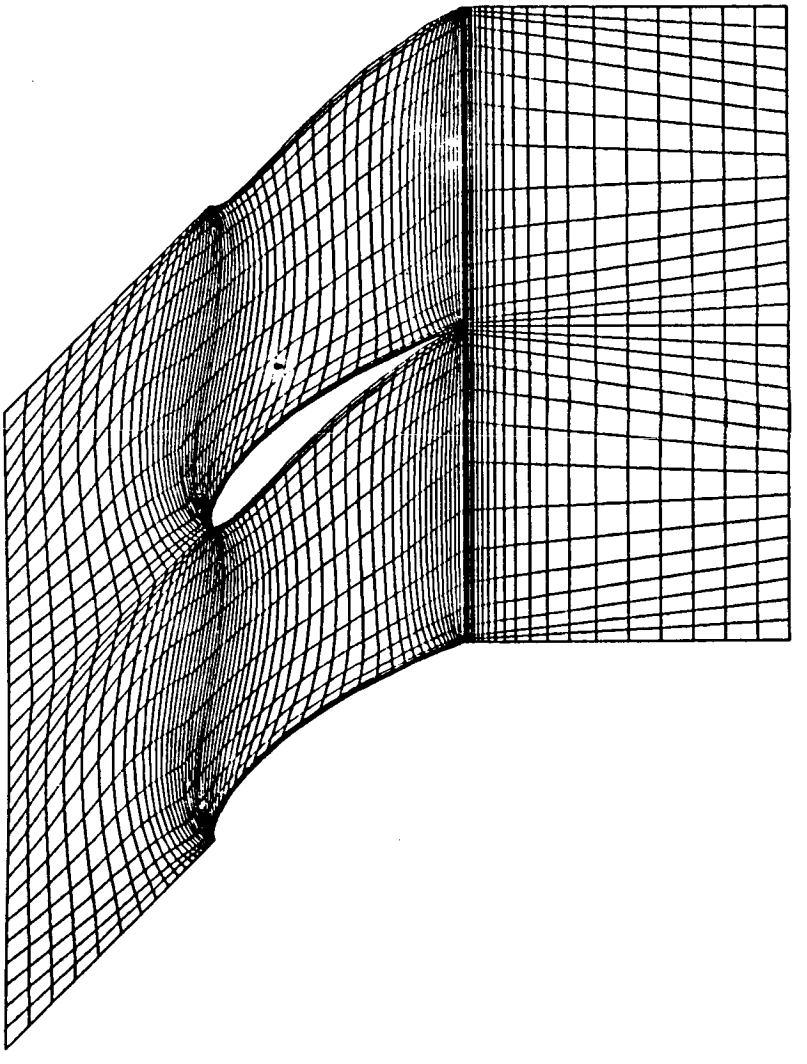

Figure 6.25: Initial grid used to calculate steady flow in Gostelow cascade. Note initially the wake is assumed to be aligned in the axial direction.

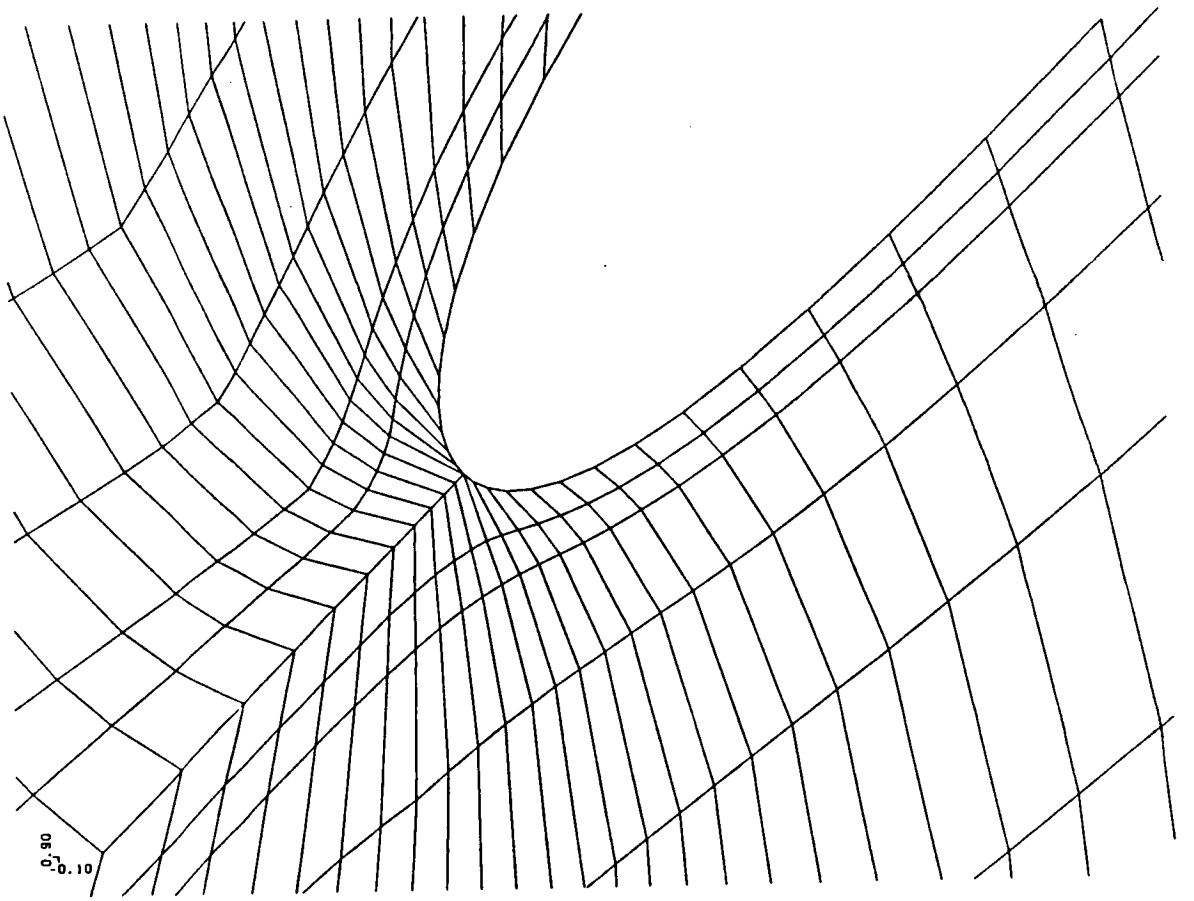

Figure 6.26: Expanded view of the grid around the leading edge of the Gostelow airfoil. High grid resolution is needed in this area to achieve good computational results.

angle was specified to be 53.5 degrees with respect to the axial direction, or 16 degrees with respect to the blade chord. Downstream, the static pressure was specified to be 0.98. This means the downstream Mach number is 0.170.

The Newton solver was used to calculate the steady flow. Shown in Figure 6.27 are the computed steady Mach number contours for this case. Note that the highest Mach number is about 0.34. Hence, the flow is somewhat compressible. Shown in Figure 6.28 are the total pressure contours. Because the flow is nominally isentropic, the total pressure should be 1.0 throughout the domain. The maximum total pressure error for this case is about 0.01. Because the flow is somewhat compressible, the computed solution cannot be compared to the analytic solution of Gostelow [48] directly. However, by using the Prandtl-Glauert transformation, the computed solution can be corrected so that it more closely approximates the incompressible solution. The result is shown in Figure 6.29 along with the analytical solution. Note the good agreement between the two solutions.

Because wake fitting is used in the present method, the converged grid (shown in Figure 6.30) is different from the initial grid. Note that the streamwise grid line starting at the trailing edge of the airfoil lies along the computed wake position. The computed outflow angle is 29.65 degrees compared to the 30.02 degrees found by Gostelow. Shown in Figure 6.31 is a blowup of the trailing edge region of the grid. Note that the wake departs the trailing edge of the airfoil at the metal angle and then turns upward slightly to its final outflow angle.

6.3.2 Unsteady Flow in the Gostelow Cascade

In this section, three types of unsteady flows will be considered. First, the unsteady flow induced by the motion of the airfoils will be considered. This is the flutter problem. The goal is to determine the unsteady pressure felt by the blades due to this prescribed airfoil motion. Next, two gust response problems will be considered. The first is a vortical gust due to an upstream obstruction. The second is an entropy gust.

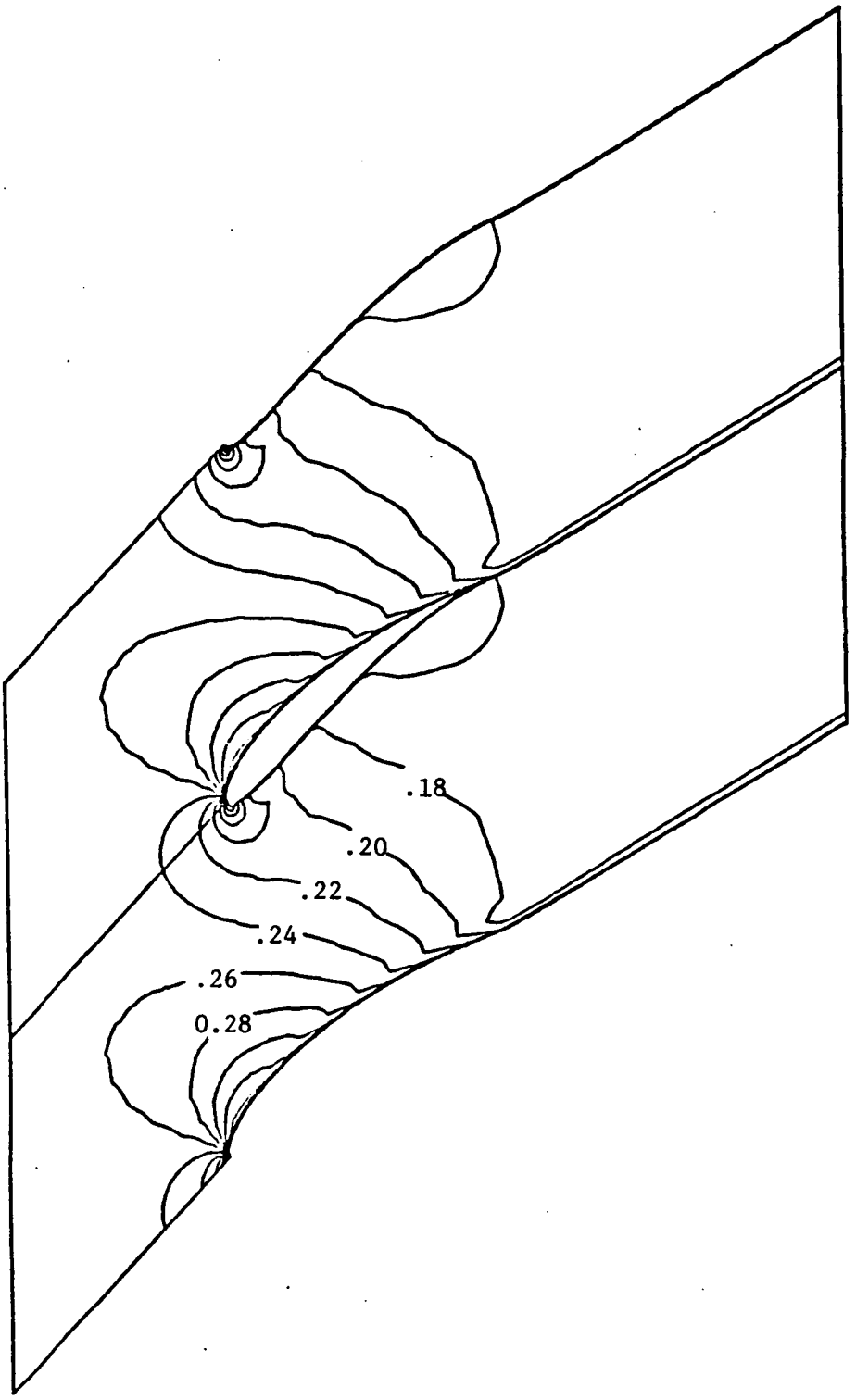

Figure 6.27: Steady flow Mach numbers for Gostelow geometry.

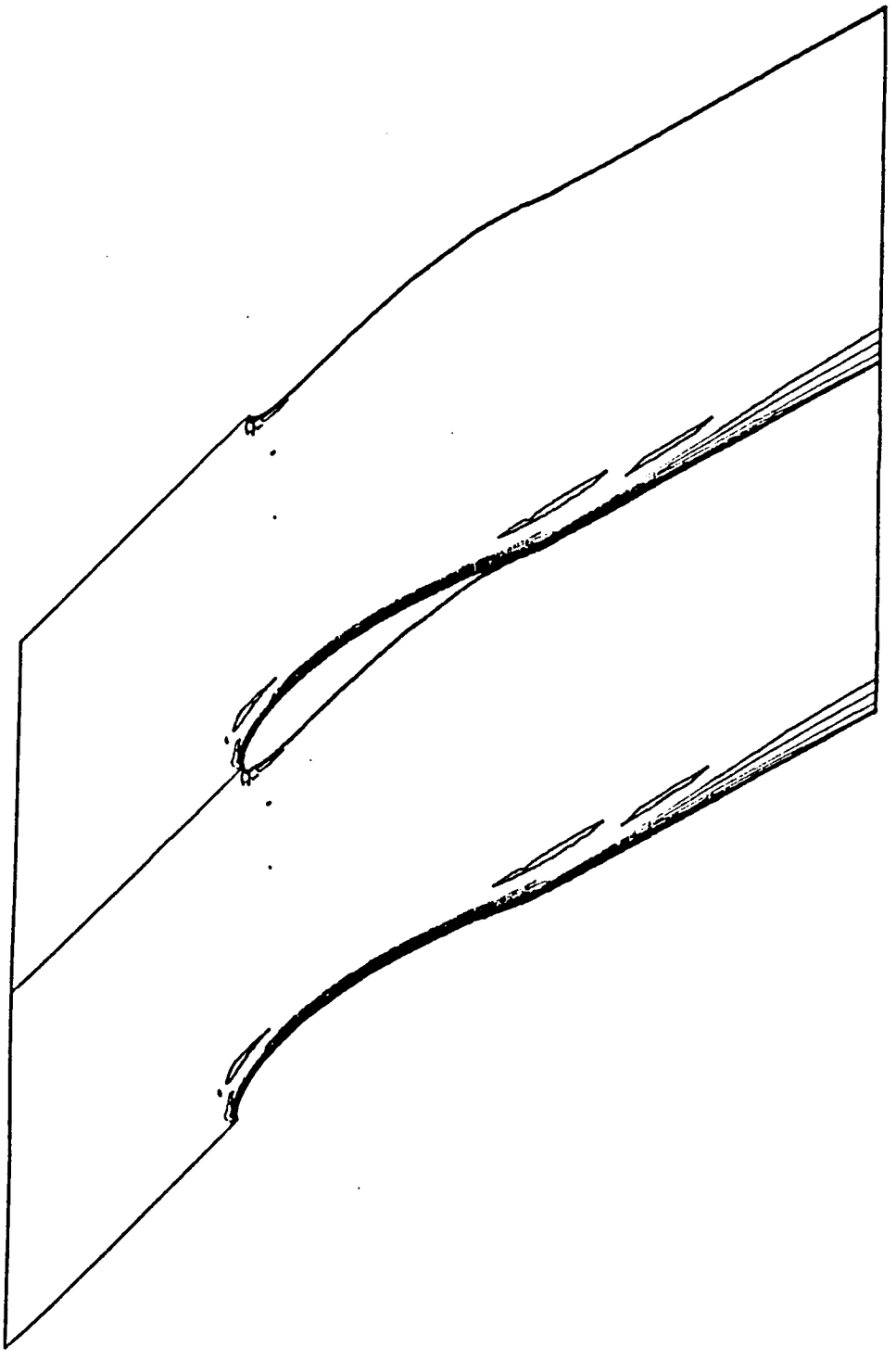

Figure 6.28: Steady flow total pressure contours. Note total pressure is nearly constant everywhere except close to the airfoil and wake surface.

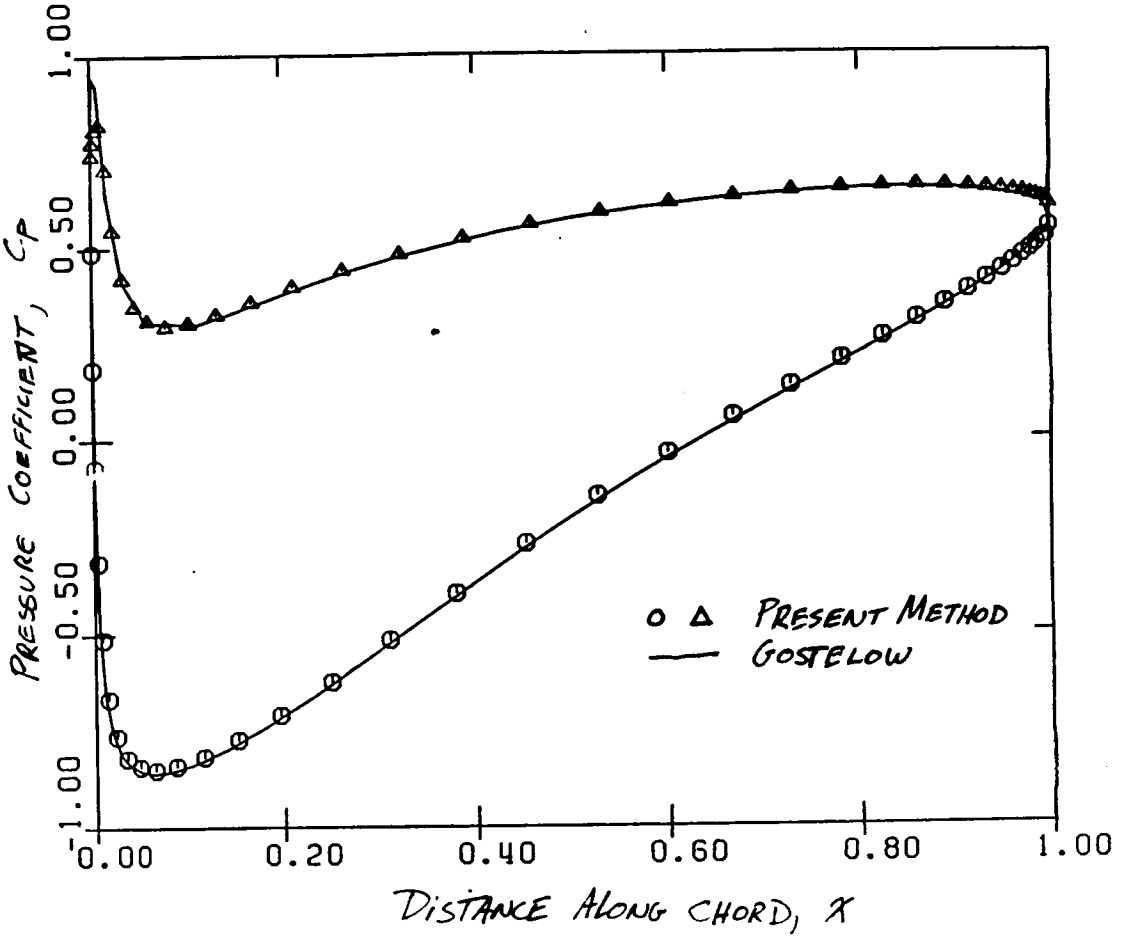

Figure 6.29: Pressure along surface of airfoil. The Prandtl-Glauert correction was used to convert the calculated compressible flow pressure coefficient to the incompressible equivalent.

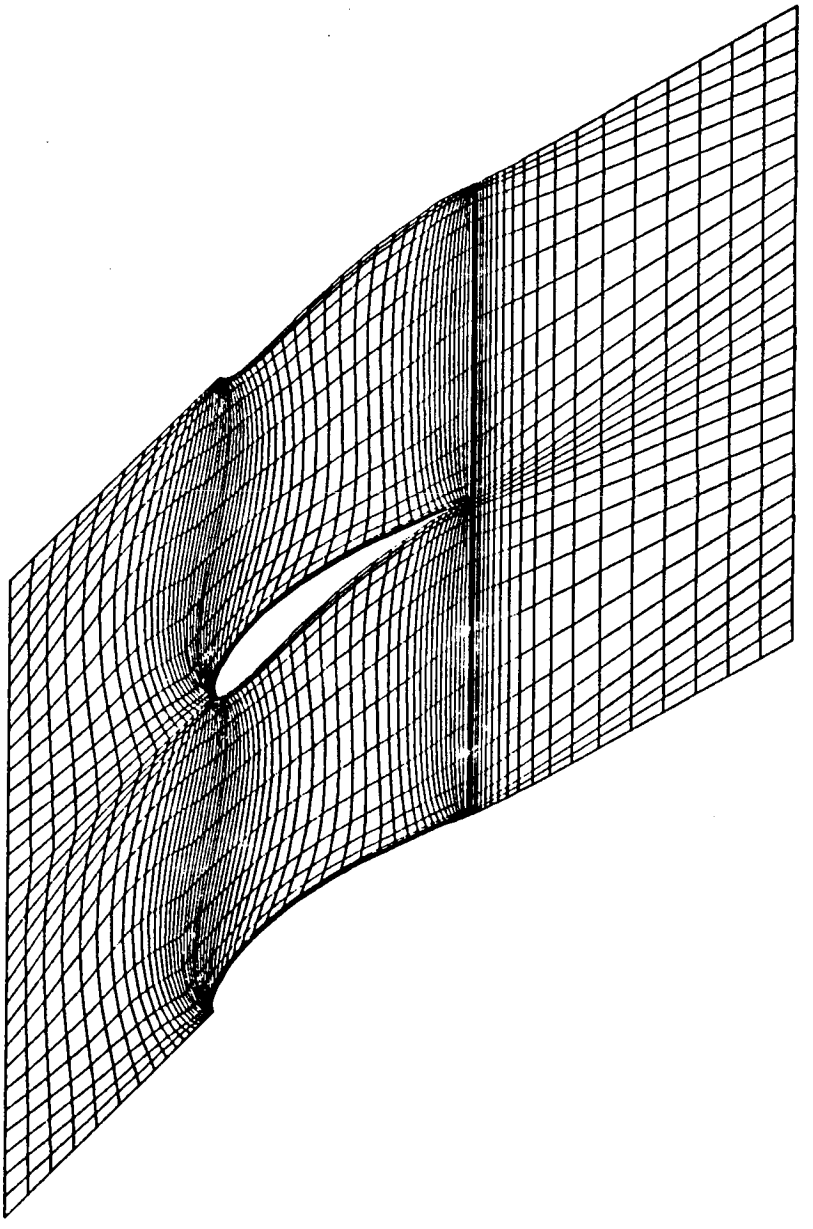

Figure 6.30: Converged Gostelow cascade grid. As part of the wake fitting method, aft part of grid is modified so that trailing edge grid line is aligned with wake. Calculated exit flow angle is 29.65 degrees.

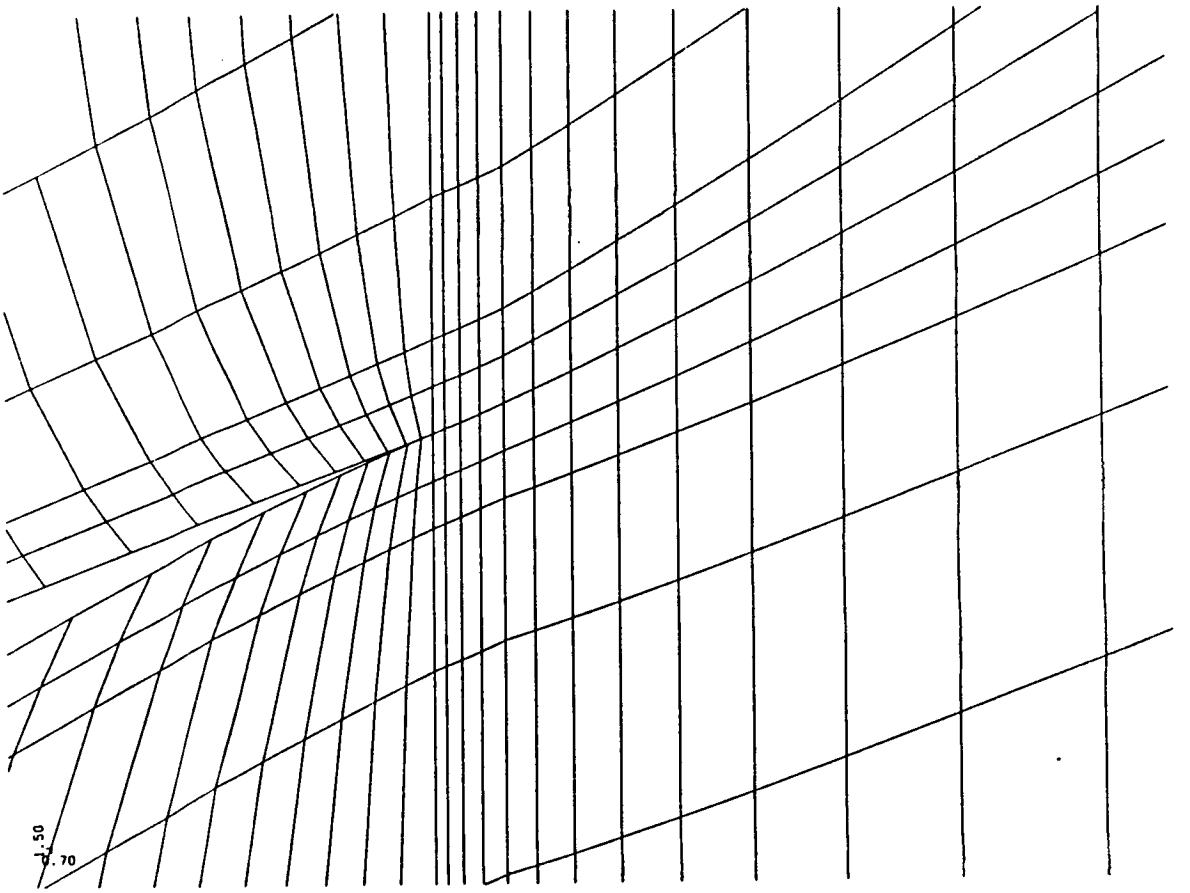

Figure 6.31: Expanded view of trailing edge region of airfoil. Note the curvature in the wake.

Aerodynamic Response Due to Torsional Vibration

For the first example, the unsteady flow induced by a cascade of vibrating airfoils is considered. The airfoils are assumed to vibrate in torsion about their midchords with a reduced frequency $\overline{\omega}$ of 0.40 based on chord and upstream velocity. (The reduced frequency is given by $\overline{\omega} = \omega c/V_{-\infty}$.) This problem was analyzed using the present linearized Euler analysis. The calculated unsteady pressure distribution on the surface of the airfoils is shown in Figures 6.32 and 6.33. Because of the difficulty in implementing the mean flow gradient terms described in Chapter 5 needed to extrapolate the boundary conditions from the mean blade location to the instantaneous blade location, these terms were "switched off" in the present analysis. This example was also analyzed by Atassi and Akai [3] using a semi-analytical technique that they developed to analyze incompressible flows. These results are also shown Figures 6.32 and 6.33. Note the generally good agreement between the present method and the results of Atassi and Akai.

Shown in Figure 6.34 are the real and imaginary parts of the unsteady pressure contours. Note, in particular, two important points. First, because of the low reduced frequency, the unsteady pressure is nearly real. That is to say that the flow is nearly quasi-steady. The real part of the flow is then primarily due to the upwash induced by the rotation of the airfoil. The imaginary part is due to the velocity of the airfoil surface which is small since it is proportional to the reduced velocity. Secondly, note the behavior of the real pressure contours near the upstream far-field boundary. This smooth behavior is due to the nonreflecting boundary conditions.

This same case was next solved for a range of interblade phase angles. Shown in Figure 6.35 is the imaginary part of the unsteady moment felt by the airfoil as a function of interblade phase angle. If the imaginary part of the moment is positive, then work is done on the blade over one complete cycle. Hence, the torsional blade vibration will grow and flutter will occur. Note that for interblade phase angles between 0 and 100 degrees, the present method predicts that flutter will occur. These results, although not in exact agreement with the results of Atassi and Akai, do show similar trends.

Atassi and Akai later included the mean flow gradient terms in their analysis [4] and

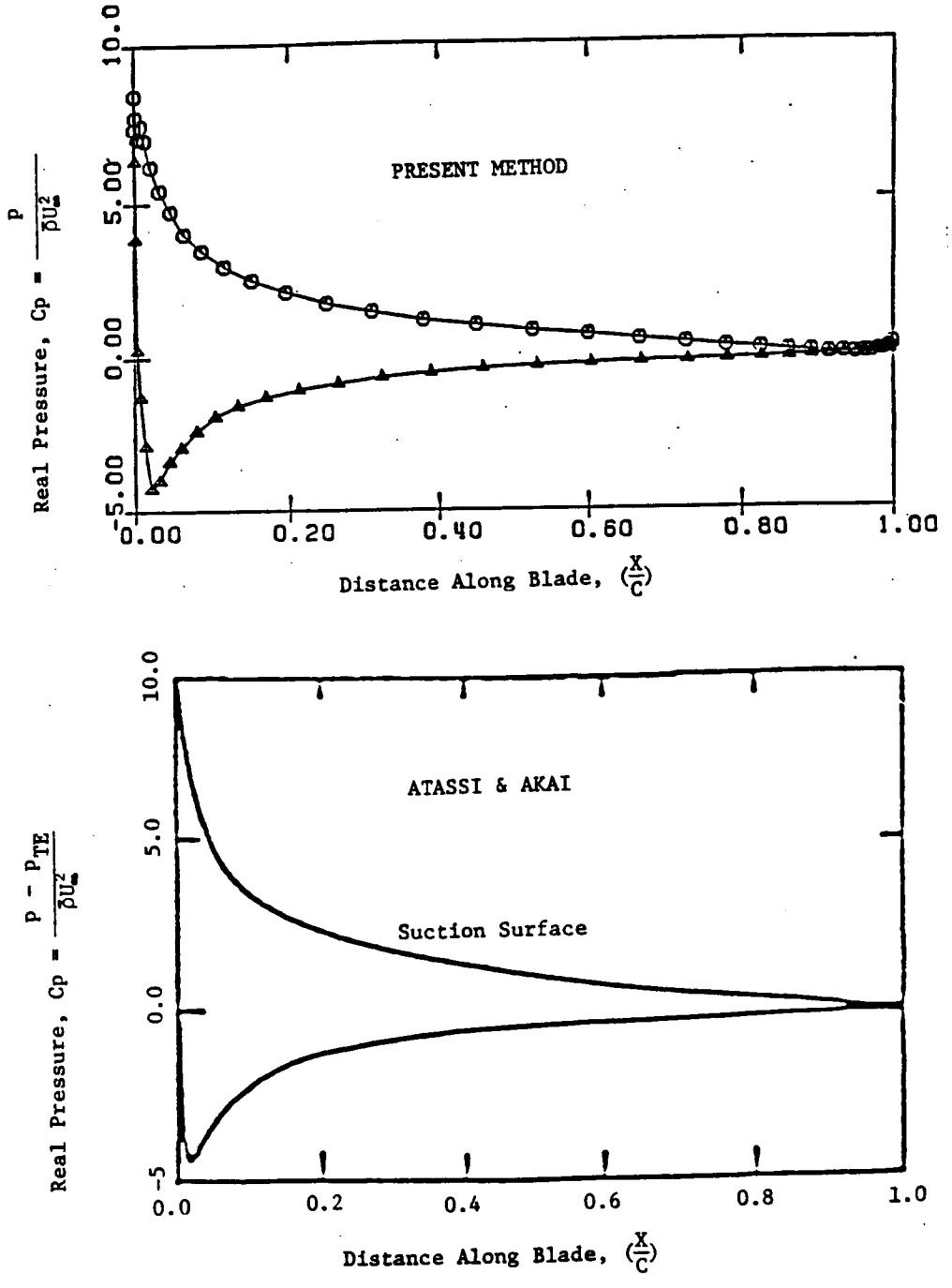

Figure 6.32: Real part of unsteady pressure on the surface of a pitching airfoil. Reduced frequency $\bar{\omega} = 0.4$, interblade phase angle $\sigma = \pi$. Lower plot is from [3].

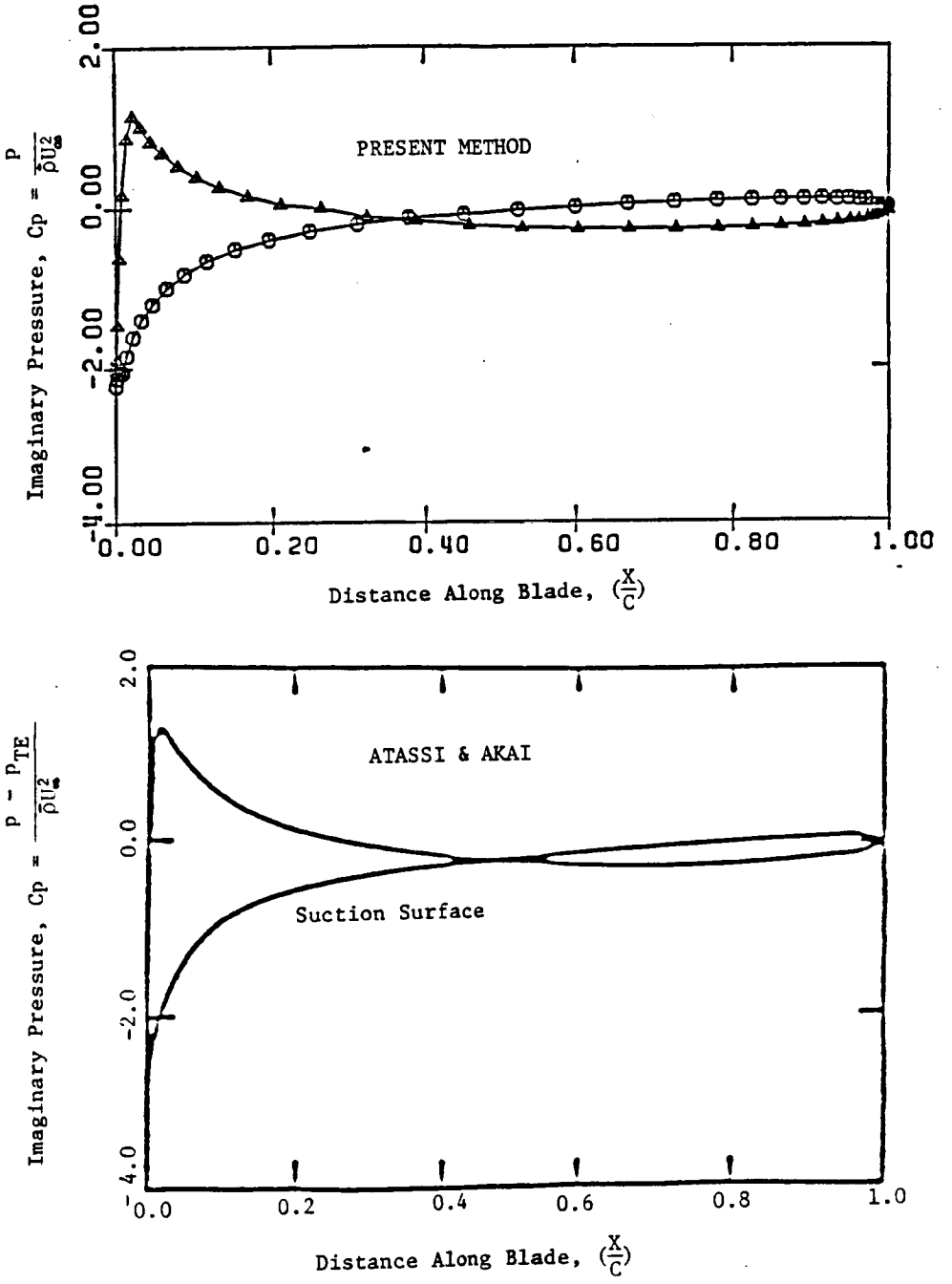

Figure 6.33: Imaginary part of unsteady pressure on the surface of a pitching airfoil. Reduced frequency $\overline{\omega} = 0.4$, interblade phase angle $\sigma = \pi$. Lower plot is from [3].

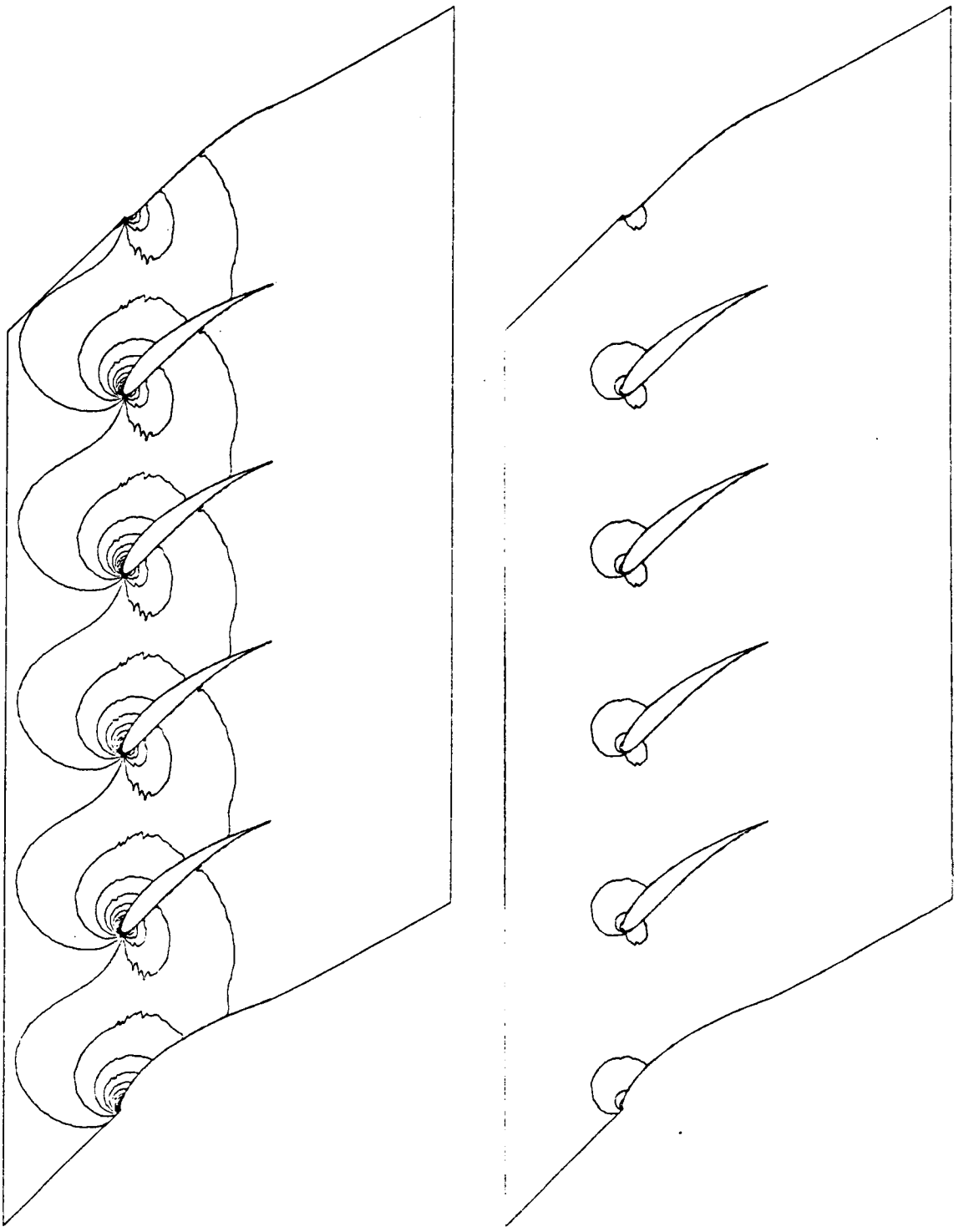

Figure 6.34: Real and Imaginary parts of pressure.

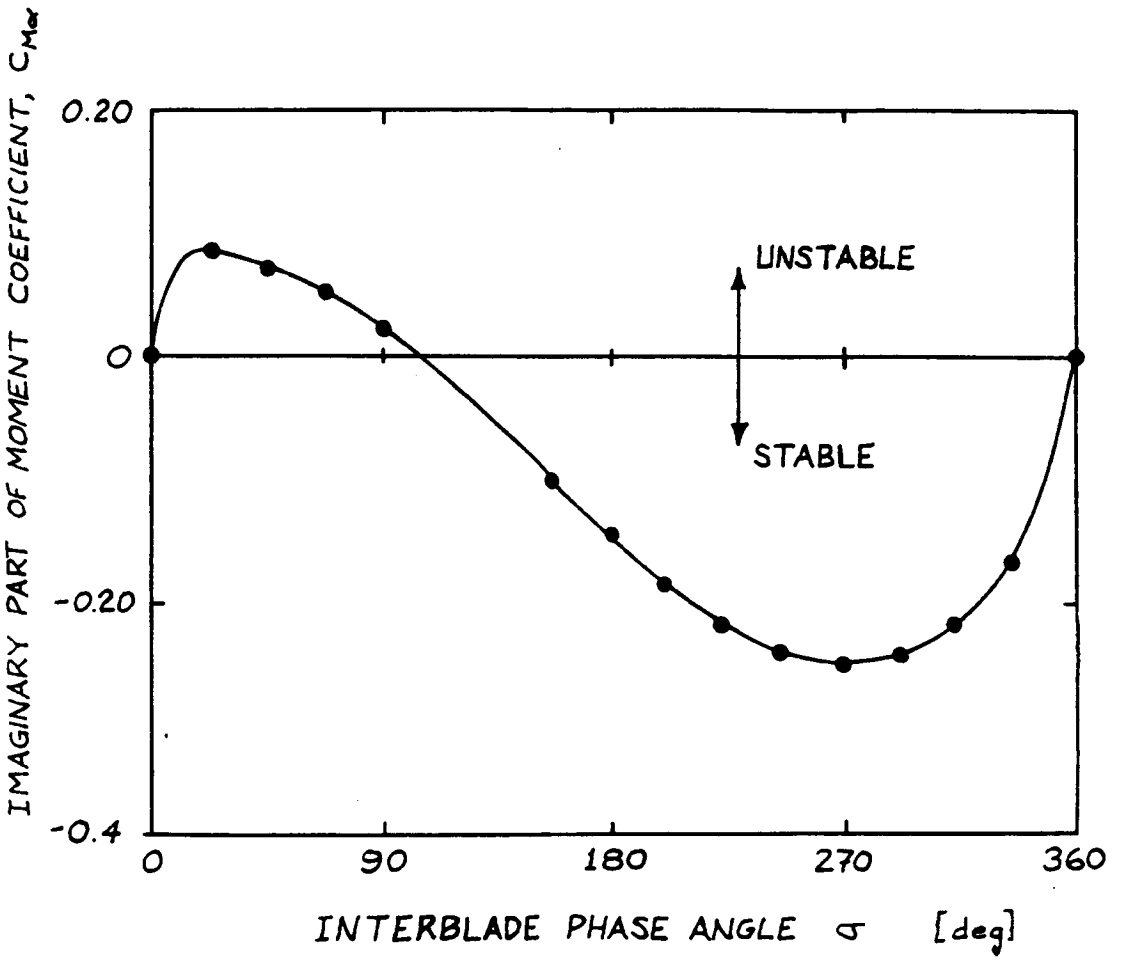

Figure 6.35: Imaginary part of unsteady moment coefficient as a function of interblade phase angle.

demonstrated that the predicted unsteady aerodynamic loads on moving airfoils are strongly influenced by the large mean flow gradients at the leading and trailing edges. Hence, these terms should be included in the linearized Euler analysis.

Aerodynamic Response Due to Vortical Gust

We wish to analyze the situation shown in Figure 6.36. Upstream of the rotor there may be some obstructions in the non-rotating frame which cause an approximately sinusoidal defect in the velocity. In the non-rotating frame, the flow is parallel, the pressure is uniform, and is uniform. In the rotating frame, however, the flow is unsteady. The blades see a sinusoidally varying inlet velocity and hence, the blades will feel an unsteady load. The object of this analysis is to predict the unsteady pressure on the blades due to this inlet distortion.

To be more specific, it is assumed that the sinusoidal variation in the axial velocity has a wavelength of 4 blade pitches. This corresponds to an interblade phase angle σ of -90 degrees. Furthermore, the tangential velocity in the tangential direction in the non-rotating frame is zero. Hence, the tangential component of velocity V in the rotating frame is due entirely to the rotational speed of the rotor. The unsteadiness the moving blades see occurs at a frequency of $\omega = -\sigma V/s$. For the case considered here, this corresponds to a *reduced* frequency of 1.275. Time $t = 0$ is defined as the time at which the maximum velocity deficit would arrive at the leading edge of the reference blade if the cascade did not alter the incoming flow.

The unsteady pressure was calculated using the present method on the grid shown in Figure 6.30. The code, which was run on an Alliant FX/8 computer, required about 8 minutes of CPU time. Shown in Figures 6.37 and 6.38 are the real and imaginary parts of the calculated unsteady pressure distribution. By integrating these pressures over the airfoil surface, one can obtain the unsteady lift and moments felt by the blade due to the inlet distortion. Also shown for comparison is the first harmonic component of the unsteady pressure as calculated by Giles using the program UNSFLO [21,22]. The method is based on the time-accurate time-marching Lax-Wendroff method of Ni [23]. Giles' code is unique in that under the right conditions a time-space transformation

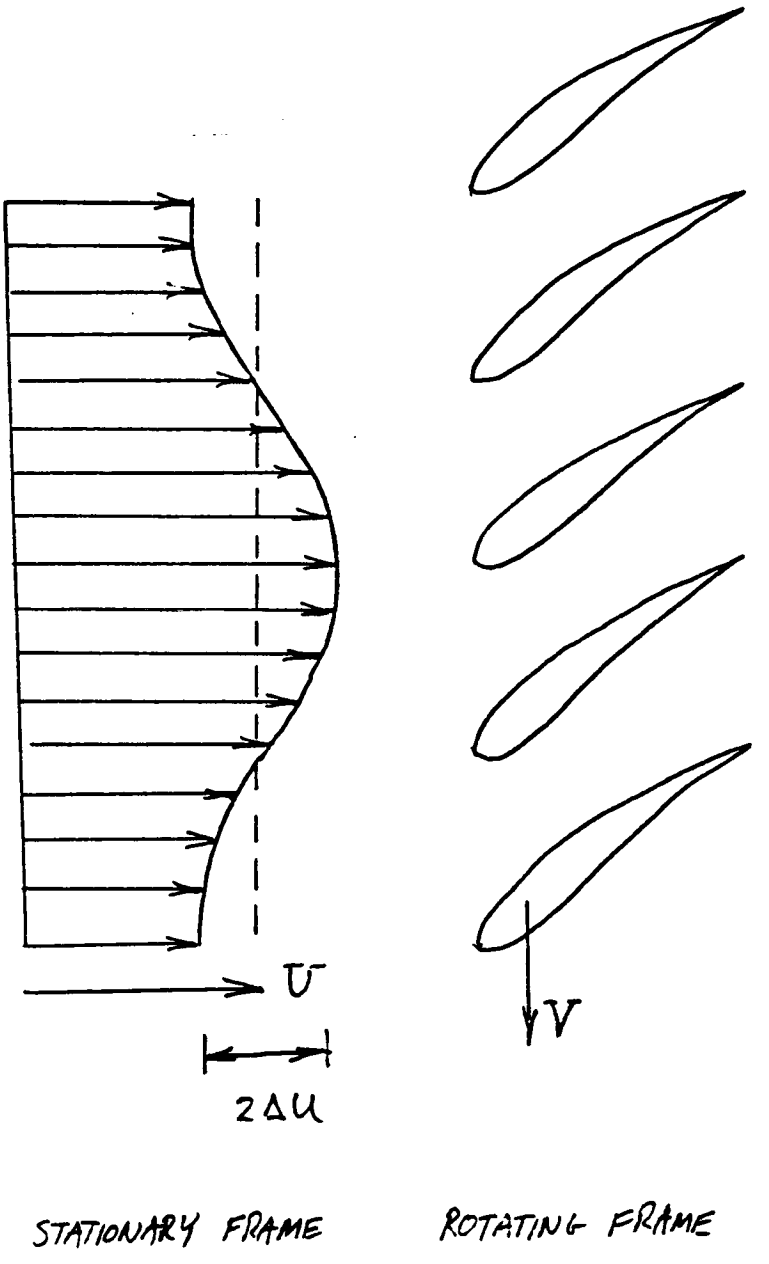

Figure 6.36: Steady inlet distortion in the non-rotating frame is seen as an unsteady distortion in the rotating frame.

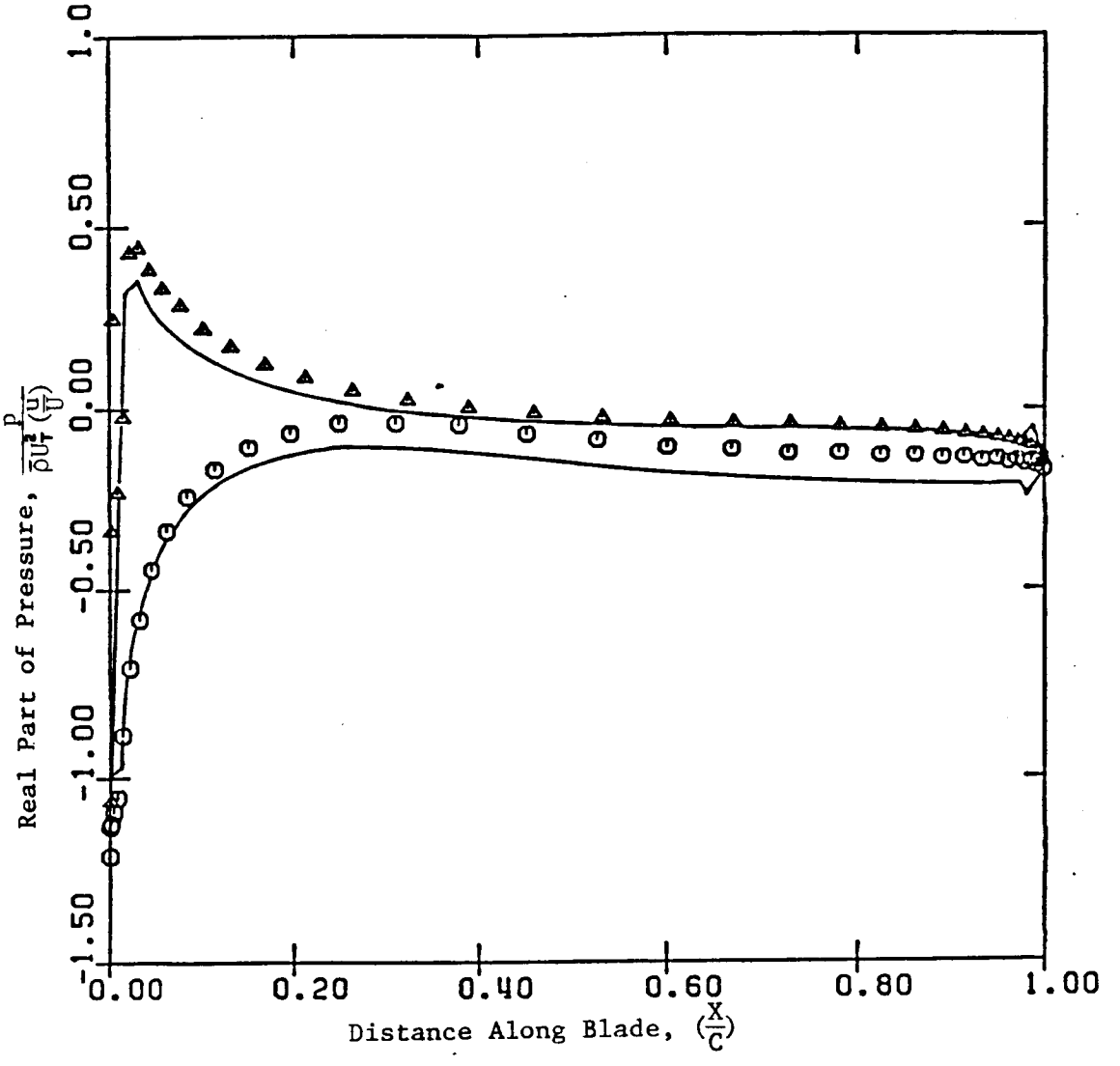

Figure 6.37: Real part of nondimensional pressure on airfoil surface due to incoming vortical gust. The interblade phase angle σ is $-\pi/2$, the reduced frequency $\overline{\omega}$ is 1.257.

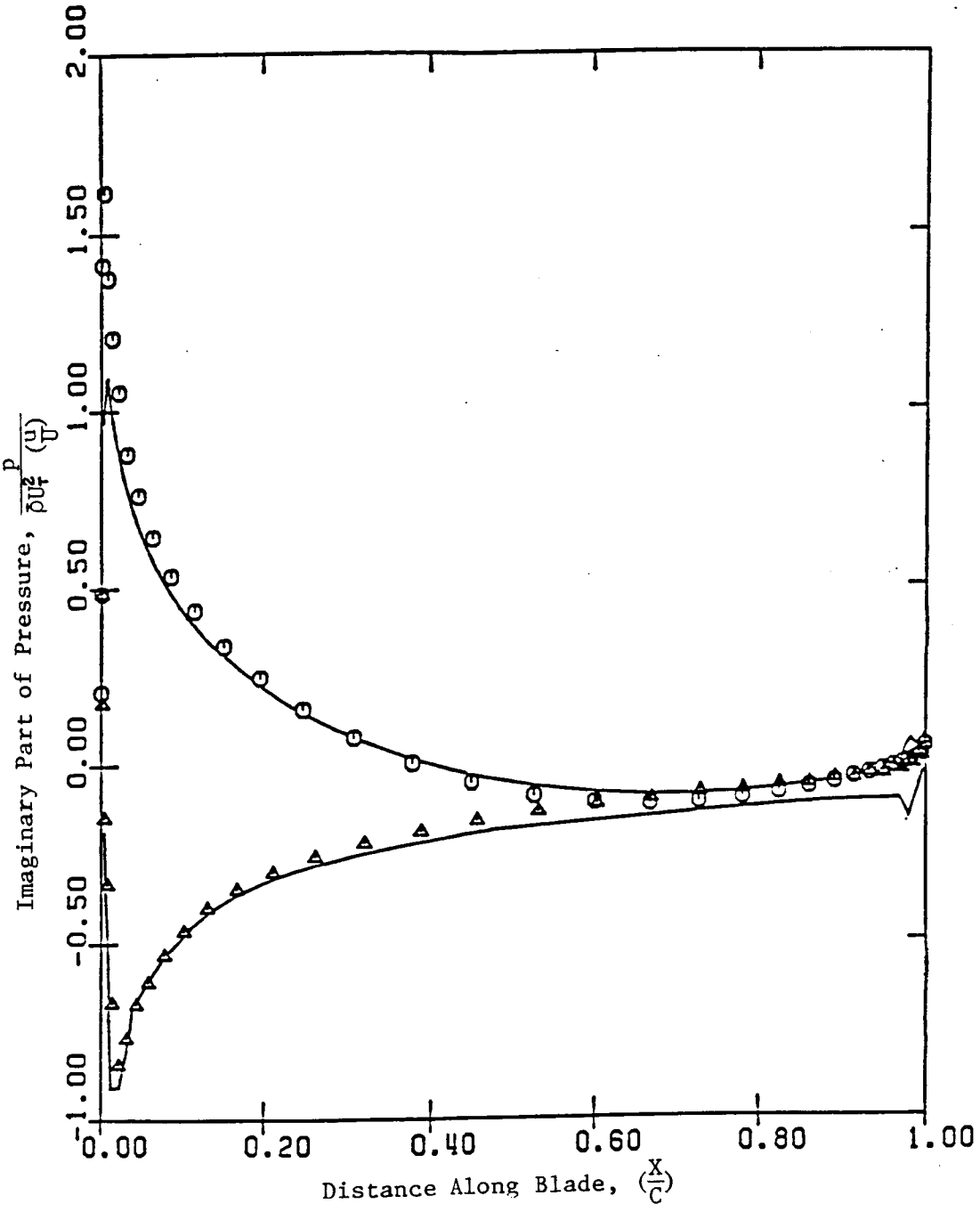

Figure 6.38: Imaginary part of nondimensional pressure on airfoil surface due to incoming vortical gust. The interblade phase angle σ is $-\pi/2$, the reduced frequency $\overline{\omega}$ is 1.257.

allows the time accurate flow field to be represented in a single passage. For low Mach numbers and low interblade phase angles, however, more than one blade passage may be needed in the calculation. For this particular example, four blade passages were required. The grid was therefore fairly large with 125×100 nodes. Eight periods were calculated so as to reach a periodic state. This required about 8 hours of computer time on an Alliant FX/8 computer. The time history of the computed pressure distribution was Fourier transformed so that the results could be compared directly to the present method. Note that the agreement is good, although not exact. At the present time, it is not clear what the cause of these difference are. However, considering the good qualitative agreement, and the fact that the present method required a factor of 60 less CPU time, these preliminary results are encouraging.

Incoming Entropy Wave

The final example is similar to the vortical wave problem. In this case, an incoming entropy wave is considered. As before, the disturbance is steady in the non-rotating frame but unsteady in the rotating frame. Upstream in the non-rotating frame, the pressure and velocity are uniform. The density, however, is nonuniform with a spatial wavelength in the tangential direction of 4 blade pitches. Hence, in the rotating frame, the rotor sees a uniform velocity and pressure but an unsteady density variation. This sort of disturbance does not cause much of a pressure disturbance on the airfoil surface, but is useful for illustrating the far-field boundary conditions as well as the slip plane representation of the wake.

Shown in Figure 6.39 is the real part of the unsteady density. Note that at the upstream far-field boundary, the contours are aligned with the axial direction. This stems from the fact that the entropy wave is steady in the non-rotating frame. As the entropy wave is convected through the blade row, the portion which passes over the suction surface arrives at the trailing edge sooner that that which passes over the pressure surface due to the circulation around the airfoil. Hence, at the wake, the density is not continuous. Note that this jump in density is easily handled with the present wake fitting technique. Finally, the wave passes out the downstream far-field

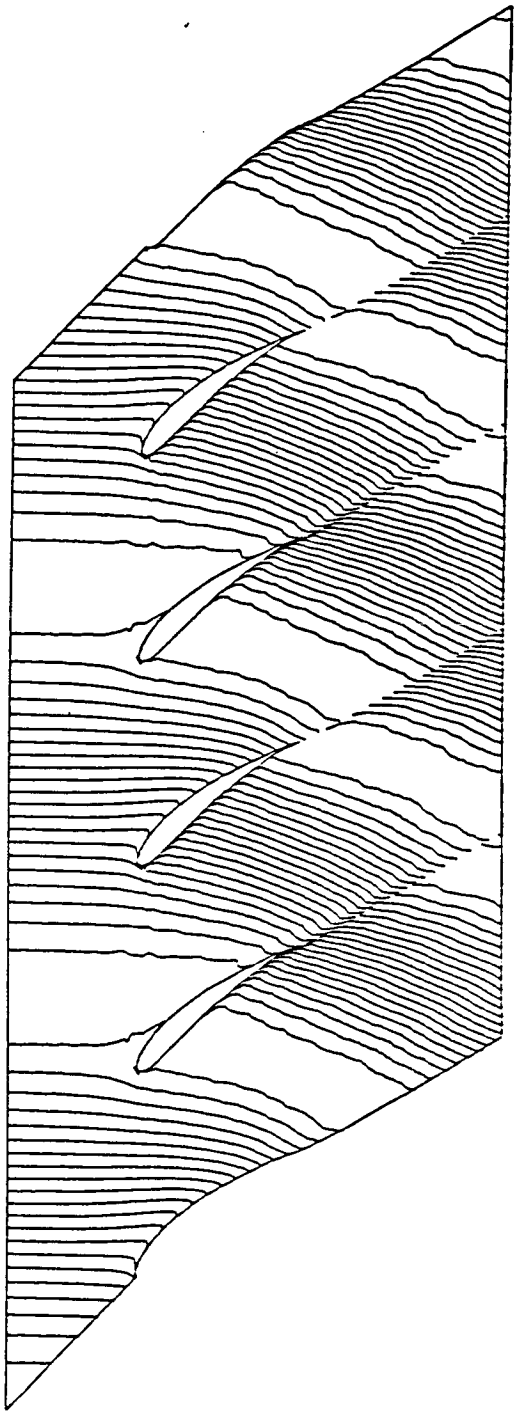

Figure 6.39: Unsteady density contours for incoming entropy wave. The interblade phase angle σ is $-\pi/2$, the reduced frequency $\overline{\omega}$ is 1.257. Note the jump in density across the wake.

boundary without causing any artificial reflections.

Chapter 7

Conclusions and Recommendations

Conclusions

In this report, a method for predicting unsteady transonic flows in turbomachinery has been presented. Such an analysis is needed to model accurately the aeroelastic behavior of turbomachinery blading. The method is based on the linearized Euler equations equations and fully accounts for blade loading, blade geometry, shock motion, and wake motion. Unlike the linearized potential methods, the generation of vorticity and entropy at shocks is correctly modelled. As shown, the steady and unsteady entropy generated at shocks has a profound influence on shock motion, and hence, the present method is thought to provide significantly better predictions of unsteady transonic flows.

The analysis is divided into two main parts. In the first part, the mean flow through the cascade is determined by solving the nonlinear steady Euler equations. Then, the nonlinear time-dependent Euler equations are linearized about this operating point to produce a set of linear variable-coefficient equations which describe the small-amplitude unsteady flow. The further assumption is made that the unsteady flow is harmonic in time so that the explicit time dependency is removed from the linearized equations. These linear equations are discretized on a computational grid and solved directly. This approach is significantly more efficient than the alternative time-marching technique

with the present method needing one to two orders of magnitude less computing time to solve a typical unsteady flow problem. Furthermore, because the present method is direct, there is no CFL restriction on the size of computational cells. Hence, grid resolution may be increased in local areas such as leading and trailing edges without much increased computational effort.

To determine the steady flow, a Newton-iteration procedure is used which reduces the problem of solving the nonlinear Euler equations to one of solving a series of linearized equations, each similar to the linearized unsteady equations. The steady linearized Euler equations are discretized on a computational grid and solved directly. The Newton-iteration procedure, as demonstrated in numerical examples, converges very quickly with typical subsonic flow problems converging in about five iterations while transonic problems may require up to ten iterations. In addition, the similarity of the Newton-iteration equations to the linearized unsteady equations greatly simplifies the effort required to develop both a steady and an unsteady Euler code. In fact, many parts of the two codes are nearly identical.

Another important feature of the present analysis is the use of steady and unsteady shock and wake fitting. Shocks and wakes are modelled as discontinuities with jump conditions applied at the shock and wake surfaces. For steady flow calculations, shock fitting provides an accurate prediction of the shock position without excessively fine grids. As demonstrated, fairly coarse grids produce surprisingly good predictions of shock positions. But more importantly, the accuracy of the steady solution will affect the accuracy of the unsteady solution. Hence, the precise modelling of shocks obtained using shock fitting is essential if one is to accurately predict the *unsteady* shock motion, and in turn, the unsteady aerodynamic loads on transonic airfoils.

Results of the present method are presented for a wide variety of steady and unsteady flow problems. These include quasi-one-dimensional channel flows, two-dimensional channel flows, and two-dimensional cascade flows. In many cases, these results were compared to those obtained from time-marching Euler codes. Generally, the agreement between the two methods is quite good, except for flows with large levels of unsteadiness. This is especially encouraging considering the computational efficiency of the present

method.

Also investigated were the effects nonlinearities have on unsteady flows. From both asymptotic analysis and numerical experiments, the effects of nonlinearities are seen to appear with the square of the flow unsteadiness. As a rough rule of thumb, the linearized theory correctly predicts the component of the flow at the fundamental frequency so long as the unsteadiness in the flow is no more than about ten percent of the steady flow. Hence, the linearized Euler analysis is not only useful for predicting the onset of flutter, but also for analyzing disturbances of moderate size such as inlet distortion and rotor/stator interaction.

Recommendations for Future Work

Although the present work has demonstrated the advantages the linearized Euler method offers in analyzing unsteady transonic flows, some issues need to be resolved before the method can be successfully applied in aeroelastic analyses of transonic cascades. The major issue is the fitting of shocks. The shock-fitting algorithm presented in this report requires that the shock be aligned with a computational grid line on a logically rectangular grid. This restricts the shock geometries which can be analyzed to normal shocks on fairly unskewed grids. Therefore, transonic flows through staggered cascade cannot be currently analyzed. with stagger. Using triangular conservation cells rather than quadrilateral cells may alleviate this problem. Furthermore, a shock ending in the flow, as in the case of a supersonic patch, cannot be modelled. Some very preliminary efforts have been made to solve this problem with encouraging results.

Another more difficult problem is to include the effects of viscosity. In real flows, the steady and unsteady flow will be affected by such viscous effects as viscous boundary layers, shock/boundary-layer interaction, and flow separation. Attempts should be made to include these effects into the current inviscid models to improve their prediction capabilities.

Bibliography

[1] D. S. Whitehead. *Force and Moment Coefficients for Vibrating Aerofoils in Cascade.* Reports and Memoranda 3254, Aeronautical Researh Council, February 1960.

[2] D. S. Whitehead. *Bending Flutter of Unstalled Cascade Blades at Finite Deflection.* Reports and Memoranda 3386, Aeronautical Researh Council, October 1962.

[3] H. Atassi and T. J. Akai. *Aerodynamic Force and Moment on Oscillating Airfoils in Cascade.* Paper 78-GT-181, ASME, 1978.

[4] H. Atassi and T. J. Akai. *Aerodynamic and Aeroelastic Characteristics of Oscillating Loaded Cascades at Low Mach Number. Part I: Pressure Distribution, Forces, and Moments.* Paper 79-GT-111, ASME, 1979.

[5] Frank Lane and Manfred Friedman. *Theoretical Investigation of Subsonic Oscillatory Blade-Row Aerodynamics.* Technical Note 4136, NACA, 1958.

[6] D. S. Whitehead. *Vibration and Sound Generation in a Cascade of Flat Plates in Subsonic Flow.* Reports and Memoranda 3685, Aeronautical Researh Council, 1970.

[7] S. N. Smith. *Discrete Frequency Sound Generation in Axial Flow Turbomachines.* Reports and Memoranda 3709, Aeronautical Researh Council, 1972.

[8] J. M. Verdon. The unsteady aerodynamics of a finite supersonic cascade with subsonic axial flow. *Transactions of the ASME: Journal of Applied Mechanics,* 40(3):667–671, September 1973.

[9] J. M. Verdon and J. E. McCune. Unsteady supersonic cascade in subsonic axial flow. *AIAA Journal,* 13(2):193–201, February 1975.

[10] T. Nagashima and D. S. Whitehead. *Linearized Supersonic Unsteady Flow in Cascades.* Reports and Memoranda 3811, Aeronautical Researh Council, February 1977.

[11] J. J. Adamczyk and M. E. Goldstein. Unsteady flow in a supersonic cascade with subsonic leading-edge locus. *AIAA Journal,* 16(12):1248–1254, December 1978.

[12] O. O. Bendiksen. Bending-torsion flutter in supersonic cascades. *AIAA Journal,* 19(6):774–781, June 1981.

[13] O. O. Bendiksen. Role of shocks in transonic/supersonic compressor flutter. *AIAA Journal*, 24(7), July 1986.

[14] M. E. Goldstein, Willis Braun, and J. J. Adamczyk. Unsteady flow in a supersonic cascade with strong in-passage shocks. *Journal of Fluid Mechanics*, 83:569–604, 1977.

[15] J. M. Verdon and J. R. Caspar. Subsonic flow past an oscillating cascade with finite mean flow deflection. *AIAA Journal*, 18(5):540–548, May 1980.

[16] F. O. Carta. *Unsteady Gapwise Periodicity of Oscillating Cascaded Airfoils.* Paper 82-GT-286, ASME, 1982.

[17] D. S. Whitehead. *Force and Moment Coefficients for High Deflection Cascades.* CUED/A-Turbo/TR 98, University of Cambridge Department of Engineering, May 1980.

[18] J. M. Verdon and J. R. Caspar. A linearized unsteady aerodynamic analysis for transonic flows. *Journal of Fluid Mechanics*, 149:403–429, 1984.

[19] D. S. Whitehead. *The Calculation of Steady and Unsteady Transonic Flow in Cascades.* CUED/A-Turbo/TR 118, University of Cambridge Department of Engineering, 1982.

[20] R. H. Ni and F. Sisto. Numerical computation of nonstationary aerodynamics of flat plate cascades in compressible flow. *Transactions of the ASME: Journal of Engineering for Power*, 98:165–170, April 1976.

[21] Michael Giles. *UNSFLO: A Numerical Method For Unsteady Inviscid Flow in Turbomachinery.* Technical Report CFDL-TR-86-6, Massachusetts Institute of Technology, Cambridge, Massachusetts, December 1986.

[22] Michael B. Giles. *Calculation of Unsteady Wake/Rotor Interactions.* Paper AIAA-87-0006, AIAA, 1987.

[23] Ron-Ho Ni. A multiple-grid scheme for solving the euler equations. *AIAA Journal*, 20(11):1565–1571, November 1982.

[24] Michael B. Giles. *Newton Solution of Steady Two-Dimensional Transonic Flows.* PhD thesis, Massachusetts Institute of Technology, Cambrigde, Massachusetts, June 1985.

[25] Mark Drela. *Two-Dimensional Transonic Aerodynamic Design and Analysis Using the Euler Equations.* Gas Turbine Laboratory Report 187, Massachusetts Institute of Technology, Cambridge, Massachusetts, February 1986.

[26] G. Moretti. Floating shock fitting technique for imbedded shocks in unsteady multidimensional flows. In *Proceedings of the 1974 Heat Transfer and Fluid Mechanics Institute*, pages 184–201, Stanford University Press, Stanford, Calif., 1974.

[27] Gino Maretti. Circumspect exploration of multidimensional imbedded shocks. *AIAA Journal*, 14(7):894–899, July 1976.

[28] Ernest D. Eason. A review of leat-squares methods for solving partial differential equations. *International Journal for Numerical Methods in Engineering*, 10:1021–1046, 1976.

[29] Martin Becker. *The Principles and Applications of Variational Methods*, chapter 3. The M.I.T. Press, Cambridge, Massachusetts, 1964.

[30] R. J. Astley, N. J. Walkington, and W. Eversman. Accuracy and stability of finite element schemes for the duct transmission problem. *AIAA Journal*, 20(11):1547–1556, November 1982.

[31] M. Giles. *Solution of 1-D Euler Equations Using a Box Method.* CFDL-TR 84-1, Massachusetts Institute of Technology, Department of Aeronautics and Astronautics, Computational Fluid Dynamics Laboratory, February 1984.

[32] Francis B. Hildebrand. *Advanced Calculus for Applications*, pages 214–225,256–257. Prentice-Hall, Englewood Cliffs, New Jersey, 1976.

[33] Joseph M. Verdon. *Linearized Unsteady Aerodynamic Theory.* UTRC Report R85-151774-1, United Technologies Research Center, November 1985. One of several articles to be published in *AGARD Manual on Aeroelasticity in Axial-Flow Turbomachines.*

[34] Holt Ashley. Role of shocks in the "sub-transonic" flutter phenomenon. *Journal of Aircraft*, 17(3):187–197, March 1980.

[35] Dennis F. Fuglsang and Marc H. Williams. *Non-Isentropic Unsteady Transonic Small Perturbation Theory.* Paper 85-0600, AIAA, 1985.

[36] Arnold M. Kuethe and Chuen-Yen Chow. *Foundations of Aerodynamics: Bases of Aerodynamic Design*, chapter 2, 3, and 8. John Wiley and Sons, third edition, 1976.

[37] Joseph M. Verdon, John J. Adamczyk, and Joseph R. Caspar. Subsonic flow past an oscillating cascade with steady blade loading — basic formulation. In R. B. Kinney, editor, *Unsteady Aerodynamics*, pages 827–851, July 1975. Proceedings of a Symposium Held at The University of Washington, March 18-20, 1975.

[38] Michael Giles. *Non-Reflecting Boundary Conditions for the Euler Equations.* Technical Report CFDL-TR-87-1, Massachusetts Institute of Technology, Cambridge, Massachusetts, February 1987.

[39] P. E. Berry. Computation of unsteady flow in a blade passage. In *Unsteady Aerodynamics of Turbomachines and Propellers*, pages 191–203, Cambridge University Engineering Department, Cambridge, Massacusetts, September 1984.

[40] Bjorn Engquist and Andrew Majda. Absorbing boundary conditions for the numerical simulation of waves. *Mathematics of Computation*, 31(139):629–651, July 1977.

[41] J. M. Tyler and T. G. Sofrin. Stop compressor noise before it starts. *SAE Journal*, 54–60, January 1962.

[42] Howard W. Emmons. *The Numerical Solution of Compressible Fluid Flow Problems.* Technical Note 932, NACA, May 1944.

[43] Howard W. Emmons. *The Theoretical flow of a Frictionless, Adiabatic, Perfect Gas Inside of a Two-Dimensional Hyperbolic Nozzle.* Technical Note 1003, NACA, May 1946.

[44] J. F. Dannenhoffer, III and J. R. Baron. *Robost Grid Adaptation for Complex Transonic Flow.* Paper AIAA-86-0495, AIAA, 1976. Presented at the AIAA 24th Aerospace Sciences Meeting.

[45] Richard A. Shapiro and Earll M. Murman. *Cartesian Grid Finite Element Solutions to the Euler Equations.* Paper AIAA-87-0559, AIAA, 1987. Presented at the AIAA 25th Aerospace Sciences Meeting.

[46] Steven R. Allmaras and Michael B. Giles. *A Second Order Flux Split Scheme for the Unsteady 2-D Euler Equations on Arbitrary Meshes.* Paper AIAA-87-1119-CP, AIAA, 1987.

[47] Steven R. Allmaras. April 1987. Private Communication.

[48] J. P. Gostelow. *Cascade Aerodynamics*, chapter 5. Pergamon Press, 1984.

[49] Joe F. Thompson, Frank C. Thames, and Wayne Mastin. A code for numerical generation of boundary-fitted curvilinear coordinate systems on fields containing any number of arbitrary two-dimensional bodies. *Journal of Computational Physics*, 24:274–302, 1977.